Master's thesis

NTNU
Norwegian University of Science and Technology
Faculty of Information Technology and Electrical Engineering
Department of Electric Power Engineering

Gaute Lyng Rødal

Online Condition Monitoring of Synchronous Generators using Vibration Signal

Master's thesis in Electric Power Engineering
Supervisor: Arne Nysveen
June 2020

NTNU
Kunnskap for en bedre verden

Gaute Lyng Rødal

Online Condition Monitoring of Synchronous Generators using Vibration Signal

Master's thesis in Electric Power Engineering
Supervisor: Arne Nysveen
June 2020

Norwegian University of Science and Technology
Faculty of Information Technology and Electrical Engineering
Department of Electric Power Engineering

NTNU
Norwegian University of
Science and Technology

Abstract

Hydropower is among the cleanest sources of energy and accounted for 95% and 16% of the total energy production in Norway and worldwide in 2018, respectively [1, 2]. The salient-pole synchronous generator is the supreme machine used for electromechanical energy conversion in hydropower plants and its duty is in this way indispensable. This type of generator is robust and provides reliable power production, however, it may be exposed to faults that impede the operation. A serious fault can require an expensive overhaul, lead to dangerous incidents, and cause generation stoppage with huge economical losses as a consequence. Thus, detection of faults at an incipient stage before their severity intensifies is essential for profitable and stable operation, and on-line condition monitoring by measuring vibration is an effective way to diagnose a generator. However, vibration monitoring of salient-pole synchronous generators has not been explored to the extent it deserves, despite the important responsibility of these machines, which causes an urgent need for more research.

This master's thesis investigates whether and how vibration signals can be used for detection of inter-turn short circuit (ITSC) in the rotor winding and static eccentricity (SE) in salient-pole synchronous generators. A novel analytical model that considers the salient-pole geometry, stator slots, iron saturation, and the effects of the two faults is formulated and used to predict the air-gap forces in a machine with topology of a typical hydropower generator. Moreover, the same generator is modeled and simulated with the finite element method (FEM) and detailed analyses of the air-gap flux density, force density, and total force during healthy and faulty condition in the time domain and the spatial domain are conducted. The resulting stator vibration is also examined and evaluated with respect to the thesis objective.

It is found that vibration at one to six times the rotor rotational frequency and at two to four times the synchronous electrical frequency can be used to detect ITSC in the rotor and SE. Classifiers to distinguish the two faults from each other are obtained and linear equations to determine the fault severity as a function of deformation are deduced. ITSC fault is found to be more dangerous for the generator than SE based on the vibration they produce due to excitation of unnatural harmonics in the time domain and the spatial domain. SE affects the spatial force distribution as well, however, causes milder vibration due to its static nature. Moreover, time harmonics and spatial harmonics of the radial force density formulated by the novel analytical model are in good agreement with the finite element analysis (FEA) and form a reliable basis for prediction of vibration.

The thesis fulfills its objective and shows that vibration signals can be used for detection of ITSC in the rotor winding and SE in salient-pole synchronous generators by evaluating the vibration level at certain frequencies. Its findings can be regarded as valuable for fault detection and on-line condition monitoring of hydropower generators, however, experimental measurements on the investigated generator should be conducted as further work to examine the validity of the results in practical applications.

Sammendrag

Vannkraft er blant de reneste energikildene og stod for 95% og 16% av den totale energiproduksjonen i henholdsvis Norge og verden i 2018 [1, 2]. Synkrongeneratoren med utpregende poler er den enerådende maskinen brukt for elektromekanisk konvertering av energi i vannkraftanlegg og dens plikt er således uvurderlig. Til tross for at denne typen generator er robust og sørger for pålitelig kraftproduksjon, kan den bli utsatt for feil som hindrer produksjonen. En alvorlig feil kan medføre kostbare reparasjoner, skape farlige situasjoner og føre til produksjonsstopp med tilhørende store økonomiske tap. Deteksjon av feil i tidlig stadium før deres alvorlighetsgrad øker er derfor viktig for lønnsom og stabil produksjon, og kontinuerlig overvåking via vibrasjonsmålinger er en effektiv måle å diagnostisere en generator. Overvåking av vibrasjoner i synkrongeneratorer med utpregede poler har likevel ikke blitt tilstrekkelig utforsket, noe som gjør forskning på dette området nødvendig.

Denne masteroppgaven undersøker om og hvordan vibrasjonssignaler kan bli brukt til feildeteksjon av kortslutningsfeil i rotor og statisk eksentrisitet i synkrongeneratorer med utpregede poler. En ny analytisk modell som inkluderer geometrien til polene, sporene i stator, metning av jernet og konsekvensene av de to nevnte feilene har blitt utledet og brukt til å predikere kreftene i luftgapet til en maskin med liknende konstruksjon som en vannkraftgenerator. I tillegg har den samme generatoren blitt modellert og simulert med elementmetoden og detaljerte analyser av flukstettheten, krafttettheten og den totale kraften i luftgapet er presentert i tids- og romdomenet. Den resulterende statorvibrasjonen er også studert og evaluert ut ifra masteroppgavens mål.

Resultatene viser at vibrasjoner med én til seks ganger rotasjonsfrekvensen til rotoren og med to til fire ganger den synkrone, elektriske frekvensen kan bli brukt til deteksjon av kortslutningsfeil i rotor og statisk eksentrisitet. Kjennetegn på hvordan de to feilene kan skilles fra hverandre er formulert og lineære likninger som anslår feilens alvorlighetsgrad som en funksjon av deformasjon er utledet. Kortslutningsfeil er funnet til å være farligere for en generator enn statisk eksentrisitet ut ifra vibrasjonene de forårsaker, på grunn av eksitasjon av unaturlige harmoniske komponenter i både tids- og romdomenet. Statisk eksentrisitet påvirker også kreftene i rommet, men skaper svakere vibrasjoner på grunn av sin statiske oppførsel. I tillegg, tids- og romharmoniske komponenter av den radielle kraften formulert av den nye analytiske modellen samsvarer godt med analysene fra elementmetoden og skaper et pålitelig grunnlag for prediksjon av vibrasjon.

Masteroppgaven innfrir sitt mål og viser at vibrasjonssignaler kan bli brukt til deteksjon av kortslutningsfeil i rotor og statisk eksentrisitet i synkrongeneratorer med utpregede poler ved å studere vibrasjonsnivået ved spesifikke frekvenser. Funnene kan ses på som verdifulle for feildeteksjon og overvåkning av vannkraftgenertorer, selv om eksperimentelle målinger på den simulerte generatoren bør bli gjennomført i fremtiden for å undersøke gyldigheten til resultatene i praksis.

Preface and acknowledgements

This report documents the work and presents the findings of a master's thesis conducted during the spring semester of 2020 at the Norwegian University of Science and Technology (NTNU). It is the finalizing part of a five-year master program at the Department of Electric Power Engineering valued with 30 ECTS credits.

The thesis investigates a salient-pole synchronous generator during healthy and faulty operation in order to determine if and how vibration signals can be utilized for fault detection in hydropower generators. Finite element analysis has been conducted and examined with respect to changes in the magnetic field, forces, and vibration of the generator.

My supervisor professor Arne Nysveen has been important for me during this thesis. Your guidance has been crucial for keeping the project on the right track and I would like to express my sincere gratitude to you. Our meetings have been of great help and importance, as well as motivational with a sense of humor. I am grateful for being one of your students.

I would also like to heartfully thank my co-supervisor Hossein Ehya for the time and effort you have spent on me. Your skills and competence in the field of condition monitoring, signal processing, and finite element analysis combined with your eagerness to help, generosity, and high standards have been indispensable for this thesis. I wish you all the best in your Ph.D. and future work.

Finally, I would like to thank Mostafa Valavi and Joel Bergström from EDR & Medeso. Your service and technical support on modeling and simulation in Maxwell and Mechanical have been invaluable and, Mostafa, the sharing of your expertise in the field of vibration in electrical machines is highly appreciated.

Table of Contents

List of Tables

List of Figures

Abbreviations

2D	=	two-dimensional
3D	=	three-dimensional
DE	=	dynamic eccentricity
EMF	=	electromotive force
FE	=	finite element
FEA	=	finite element analysis
FEM	=	finite element method
FFT	=	fast Fourier transform
GCD	=	greatest common divisor
HHT	=	Hilbert-Huang transform
ITSC	=	inter-turn short circuit
ME	=	mixed eccentricity
MMF	=	magnetomotive force
NTNU	=	Norwegian University of Science and Technology
RPM	=	rotations per minute
SE	=	static eccentricity
UDP	=	user defined primitive
UMP	=	unbalanced magnetic pull
WT	=	wavelet transform

Symbols

b	=	magnetic flux density
B	=	amplitude of magnetic flux density
C_c	=	Carter's coefficient
f_s	=	synchronous electrical frequency (fundamental frequency)
f_r	=	rotor frequency, force density in radial direction
$\hat{f}_m$	=	amplitude of radial force density of mode *m*
f_{rr}	=	radial force density caused by the radial flux density
f_{rt}	=	radial force density caused by the tangential flux density
f_m^{res}	=	resonance frequency due to mode number m
F	=	amplitude of force density in radial direction
F_{tooth}	=	force acting on a stator tooth
$\mathcal{F}$	=	MMF
$\mathbb{F}$	=	total force
$\mathtt{F}$	=	amplitude of total force
g	=	air-gap function
g_0	=	nominal air-gap length
i	=	integer
j	=	current density
J	=	amplitude of current density
k	=	order of time harmonic
k_{sat}	=	saturation factor
K_r	=	constant related to estimation of resonance frequency in eq.
K_s	=	stator bore deformation coefficient for mode $m \geq 2$
L_s	=	stator stack length
L_t	=	tooth line
N	=	data size
m	=	mode number
N_p	=	number of phases
n_s	=	synchronous mechanical speed
n	=	summation index
p	=	number of pole pairs
q	=	number of slots per pole and phase
Q_s	=	number of slots
RD	=	Relative deformation
S	=	Fault severity
t	=	time
Y_m	=	amplitude of static deformation of stator due to mode number *m*
w_{ss}	=	width of stator slot

α_1, α_2	=	geometry coefficient of salient poles
δ_{ec}	=	degree of eccentricity
θ_r	=	angular mechanical position of rotor
Λ	=	air-gap permeance
μ_0	=	permeability of free space
τ	=	slot pitch
υ	=	summation index (any whole number)
ϕ	=	angle along inner surface of stator
ϕ_r	=	angle in the rotor reference plane
ψ	=	eccentricity angle
ω_s	=	angular electrical synchronous frequency = $2\pi f_s$
ω_r	=	angular velocity of rotor

Subscripts

de, se, me	=	DE, SE, ME
s	=	synchronous
r	=	radial, rotor
t	=	tangential

Superscripts

r	=	rotor
s	=	stator

Chapter 1

Introduction

1.1 Motivation

The synchronous generator has been among the most important electro-mechanical power conversion devices for a long time. One of the very first specimens was built in 1887, had four salient poles, a three-phase armature, and produced 2.8 kW [3]. Since then, the machine has been a key component in the power production industry as the energy demand of the world has experienced exponential growth, and tremendous design improvements have been made to optimize loss reduction, cooling systems, winding insulation, and rated parameters. In this process, various forms of condition monitoring have played an important role to evaluate the performance and health of the evolving construction layouts. Today, synchronous generators are found in every power station and are producers of nearly all electrical energy consumed in the world [4, 5]. One sixth of this originates from hydroelectric generators in which salient poles are the supreme rotor design and, in 2018, such generators were responsible for 95% of the total energy production in Norway [1]. Evidently, the duty of salient-pole synchronous generators is essential today and has been so for over a hundred years.

As a result of continuous layout refinements since 1887, the typical hydropower generator today is large with a production capacity up to hundreds of megawatts. It is a complex machine with delicate design to achieve high efficiency, and usually custom-made to fit specific input and output parameters, as well as geographical and practical circumstances related to construction, transportation, and assembling of generator parts. Consequently, the investment costs of a new generator are huge and a dependable operation without unscheduled production stoppages and expensive instaurations are fundamental for a profitable service. As a result, a synchronous generator is robust with a lifetime that can exceed a hundred years. However, even though reliable, it may be subject to some types of faults.

The consequences of a generator fault can be serious, both in terms of economical losses and regarding the safety of the power station employees. Hence, detecting defects at an

early stage, such that their severity can be limited, is important. Proper condition monitoring is therefore of high value and numerous methods to diagnose a generator have been developed over the years. Since most faults affect the machine's vibration behavior, condition monitoring by using vibration signals can reveal detailed information about its health. Vibration measurements are easy to perform and can be executed while the generator is on-line without production adjustments. Such advantages have made vibration monitoring a well-established method with long traditions and over 90 years of accumulated literature [6]. However, vibration monitoring of salient-pole synchronous generators is not explored to the same extent as asynchronous or round-rotor machines, despite their important duty. Thus, research in this area is desirable and can be an important contributor to safe and profitable power production.

1.2 Objective and scope

The objective of this thesis is to determine whether and how online condition monitoring with vibration signals can be used for detection and classification of faults in salient-pole synchronous generators. This type of machine is chosen such that the findings are applicable to hydropower generators. In order to achieve the objective, analyses of the vibration frequency spectrum acquired from numerical finite element simulations of a salient-pole synchronous generator located in the National Smart Grid Laboratory at NTNU have been conducted. The thesis also contains detailed examinations of the flux and forces that arise in the generator air-gap during healthy and faulty operation in order to explain the origin of the vibration. Moreover, a novel analytical model has been formulated and used for prediction of force characteristics and later compared to the numerical simulation results. The investigated faults have been static eccentricity and inter-turn short circuit in the rotor winding during no load and loaded condition, and of different severities in order to decide if the fault degree can be classified from the frequency content of the vibration. The methods utilized during this thesis project are explained in detail to enlighten and benefit forthcoming master students, or other researchers, that shall work on similar projects.

1.3 Annotations

A part of the original plan for this master's thesis project was to perform experimental vibration measurements on the mentioned laboratory generator. The measurements were to be used to compare practice to theory and simulations. However, the outbreak of the coronavirus SARS-CoV-2 forced the Norwegian Directorate of Health to shut down all universities from the 12th of March 2020, including NTNU and the National Smart Grid Laboratory, to the end of the project. Consequently, practical laboratory work was not possible to conduct and the thesis was redefined to contain theoretical analyses only. Some additional theoretical tasks that were not a part of the original plan have been added to the thesis as a consequence.

This master's thesis is a continuation of a preliminary specialization project conducted during the fall 2019 with the same field of interest [7]. The specialization project report contained a literature review on condition monitoring of rotating electrical machines and results from a few simulations with constituting analyses. The simulation software used in this thesis are the same as for the specialization project and the procedure of creating the simulation models is similar. According to novel guidelines on plagiarism from NTNU, it is therefore stated explicitly here that some of the content in chapter 2, 3, 4, and 7 is adopted from the specialization project and contains similarities [8].

1.4 Outline

Chapter 2 forms a foundation of theory relevant for the further content of the thesis. This includes general principles of salient-pole synchronous generators, presentation of the two investigated faults, and theoretical details on vibration and how it is used for condition monitoring. Moreover, a novel analytical model that describes the forces in a salient-pole synchronous generator in a way that has not published done before is formulated.

Chapter 3 presents the generator that has been used for simulations and evaluates the analytical model from chapter 2 based on the characteristics of the generator.

Chapter 4 outlines the process of modeling and simulation, which includes detailed descriptions about how the generator model is created and simulated in the two simulation software utilized in the thesis.

Chapter 5 presents and briefly comments on the simulation results.

Chapter 6 contains discussion of the content included in chapter 3, 4 and 5 in light of the theory presented in chapter 3 and other literature. This chapter also suggests tasks for further work.

Chapter 7 concludes the thesis by summarizing the most important findings.

Chapter 2

Theoretical background

Initially, this chapter presents some fundamental concepts of the generator typically found in hydropower stations, which is the three-phase salient-pole synchronous generator with rotor field winding, relevant for the continuation of the thesis. Moreover, the investigated faults, that is short circuit and static eccentricity, are described. Basic knowledge of generators and electromagnetism is assumed to be in the reader's possession. Further, how vibration signals are used for condition monitoring is presented and, finally, vibration in generators is elaborated and the forces that produce vibration in the generator stator are mathematically modeled.

2.1 Functioning of salient-pole synchronous generators

Due to the relatively low rotating speed of hydro turbines, compared to for instance steam turbines, the generators used in hydropower stations normally have a number of poles equal to six or more. The low speed allows for large diameter rotors with short axial length and poles projected out of the core without problematic centrifugal forces. Copper winding is twirled around the pole body and carries direct current that produces magnetomotive force (MMF), and following a magnetic field, in the air-gap between the rotor and the stator. The stator is equipped with an armature, usually embedded in slots, that capture the rotor flux and electromotive force (EMF) is produced as a result.

The working principle of a generator relies on linkage of magnetic flux between the rotor and the stator. Rotation of the shaft causes the magnetic field produced by direct current in the rotor winding to move in the air-gap. Despite the constant current, this field is alternating due to the spatial distribution the generator's salient poles and the change of polarity from one pole to the next. The air-gap magnetic field produced by the rotor consists, thus, of traveling waves which cause flux variations and induced EMF in the stator windings. If a load is connected to the generator terminals, alternating currents will flow from the armature to the load. In this way, mechanical energy in the rotating shaft, for instance provided by falling water in a hydropower generator, is converted into electrical energy in terms of current and voltage.

As for the currents in the rotor winding, MMF is produced by the currents flowing in the armature during loaded operation, causing another magnetic field in the air-gap. The combination of time-varying induced EMF and the spatial distribution of a balanced three-phase winding causes the stator magnetic field to consist of traveling waves as well. Known as the armature reaction, this field interacts with the rotor field and creates a resultant air-gap magnetic field. The resultant field is the basis for development of electrical power in the generator, as well as excitation of forces and vibration as later described in section 2.2.5.

Each rotor pole pair contribute with one period of the fundamental flux component which moves in the air-gap in the same direction and at the same angular speed as the rotor. Seen from the stator, which is stationary, each pole pair induces one period of EMF in the armature. Thus, the electrical frequency in a synchronous generator is p times the mechanical frequency, where p is the number of pole pairs. The MMF and magnetic field produced by the stator, given that currents flow in the armature, are synchronous with the fields produced by the rotor, meaning that they rotate at the same speed, consequently called the synchronous speed. This leads to the coherence in equation 2.1. ω_s is the synchronous electrical angular speed given in electrical radians per second, ω_r is the synchronous mechanical angular speed of the rotor given in mechanical radians per second, n_s is the synchronous mechanical speed given in rotations per minute (RPM) and f_s is the synchronous electrical frequency given in hertz (Hz). f_s is also called the fundamental frequency and is the frequency of the induced EMF in the armature and the current that flows to the load.

$$\omega_s = p\omega_r \Rightarrow 2\pi f_s = p\frac{2\pi n_s}{60} \Rightarrow n_s = \frac{60 f_s}{p} \tag{2.1}$$

The fundamental component of the resultant air-gap magnetic field, hereafter simply termed the air-gap magnetic field, provides a sinusoidal shape of the field with a frequency equal to f_s. However, in healthy salient-pole generators, the air-gap magnetic field consists of several additional time harmonics with lower amplitude and higher frequency than the fundamental. Harmonics with frequency equal to odd multiples of the fundamental occur naturally in no load operation, mainly due to the shape of the salient poles and the concentrated field winding [9]. During balanced load operation, these are also produced by the MMF from the sinusoidal armature currents interacting with the non-uniform air-gap permeance created by the salient-poles [10]. It can be seen from Fourier analysis that the even number harmonics caused by the stator currents are eliminated because of their symmetric shape within a period of π radians. Thus, in a salient-pole generator, the frequency spectrum of the air-gap magnetic field in the time domain will contain the fundamental component at f_s Hz and odd multiple harmonics with frequency $3f_s, 5f_s, 7f_s$, and so on. The magnetic field also consists of harmonics in the spatial domain determined by the generator topology. All flux density harmonics, in both the time domain and the spatial domain, affect the forces in the air-gap and the resulting vibration behavior of the generator. Time harmonics, spatial harmonics and their influence on vibration are further explained in section 2.2.5.

2.2 Faults in synchronous generators

A generator can suffer from faults categorized as either mechanical or electrical. Examples of mechanical faults are eccentricity, broken damper bar, bearing deterioration, and core looseness, while short circuits and open circuits in the field winding or in the armature are possible electrical faults [11, 12]. Their origin can vary between a wide range of reasons, from improper manufacturing or installation to detrimental operation or ambient conditions. Section 2.2 is dedicated to two faults in synchronous generators: short circuit in the rotor field winding and eccentricity. Each of them is described and common causes and consequences are presented.

2.2.1 Short circuit in the rotor field winding

A short circuit caused by insulation defect is one of the most common faults in synchronous generators, accounting for more than 40 % of all faults [12, 13]. The winding insulation will deteriorate over time due to thermal, electrical, and mechanical stresses, as well as aging and contamination, which normally results in insulation breakdown after some decades of normal operation. This process can be accelerated by sub-optimal operating conditions such as thermal cycling caused by large, frequent load variations, excessive vibration, or overheating due to overloading or insufficient cooling. Additionally, other generator faults such as broken damper bars and eccentricity can lead to temperature rise in the rotor core and increased thermal stress on the field winding insulation. Short circuits in the field winding can happen between a turn and a grounded point, called a ground fault, or between turns, called an inter-turn fault.

The danger of a ground fault is the possibility of developing a second instance. While a single ground fault itself is not dangerous to the generator, two separated short circuits to ground can result in large ground loop currents and severe damage of the winding in a short time [14]. A first instance establishes a new ground reference which increases the stress at other points in the winding, such that a second ground fault is more likely to occur than the first. Due to the serious consequences of multiple ground faults, the first short circuit to ground is usually handled by an alarm or immediate trip of a protection relay.

As the insulation between turns usually degrades before the insulation between conductors and ground, inter-turn faults are more common than ground faults. A single ITSC may not be critical for the machine and can be present without affecting the generator performance to a noticeable degree. When an ITSC occurs, the number of ampere-turns in the affected pole is decreased, which weakens the MMF and magnetic field produced by that pole. Thus, the effect of one short circuit will depend on the total number of ampere-turns per pole, and generators with few rotor turns will suffer relatively larger consequences than generators with more turns.

The weakened magnetic field produced by a pole with an ITSC causes asymmetrical air-gap field which results in distorted force distribution and possibly increased vibration. The air-gap forces in a generator are attracting, or pulling, the stator towards the rotor and the modified force distribution caused by an ITSC is therefore called unbalanced magnetic pull (UMP). UMP can increase the vibration level of the generator which intensifies the mechanical stress on the winding insulation. Additionally, uneven distribution of losses in the coil due to a short circuit changes the rotor heating pattern, leading to increased thermal stress. Non-uniform rotor temperature can also develop shaft bowing and further increased UMP. These consequences can aggravate the fault by short-circuiting several turns, which will further amplify the UMP. Enhanced insulation deterioration will also increase the probability of ground fault occurrence. Hence, even a single short-circuit with minor impact on the generator's operation may develop into a highly destructive machine condition, and monitoring with early fault detection is clearly of high value.

2.2.2 Eccentricity

A generator suffers from eccentricity when there is a non-uniform distance between the rotor and the stator in the air-gap. The fault is termed SE if the minimal air-gap length varies only by position, excluding the natural variations caused by the saliency of the rotor poles. During this state, as shown in figure 2.1 (b), the center of the rotor is shifted from the stator center while it rotates around its center axis. On the other hand, when dynamic eccentricity (DE) occurs, the rotor revolves around the stator center axis while having center point displaced from the stator. In this way, as seen in figure 2.1 (c), the minimum air-gap length varies with both position and time. Static and dynamic eccentricity can exist simultaneously, which is termed mixed eccentricity (ME) and shown in figure 2.1 (d). It has been found that operation with SE can develop DE and, thus, cause ME [15, 16].

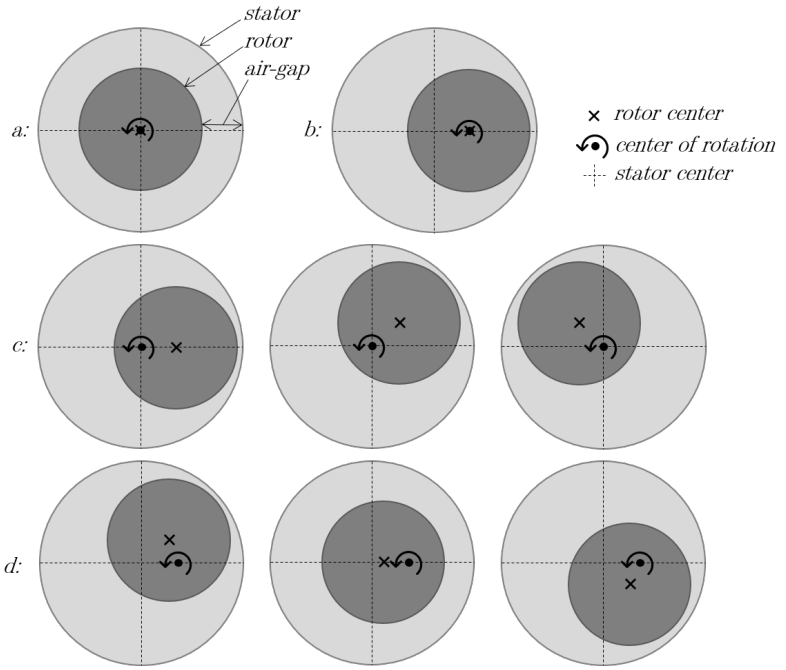

Figure 2.1: Stator and rotor during healthy operation (a), static eccentricity (b), and three time instants of dynamic eccentricity (c) and mixed eccentricity (d). Air-gap length is not scaled to reality.

Displaced or bent rotor shaft, bearing deterioration, loose bolts, rotor unbalance, and non-circular stator are typical causes of eccentricity [15, 17, 18]. It is a mechanical fault that may exist inherently in hydropower generators as the large dimensions and the high ratio between the stator diameter and the air-gap makes some degree of eccentric imperfections hard to avoid during manufacturing or assembly [19].

The asymmetry caused by eccentricity results in UMP with vibration as a possible symptom [12, 15]. Eccentricity also wears the bearings which can further increase the fault degree and create a vicious loop that eventually ends in rotor-to-stator rub and serious damages. Other consequences are reduced generator efficiency, amplified torque pulsation, and distorted harmonic content for the terminal voltage and currents. Furthermore, the increased vibration level may result in acoustic noise and development of other faults, such as short circuits due to intensified insulation deterioration. The consequences of eccentricity show that proper monitoring of this fault is of great importance.

Regardless of type, a serious generator fault can be critical for a power plant. Repairing costs are huge due to the size, weight, and complexity of the machine, and the instauration process requires a stoppage in power production leading to loss of income. If the defect is irreparable on-site, tailored parts must be manufactured and transported which can be a costly, long-lasting, and practically challenging process, especially in Norway where the

hydropower stations are often located in remote areas or inside the mountain. If a fault leads to shutdown of the machine, other aggregates may be overloaded in an attempt to compensate for lost power production and the risk of new incidents increases. Moreover, a generator in faulty operation can result in dangerous situations or a harmful work environment for the station's employees.

As presented above, even a small instance of ITSC in the rotor winding or eccentricity can evolve over time with gradually increasing severity. In addition to damaging the machine, such faults impact the entire generator behavior which leads to development of new defects if they are not cleared in time. Conclusively, effective condition monitoring with early fault detection is highly desirable.

2.2.3 Condition monitoring using vibration

The history of fault diagnosis and protection of synchronous generators is as archaic as the machines themselves [11]. Before the time of effective condition monitoring systems, protective relays played a lonely role in ensuring safe and reliable operation. Such protection systems differ from condition monitoring as they are retroactive, which means that they are designed to act only once a fault has evolved into a state so severe that a defined limit is reached, usually by tripping a circuit breaker. Before this happens, the fault can cause damage to the generator and, as mentioned in the previous section, the unscheduled shutdown of power production caused by disconnection of the generator may result in undesirable consequences. As well summarized in [20]: "the function of protective equipment is not the preventive one its name would imply, in that it takes action only after a fault has occurred; it is the ambulance at the foot of the cliff rather than the fence at the top". Condition monitoring aims to be this "fence at the top".

Condition monitoring consists of evaluation of the generator's health throughout its serviceable life [6]. It allows for condition-based maintenance with proactive intervention and provides safety and confidence to the operator, corresponding to the metaphorical fence at the top of the cliff. This is a unique ability compared to the two other types of maintenance: breakdown maintenance and fixed-time interval maintenance. The former relies on a strategy that runs the equipment until it breaks and then replaces it. This can only be effective if there is a substantial amount of redundant capacity and a breakdown does not cause a complete system failure. Fixed-time interval maintenance is based on occasional inspections on the machine and allows for scheduling of outage work and load planning. However, the lack of continuous monitoring may cause development of severe faults between the inspections. Moreover, it is estimated that only 10 percent of components replaced during fixed-interval maintenance actually need to be replaced at that time, which implies that 90 percent of the component replacements are unnecessary [6].

On the other hand, a condition monitoring system is designed to recognize incipient faults such that the plant operator is alerted as early as possible and significant damage to the generator can be prevented. This type of system gives freedom to schedule outages in the most convenient manner depending on the fault characteristics and the production fore-

cast, resulting in lower downtime and milder consequences. Furthermore, the operator can be regularly updated on the generator performance, which can improve operational efficiency. Conclusively, condition monitoring can lead to significant benefits such as greater plant efficiency, reduced economical losses from production shutdown, lower replacement costs due to detection at low fault severity, and improved safety due to optimized maintenance. It also allows the operator to build a database that can be used for trend analysis and further improvements in maintenance planning.

The desire for reliable recognition of faults in rotating electrical machines has throughout the years led to development of numerous monitoring techniques. One of the first references to machine condition monitoring can be found in [21] from 1921 where the author proposed a method for diagnosis of motors by analyzing temperature changes in the cooling air. Today, analyses of electrical parameters such as output currents and voltages, chemical properties such as lubrication oil, or mechanical quantities such as rotational speed and vibration are used for determining the health of the machine. Different methods offer different advantages and there are some general characteristics that determine the value of a method.

An important factor of a monitoring technique is on-line execution, which means that it can be utilized without shutting down the generator. A method that requires shutdown can cause sub-optimal production stoppages and does not give a continuous overview of the machine's health. In addition, some faults present during operation may not be present during standstill, due to lack of for instance centrifugal forces or currents in the stator windings. Another important aspect of a monitoring technique is whether or not it is invasive. An invasive method relies on installing equipment inside the generator, such as flux sensors in the air-gap, while the non-invasive collect information from external parameters, such as terminal voltage. Invasive methods are usually disadvantageous as accessing internal places might be impractical or even impossible.

Most of the electrical or mechanical faults in synchronous generators affect the air-gap magnetic field, leading to distorted air-gap forces and change of vibration behavior. Thus, measuring vibration is an effective monitoring method that provides detailed information about the condition of the generator. With almost one hundred years of accumulated research, it is a well-established technique with standards covering a wide range of electrical machines [6]. The vast development of hardware and software the last decades has enabled usage of advanced measuring equipment, signal processing tools and artificial intelligence, which have been utilized in detection of various faults, such as eccentricity [16, 22–26], winding faults in stator and rotor [27–32], broken damper bar [33–39], rotor unbalance [40–42] and bearing faults [41, 43–45]. However, an extensive literature review conducted during the specialization project preceding this thesis revealed that most of the research on vibration in rotating electrical machines concerns asynchronous machines, and salient-pole synchronous generators have not been explored to a sufficient extent [11, 12, 16, 22–48]. Further research to establish reliable methods for detection and classification of faults in these machines is therefore needed.

Vibration is normally measured with accelerometers, where piezoelectric shear-type being most commonly used [49]. As shown in figure 2.2, the proof masses in these transducers oscillate in a direction perpendicular to the base, which is mounted on the area of interest with a magnet or a screw. Consequently, the piezoelectric elements move in a shear manner and generate an electric charge that is transmitted through the output connector to a signal processing device. Piezoelectric accelerometers have a natural frequency far above the frequency range of the vibration, normally at least 20 kHz, such that the output signal is not distorted by resonance in the transducer.

As faults in both rotor and stator can distort the air-gap magnetic field that leads to vibration in the stator, mounting an accelerometer on the stator frame or on the outside of the yoke is an efficient way to measure generator vibration. These areas are easily accessible and do not require generator shutdown, making it a non-invasive and on-line monitoring technique.

Besides acceleration, vibration if often described by means of displacements and velocity, which are quantities easily obtained from integration of the measured acceleration. For fault detection purposes, a frequency domain representation provides useful information and signal processing tools such as fast Fourier transform (FFT) is commonly employed to produce the frequency spectrum.

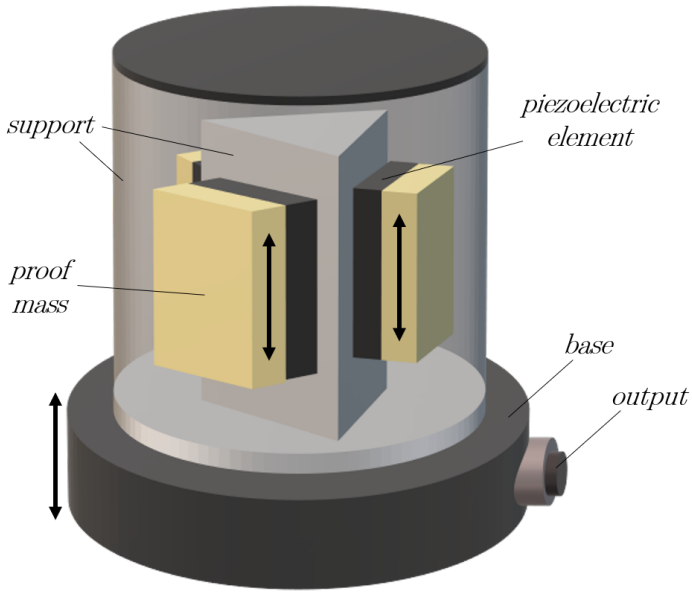

Figure 2.2: Piezoelectric shear-type accelerometer.

2.2.4 Signal processing

Processing of a signal lays the foundation for proper analysis and is an important part of condition monitoring. Time domain characteristics of a signal, such as its amplitude, period, or variance, can be used used to reveal information about the signal source. However, the frequency spectrum is more commonly utilized in condition monitoring of electrical machines and various processing tools can be employed to transform the time domain information to a frequency domain representation. Different tools have dissimilar mathematical structures that make them suitable for analysis of different types of signals. Two important properties of a signal when a suitable processing tool is to be chosen are stationarity and linearity. In a stationary signal, the mean, variance, and autocorrelation do not change over time, such that it can be expressed as a discrete sum of sinusoidal terms. In a linear signal, the output, for instance the flux produced by a field winding, changes linearly when the input, for instance the current in the field winding, is changed.

Examples of signal processing tools commonly used for various kinds of signals are Hilbert-Huang transform (HHT) and wavelet transform (WT). The former decomposes the signal to obtain its instantaneous frequencies and can be applied to non-stationary and non-linear signals. The latter represents the signal by wavelets in a way that preserves time information while extracting the frequencies. This means that information about when certain frequencies occur in the signal is obtained which makes this tool well suited for non-stationary and linear signals. However, in a generator that operates at steady-state, the flux density at a certain point in the air-gap repeats itself every rotor revolution. The same accounts for signals that are results of the flux, such as force and vibration. These are stationary and linear with periodic behavior, which makes processing tools as HHT and WT unnecessary. As a result, the fast Fourier transform (FFT) is by far the most utilized signal processing tool for condition monitoring in rotating electrical machines in the literature.

The FFT calculates the discrete Fourier transform, which involves converting a discrete time signal recorded at fixed sampling intervals into a discrete representation of the signal in the frequency domain, in an accelerated manner by significantly reducing the computing complexity compared to normal discrete Fourier transform. Besides being a time-efficient algorithm, the FFT is easy to handle with low requirements for signal processing skills and less complicated as tools like HHT and WT. As a result of its mathematical structure, the FFT is not convenient for analysis of non-stationary and non-linear signals. However, due to the design and repetitive operating behavior of rotating electrical machines, and as condition monitoring usually takes place during steady-state operation, the measured signal from generators is both stationary and linear which makes the FFT well suited for condition monitoring.

An FFT can be adjusted to the signal characteristics to enhance the quality of the transformation. One of these is the choice of window function, where the window represents the shape of the function used to analyze the time signal. How well a window fits the variations in the signal affects the quality of the produced frequency spectrum. Another adjustment is the choice of sampling frequency such that the desired frequency resolution

is obtained. Frequency resolution is equal to the sampling frequency divided by the number of data points used in the FFT and, according to the Nyquist sampling theorem, the highest frequency that appears in the spectrum is half of the sampling frequency.

2.2.5 Vibration in salient-pole synchronous generators

Vibration in rotating electrical machines is mainly caused by radial forces acting on the stator through the air-gap, which again descends from the resultant air-gap magnetic field [49]. The forces in the air-gap can be decomposed into radial and tangential components, whereas the tangential component creates useful electromagnetic torque and forms the basis for power generation, while the radial component is the reason for vibration. They can be expressed as force per square meter, hereafter termed force density, by calculating the Maxwell stress tensor according to equation 2.2 in the tangential direction and 2.3 in the radial direction.

$$f_t = \frac{1}{\mu_0}(b_r b_t) \tag{2.2}$$

$$f_r = \frac{1}{2\mu_0}(b_r^2 - b_t^2) \tag{2.3}$$

b_r and b_t represent the radial and tangential component of the air-gap magnetic flux density, respectively, and μ_0 is the vacuum permeability. Due to the small air-gap length in rotating electrical machines, and the fact that the magnetic permeability of the rotor and stator iron is much higher than of air, the air-gap flux density is dominated by the radial component. Consequently, b_t has traditionally been neglected in analytical calculations of the radial air-gap forces [49–53]. More recent studies have shown that the tangential component can cause a noteworthy impact on radial force calculation in large round-rotor permanent-magnet machines with open slots which should be kept in mind when generators with salient poles are investigated as well [54, 55].

In general, the radial force density from equation 2.3 can be expressed as equation 2.4, where $\hat{f}$ is the amplitude, t and ϕ represent the time and angular position, respectively, ω_r denotes the angular speed of the rotor, k is the time harmonic order and m is the spatial harmonic order. f_r is a radial force density wave that causes attraction between the rotor and the stator, and it rotates in the air-gap with an angular speed of $k\omega_r/m$, either in the same or opposite direction of the rotor [49, 50]. It acts on the stator teeth surface that faces the air-gap and a total tooth force propagates into the stator yoke where it can cause significant deformations. This total force acting on a tooth can be calculated by integrating the force density over the tooth line, L_t, and multiplying with the stator stack length, L_s, as shown in equation 2.5 and figure 2.3.

$$f_r(\phi, t) = \hat{f} cos(k\omega_r t - m\phi) \tag{2.4}$$

$$F_{tooth} = L_s \int_{L_t} f_r \, dl \tag{2.5}$$

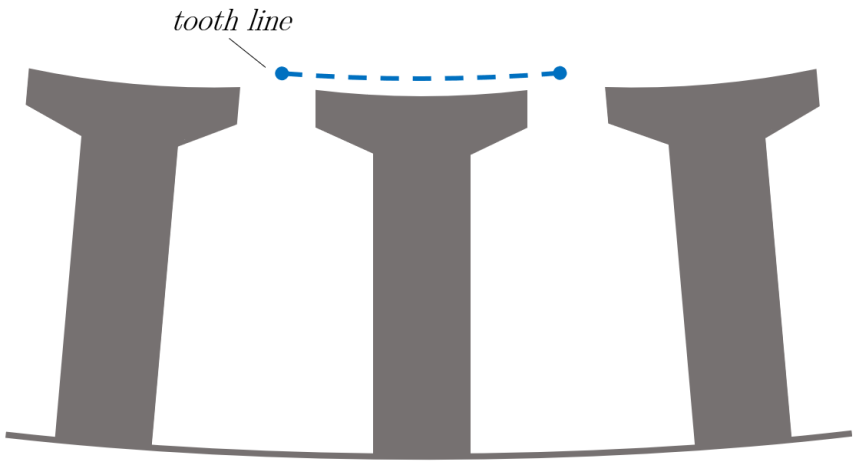

Figure 2.3: Stator teeth and the tooth line of the midmost tooth.

2.2.5.1 Time harmonics and spatial harmonics

According to equation 2.4, the radial force density in the air-gap is a function of both time and position. A general wave f_r is characterized by a time harmonic order, k, dependent on its electrical frequency in the time domain, and by a spatial harmonic order, m, dependent on its periodicity in the spatial domain. In relation to condition monitoring, time harmonics are important because their frequency decides the frequency of vibration. This can be used for fault detection through measurements with accelerometers and is also linked to resonance. Moreover, the vibration of a generator at a certain frequency depends on the amplitude of the radial forces with this frequency, which can be found from the harmonics obtained through FFT of a simulated or measured time domain signal. Spatial harmonics are also important as their order has a great impact on the stator deformation caused by a force wave. To understand the origin of vibration in a generator, both time harmonics and spatial harmonics must be considered and this section aims to clarify some important features of these two force characteristics.

Time harmonics

Time harmonics are results of time-varying phenomena, such as the alternating stator currents and the revolving rotor. The magnetic flux field produced by a balanced three-phase armature rotates in the air-gap with the same fundamental frequency as the currents, for instance 50 Hz. According to Maxwell stress tensor in equation 2.3, the radial force density peaks whenever the flux is at its maximum and its minimum. Thus, the main time harmonic

of f_r has twice the frequency of the main flux harmonic, that is twice the fundamental frequency. In synchronous machines, the rotational speed of the rotor is synchronized with the stator current frequency based on the number of poles according to equation 2.1. Consequently, even at no load operation, the air-gap magnetic field, and thus f_r, consist of time harmonics produced by the rotating poles similar to those of the stator field. The order of the fundamental flux density harmonic equals the number of pole pairs, which make $k = 2p$ the time harmonic order for the main force density component, where p is the number of pole pairs.

As mentioned in section 2.1, the magnetic field also consists of harmonics with orders equal to odd multiples of the fundamental, which produce natural time harmonics of higher orders in the force density distribution as well. These are results of the interaction between two harmonics in the air-gap flux density, either between two components from the stator field, two components from the rotor field, or one from each. An interaction means that their frequencies and spatial orders are subtracted or added and can be explained mathematically with trigonometric identities in the following way. From Maxwell stress tensor in equation 2.3, the radial air-gap force density is calculated from the square of the air-gap magnetic flux density, which can be expressed as a summation of several cosine terms that represent all the various harmonics from the rotor field and the stator field. When the expression for the air-gap flux density is squared, all these terms are multiplied together. Consequently, and according to the cosine identity $Acos(a) \cdot Bcos(b) = \frac{AB}{2}cos(a \pm b)$, every force density harmonic is a result of the multiplication, or the interaction, between two flux harmonics. The multiplication can be between two flux harmonics of the same order or with different orders. Hence, the air-gap force density of a generator with synchronous electrical frequency equal to 50 Hz and natural flux density harmonics at 50 Hz, 150 Hz, 250 Hz, ..., has time harmonics of frequency 100 Hz, 200 Hz, 300 Hz, ... with $k = 2p, 4p, 6p...$, respectively.

Determination of the time distribution of the force density in a generator can be done by measuring the flux density at a fixed location in the air-gap, achieved by a sensor attached to the edge of a tooth, and calculating the Maxwell stress tensor. This is exemplified for a eight-pole 50 Hz generator in figure 2.4, where the blue point on the rightmost tooth represents a flux measuring sensor. The sensor capture the varying field produced by the rotating poles, and the stator currents if the generator is loaded, as a function of time. For the same generator, figure 2.5 illustrates the waveform of the acquired flux density field (top) and the calculated force density field (bottom) during one rotor revolution. It is highly simplified by including only the fundamental component of the magnetic field and, thus, only the main force density time harmonic. The frequency of these signals can be found by measuring how many times one period passes by the fixed sensor per second and the corresponding time harmonic order, k, can be read from in the signal as the number of periods per revolution. Thus, the k of the flux signal is four and equal to the generator's number of pole pairs due to the alternating positive and negative excitation of the field winding from one pole to the next, while the k of the force signal is eight and equal to the number of poles.

If the generator suffers from a fault that changes the time variation of the flux density, the force density will also be affected. Consequently, the frequency spectrum will be enriched by unnatural time harmonics. These can appear in between the natural components in the frequency spectrum, then termed interharmonics, or between the fundamental and zero hertz, called subharmonics. Faults that may induce interharmonics and subharmonics are dynamic eccentricity, ITSC in the filed winding, or unbalance in the line currents.

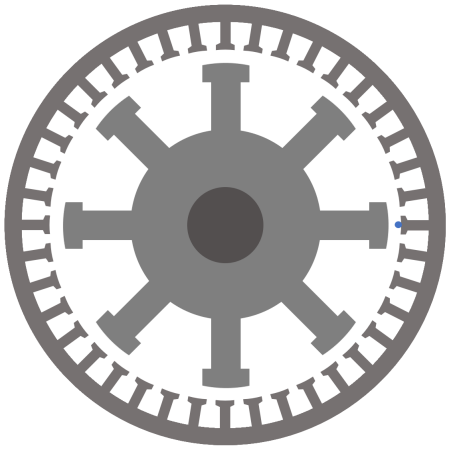

Figure 2.4: Generator with a single measuring point for acquirement of time distributions. Windings are excluded from the figure.

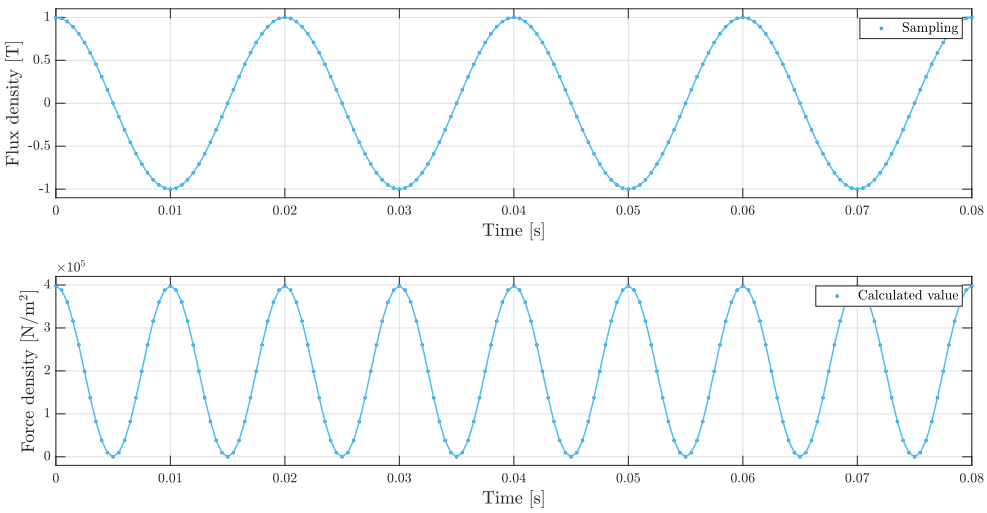

Figure 2.5: Time distribution of simplified air-gap flux density (top) and force density (bottom) acquired by the measuring point.

Spatial harmonics
Spatial harmonics, on the other hand, are time-independent and results of geometrical properties such as the stator slots, distribution of the stator winding, saturation of the stator teeth, and the rotor pole saliency. The spatial order m of a force density wave f_r describes the number of periods that are distributed around the air-gap. The main spatial harmonic in the force density will have m equal to the number of poles. As for the time harmonics, this is generated by the square of the main spatial flux density harmonic which has order equal to the number of pole pairs. Spatial force density harmonics will appear at multiples of the main component due to interactions between natural spatial flux density harmonics as described above.

Moreover, the stator slots induce spatial harmonics in the flux density determined by the number of slots, Q_s, and the number of pole pairs, p, according to equation 2.6 [54]. The interaction between these and the main flux density harmonic of order $m = p$ will cause spatial force density harmonics of orders according to equation 2.7.

$$m_{slot,flux} = Q_s \pm p \tag{2.6}$$
$$m_{slot,force} = Q_s, \;\; Q_s \pm 2p. \tag{2.7}$$

As will be elaborated further in the next subsection, the forces of low spatial harmonic orders normally cause the worst vibration due to their impact on deformation in the stator. The number of identical magnetic parts of the generator is decisive for the lowest spatial periodicity of the forces and, consequently, the lowest harmonic order. This number can be determined based on the generator's number of stator slots and rotor poles [56]. Specifically, the lowest non-zero order that occurs naturally in a generator in no load operation is equal to the greatest common divisor (GCD) between the number of slots and the number of poles. Thus, some generators can have a spatial harmonic of low order due to their topology and potentially a high vibration level even during healthy operation.

Conclusively, some of the prominent force density spatial harmonic orders in a healthy generator are the number of poles and its multiples, the ones related to the stator slots, and the GCD between the number of slots and poles. Other less dominant harmonics may also be present due to different geometrical properties.

The air-gap of a generator with a fault that distorts the spatial distribution of the flux density will contain unnatural spatial harmonics. As described above, interaction between these will result in additional spatial harmonics in the force density spectrum as well. For instance, two flux density harmonics with orders that differ by one will interact and produce a force density harmonic with $m = 1$. As mentioned, subharmonics are most important for vibration due to their low m and eccentricity and ITSC in the field winding are examples of faults that may induce subharmonics due to the UMP they impose to the air-gap.

Determination of the spatial distribution of the air-gap force density is hardly feasible in practice for real hydropower generators. In contrast to finding the time distribution, which requires one fixed point of flux measurement, deciding the spatial distribution requires flux measuring sensors installed along the entire inner circumference of the stator. This is illustrated in figure 2.6 where each blue point represents a flux measuring sensor located three mechanical degrees apart from each other. In this way, the flux around the air-gap can be measured at a single time instant and Maxwell stress tensor can be calculated for each point. Figure 2.7 illustrates the acquired flux density and force density signal as a function of the angular position when only a single arbitrary flux density wave is considered as an example. The order of the signals can be recognized by their number of periods and the force is a result of multiplying the flux wave with itself such that the order is summated and increased from two to four.

If the spatial distribution is to be measured, the flux sensors should be placed with minimal spacing between each other and at the same distance from the rotor center for accurate and reliable acquirement of the spatial distribution. This could be problematic with a slotted stator. Furthermore, the wires that transfer the measurement from each sensor would be impractical to handle and wireless sensors are usually larger in size and could be infeasible to install in the air-gap. A synchronous measurement at the exact same time instant for all sensor may also be a challenge. Consequently, finding the spatial distribution of the force density in a real generator is in practice not achievable. However, due to its important relation to how vibration in the stator is produced, analysis of the spatial distribution through analytical models or numerical software simulations can help understand the generator's vibration behavior and is therefore of high value for condition monitoring.

It should be mentioned here that it is possible to find the dominant vibration mode of a generator through vibration measurements with several accelerometers distributed around the stator [57]. This is called mode observation and provides the order of the spatial force density harmonic that has the largest impact on the vibration, which is usually the lowest order. However, this does not provide the full spatial distribution of all the air-gap forces as the arrangement in figure 2.6.

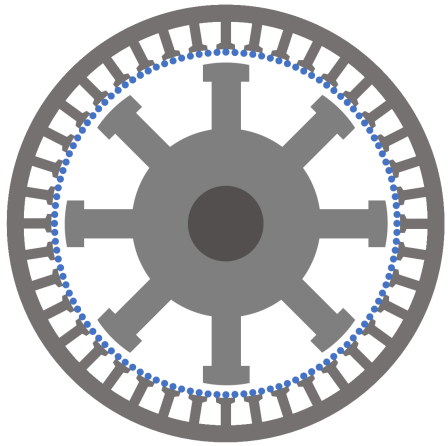

Figure 2.6: Generator with measuring points distributed along the inner surface of the stator for acquirement of spatial distributions. Windings are excluded from the figure.

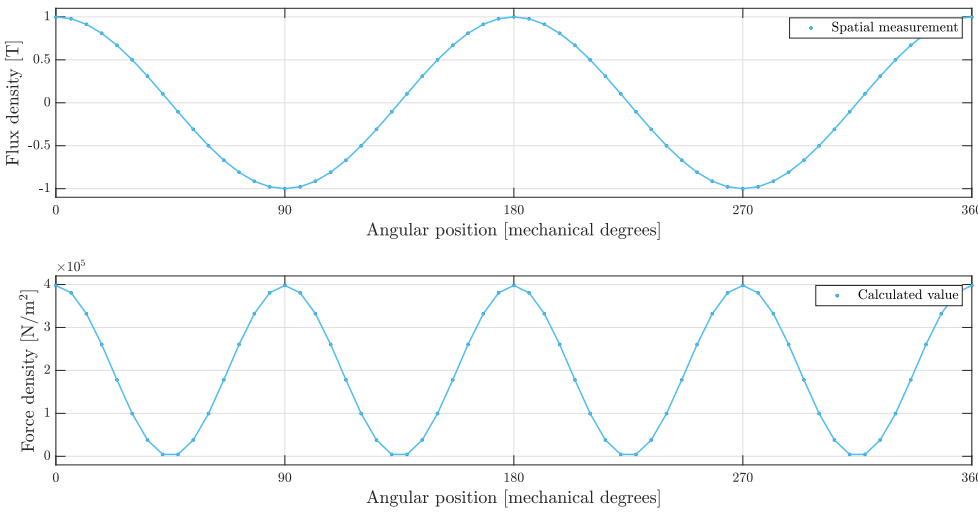

Figure 2.7: Spatial distribution of simplified air-gap flux density (top) and force density (bottom) acquired by the distributed measuring points.

As seen, the time distribution of the force density can be found by measuring the flux over a period of time at a fixed location in the stator, while the spatial distribution can be acquired by measurements around the entire air-gap at a specific time instant. In the simplified examples given above for an eight-pole 50 Hz generator, only the main time harmonic and the fourth spatial harmonic are present in the air-gap, meaning that there is a single force

density wave with frequency 100 Hz, which corresponds to a time harmonic order $k = 16$, and with spatial harmonic order $m = 4$. That is, $f_r(\phi, t) = \hat{f}cos(16\omega_r t - 4\phi)$. Both k and m, combined with the rotating angular velocity of the rotor, is decisive for the speed of which the wave rotates in the air-gap, given by $k\omega_r/m$. Seen from another perspective: the rotating speed of the force wave determines its frequency based on how many spatial periods it consists of.

The coherence between k and m for a given force density wave is of interest because the force wave's frequency corresponds to the frequency of vibration produced by that wave, while the spatial harmonic order has a high influence on the magnitude of the produced vibration. During healthy operation, the amount of time harmonics and spatial harmonics in the air-gap is limited to the naturally occurring components. Thus, it can be assumed that the spatial harmonics belong to forces with frequencies equal to the main force density time harmonic and its multiples. However, during faulty operation when the frequency content of the magnetic field is changed from healthy condition, the relationship between k and m is not as easily determined due to the high number of interactions that happen in the air-gap. It may vary from fault type to faulty type and there can be several waves with different k that have the same m, and vice versa [58, 59]. This means that a specific spatial harmonic may influence the vibration level of the generator at more than one frequency. Thus, estimations on the coherence between k and m can be difficult to obtain.

2.2.5.2 Mode number and deformation

The *m* in equation 2.4, which represent the spatial harmonic order, is also called mode number and is the most important parameter for investigating vibration due to its significant impact on how the stator responses to radial forces [49]. A low mode number represents a force wave with few maxima and long wavelength and these are usually the most harmful waves for vibration. In fact, as shown in equation 2.8, the amplitude of the static deformation in the stator yoke due to mode number *m*, that is Y_m, is inversely proportional to m^4 for $m \geq 2$ [50]. K_s is a coefficient determined by dimensions and structural properties of the stator and $\hat{f}_m$ is the amplitude the radial force density wave with the specific spatial harmonic order m.

$$Y_m = \frac{K_s \hat{f}_m}{(m^2 - 1)^2}, \qquad m \geq 2 \tag{2.8}$$

As indicated by equation 2.8, the static deformation for a specific mode is proportional to the amplitude of the force density wave with that spatial harmonic order. More importantly, the m^4 term in the denominator shows that the low mode numbers more easily cause severe deformation and is therefore the most important in vibration analysis. In fact, according to [50], it is not practically useful to consider forces having mode numbers higher than eight as they will not cause noteworthy deformation. For the special case when

$m = 1$, Y_m can be estimated based on different generator dimensions than included in K_s.

Vibration is directly related to static deformation as the air-gap forces vary with sinusoidal behavior causing oscillating deformation, which is vibration. Thus, the dominant vibration, that means the vibration with the highest amplitude, is therefore generally the one of the lowest mode. The frequency of oscillation caused by a force wave is decided by the wave's frequency represented by the time harmonic order, k. However, as described in section 2.2.5.1, the relationship between k and m can be complex and the frequency at which the deformation takes place is not included in equation 2.8. This means that the spatial harmonic of order m, with amplitude $\hat{f}_m$ in the above equations, may cause vibration at several frequencies.

In reality, calculation of stator deformation is complicated and should be carried out with numerical simulation software. Structural support may influence both natural vibration frequencies of the stator and the amplitude of the deformation, which is not in included in the analytical expression for Y_m. In short, equation 2.8 is not sufficient for complete vibration calculation. Moreover, the equation contains no time domain characteristics of the forces which are important from a condition monitoring point of view where the frequency of vibration may be used for fault detection. However, it provide an understanding of how different spatial orders of radial force produce deformation in the stator yoke and shows the importance of low mode forces for vibration.

The coefficient K_s introduced in equation 2.8 illustrates how the stator geometry influences the vibration. It can be expressed as

$$K_s = \frac{12RR_y^3}{ET_y^3}, \tag{2.9}$$

where R is the internal radius of the stator according to figure 2.8, R_y is the average yoke radius, T_y is the radial thickness of the yoke and E is the stiffness coefficient Young's modulus [50]. Hydropower generators usually have a large rotor diameter which makes R and R_y relatively large compared to T_y. Y_m increases with K_s, which further emphasizes the importance of vibration from magnetic forces in hydropower generators.

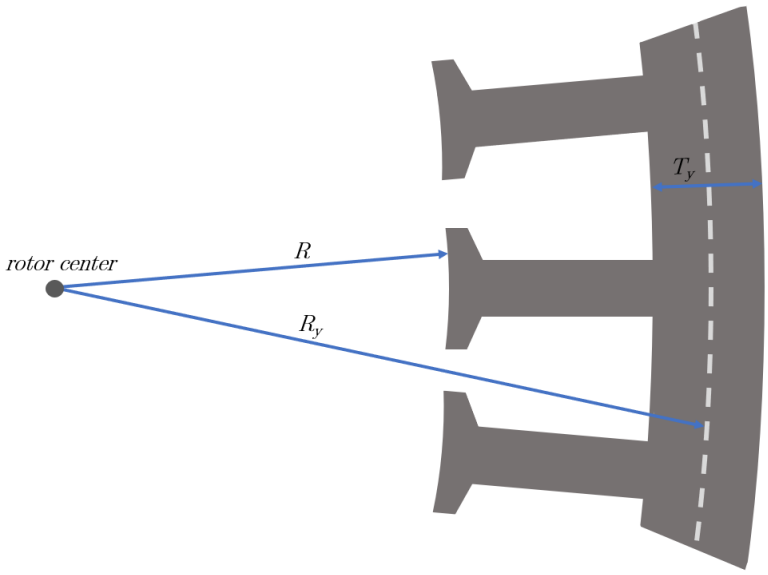

Figure 2.8: Stator geometry parameters used for the estimation of static deformation.

The mode number of a force density wave also corresponds to the number of attraction points imposed on the stator. Figure 2.9 depicts how the radial force acts on the stator yoke for different m. The red arrows represent the points of maximum attraction and the red, broken lines show how the stator is deformed at a given time instant. The black arrows illustrate that the deformation rotates around the stator circumference according to the speed of the waves. The asymmetric attraction during $m = 1$ is a symptom of UMP. As the mode number increases, the attraction points become symmetrical with lower amplitude, reducing the deformation severity. If $m = 0$ there is a uniform attraction between the stator and the rotor along the air-gap and the vibration is termed pulsating.

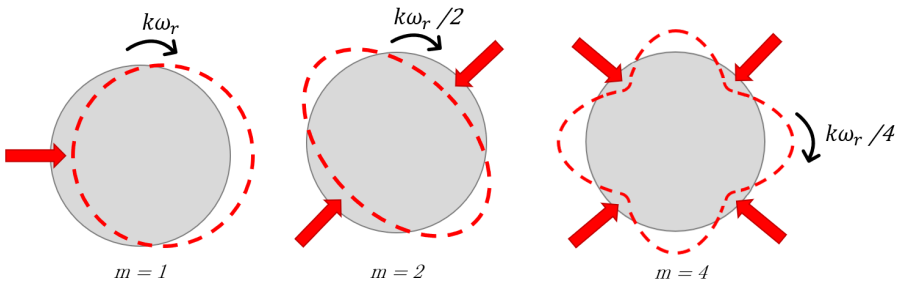

Figure 2.9: Deformed shape (red, broken lines) and original shape (grey) of the stator for different mode numbers.

2.2.5.3 Resonance

An important aspect of vibration that is not included in equation 2.8 is resonance. All systems have frequencies at which they tend to oscillate naturally determined by their geometry, material properties, and supporting structure. These natural frequencies also depend on the mode number of the vibration, such that in a given system, the natural frequency of an oscillation with a given mode number m_1 is different from the natural frequency of an oscillation of mode m_2 due to the way the stator is deformed. If an excited air-gap force with mode number m_1 has an electrical frequency at or sufficiently close to the natural vibration frequency of mode m_1, resonance occurs and the resulting vibration is significantly amplified.

Natural frequencies are not easy to predict in complex mechanical systems such as electrical machines, and numerical methods should be used for accurate computation [50]. Simple analytical estimations can, however, illustrate the relationship between natural frequencies and modes numbers. For $m \geq 2$, the natural frequency for a given mode, f_{nat}^{m}, is proportional to the following term [50]:

$$f_{nat}^{m} \propto \frac{m(m^2-1)}{\sqrt{m^2+1}}. \tag{2.10}$$

Equation 2.10 shows that the natural frequency increases with the mode number. Consequently, if low mode vibration is excited, the corresponding natural frequency could be sufficiently low and intensify the vibration. This further emphasizes the importance of low mode forces.

The FEM is a commonly utilized technique for simulation of electrical machines in the literature. This is a technique that divides the area of interest into smaller parts called finite elements. The magnetic field within each element is represented by partial differential equations which are assembled into a sparse matrix equation system and thereafter solved numerically, from which a solution for the whole model is obtained. Using the FEM for determination of the natural frequencies of a generator is called modal analysis. During a modal analysis, no forces are applied to the stator and only the structural details are considered. Supporting structure is likely to have a stiffening effect on the stator which increases the resonance frequencies and should be included [50]. Modal analysis is an important part of the design process of a generator to ensure that its natural frequencies are well separated from the natural vibration of the machine before it is constructed. It is also valuable to be aware of the natural frequencies of the investigated generator during condition monitoring such that possible amplifications in the measured vibration signal can be explained.

2.2.6 Analytical modeling of the air-gap force

Using processing tools to extract the frequency content of an acquired vibration signal is an important part of condition monitoring and knowing what the various components of the spectrum represent is essential for diagnosis. Such knowledge can be obtained by comparing simulation results of healthy and faulty conditions to each other or through development of analytical models that describe the vibration-producing forces mathematically.

As mentioned, FEA is commonly used when electrical machines are examined. The FEM provides results with high accuracy but requires a significant amount of computational resources. On the other hand, analytical models describe the area of interest in a more approximate fashion. Consequently, they are not as computational expensive but their solutions can still be sufficient for simple representation of the magnetic quantities in the air-gap. Moreover, they can provide a greater understanding of the underlying physics, since FEM software are usually designed with user-friendly interface that hides the mathematical procedures. These advantages have led to development of various analytical methods for describing forces in generators and their intention is usually to extract the frequencies that appear during faulty operation for condition monitoring purposes.

In this section, the forces in a salient-pole synchronous generator that suffers from eccentricity or ITSC in the rotor winding has been analytically modeled by using a method called permeance-wave. The permeance-wave method treats the air-gap permeance, MMF, and flux density as circumferential distributed along the air-gap such that they can be modeled and expressed as waves. Thereafter, the Maxwell stress tensor and the tooth line integration can be utilized to calculate the radial force density and the total force. These two quantities, the force density in particular, are important parts of this thesis and broadly analyzed in the following chapters.

In the literature, the permeance-wave method has been utilized for describing the distribution of forces in synchronous and asynchronous machines. For instance, [16] expresses the radial force density in induction motors with static eccentricity, stator slots and saturation taken into account, [18] formulates the UMP caused by SE and DE in permanent magnet synchronous motors with slotted stator and saturation effects considered, [22] finds the UMP caused by SE and DE in induction motors with smooth stators, [51] includes the rotor geometry and stator slot effects in calculation of the radial force density of healthy salient-pole synchronous generators by neglecting saturation, [60] formulates the radial air-gap forces in healthy wound rotor induction machines by considering the effects of stator slots and magnetic saturation, [61] formulates the UMP caused by rotor eccentricity in generators with round rotor and smooth stator surface and [62] computes the radial force density in permanent magnet-assisted synchronous reluctance machines.

However, through extensive exploration of published research during this thesis combined with a literature review conducted as a part of the preliminary specialization project, there was found no published work that presents an accurate representation of forces in faulty salient-pole synchronous generators. Thus, this is done here by taking into account the

geometry of the salient poles of the rotor, the geometry of the slots in the stator, the effects of iron saturation and the impact of eccentricity and ITSC in the field winding. The analytical model can be regarded as a novel contribution to the field or research.

The section is divided into several subsections for step-wise formulation towards the air-gap for density and total force, with the aim of determining orders of the time and spatial harmonics that influence the vibration in a generator stator and can be used for fault detection. First, the air-gap permeance is formulated by the inverse of the air-gap length and then multiplied with the MMF caused by the rotor and the stator currents to obtain the radial air-gap flux density. These calculations are one-dimensional and only the radial direction has been analyzed, which means that the tangential component of the flux density is assumed relatively much smaller than the radial component and, consequently, neglected. Thereafter, the radial force density is calculated based on the Maxwell stress tensor presented in equation 2.3 and the total air-gap force is obtained by integration.

A few references are employed for well-proven analytical description of basic characteristics in a generator, such as the rotor pole saliency, the stator slot geometry, and the effects of magnetic saturation. To limit the extent of the model, amplitudes of the various quantities have not been calculated in detail as they do not affect the frequencies or modes of the forces. Furthermore, a few comprehensive derivations are included in the appendix. The computing software Maple has been used for large-scale calculations [63].

Originally, the results from this model were meant to be used in the analysis of laboratory measurements to evaluate their validity and compare theory to practice. However, due to the laboratory close down caused by the coronavirus, they serve the purpose of comparing analytical predictions to numerical simulations and, together with the FEA, creating a theoretical foundation for vibration-based condition monitoring of salient-pole synchronous generators.

2.2.6.1 Air-gap length

In order to calculate the air-gap permeance, an air-gap function $g(\phi, t)$, describing the effective length of the air-gap due to the rotor geometry, stator slots and iron saturation, has been formulated as follows.

Rotor pole saliency
For round rotors, the air-gap length, g_0, is a constant in healthy condition. In salient-pole machines, on the other hand, g_0 varies due to the geometry of the rotor poles and has been approximated by equation 2.11 [18, 64].

$$g_0(\phi, t) = \frac{1}{\alpha_1 + \alpha_2 cos(2p(\theta_r - \phi))} \tag{2.11}$$

p is the number of pole pairs, ϕ is an angle along the inner stator surface, θ_r is the rotor position, and α_1 and α_2 are coefficients decided by the rotor geometry described in [64].

Stator slots
The non-smooth surface of a slotted stator causes uneven reluctance in the air-gap. The increased reluctance and air-gap length caused by the slot openings has been incorporated into the air-gap function by the Carter coefficient, C_c, according to equation 2.13 [15, 49, 60, 65–67]. According to [67], C_c has been estimated by the effective slot pitch, τ, and the ratio between the slot width, W_{ss}, and the air-gap length in the following way

$$C_c = \frac{\tau}{\tau - \frac{W_{ss}^2/g_0}{5W_{ss}+W_{ss}^2/g_0}}, \tag{2.12}$$

$$g_{ss}(\phi, t) = C_c \cdot g_0. \tag{2.13}$$

Magnetic saturation
The small area of the stator teeth, compared to other iron parts in a generator, and the resulting high flux density can cause magnetic saturation. This decreases the relative permeability of iron and increases its reluctance, which has been taken into account through the air-gap function. As the air-gap has a constant relative permeability of μ_0, the gap length has been modified to accommodate the reluctance variation due to saturation, which is commonly done by modulation of the air-gap function with twice the number of poles and twice the frequency of the fundamental flux density wave [15, 18, 49, 68–71]. Hence, the air-gap function with saturation of the teeth taken into account becomes

$$g_{sat}(\phi, t) = g_{ss}\left(k_m - k_e cos(2\omega_s t - 2p\phi)\right) \tag{2.14}$$

where the coefficients

$$k_m = \frac{3k_{sat}}{k_{sat}+2}, \tag{2.15}$$

$$k_e = \frac{2k_{sat}-2}{3k_{sat}}, \tag{2.16}$$

and the saturation factor k_{sat} is the ratio between the fundamental component of the air-gap line voltage, which is the no load terminal voltage of a non-saturated machine, and the fundamental component of the terminal voltage at full load [71].

The air-gap function of a salient-pole synchronous generator with slotted stator and saturation effects can now be written as

$$g(\phi, t) = g_{sat}(\phi, t) = \frac{C_c(k_m - k_e cos(2\omega_s - 2p\phi))}{\alpha_1 + \alpha_2 cos(2p(\frac{\omega_s t}{p} - \phi))}, \tag{2.17}$$

where the coherence $\theta_r = \omega_r t = \omega_s t/p$ has been used in the denominator. $g(\phi, t)$ is valid for healthy generators and for generators with short circuits and other faults that do not

influence the air-gap length. On the other hand, defects that modify the air-gap length, such as eccentricity, must be included exclusively.

Eccentricity
Eccentricity has been modeled by including the variable air-gap length that occurs during eccentric operation into the air-gap function. The mathematical formulation of this is shown in appendix A and the resulting equations are repeated here. That is, the air-gap function from equation 2.17 of a generator that suffers from eccentricity is expressed as

$$g_{ec}(\phi,t) = g(\phi,t)(1-\delta_{ec}cos(\psi)) = \frac{C_c(k_m - k_e cos(2\omega_s - 2p\phi))(1-\delta_{ec}cos(\psi))}{\alpha_1 + \alpha_2 cos(2p(\frac{\omega_s t}{p} - \phi))}, \tag{2.18}$$

where δ_{ec} is the degree of eccentricity defined in appendix A summarized as

$$\delta_{ec} = \begin{cases} \delta_{se}, & \text{if SE} \\ \delta_{de}, & \text{if DE} \end{cases} \tag{2.19}$$

and the eccentricity angle, ψ, as

$$\psi = \begin{cases} \phi, & \text{if SE} \\ \frac{\omega_s t}{p} - \phi, & \text{if DE} \end{cases} \tag{2.20}$$

2.2.6.2 Air-gap permeance

In order to calculate the magnetic flux density that produces the air-gap forces, the air-gap permeance is multiplied with the MMF from the rotor and the stator. As shown in equation 2.20 above, the effect SE has on the air-gap length is a function of position only, while DE imposes a cosine term that varies with both time and position. Thus, the remaining formulations have been performed for both SE and DE and will hereafter be presented individually by subscripts *se* and *de*, respectively, starting with the latter. ITSC in the rotor winding has also been treated separately and will be labeled with subscript *sc*.

Dynamic eccentricity
The air-gap permeance, Λ, can be obtained by the inverse of the air-gap length. Under DE, Λ_{de} has been formulated as

$$\Lambda_{de} = \frac{\mu_0}{g_{de}} = \frac{\mu_0(\alpha_1 + \alpha_2 cos(2\omega_s t - 2p\phi))}{C_c(k_m - k_e cos(2\omega_s t - 2p\phi))(1 - \delta_{de} cos(\frac{\omega_s t}{p} - \phi))} =$$
$$\frac{\mu_0}{C_c} \cdot \frac{\alpha_1 + \alpha_2 cos(2\omega_s t - 2p\phi)}{k_m - k_m \delta_{de} cos(\frac{\omega_s t}{p} + \phi) - k_e cos(2\omega_s t - 2p\phi) + 0.5 k_e \delta_{de} cos((2 \pm \frac{1}{p})\omega_s t - (2p \pm 1)\phi))}$$
$$= \frac{\alpha_1' + \alpha_2' cos(2\omega_s t - 2p\phi)}{1 - [\beta_1 cos(\frac{\omega_s t}{p} + \phi) + \beta_2 cos(2\omega_s t - 2p\phi) + \beta_3 cos((2 \pm \frac{1}{p})\omega_s t - (2p \pm 1)\phi))]}, \tag{2.21}$$

where trigonometric identities have been used for multiplication of two cosine terms. As the purpose of this analytical model has been to extract the frequencies of the air-gap forces, the amplitudes of the oscillations have been substituted for simplicity in the following way

$$\begin{aligned} \alpha_1' &= \alpha_1 \frac{\mu_0}{C_c k_m} \\ \alpha_2' &= \alpha_2 \frac{\mu_0}{C_c k_m} \\ \beta_1 &= \frac{\delta_{de}}{C_c} \\ \beta_2 &= \frac{k_e}{k_m C_c} \\ \beta_3 &= -0.5 \frac{k_e \delta_{de}}{C_c} \end{aligned} \tag{2.22}$$

By replacing the expression inside the square brackets in 2.21 with x, Taylor series expansion has been employed in the following way to approximate the division

$$\Lambda_{de} = (\alpha_1' + \alpha_2' cos(2\omega_s t - 2p\phi)) \cdot \frac{1}{1 - x} =$$
$$(\alpha_1' + \alpha_2' cos(2\omega_s t - 2p\phi)) \cdot (1 + x + x^2 + x^3 + ...). \tag{2.23}$$

Calculation and analysis of 2.23 including the first eight terms of the Taylor series, that is from 1 to x^7, resulted in the following compact notation

$$\Lambda_{de} = \sum_{\upsilon_1,...,\upsilon_4} \hat{\Lambda}_{de} cos\left(\left(\frac{2\upsilon_1 p \pm \upsilon_1}{p} \pm \upsilon_2\right)\omega_s t - (2p(\upsilon_3 \pm 1) \pm \upsilon_4)\phi\right), \tag{2.24}$$

where p is the number of pole pairs and $\hat{\Lambda}_{de}$ is the amplitude of the permeance wave under DE. The summation indices $\upsilon_1, \upsilon_2, \upsilon_3$ and υ_4 take the value of every whole number, that is $\upsilon_1, ..., \upsilon_4 \in \mathbb{W} = \{0, 1, 2, ..., \infty\}$. The sigma notation is a compact form of summation over every index, that is

$$\sum_{\upsilon_1,\ldots,\upsilon_4} = \sum_{\upsilon_1}\sum_{\upsilon_2}\sum_{\upsilon_3}\sum_{\upsilon_4} = \sum_{\upsilon_1=0}^{\infty}\sum_{\upsilon_2=0}^{\infty}\sum_{\upsilon_3=0}^{\infty}\sum_{\upsilon_4=0}^{\infty}.$$

The summation in equation 2.24 provides all possible frequencies and mode numbers. However, it was noted during the calculations that the amplitudes of the cosine terms in general decreased as their frequency and mode number increased. Thus, excited high order harmonics will be small compared to low order harmonics.

The resulting expression which led to the summation in equation 2.24 was not suitable to include in the thesis as it consisted of nearly 900 cosine terms after simplifying with trigonometric identities. Compact sigma notation is employed to represent long expressions throughout the rest of the analytical model for feasible presentation. However, the full series of cosine terms, and not just the simplified expression inside the sigma signs, have been used in every calculation to ensure correct results.

Static eccentricity

Under SE, the eccentricity angle, ψ, is constant with respect to time as shown in equation 2.20. Thus, the air-gap permeance becomes

$$\Lambda_{se} = \frac{\mu_0}{g_{se}} = \frac{\mu_0(\alpha_1 + \alpha_2 cos(2\omega_s t - 2p\phi))}{C_c(k_m - k_e cos(2\omega_s t - 2p\phi))(1 - \delta_{de} cos(\phi))} = \frac{\alpha_1' + \alpha_2' cos(2\omega_s t - 2p\phi)}{1 - [\beta_1 cos(\phi) + \beta_2 cos(2\omega_s t - 2p\phi) + \beta_3 cos((2\omega_s t - (2p \pm 1)\phi))]}. \tag{2.25}$$

Calculation of the Taylor series expansion, as for DE in equation 2.23, resulted in

$$\Lambda_{se} = \sum_{\upsilon_1,\ldots,\upsilon_3} \hat{\Lambda}_{se} cos((2\upsilon_1 + 2)\omega_s t - (2p(\upsilon_2 \pm 1) \pm \upsilon_3)\phi). \tag{2.26}$$

Inter-turn short circuit in the rotor winding

In absence of eccentricity, the air-gap function from equation 2.17 has been employed in the calculation of air-gap permeance, such that

$$\begin{aligned} \Lambda_{sc} = \frac{\mu_0}{g_{sc}} &= \frac{\mu_0(\alpha_1 + \alpha_2 cos(2\omega_s t - 2p\phi))}{C_c(k_m - k_e cos(2\omega_s t - 2p\phi))} \\ &= \frac{\alpha_1'' + \alpha_2'' cos(2p\phi - 2\omega_s t)}{1 - k_e/k_m cos(2\omega_s t - 2p\phi)}, \\ \alpha_1'' = \frac{\mu_0\alpha_1}{C_c k_m}, &\qquad \alpha_2'' = \frac{\mu_0\alpha_2}{C_c k_m}. \end{aligned} \tag{2.27}$$

Taylor series expansion of 2.27 has been simplified into

$$\Lambda_{sc} = \sum_{\upsilon_1,\upsilon_2} \hat{\Lambda}_{sc} cos((2\upsilon_1 + 2)\omega_s t - 2p(\upsilon_2 \pm 1)\phi). \tag{2.28}$$

Summary
The air-gap permeances of a salient-pole synchronous generator with stator slots and saturation effects under DE, SE, and ITSC in the rotor winding are summarized below in equation 2.29 - 2.31.

$$\Lambda_{de} = \sum_{\upsilon_1,\ldots,\upsilon_4} \hat{\Lambda}_{de} cos\left(\left(\frac{2\upsilon_1 p \pm \upsilon_1}{p} \pm \upsilon_2\right)\omega_s t - (2p(\upsilon_3 \pm 1) \pm \upsilon_4)\phi\right) \tag{2.29}$$

$$\Lambda_{se} = \sum_{\upsilon_1,\ldots,\upsilon_3} \hat{\Lambda}_{se} cos((2\upsilon_1 + 2)\omega_s t - (2p(\upsilon_2 \pm 1) \pm \upsilon_3)\phi) \tag{2.30}$$

$$\Lambda_{sc} = \sum_{\upsilon_1,\upsilon_2} \hat{\Lambda}_{sc} cos((2\upsilon_1 + 2)\omega_s t - 2p(\upsilon_2 \pm 1)\phi) \tag{2.31}$$

2.2.6.3 MMF

Dynamic and static eccentricity
During no load operation, the air-gap MMF is produced by the rotor field winding only, while in loaded operation, the armature currents also contribute. Both the stator and the rotor windings have been treated here, denoted by superscript *s* and *r* respectively.

A balanced three-phase stator winding with alternating current results in MMF waves that travel with synchronous speed. These can, with good approximation, be expressed as a sinusoidal function, especially if the winding is distributed which is commonly used in hydropower generators. Hence, by assuming sinusoidal stator MMF, the current density at the inner surface of the stator has been expressed as

$$j^s(\phi, t) = J^s sin(\omega_s t - p\phi), \tag{2.32}$$

where J^s is the maximum value of the stator current density. The same assumption can be made for the rotor MMF without much loss of accuracy. The DC current flowing in each of the rotating poles causes traveling MMF waves in the air-gap seen from the stator such that the current density produced by a healthy field winding has been written as

$$j^r(\phi, t) = J^r sin(\omega_s t - p\phi), \tag{2.33}$$

where J^r is the maximum value of the rotor current density. With J^s and J^r being equal under SE and DE, the stator MMF and rotor MMF has been achieved by Ampère's law and the surface integral of the current densities around a closed path as follows

$$\mathcal{F}^s_{de}(\phi,t) = \mathcal{F}^s_{se}(\phi,t) = \oint j^s(\phi,t)\,d\phi = \oint J^s sin(\omega_s t - p\phi)\,d\phi$$
$$= \frac{J^s}{p} cos(\omega_s t - p\phi), \tag{2.34}$$
$$\mathcal{F}^r_{de}(\phi,t) = \mathcal{F}^r_{se}(\phi,t) = \oint j^r(\phi,t)\,d\phi = \oint J^r sin(\omega_s t - p\phi)\,d\phi$$
$$= \frac{J^r}{p} cos(\omega_s t - p\phi). \tag{2.35}$$

Inter-turn short circuit in the rotor winding
The armature MMF under rotor winding fault is equal as for eccentricity, that is

$$\mathcal{F}^s_{sc}(\phi,t) = \oint j^s(\phi,t)\,d\phi = \oint J^s sin(\omega_s t - p\phi)\,d\phi = \frac{J^s}{p} cos(\omega_s t - p\phi). \tag{2.36}$$

However, when there is an ITSC in the rotor winding, the MMF produced by the pole with faulty winding is reduced. The resulting rotor MMF has been formulated by superimposing the original MMF field, $\mathcal{F}_h$, and a demagnetizing component caused by the short circuit, $\mathcal{F}_f$. This is elaborated in appendix B with the result interpreted in equation 2.37.

$$\mathcal{F}^r_{sc}(\phi,t) = \mathcal{F}_h(\phi,t) + \mathcal{F}_f(\phi,t) =$$
$$\frac{J^r}{p} cos(\omega_s t - p\phi) + \sum_{n=1}^{\infty} F_{f,n} cos\left(\frac{n}{p}\omega_s t - n\phi\right) \tag{2.37}$$

2.2.6.4 Magnetic flux density

The air-gap magnetic flux density, b, can be obtained by multiplication of the air-gap permeance and MMF. As the resultant air-gap magnetic field is a superposition between the rotor field and the stator field, these two fields have been calculated separately and then added together. As mentioned, for accurate computation, the full series of cosine terms which make up the air-gap permeance summations in equation 2.29 to 2.31 have been used for multiplication with the MMF. However, only the summation notation is used for suitable presentation.

Dynamic eccentricity
The b produced by the armature has been calculated in the following way

$$b^s_{de}(\phi,t) = \Lambda_{de}(\phi,t)\cdot\mathcal{F}^s_{de}(\phi,t) =$$
$$\left[\sum_{\upsilon_1,\dots\upsilon_4}\hat{\Lambda}_{de}cos\left(\left(\frac{2\upsilon_1 p\pm\upsilon_1}{p}\pm\upsilon_2\right)\omega_s t-(2p(\upsilon_3\pm1)\pm\upsilon_4)\phi\right)\right]\cdot\frac{J^s}{p}cos(\omega_s t-p\phi)$$
$$=\sum_{\upsilon_1,\dots,\upsilon_4}B^s_{de}cos\left(\left(\frac{2\upsilon_1 p\pm\upsilon_1}{p}\pm\upsilon_2\right)\omega_s t-(2p(\upsilon_3\pm1)\pm\upsilon_4)\phi\right), \tag{2.38}$$

where B^s_{de} denotes the amplitude of the stator flux density under DE. Similarly, the rotor flux has been formulated as

$$b^r_{de}(\phi,t) = \Lambda_{de}(\phi,t)\cdot\mathcal{F}^r_{de}(\phi,t) =$$
$$\left[\sum_{\upsilon_1,\dots,upsilon_4}^{\infty}\hat{\Lambda}_{de}cos\left(\left(\frac{2\upsilon_1 p\pm\upsilon_1}{p}\pm\upsilon_2\right)\omega_s t-(2p(\upsilon_3\pm1)\pm\upsilon_4)\phi\right)\right]\cdot\frac{J^r}{p}cos(\omega_s t-p\phi)$$
$$=\sum_{\upsilon_1,\dots,\upsilon_4}B^r_{de}cos\left(\left(\frac{2\upsilon_1 p\pm\upsilon_1}{p}\pm\upsilon_2\right)\omega_s t-(2p(\upsilon_3\pm1)\pm\upsilon_4)\phi\right). \tag{2.39}$$

The resultant air-gap flux density under DE has been found by equation 2.40

$$b_{de}(\phi,t) = b^s_{de}(\phi,t)+b^r_{de}(\phi,t) =$$
$$\sum_{\upsilon_1,\dots,\upsilon_4}B_{de}cos\left(\left(\frac{2\upsilon_1 p\pm\upsilon_1}{p}\pm\upsilon_2\right)\omega_s t-(2p(\upsilon_3\pm1)\pm\upsilon_4)\phi\right). \tag{2.40}$$

Static eccentricity
The same procedure has been executed for SE.

$$b^s_{se}(\phi,t) = \Lambda_{se}(\phi,t)\cdot\mathcal{F}^s_{se}(\phi,t) =$$
$$\left[\sum_{\upsilon_1,\dots,\upsilon_3}\hat{\Lambda}^s_{se}cos((2\upsilon_1+2)\omega_s t-(2p(\upsilon_2\pm1)\pm\upsilon_3)\phi)\right]\cdot\frac{J^s}{p}cos(\omega_s t-p\phi)$$
$$=\sum_{\upsilon_1,\dots,\upsilon_3}B^s_{se}cos((2\upsilon_1+1)\omega_s t-(2p(\upsilon_2\pm1)\pm\upsilon_3)\phi) \tag{2.41}$$

$$b^r_{se}(\phi,t) = \Lambda_{se}(\phi,t)\cdot\mathcal{F}^r_{se}(\phi,t) =$$
$$\left[\sum_{\upsilon_1,\ldots,\upsilon_3}\hat{\Lambda}_{se}cos((2\upsilon_1+2)\omega_s t-(2p(\upsilon_2\pm1)\pm\upsilon_3)\phi)\right]\cdot\frac{J^r}{p}cos(\omega_s t-p\phi)$$
$$=\sum_{\upsilon_1,\ldots,\upsilon_3}^{\infty}B^r_{se}cos((2\upsilon_1+1)\omega_s t-(2p(\upsilon_2\pm1)\pm\upsilon_3)\phi) \tag{2.42}$$

$$b_{se}(\phi,t) = b^s_{se}(\phi,t)+b^r_{se}(\phi,t) =$$
$$\sum_{\upsilon_1,\ldots,\upsilon_3}B_{se}cos((2\upsilon_1+1)\omega_s t-(2p(\upsilon_2\pm1)\pm\upsilon_3)\phi) \tag{2.43}$$

Inter-turn short circuit in the rotor winding

The flux density produced by the armature during operation with short circuit in the rotor is the same as for healthy operation and has been calculated in the following way

$$b^s_{sc}(\phi,t) = \Lambda_{sc}(\phi,t)\cdot\mathcal{F}^s_{sc}(\phi,t) =$$
$$\left[\Lambda_{sc}=\sum_{\upsilon_1,\upsilon_2}\hat{\Lambda}_{sc}cos((2\upsilon_1+2)\omega_s t-2p(\upsilon_2\pm1)\phi)\right]\cdot\frac{J^s}{p}cos(\omega_s t-p\phi)$$
$$=\sum_{\upsilon_1,\upsilon_2}B^s_{sc}cos((2\upsilon_1+1)\omega_s t-((2\upsilon_2+1)p\pm2p)\phi). \tag{2.44}$$

For the rotor, the modified MMF field due to the short circuit fault has been taken into account which resulted in

$$b^r_{sc}(\phi,t) = \Lambda_{sc}(\phi,t)\cdot\mathcal{F}^r_{sc}(\phi,t) =$$
$$\left[\sum_{\upsilon_1,\upsilon_2}\hat{\Lambda}_{sc}cos((2\upsilon_1+2)\omega_s t-(2\upsilon_2(p\pm1))\phi)\right]\cdot$$
$$\left[\frac{J^r}{p}cos(\omega_s t-p\phi)+\sum_{n=1}^{\infty}F_{f,n}cos\left(\frac{n}{p}\omega_s t-n\phi\right)\right]$$
$$=\sum_{\upsilon_1,\ldots,\upsilon_4}^{\infty}B^r_{sc}cos\left(\left(2\upsilon_1\pm\frac{\upsilon_2}{p}\right)\omega_s t-(2p\upsilon_3\pm\upsilon_4)\phi\right), \tag{2.45}$$

where the first 20 terms of the Fourier series, that is n ranging from 1 to 20, have been included in the calculations. The combination of 2.44 and 2.45 forms the resultant flux density under rotor ITSC as follows

$$b_{sc}(\phi,t) = b^s_{sc}(\phi,t) + b^r_{sc}(\phi,t) = \sum_{\upsilon_1,\ldots,\upsilon_4} B_{sc} cos\left(\left(2\upsilon_1 \pm \frac{\upsilon_2}{p}\right)\omega_s t - (2p\upsilon_3 \pm \upsilon_4)\phi\right). \quad (2.46)$$

Summary
The calculated resultant air-gap magnetic flux density under DE, SE and ITSC in the rotor field winding are summarized in equation 2.47 to 2.49.

$$b_{de}(\phi,t) = \sum_{\upsilon_1,\ldots,\upsilon_4} B_{de} cos\left(\left(\frac{2\upsilon_1 p \pm \upsilon_1}{p} \pm \upsilon_2\right)\omega_s t - (2p(\upsilon_3 \pm 1) \pm \upsilon_4)\phi\right) \quad (2.47)$$

$$b_{se}(\phi,t) = \sum_{\upsilon_1,\ldots,\upsilon_3} B_{se} cos((2\upsilon_1 + 1)\omega_s t - (2p(\upsilon_2 \pm 1) \pm \upsilon_3)\phi) \quad (2.48)$$

$$b_{sc}(\phi,t) = \sum_{\upsilon_1,\ldots,\upsilon_4} B_{sc} cos\left(\left(2\upsilon_1 \pm \frac{\upsilon_2}{p}\right)\omega_s t - (2p\upsilon_3 \pm \upsilon_4)\phi\right) \quad (2.49)$$

2.2.6.5 Force density

According to Maxwell stress tensor presented in equation 2.3, the radial force density can be found by squaring the flux density. As this mathematical model only considers the radial direction, the equation is simplified to equation 2.50, where f is the radial force density and μ_0 is the vacuum permeability. As before, the full cosine series have been included in the calculations.

$$f(\phi,t) = \frac{b^2(\phi,t)}{2\mu_0} \quad (2.50)$$

Dynamic eccentricity
The radial force density under DE has been calculated to be

$$f_{de}(\phi,t) = \frac{b^2_{de}(\phi,t)}{\mu_0} = \frac{1}{\mu_0}\left[\sum_{\upsilon_1,\ldots,\upsilon_4} B_{de} cos\left(\left(\frac{2\upsilon_1 p \pm \upsilon_1}{p} \pm \upsilon_2\right)\omega_s t - (2\upsilon_3(p \pm 1) \pm 2p \pm \upsilon_4)\phi\right)\right]^2 = \sum_{\upsilon_1,\ldots,\upsilon_4} F_{de} cos\left(\left(\frac{2\upsilon_1 p \pm \upsilon_1}{p} \pm 2\upsilon_2\right)\omega_s t - (2\upsilon_3(p \pm 1) \pm \upsilon_4)\phi)\right), \quad (2.51)$$

where F_{de} is the amplitude of the radial force density under DE.

Static eccentricity
For SE, the radial force density has been calculated to be

$$f_{se}(\phi,t) = \frac{b_{se}^2(\phi,t)}{\mu_0} = \frac{1}{\mu_0}\left[\sum_{\upsilon_1,\ldots,\upsilon_3} B_{se} cos((2\upsilon_1+1)\omega_s t - (2\upsilon_2(p\pm1)\pm\upsilon_3(2p\pm p+1))\phi)\right]^2 = \sum_{\upsilon_1,\ldots,\upsilon_3} F_{se} cos(2\upsilon_1\omega_s t - (2\upsilon_2\pm\upsilon_3)\phi). \quad (2.52)$$

Inter-turn short circuit in the rotor winding
The radial force density under ITSC in the rotor winding has been found as

$$f_{sc}(\phi,t) = \frac{b_{sc}^2(\phi,t)}{\mu_0} = \frac{1}{\mu_0}\left[\sum_{\upsilon_1,\ldots,\upsilon_4} B_{sc} cos\left(\left(2\upsilon_1 \pm \frac{\upsilon_2}{p}\right)\omega_s t - (2p\upsilon_3\pm\upsilon_4)\phi\right)\right]^2 = \sum_{\upsilon_1,\ldots,\upsilon_4} F_{sc} cos\left(\left(\frac{2\upsilon_1 p\pm\upsilon_1}{p}\pm 2\upsilon_2\right)\omega_s t - (p\upsilon_3\pm\upsilon_4)\phi\right). \quad (2.53)$$

Summary
The calculated the calculated radial force density under DE, SE and ITSC in the rotor field winding are summarized in equation 2.54 to 2.56.

$$f_{de}(\phi,t) = \sum_{\upsilon_1,\ldots,\upsilon_4} F_{de} cos\left(\left(\frac{2\upsilon_1 p\pm\upsilon_1}{p}\pm 2\upsilon_2\right)\omega_s t - (2\upsilon_3(p\pm1)\pm\upsilon_4)\phi)\right) \quad (2.54)$$

$$f_{se}(\phi,t) = \sum_{\upsilon_1,\ldots,\upsilon_3} F_{se} cos(2\upsilon_1\omega_s t - (2\upsilon_2\pm\upsilon_3)\phi) \quad (2.55)$$

$$f_{sc}(\phi,t) = \sum_{\upsilon_1,\ldots,\upsilon_4} F_{sc} cos\left(\left(\frac{2\upsilon_1 p\pm\upsilon_1}{p}\pm 2\upsilon_2\right)\omega_s t - (p\upsilon_3\pm\upsilon_4)\phi\right) \quad (2.56)$$

2.2.6.6 Total force

The radial force density is the force per square meter that acts on the stator teeth. In order to calculate the total force that acts on one tooth or on all the teeth, the radial force densi-

ties in equation 2.54 to 2.56 must be multiplied with the stack length, L_s, and integrated over the tooth line, as shown in figure 2.3, or around the full inner stator circumference, respectively. In the following formulations, a general integration without specifying the evaluated integration angle has been used.

Dynamic eccentricity
The total force under DE, $\mathbb{F}_{de}$, has been calculated in the following way

$$\mathbb{F}_{de}(\phi,t) = L_s \int f_{de}(\phi,t)\cdot cos(\phi)\, d\phi =$$
$$L_s \int \left[\sum_{\upsilon_1,\ldots,\upsilon_4} F_{de} cos\left(\left(\frac{2\upsilon_1 p \pm \upsilon_1}{p} \pm 2\upsilon_2 \right) \omega_s t - (2\upsilon_3(p\pm 1) \pm \upsilon_4)\phi \right) \right] d\phi =$$
$$\sum_{\upsilon_1,\ldots,\upsilon_4} \mathtt{F}_{de} sin\left(\left(\frac{2\upsilon_1 p \pm \upsilon_1}{p} \pm 2\upsilon_2 \right) \omega_s t - (2\upsilon_3(p\pm 1) \pm \upsilon_4)\phi \right), \tag{2.57}$$

where $\mathtt{F}_{de}$ is the amplitude of the total force under DE.

Static eccentricity
$\mathbb{F}_{se}$, which is the total force under SE, has been calculated as

$$\mathbb{F}_{se}(\phi,t) = L_s \int f_{se}(\phi,t)\cdot cos(\phi)\, d\phi =$$
$$L_s \int \left[\sum_{\upsilon_1,\ldots,\upsilon_3} F_{se} cos(2\upsilon_1\omega_s t - (\pm 2\upsilon_2 \pm \upsilon_3)\phi \right] d\phi =$$
$$\sum_{\upsilon_1,\ldots,\upsilon_3} \mathtt{F}_{se} sin(2\upsilon_1\omega_s t - (2\upsilon_2 \pm \upsilon_3)\phi). \tag{2.58}$$

Inter-turn short circuit in the rotor winding
For operation with ITSC in the field winding, the total force has been calculated as follows

$$\mathbb{F}_{sc}(\phi,t) = L_s \int f_{sc}(\phi,t)\cdot cos(\phi)\, d\phi =$$
$$L_s \int \left[\sum_{\upsilon_1,\ldots,\upsilon_4} F_{sc} cos\left(\left(\frac{2\upsilon_1 p \pm \upsilon_1}{p} \pm 2\upsilon_2 \right) \omega_s t - (p\upsilon_3 \pm \upsilon_4)\phi \right) \right] d\phi =$$
$$\sum_{\upsilon_1,\ldots,\upsilon_4} \mathtt{F}_{sc} sin\left(\left(\frac{2\upsilon_1 p \pm \upsilon_1}{p} \pm 2\upsilon_2 \right) \omega_s t - (p\upsilon_3 \pm \upsilon_4)\phi \right). \tag{2.59}$$

Summary
Expression 2.57 to 2.59 describes the oscillating total forces that act on the inner stator circumference and cause the iron to vibrate. The parameters in the expressions has been chosen to be as general as possible, such that the analytical model can be easily applicable to a wide range of generators. The number of pole pairs, p, and the synchronous electrical angular frequency, $\omega_s = 2\pi f_s$, are known quantities in all machines and therefore suitable for the model. The time harmonic order, k, and spatial harmonics order, m, from the general f_r in equation 2.4, can be recognized in the expressions. That is, with SE as an example, $2\upsilon_1\omega_s t = 2\upsilon_1 p\omega_r t = k\omega_r t \Rightarrow k = 2\upsilon_1 p$, and $(2\upsilon_2 \pm \upsilon_3)\phi = m\phi \Rightarrow m = 2\upsilon_2 \pm \upsilon_3$.

All three faults impose unnatural spatial harmonics with orders represented by the expression in front of ϕ. As a results, the vibration level during these faults may be changed from healthy condition. DE and ITSC in the rotor winding also produce harmonics in the time domain, while the air-gap force during SE consists of time harmonics at $2\upsilon_1$ times the fundamental. As described in section 2.2.5.1, this is identical to healthy operation. Since only the time distribution of the force is in practice possible to measure in a real hydropower generator, using the actual air-gap force for fault detection of SE would not be ideal according to the model as no additional frequency component is produced. An exception could be if the amplitude of the natural components were significantly changed such that SE could be recognized based on this. On the other hand, SE do impose spatial harmonics and, as described in the previous sections of this chapter, these could have serious impact on the generator's vibration behavior. This means that SE could possibly be detected by measuring a generator's vibration, despite the unaffected time distribution of the forces. This is further investigated through finite element (FE) simulations in chapter 5.

It has not been in the scope of this thesis to analytically determine the coherence between the time harmonic order, k, and the spatial harmonic order, m. According to the analytical model, every combination of k and m is possible since there are separate summation indices used for k, that is υ_1 and υ_2, and for m, that is υ_3 and υ_4. However, the air-gap does most likely not contain forces with all these combinations. In healthy condition, the frequency spectrum in time and space consist of the natural harmonics only and analytical determination of the coherence between k and m is feasible. However, as mentioned in section 2.2.5.1, the distorted air-gap field during faults such as eccentricity or ITSC in the rotor results in a high number of interactions between the flux density harmonics and a more chaotic and complicated relationship between k and m which has not been investigated analytically. However, the expressions from the model are still mathematically valid by assuming that the amplitude of the predicted waves that are not present in the air-gap is zero.

Table 2.1 summarizes the expressions for the frequency components and time harmonic orders that appear in the total force during faulty operation, while table 2.2 summarizes the expressions for the induced spatial harmonic orders. It is possible to express the spatial orders as frequencies in the spatial domain as well, but this is not of interest and therefore excluded. In the tables, f_s is the synchronous electrical frequency, p is the number of rotor pole pairs and $\upsilon_1, \upsilon_2, \upsilon_3$ and υ_4 are any whole number.

It can be seen from the calculations in section 2.2.6.5 and 2.2.6.6 that the analytical expressions for force density are the same as for the total force. This means that the general force density wave f_r from equation 2.4 can be characterized with the same expressions as given in the tables below. This is emphasized here since both the total force and the force density will be treated in the next chapters, with particular focus on the force density, as they are both interesting in vibration analysis.

Table 2.1: Time harmonics of the air-gap force density and total force caused by DE, SE and ITSC in the rotor winding.

	Dynamic eccentricity	Static eccentricity	ITSC in the rotor winding
Frequency	$\left(\frac{2\upsilon_1 p \pm \upsilon_1}{p} \pm 2\upsilon_2\right) f_s$	$2\upsilon_1 f_s$	$\left(\frac{2\upsilon_1 p \pm \upsilon_1}{p} \pm 2\upsilon_2\right) f_s$
Order, k	$2\upsilon_1 p \pm \upsilon_1 \pm 2p\upsilon_2$	$2\upsilon_1 p$	$2\upsilon_1 p \pm \upsilon_1 \pm 2p\upsilon_2$

Table 2.2: Spatial harmonic orders of the air-gap force density and total force caused by DE, SE and ITSC in the rotor winding.

	Dynamic eccentricity	Static eccentricity	ITSC in the rotor winding
Order, m	$2\upsilon_3(p \pm 1) \pm \upsilon_4$	$2\upsilon_3 \pm \upsilon_4$	$p\upsilon_3 \pm \upsilon_4$

Chapter 3

The investigated generator

3.1 Generator specifications

The generator in scope of this thesis is a 100 kVA salient-pole synchronous generator located in the NTNU National Smart Grid Laboratory. The machine, termed the *laboratory generator*, resembles a typical hydropower generator in the Norwegian power system with several topology similarities. It is custom-made for the purpose of testing and analysis under various operating conditions with the possibility of varying the loading, connecting the armature winding in series or in parallel, and inducing faults. Static eccentricity can be applied by moving the stator frame relative to the rotor with bolts at the sides of the housing as shown in figure 3.1 (a), controlled by calibrator clocks that indicate the displacement. Moreover, ITSC fault can be imposed by shorting up to ten of the 35 turns in two rotor poles, as shown in figure 3.1 (b) where a short-circuit is applied between turn number 33 and 35 in one of the poles. Damper winding faults can also be induced by removing bars, replacing them with cracked bars or modifying the end ring, as shown in figure 3.1 (c). The complete generator is shown in figure 3.2. The prime mover of the generator is a converter-controlled 90 kW induction motor.

The generator has seven pole pairs and a synchronous electrical frequency of 50 Hz. According to equation 2.1, the rated speed, which is the synchronous speed, is then $n_s = \frac{60 f_s}{p} = \frac{60 \cdot 50}{7}$ = 428.6 RPM = 7.143 Hz. The generator has 114 slots with a double-layer, fractional slot winding, and a number of slots per pole and phase, q, equal to 2 + 5/7. This is shown in equation 3.1 where Q_s is the number of slots and N_p is the number of phases. This implies that approximately 2.71 slots are occupied by one phase on average, which is shorter than one pole pitch, meaning that the generator is short-pitched. The layout of the winding is given in appendix C and depicted in figure 4.5. The GCD between the number of slots and the number of poles, which corresponds to the lowest spatial harmonic order that can appear in the machine during healthy operation, is two as shown in equation 3.2. Other specifications and nameplate values are presented in table 3.1 and 3.2, respectively.

Table 3.1: Specification of the laboratory generator.

Specifications	
Number of poles	14
Number of slots	114
Damper bars per pole	7
Outer rotor diameter	646.5 mm
Nominal air-gap length	1.75 mm
Outer stator diameter	780 mm
Turn per field winding pole	35
Winding layout	Star

Table 3.2: Rated values of the laboratory generator.

Nameplate values	
Nominal power	100 kVA
Nomival voltage	400 V
Nominal current	144.3 A
Nominal speed	428.6 RPM
Nominal frequency	50 Hz
Nominal power factor	0.9
No load exc. current	53.2 A
Nominal exc. current	103 A

$$q = \frac{Q_s}{2p \cdot N_p} = \frac{114}{14 \cdot 3} = 2 + \frac{5}{7} \approx 2.71 \tag{3.1}$$

Lowest spatial harmonic order:

$$\begin{aligned} Q_s &= 114 = \mathbf{2} \cdot 3 \cdot 19 \\ 2p &= 14 = \mathbf{2} \cdot 7 \\ GCD &= m = 2 \end{aligned} \tag{3.2}$$

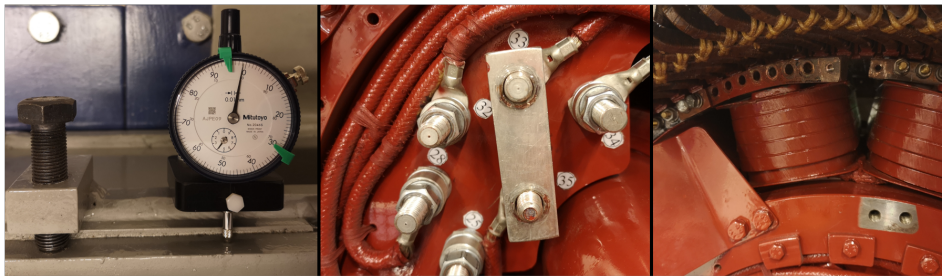

(a) *(b)* *(c)*

Figure 3.1: Calibrator for SE (a), shorting of two rotor turns (b) and damper winding modification (c) in the laboratory generator.

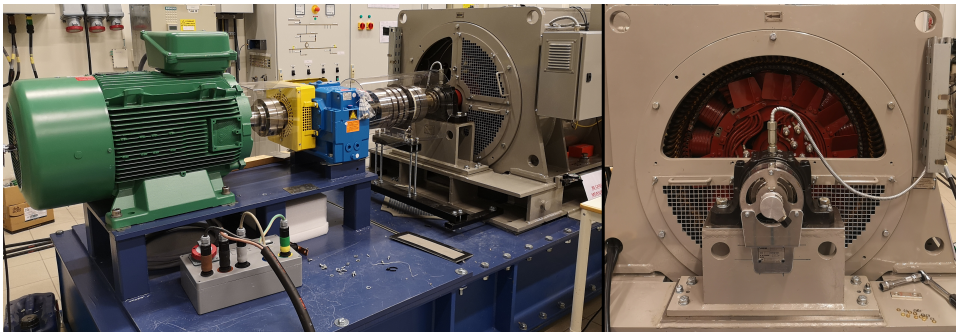

Figure 3.2: Left: the back of the laboratory generator connected to a green induction motor driving the shaft. Right: the front of the laboratory generator.

3.2 Prediction of vibration

The expressions from the analytical model formulated in section 2.2.6 have here been evaluated with respect to the topology of the laboratory generator. Thereafter, the results have been used to predict how the vibration behavior of the generator can be during faulty conditions. The analytical model describes the radial force density and the total force caused by eccentricity and ITSC in the rotor winding that acts on the stator teeth in a salient-pole synchronous generator with slotted stator and saturation effects taken into account. The predictions will here be compared to expectations during healthy operations and, in chapter 5, to the simulation results in order to evaluate how analytical predictions match numerical FEA. Originally, the analytical and numerical results were to be used as a part of the analysis and evaluation of the real vibration measurement results, but the shut down of the university made laboratory work impossible.

3.2.1 Time harmonics

Table 3.3 compares predicted frequencies and orders of the time harmonic forces during DE, SE, and ITSC in the field winding to expectations during healthy condition described in section 2.2.5.1. The expressions in the first row of the table are evaluated until the first natural force harmonic, i.e. 100 Hz, for υ_1 and υ_2 being whole numbers. All harmonics are listed as positive, although some harmonics can be regarded as negative if they rotate in the opposite direction of the rotor. The fundamental frequency of the laboratory generator, that is the synchronous electrical frequency f_s in the table, is 50 Hz and p, the number of pole pairs, is 7.

Table 3.3: Expected time harmonics of radial force density and total forces in the laboratory generator under healthy and faulty condition.

Order, k	Healthy	DE	SE	ITSC
		$\left(\frac{2v_1 p \pm v_1}{p} \pm 2v_2\right) f_s$	$2v_1 f_s$	$\left(\frac{2v_1 p \pm v_1}{p} \pm 2v_2\right) f_s$
1st		7.14 Hz		7.14 Hz
2nd		14.29 Hz		14.29 Hz
3rd		21.43 Hz		21.43 Hz
4th		28.57 Hz		28.57 Hz
5th		35.71 Hz		35.71 Hz
6th		42.86 Hz		42.87 Hz
7th		50.0 Hz		50.0 Hz
8th		57.14 Hz		57.14 Hz
9th		64.29 Hz		64.29 Hz
10th		71.43 Hz		71.43 Hz
11th		78.57 Hz		78.57 Hz
12th		85.71 Hz		85.71 Hz
13th		92.86 Hz		92.86 Hz
14th	100.0 Hz	100.0 Hz	100.0 Hz	100.0 Hz

Table 3.3 shows that SE does not excite any unnatural harmonics. Thus, based on the these results only, the vibration of the generator can not be expected to change in this condition. On the other hand, DE and ITSC in the rotor winding impose time harmonics at every 7.14 Hz, which is every multiple of the rotor speed. If the waves have an adequate amplitude and also low spatial harmonic orders, the resulting vibration can be significant at these frequencies. The reason why DE and ITSC induce the same time harmonics is that they cause the same type of UMP in the generator. That is, during DE, the smallest distance between the rotor and the stator revolves around the air-gap as the rotor rotates, causing a moving point of maximum field strength subjected to the teeth. Naturally, the opposite side of the stator experiences a rotating point of minimum field strength. This is similar to the weakened flux field produced by a pole with an ITSC. The air-gap force is caused by the magnetic field and, thus, both DE and ITSC cause dynamic UMP in the generator.

3.2.2 Spatial harmonics

Table 3.4 presents the expected spatial harmonic orders of the radial forces to appear during DE, SE, and ITSC in the rotor winding. The expressions from the analytical model, listed in the first row of the table, are evaluated until the main force component, which is the 14th, for υ_3 and υ_4 being whole numbers. The direction of rotation of the harmonics, which corresponds to a positive or negative sign, is not considered. Some of the natural spatial harmonics that are expected to appear during healthy operation are the second, caused by the GCD between the number of slots and poles, the 14th, which is twice the fundamental flux harmonic caused by the seven pole pairs, and the three related to the stator slots. These are also expected to be present during faulty operation.

The table shows that all three faults modify the spatial harmonic content of the air-gap forces. They distort the periodicity in the spatial domain which causes appearance of all low order harmonics. As described in section 2.2.5.2, the lowest orders will have significant impact on the vibration of the generator as the amplitude of static deformation is proportional to $1/m^4$.

Table 3.4: Expected spatial harmonic orders of radial forces in the laboratory generator under healthy and faulty condition.

Healthy	DE	SE	ITSC
	$2\upsilon_3(p \pm 1) \pm \upsilon_4$	$2\upsilon_3 \pm \upsilon_4$	$p\upsilon_3 \pm \upsilon_4$
	1st	1st	1st
2nd	2nd	2nd	2nd
	3rd	3rd	3rd
	4th	4th	4th
	5th	5th	5th
	6th	6th	6th
	7th	7th	7th
	8th	8th	8th
	9th	9th	9th
	10th	10th	10th
	11th	11th	11th
	12th	12th	12th
	13th	13th	13th
14th	14th	14th	14th
100th	100th	100th	100th
114th	114th	114th	114th
128th	128th	128th	128th

3.2.3 Vibration

Table 3.3 and 3.4 presented above list the magnetic force harmonics that are expected to appear in the time domain and the spatial domain during various operating conditions. This subsection aims to formulate the expected vibration behavior of the laboratory generator based on the theory presented in chapter 2 and the two tables. The order of the spatial harmonics has a great influence on the static deformation, while the time harmonic order decides at which frequency the vibration occurs. Thus, both domains are of interest and must be considered in combination when vibration is predicted.

The amplitude of the air-gap forces influences the produced amount of stator bore deformation. These can be found by analyzing both the time domain and the spatial domain, but are not calculated in detail in the analytical model. However, as mentioned before, it was experienced during the formulation of the expressions that the amplitude of the cosine expressions in general decreased as the frequency and spatial order increased.

DE and ITSC in the rotor winding both produce harmonics of low orders in the time domain and in the spatial domain. The lowest spatial harmonic order is one and it is therefore expected that the dominant vibration mode will be the first, with a stator deformation caused by a single attraction point. At which frequency this occurs is not easily determined based on the spatial harmonics only. However, as every subharmonic in both domains are expected to be excited, it may be natural to assume that time harmonics and spatial harmonics of the same order belongs to the same force wave, that is $k = m$ in f_r. If so, it is expected that the dominant vibration mode during these faults will be the first mode at 7.14 Hz. Vibration at higher frequencies will then also be amplified compared to healthy operation, but their increased mode number will limit the magnitude significantly. Conclusively, by this assumption, low-frequency vibration, at rotor frequency in particular, will be a symptom of DE and ITSC in the rotor winding.

The first order spatial harmonic is also expected to be present during SE causing the same dominant vibration mode as for ITSC and DE with a single attraction point. However, predicting the dominant vibration frequency is more uncertain during SE. Deformation is dependent on the amplitude of the force waves and the predictions state that time harmonics at low frequencies are absent, which means that their amplitude is zero. If this is true, the dominant vibration frequency may be the frequency of the lowest natural time harmonic, which is at 100 Hz. In this case, vibration at 100 Hz will be amplified compared to healthy operation due to the presence of the first-order spatial harmonic that is not excited in healthy condition. On the other hand, a time harmonic may be present in the air-gap with a very low amplitude even though it is not specifically excited by faults due to the generator topology. If so, the large influence of low spatial orders might be enough to produce vibration at low frequencies. However, this is not the case according to the analytical model and, based on the predictions, vibration at 100 Hz is expected to be the largest during SE dominated by the first mode.

The same discussion can be made for prediction of vibration during healthy operation. The dominant vibration mode is expected to be two according to the second-order spatial

harmonic. However, the absence of a fault and distortions of the time and spatial force distributions makes it easier to predict the dominant vibration frequency. It is commonly known that the vibration of a healthy generator is characterized by two times the fundamental frequency caused by the main force harmonic [49]. Thus, the dominant vibration of the healthy laboratory generator is expected to be at 100 Hz with deformation caused by two attraction points.

The conclusions presented above serve as a base in analysis of the numerical FE simulations in chapter 5. Some uncertainty is attached to the predictions due to their analytical nature and the FEA is expected to provide more detailed information about the air-gap forces and the resulting vibration. FEA is considered more reliable and can be regarded as verification or falsification of the predictions. Thus, comparisons and discussions between the analytical and numerical results will be presented in chapter 6.

As DE is not possible to apply to the laboratory generator, it has not been investigated further in this thesis. However, based on the results presented in the tables above and the fact that they both induce dynamic UMP to the generator, it may be assumed that the consequences of DE will resemble those of ITSC in the rotor winding in a vibration point of view.

Chapter 4

Modeling and simulation procedure

In this thesis, the FEM has been used to simulate the air-gap flux density in the laboratory generator, to calculate the force density and total force that act on the stator teeth and to compute the resulting stator deformation. According to equation 2.3, b_r and b_t must first be found in order to calculate the radial force that cause vibration. FEA provides accurate information and has been used to gain insight into how the force develop from the magnetic field and cause vibration during healthy and faulty operation. The simulation results have also been used to compare numerical calculations to the analytical predictions.

This chapter presents how the laboratory generator has been modeled and simulated. Two FE software has in total been employed for simulation of magnetic flux density, force calculations and to investigate how the force causes vibration in the stator. In the following sections, the modeling procedure of the laboratory generator and how the simulations were defined is described for each of these two software.

4.1 Simulation software

Time-stepping FEA has been performed in two software from the company ANSYS: Maxwell and Mechanical [72, 73]. Maxwell has been utilized to compute the magnetic flux density, force density, and total force in the air-gap of a two-dimensional (2D) cross-section of the laboratory generator. The total force was later transferred to Mechanical to find how the stator responds when the force acts on the stator teeth. Information about the deformation of the yoke has been collected and is, together with information about the magnetic characteristics obtained in Maxwell, presented in chapter 5.

4.2 Modeling in Maxwell and simulation of flux and force

The laboratory generator was accurately modeled in Maxwell based on technical drawings in order to replica the rotor and stator geometries as detailed as possible. It was limited to 2D which implies that end-effects were neglected and that the generator was identical in axial direction. These assumptions were considered appropriate without noteworthy loss of accuracy for the scope of this thesis as axial components of the flux and force are not of interest for the vibration analysis. A 2D model requires less computational resources, that is usage of computer memory and loading of the computer processor unit, than a three-dimensional (3D) model and was therefore chosen to avoid memory leak, computer overloading and to limit the duration of the simulations. All simulations were run on one of NTNU's local servers which has 28 physical processor cores, 28 virtual processor cores, and 384 gigabyte RAM. The following subsections describe the modeling and simulation procedure in Maxwell.

4.2.1 Rotor

The rotor core with salient poles was created with a user-defined primitive (UDP) called SalientPoleCore. A UDP is an adjustable template provided by Maxwell which allows for automated creation and parameterization of complicated geometrical objects. The input values were chosen according to a technical drawing of the rotor and can be seen in appendix D.1. A circle with a diameter equal to the inner diameter of the laboratory rotor was subtracted from the SalientPoleCore. However, the structure inside this circle, such as the shaft, was not included in the design as its effects on the simulations, other than increased computational time, were considered negligible. The rotor was assigned the material properties of steel 1010. Despite that real rotors are made of thin laminations in order to reduce eddy currents, only one solid piece was used for the model as core losses were not in the scope of this thesis. This simplification was considered to have inconsiderable effects on the conducted analyses.

The field winding was modeled as rectangles on each side of the poles. These were also solid objects, thus disregarding eddy current effects in the conductors. The rectangles were assigned the properties of copper and excited as stranded-type windings, such that the current density across the rectangles was averaged. The conductor objects at each side

of one pole were given opposite polarity to ensure correct flux distribution in the pole, and adjacent poles were defined differently to create positive and negative poles. The damper winding was also included in the model by creating seven copper bars in each pole shoe with geometry according to the technical drawing. They were excited with an end-connection that short circuited the bars at each end.

Finally, a so-called rotating band was created by defining a circle encapsulating everything inside the middle of the air-gap. It was assigned a motion setup which caused the rotor core, field winding, and damper bars to rotate counter-clockwise around the rotor center at $3000/7 \approx 428$ RPM according to the rated speed in table 3.2. The rotor model is shown in figure 4.1, where the field coils with dark brown color have negative polarity and the light orange coils have positive polarity.

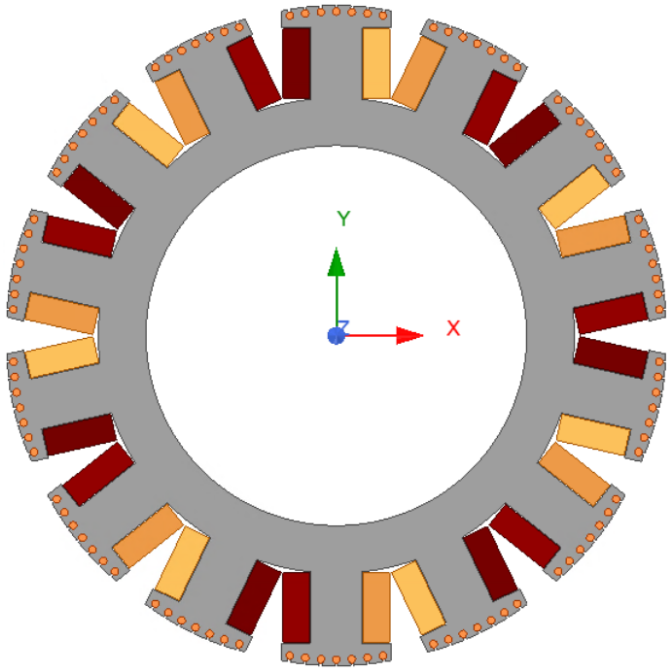

Figure 4.1: The rotor of the generator model in Maxwell.

4.2.2 Stator

The stator was manually modeled as none of the UDPs matched the geometry of the technical drawing of the laboratory generator stator. As for the rotor, the stator core was solid and core losses were neglected. After assigning the material properties of M400-50A to the stator, the yoke and teeth were separated into two parts such that the deformation of the yoke could be investigated separately. Moreover, a circle with a diameter equal to the outer stator was created and assigned a vector potential of zero flux to ensure no leakage flux exiting the outer stator edges. This was considered a valid simplification as long as the iron was not saturated, which was assumed based on similar simulations performed in the preliminary specialization project [7]. The same circle was also given the properties of air, such that all areas inside it without any material assignments were modeled as air, for instance the air-gap, the damper bar wedges, and the empty circle in the middle of the rotor.

The laboratory generator does not have a frame directly in contact with the stator. However, six rigid bars are attached to the outer stator surface acting as a supporting structure. As these bars are located outside of the defined zero flux potential at the rim of the stator model, they did not impact the simulations in Maxwell. However, they were still modeled since a 3D version of the stator from Maxwell were to be used for vibration simulations in Mechanical in which supporting structure may have an influence.

As for the rotor field winding, the stator armature was modeled as solid copper rectangles and placed in two layers in every slot. Since the model was 2D, winding transposition which can be used in real generators to reduce eddy currents was not included in the model. This, along with representing the armature as solid objects, can be justified by the exclusion of eddy current effects. To ensure the correct terminal voltage, the number of conductors in each coil was set to be equal to the number of turns per coil in the laboratory generator, which is two. The armature rectangles were excited with correct polarity and assign to three-phase windings according to the winding layout of the laboratory generator shown in appendix C.

Furthermore, two separate actions were made for the purpose of analyzing the air-gap flux and force. First, a vector arc was created in front of each tooth with a length corresponding to the tooth line depicted in figure 2.3. These arcs were assigned a feature called harmonic force calculation that uses Maxwell stress tensor from equation 2.2 and 2.3 to calculate the total force acting on each tooth at multiple time steps by integrating the radial and the tangential force density over the tooth line according to equation 2.5. Technically, an arc consists of a very high number of separate points. The distance between them is small, such that calculation of force density at each point in practice corresponds to a continuous representation of the tooth line. The reason for this feature assignment was that the frequency content of the radial and the tangential total force for each tooth was to be transferred to Mechanical for vibration analysis. In addition to the total force, the harmonic force calculation feature calculates the moment that acts on each tooth. Moment may cause twisting of the teeth and were to be transferred to Mechanical together with the force. The procedure described in this paragraph related to acquirement of the air-gap total force through harmonic force calculation is the most common approach for FE vibration

analysis of rotating electrical machines [74].

The settings chosen for harmonic force calculation resulted in a computed frequency resolution of 3.57 Hz. According to the predicted frequencies in table 3.3, air-gap force harmonics could appear at every 7.14 Hz. Thus, the interval between these was divided into two harmonic calculations, resulting in high-precision force calculation. Moreover, splitting the interval into two calculations made it possible to verify that the frequency spacing of the force was according to expectations, which was that the calculated harmonics at 3.57 Hz, 10.71 Hz, 17.85 Hz and so on should have zero amplitude in contrast to those at 7.14 Hz, 14.3 Hz, 21.4 Hz and so forth.

The arcs in front of each tooth formed a circle of calculation points around the entire air-gap, similar to the setup presented in figure 2.6. Thus, another advantage of the arcs was the possibility for analysis of flux and force in the spatial domain. For these spatial analyses, each arc was defined to consist of 30 separate measuring points, such that the points were tightly distributed 0.11 mechanical degrees apart from each other, and assigned calculation of flux density, force density, and total force at a single time step of the simulations.

To avoid possible numerical calculation errors in Maxwell due to the large difference between the permeability of air and iron, the arcs were not located at the very edge of the teeth but moved further into the air-gap. A sensitivity analysis was conducted to investigate the impact of arc location on the force calculation. Ten arcs were created in front of a tooth with 1 mm spacing between them, starting at 0 mm from the tooth and ending at 9 mm into the air-gap. This is shown in figure 4.2. The middle-point between the tooth edge and the closest rotor pole edge was at 0.875 mm from the tooth, which means that the ten arcs covered the whole distance from the tooth to the middle of the air-gap. The points constituting the arcs were assigned calculation of radial and tangential force density at one single time instant during no load operation and then integrated to obtain the total force. The result is shown in figure 4.3 where the total force normalized to the largest value is plotted, as a function of the distance from the tooth, for the given time instant. As shown, the total radial force at 0 mm from the tooth edge is negative while the remaining graph is constant. The total tangential force at 0 mm is around five times higher than the force calculated further into the air-gap, where the values are practically constant from 0.4 mm to 0.9 mm.

The large deviation in the total force calculated at 0 mm is most likely a result of numerical errors. The analysis shows that calculating the total radial force and the total tangential force at the very edge of the teeth is not reliable and would cause false results in simulation of vibration. As a result of the sensitivity study, supported by reference [75] where it was found that force calculation near the middle of the air-gap was more reliable than closer to the stator, the arcs were placed at 0.8 mm from the teeth. Figure 4.4 (left) shows an arc for one of the teeth located at 0.8 mm into the air-gap.

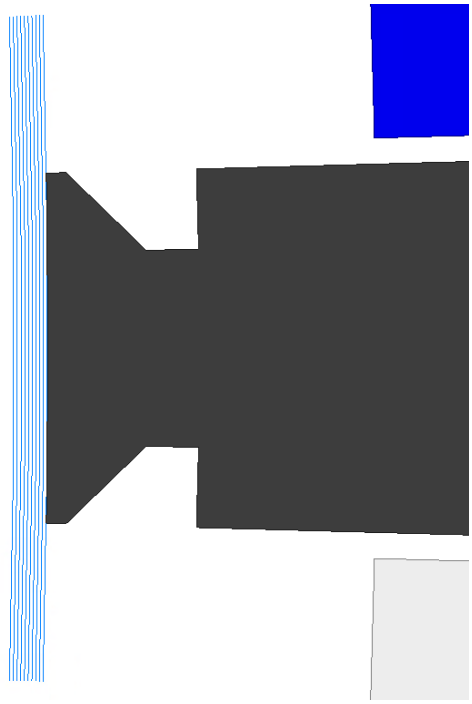

Figure 4.2: The ten arcs defined for sensitivity analysis of total force calculation in the air-gap.

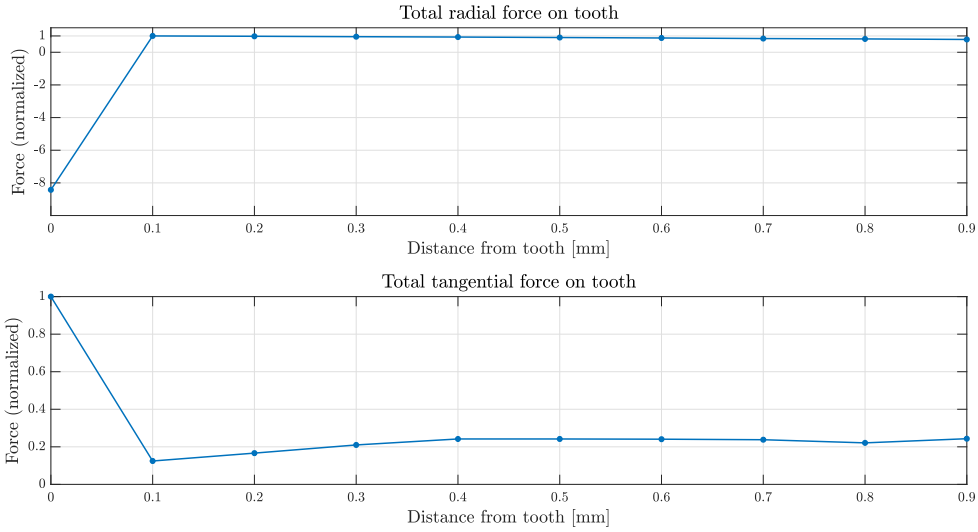

Figure 4.3: The total radial force (top) and the total tangential force (bottom) calculated at different distances from a tooth in the air-gap.

The tooth arcs described above enabled vibration analysis through the harmonic force calculation feature and made spatial analysis of flux and force possible. To get a detailed insight in how these behaved in the time domain as well, the second act regarding flux and force analysis was to create a geometry point, separately from the points that composed the arcs, and assign time-stepping computation of radial flux density, tangential flux density, and radial force density to this point according to Maxwell stress tensor. The calculations were performed at each time-step of the simulations. The point was located in front of the tooth lying on the positive x-axis of the model, 0.8 mm into the air-gap as shown in figure 4.4 (right). The programming software MATLAB has been utilized for spatial domain and time domain analyses of the flux density and force density, included transformation to the frequency domain through FFT, of which the results are presented in chapter 5 [76].

The stator core, support bars, armature, and tooth arcs are shown in figure 4.5 (left), where the different colored coils represent different phases. The fractional slot winding of $2 + \frac{5}{7} \approx 2.71$ is clearly visible as either two or three adjacent slots are occupied by the same coil for each layer. The complete Maxwell model, with the tooth arcs hidden, is depicted in figure 4.5 (right). Here, the short-pitch is visible as a coil group of one phase is shorter than the pole span.

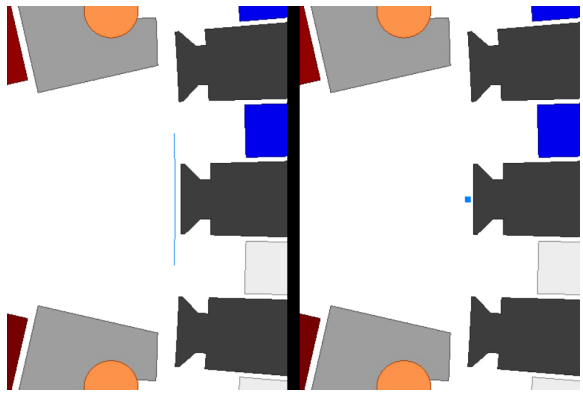

Figure 4.4: Arc (left) and point (right) used for calculation of total force and force density, respectively, in Maxwell.

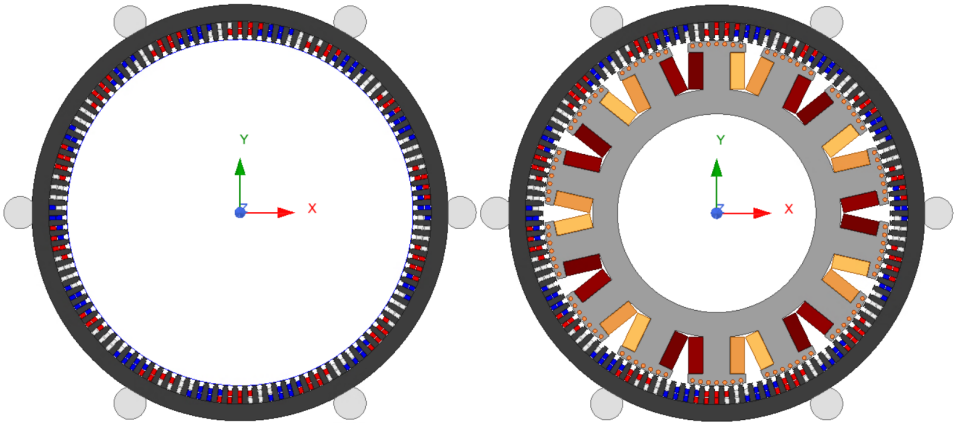

Figure 4.5: Stator core, armature and tooth arcs (left) and the complete generator model (right).

4.2.3 Mesh

The mesh describes how the model is divided into finite elements. For each time-step of a simulation, equations for nodes on the border between the elements are formulated. These equations are organized and solved numerically, while solutions for the area inside the elements are found by interpolation. Based on this, a representation of the whole model is created. A dense mesh, which contains a high number of small elements, would therefore give a more accurate representation than a coarse mesh with larger elements. However, as the number of equations to be solved each time step increases with the number of elements, a fine mesh also intensifies the computational effort and simulation time. Consequently, critical areas where accurate calculation of flux density is needed, such as the air-gap, were given a denser mesh than areas that did not require equally high resolution, such as the rotor core.

A combination of two mesh configuration techniques, called inside-selection and on-selection, were utilized to create the desired resolution in all the different parts on the generator. First, the maximum size of each element inside the boundaries of a selected object was restricted, consequently called inside-selection. Next, by using the on-selection technique, the maximum size of each element along the edges of an object was limited. Table 4.1 shows how the two configurations techniques were employed to restrict element size inside selected objects or along selected edges. As seen, the air-gap was given the highest element resolution by restricting the elements along with the rotating band in the middle of the air-gap to 0.5 mm, while the rotor winding had the most coarse mesh with an inside element size restriction of 5 mm. The support bars were left un-meshed as the defined zero flux potential at the stator rim prevented all flux from entering the bars. The resulting mesh for the various model objects is presented in table 4.2 and depicted in figure 4.6. The total number of elements was 211874 which was considered appropriate based on experience from the preliminary specialization project [7].

Table 4.1: Definitions of the finite element mesh.

Object	Configuration technique	Size restriction
Rotor core	Inside-selection	3.5 mm
Field winding	Inside-selection	5.0 mm
Stator windings	Inside-selection	2.5 mm
Stator teeth	Inside-selection	3.5 mm
Stator yoke	Inside-selection	3.5 mm
Rotor core edges	On-selection	2.0 mm
Rotating band	On-selection	0.5 mm
Stator teeth edges	On-selection	1.5 mm

Table 4.2: The resulting mesh of different model areas.

Object	Number of elements
Rotor core	60934
All field winding objects	10360
All damper bars	2058
All stator winding objects	14136
All stator teeth	27340
Stator yoke	29184
Air-gap	36863
Remaining areas with air	30999
Total	211874

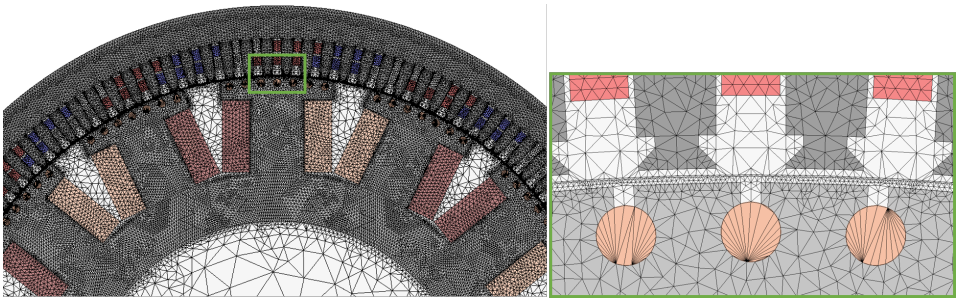

Figure 4.6: The finite element mesh with a zoomed section of the air-gap.

4.2.4 Solution setup

The solution setup of a simulation decides important parameters that affect both the accuracy of the results and the computational time and resources. One mechanical period of the laboratory generator is 140 ms. Based on guidelines for force calculation provided by ANSYS, eight revolutions, which correspond to 1120 ms, were evaluated to be sufficient for high-resolution FFT and identifying all frequency components of the calculated flux density, force density and total force assigned to the tooth arcs and point described in section 4.2.2 [77]. Moreover, to ensure that any possible transients in the calculated signals did not affect the analyses, one and two revolutions were added to the simulation time for no load and full load operation, respectively, such that the first 140 ms and 280 ms could be removed from the calculated signals before analysis. Thus, the total simulation time was 1260 ms and 1400 ms for no load and full load condition, respectively.

A sensitivity analysis containing simulations with time step ranging from 0.2 ms to 0.02 ms was performed to investigate the effects of increased sampling frequency on the air-gap flux density and force density. No noteworthy differences were found in the flux and force distributions acquired with sampling frequency higher than 8 kHz. Consequently, the time step was chosen to be 0.1 ms, causing a sampling frequency of 10 kHz. According to the Nyquist sampling theorem, this resulted in a maximum possible frequency of an FFT analysis to be 5000 Hz. The Transient Solver, which computes instantaneous values of the time-varying magnetic field at each time-step, was used for all simulations.

4.2.5 No load and full load simulation

During no load operation, the generator is disconnected from load causing no current to flow in the armature. This was simply modeled by setting the current in each phase winding to zero. The current of the rotor winding was set according to the required field current of the laboratory generator which produced a phase voltage of 230 V at the terminals, which was found to be 56 A. This was somewhat higher than the nameplate specification listed in table 3.2, but to ensure best possible agreement between simulations and laboratory measurements, 56 A was chosen.

Operation with a load connected to the generator terminals was also simulated in order to investigate how the vibration behavior differed from no load operation. This was modeled by using an external circuit, such that load impedance could be defined for each phase of the armature. Leakage flux, which occurs when current flows in the end-winding, was included in the circuit and the end-winding inductance was calculated to be 0.236 mH, as shown in appendix D.2. The total winding resistance of 0.049 Ω was also included for each phase. The external circuit is shown in figure 4.7. The leftmost inductors of each phase represent the windings of the armature, while the volt-meters and ampere-meters were included to enable measurement of the terminal voltages and the load currents.

For laboratory measurements, the nominal load operation listed in table 3.2, that is 100 kVA at a 0.9 power factor, would be of interest. However, the available setup in the labora-

tory set some limitations. These were taken into account in the external circuit such that the simulations would correspond to the operating conditions during measurements. The maximum possible output power of the generator is about 65 kVA with a power factor of 0.93. This can be achieved by connecting a resistance of 2.78 Ω per phase, which is the smallest resistance available, in parallel to a series of one inductance of 5 mH and one of 3 mH. The inductances are referred to the generator terminal side through a delta-star transformer with a winding ratio of 1.015:1, such that the inductance on the generator side is increased from 8 mH to 21.84 mH. Since indoctors can not be modeled in parallel in Maxwell, the load resistance and inductance were converted to an equivalent series impedance with value $\mathrm{Z_{load}} = \mathrm{R_{load}} + \mathrm{jX_{load}} = 2.38\Omega + \mathrm{j}\omega_s 3.08\mathrm{mH}$. Hereafter, this maximum possible loading condition will be termed *full load*.

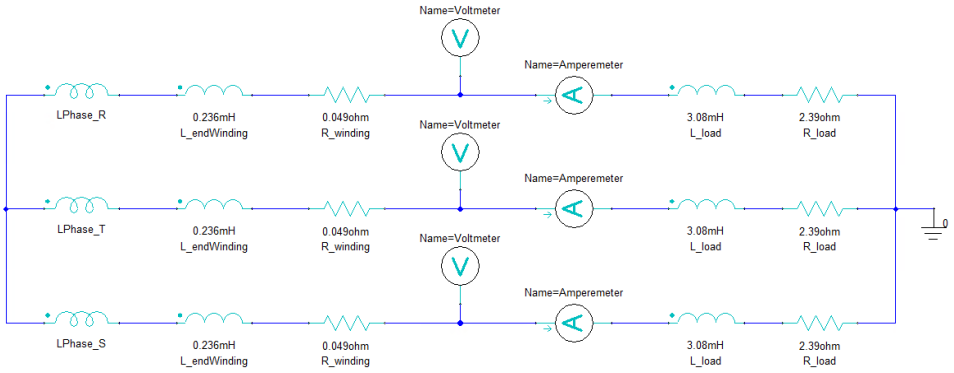

Figure 4.7: The external circuit used for full load simulations.

4.2.6 Fault modeling

The laboratory generator is custom-made for fault investigation in the sense that SE, damper winding fault and ITSC in the field winding of one, two, three, seven and ten turns can be achieved, and the simulated fault scenarios were chosen based on the possibilities to apply them to the generator. The damper winding is active when the rotor accelerates and there is a relative deviation between the speed of the rotor and the air-gap magnetic field. Consequently, faults in the bars or the end ring of the damper winding should be investigated when the generator operates at this condition. All measurements were planned to be performed in steady-state operation and damper winding faults were not in the scope of this thesis. Thus, the simulated faults were SE and ITSC in the rotor winding of one pole, both in no load and full load operation. How these were modeled is described in the two following subsections.

4.2.6.1 Inter-turn short-circuit in field winding

As described in section 2.2.1, a short circuit is categorized as inter-turn if there is a non-insulated connection point between conductors of the same winding, reducing the effective number of ampere-turns. This fault was applied to the top rotor pole, indicated in figure 4.8, simply by lowering the number of conductors in the rotor field winding excitation with one, two, three, seven and ten turns from the original 35 turns. Table 4.3 presents the modeled scenarios together with the fault degree, defined as the number of shorted turns divided by the total number of turns in one pole.

Table 4.3: The five modeled scenarios with different degree of inter-turn short-circuit (ITSC) based on number of shorted turns (ST) in the field winding.

Degree of ITSC	Number of ST
2.86 %	1
5.71 %	2
8.57 %	3
20.0 %	7
28.6 %	10

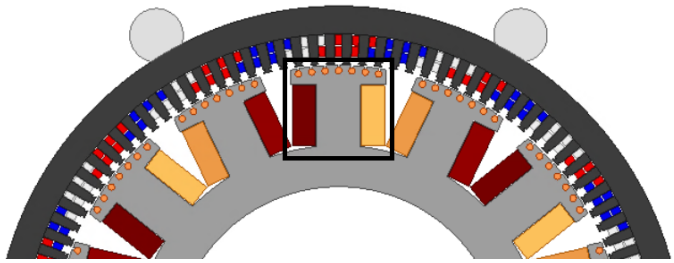

Figure 4.8: The pole with faulty field winding.

4.2.6.2 Static eccentricity

During SE, as described in subsection 2.2.2, the rotor rotates around its center axis which does not coincide with the stator center. SE in radial direction caused by rotor displacement was modeled by the following procedure. First, a new relative coordinate system was defined. It was displaced along the positive x-axis from the original coordinate system, which had origin in the center of the generator as shown in figure 4.5. Furthermore, all rotating objects, which were the rotor core, the field winding, the damper winding, and the rotating band, was moved to the center of the new coordinate system, such that the distance between the origins of the two systems corresponded to the degree of eccentricity. Finally, the reference orientation of these objects and the motion setup was assigned to the new coordinate system, such that they rotated around the displaced origin and SE was achieved. The degree of static eccentricity is defined as the displacement distance divided by nominal air-gap length, which is 1.75 mm in the laboratory generator, such that a rotor-stator-rub would occur during 100% eccentricity and rotor displacement equal to the nominal air-gap length.

The arcs and the point in the air-gap, described in section 4.2.2, were located 0.8 mm from the teeth, which was 0.087 mm from the rotating band located in the middle of the air-gap. Thus, when SE was imposed and the rotating objects were moved, the point and some of the air-gap arcs ended up inside the band. Since the point and arcs needed to be stationary in front of the teeth for correct calculations, the radius of the rotating band was adjusted after SE was imposed such that it was located at the midpoint between the rightmost rotor pole edge and the closest air-gap arc. In this way, the entire rotor was still encapsulated by the band while the point and arcs were left outside such that correct force calculation was achieved as in healthy operation. Finally, an additional air-gap point was created for simulation of SE. It was located at the opposite side of the original point, such that the difference in flux and force between the reduced air-gap length and the increased air-gap length could be analyzed.

Three models with different degrees of eccentricity were made to examine the effect of fault severity on generator vibration. These are presented in table 4.4.

Table 4.4: The three modeled scenarios with different degree of static eccentricity (SE).

Degree of SE	Rotor displacement
10 %	0.175 mm
20 %	0.350 mm
30 %	0.525 mm

4.3 Modeling in Mechanical and simulation of vibration

ANSYS Mechanical was employed for vibration analysis of the same scenarios simulated in Maxwell. The stator geometry, the total force, and the moment calculated at the air-gap arcs were transferred from Maxwell to Mechanical via a third ANSYS software called Workbench [78]. Workbench allows for interaction between different ANSYS software and ensures proper transfer of design and result files. Despite that the stator was accurately modeled in Maxwell, some adjustments had to be made before the vibration could be simulated.

4.3.1 Model adjustments

First of all, before the transfer to Mechanical, the stator teeth, yoke, and support bars were converted from 2D to 3D in Maxwell. This was done by using a feature called sweep along a 0.208 meter long vector which was located in the middle of the rotor and pointing in the axial direction, such that these objects were extended equally long as the stator depth in the laboratory generator. The 3D stator was then imported to Mechanical. Stator windings were not included in Mechanical as they were assumed to have an inconsiderable effect of the stator vibration.

Several different features are available in Mechanical for defining supporting structure. Some of these which were relevant for the support bars in the laboratory generator are the stiffness of the material and how the bars are connected to the stator bore and to larger external foundation structures. For correct implementation of the support bars, these parameters had to be investigated and measured. However, this was not possible due to the shut down of the laboratory caused by the coronavirus. There were also no available drawings or other documentation with relevant information that could replace such an inspection. Thus, without any other choice, it was decided to exclude the support bars from the vibration simulations simply by removing them from the stator model in Mechanical.

A new mesh had to be defined in Mechanical since the geometry from Maxwell was converted from 2D to 3D. A sensitivity analysis was conducted to find the appropriate method and maximum element size for the mesh of the teeth and the yoke. This was done by comparing results of simulated deformation under different methods and restrictions, starting from a coarse mesh and tuning it until the results converged. It was found that a method called sweep resulted in elements having as equal shape as possible, which is favorable to avoid numerical calculation errors. The size restrictions decided from the sensitivity analysis and the resulting number of elements are presented in table 4.5. The total number of elements in the model was 329181. The generator model in Mechanical is depicted in figure 4.9.

Table 4.5: Mesh characteristics of the model in Mechanical

Area	Element size restriction	Number of elements
Stator teeth	3.6 mm	181048
Stator yoke	5.0 mm	148133

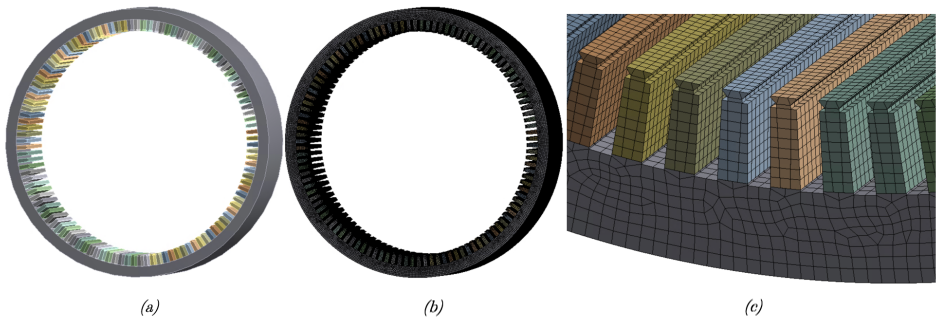

Figure 4.9: The generator model in Mechanical: un-meshed (a), meshed (b) and zoomed section of the mesh (c).

4.3.2 Solution setup

Several solution features are available in Mechanical. Two of them, called Modal and Harmonic Response, have been utilized in this thesis. Each of them serves their own purpose and require their own solution setup.

4.3.2.1 Modal analysis with Modal

A modal analysis with the solution feature Modal was performed to find the natural vibration frequencies of the stator. Since supporting structure was not included in the stator model, the natural frequencies from Modal were expected to differ from the ones present in the real laboratory generator. The analysis was still executed since the natural frequencies could affect the Harmonic Response vibration simulation. Moreover, a modal analysis reveals the deformation shape of the stator at the natural frequency of each vibration mode and it is interesting to compare these to the presented theory on how the number of attraction points increases with the mode number. The solution setup of Modal was specified to find the natural frequencies of the first six vibration modes and damping was excluded due to the absence of the support bars.

4.3.2.2 Vibration analysis with Harmonic response

Harmonic response simulates the vibration caused by the total force and moment calculated in Maxwell. These were imported to Mechanical and, for each tooth, the radial and tangential force components were added together to form a resultant force vector, which was defined to act on the tooth area facing the air-gap. As mentioned, the feature that was assigned to the arcs in front of the teeth in Maxwell was called harmonic force calculation. This implies that the frequency content, and not the time distribution, of the total force was imported to Mechanical. Thus, the force was applied to the teeth at several frequencies and from there utilized to simulate the resulting vibration at each frequency. This means that no time domain information was obtained in Mechanical, only the frequency distribution of the vibration. The moment was also defined to act on each tooth area facing the air-gap.

The analysis settings decide the frequencies of which the vibration shall be calculated. That is, for each defined frequency, the vibration is calculated based on the imported total force with this frequency. If there is no force with the same frequency as defined for vibration calculation, the force at the two closest frequencies are interpolated. The calculation frequencies had to be defined with care to ensure sufficient accuracy in the results while limiting the simulation duration and resources. First, a simulation with frequencies from 0 Hz to 2000 Hz was performed to form an overview of the dominant vibration frequencies in the generator. The results showed that vibration was of interest up to 400 Hz and, thus, the settings for Harmonic Response were chosen to calculate vibration from 7.14 Hz to 400 Hz. The frequency interval between the imported harmonics was 3.57. However, inspection revealed that the harmonics outside every 7.14 Hz had an amplitude of zero and that the force harmonics appeared at every 7.14 Hz, as expected. Consequently, the spacing between each frequency for vibration calculation in Harmonic Response was set to 7.14 Hz.

An additional consideration regarding the choice of frequency resolution had to be made related to the natural frequencies found from the modal analysis. If resonance effects are to be detected in the vibration simulation, the exact value of the natural frequency must be defined for calculation. Thus, with the chosen resolution, resonance would be detected if the natural frequencies were located at a multiple of 7.14 Hz. However, the modal analysis revealed that this was not the case and additional frequencies had to be defined specifically for calculating the vibration at the natural frequencies. The resolution of these had to be very high, causing a large increase in computational time and effort of the simulation. Since the stator was unsupported and the simulated natural frequencies would likely differ from the real laboratory generator, only a few simulations with high frequency resolution were performed. This was no load and full load operation in healthy condition, and the most severe scenario of both faults at no load operation. These simulations were performed in order to investigate the coherence between the excited force harmonics and possible resonance effects at the natural frequencies. Their frequency range was limited to be between 7.14 Hz and 400 Hz as for the main vibration simulations.

Chapter 5

Simulation results

This chapter presents the simulation results from Maxwell and Mechanical with focus on magnetic and mechanical properties during healthy and faulty operation. In order to properly understand the reasons for vibration, the flux and force in the air-gap have be analyzed in detail. Thus, results regarding the magnetic flux density, magnetic force density, and total magnetic force are presented in subsections labeled *magnetic analysis*, which again are divided into results from the time domain and from the spatial domain. Since deformation can be easily obtained from vibration measurements with accelerometers through integration, stator deformation is used for vibration analysis in this thesis and presented in subsections labeled *mechanical analysis*. The results are shortly commented in this chapter and further discussions are presented in chapter 6.

As mentioned before, the simulated scenarios embrace no load and full load operation of healthy condition, with ITSC in the field winding and with SE. The various fault degrees are summarized in table 5.1. In the following presentations of fault scenarios, results from no load operation will be included while the full load simulation results are left to appendix E. In this way, the length of this chapter is limited and, besides, the no load and full load simulation results do not differ by much, meaning that the same trends and conclusions have been found for both conditions. Simulation results of both no load and full load operation are presented for healthy condition to clarify the effects of loading.

Table 5.1: Simulated fault scenarios.

Short circuit		Static eccentricity	
1 turn	2.86 %	0.175 mm	10 %
2 turns	5.71 %	0.350 mm	20 %
3 turns	8.57 %	0.525 mm	30 %
7 turns	20.0 %		
10 turns	28.6 %		

The magnetic analyses presented in this chapter have been conducted in order to give a detailed insight into how the air-gap magnetic properties, that is the flux density, radial force density and total force, behave in the time domain and in the spatial domain. In both domains, frequency spectra have been obtained from FFT in MATLAB. The figures that contain the FFT of time domain information are equipped with two x-axes, one at the bottom of the figure and one at the top. The bottom axis is labeled with frequency in hertz like FFT presentations commonly are, while the top axis is labeled with the corresponding time harmonic order as this is also of interest in a vibration point of view. The y-axis of these figures is scaled logarithmically such that harmonics with large amplitude differences can be practically presented in the same figure. The logarithmic decibel values are obtained by the following conversion:

$$A_{dB} = 20 \cdot log_{10} \left(\frac{A_{harmonic}}{A_{ref}} \right), \tag{5.1}$$

where A_{dB} is the logarithmically converted amplitude, $A_{harmonic}$ is the amplitude of the harmonic, and A_{ref} is a reference value equal to 1 unit. The y-axis range of the figures containing flux density harmonics is limited from 0 dB to -90 dB, corresponding to 1 T and 31.6 μT respectively, while the figures containing force density harmonics range from 100 dB to 20 dB, corresponding to 100 $\mathrm{kN/m^2}$ and 10 $\mathrm{N/m^2}$ respectively. The lower limits ensure appropriate representation of the results as values around these limits are considered too small to affect the generator to a noticeable degree.

As only the harmonic order is of interest in the spatial domain, the figures containing FFT of spatial domain information are equipped with only one x-axis labeled with the spatial harmonic order. They are intentionally plotted in a different style than the FFTs from the time domain for practical purposes and to distinguish them from each other. According to common practice in the literature, the y-axis of these figures is not scaled logarithmically but labeled with their actual force density amplitude.

The figures obtained from vibration analysis consist of two plots with the same data but with different y-axis scaling. One of the plots is presented with their actual value of deformation in millimeters while the other is scaled logarithmically with the same conversion as presented in equation 5.1 for practical presentation of large differences. Both plots are equipped with a single x-axis labeled with frequency. Vibration can be expressed in units of acceleration, velocity or deformation and will be described by deformation in this thesis due to the convenient relation to the presented theory. The shape of stator deformation at various frequencies has also been analyzed in order to study the influence of the vibration modes based on the number of attraction points in the stator. This is illustrated in figures where the severity of deflection is increased and the deformation shape is emphasized. This means that in reality, the stator would not be as dramatically modified as depicted in these figures but the deformation profile will be the same.

It should be mentioned that the presented FFT figures in general contain the absolute value of the harmonics. This is despite the fact that a harmonic can have a negative sign if it rotates in the opposite direction of the rotor. This is done for practical purposes and because

the sign of the harmonics is rarely of interest. For instance, the direction of rotation of a force wave does not influence its effect on stator deformation. However, the sign is included in the analysis for a few specific cases where it is important. This will be emphasized in the relevant sections.

A final note regarding the figures presented in this chapter concerns how they are plotted. In MATLAB, which is the software used for creation of all plots in this thesis, the graphs that represent flux distributions, force distributions, FFTs, and vibration spectra, are plotted subsequently. Consequently, a graph may cover another graph that is previously plotted in the same figure. This is emphasized here since most of the figures presented in this chapter contains more than one graph, for instance in the simulations results from ITSC fault where all the five fault severities and the healthy condition is plotted in the same figure. In the FFT figures, the scenario with highest harmonics are usually plotted first, such that these are visible even though harmonics with lower amplitudes are plotted afterwards.

The following sections present the simulation results of healthy generator followed by operation with ITSC in the rotor winding and then SE. However, first, the results from the modal analysis are presented.

5.1 Modal analysis

The natural frequencies of the first six vibration modes of the unsupported stator are presented in table 5.2 as f_{nat}^{m}. If an excited force with a certain mode number, that is its spatial harmonic order, has a frequency at or sufficiently close to the natural frequency of that mode, resonance effects will intensify the resulting vibration. The table shows that the mode numbers follow the order of the natural frequencies, such that the first natural frequency belongs to the first mode, the second natural frequency to the second mode, and so on. Based on the results, the second mode is of interest during healthy operation as the expected lowest spatial harmonic order in the laboratory generator is two and the main force harmonic has a frequency of 100 Hz with $k = 14$. Thus, if it is assumed that a force wave with $k = 14$ and $m = 2$ is present in the air-gap, the second natural frequency may be close enough to cause resonance. Moreover, if the generator suffers from a fault that excites a force with the first-order spatial harmonic and the first-order time harmonic at 7.14 Hz, the first natural frequency may be close enough to cause resonance. The modal analysis is conducted with supporting structure excluded and, thus, the presented natural frequencies can differ somewhat from the real laboratory generator. However, they may influence the results from the vibration simulations presented in the following sections and are therefore important to be aware of.

Figure 5.1 shows the static deformation of the unsupported stator at the six natural frequencies. Red color represents large deformation and blue color represents low deformation, and the severity of geometry deflection is increased in the figure in order to emphasize the deformation profile of the stators. The mode numbers, which correspond to the number of attraction points, are clearly visible if the deformed shapes. Mode number zero, which is a pulsating and not rotating mode, and modes that do not impose radial deformation are not in the scope of this thesis and not included in the figure.

Table 5.2: The first six natural frequencies of the unsupported stator.

Mode, m	f_{nat}^{m}
1	0.21 Hz
2	118.3 Hz
3	327.7 Hz
4	620.1 Hz
5	983.8 Hz
6	1409.4 Hz

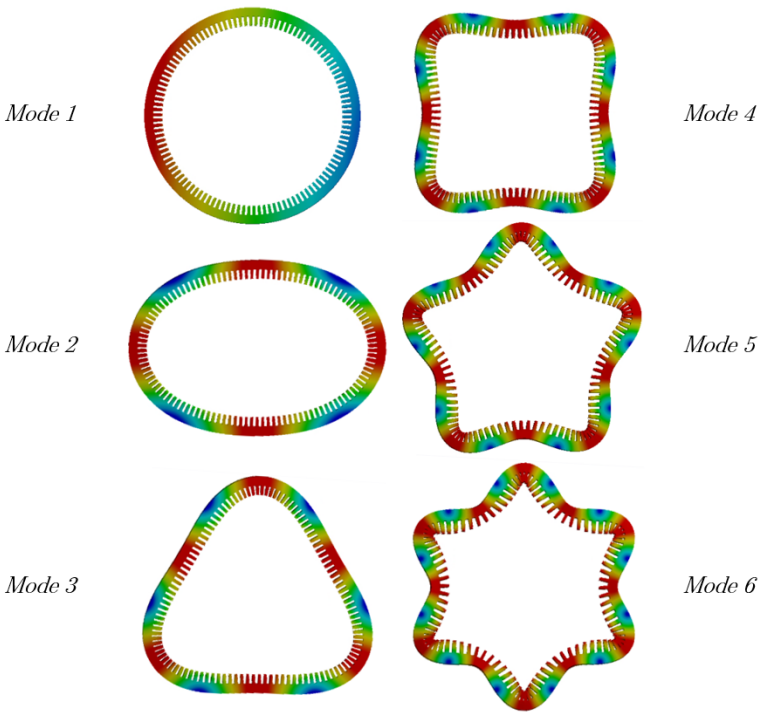

Figure 5.1: Deformation profiles of the first six vibration modes at their natural frequencies.

5.2 Healthy generator

5.2.1 Magnetic analysis

5.2.1.1 Time domain distributions with FFTs

The time domain distribution of the radial flux density in the air-gap caused by four of the top poles passing the air-gap point in front of the rightmost tooth is shown in figure 5.2. Full load and no load operation are compared and, as seen, the armature reaction caused by the load influences the shape of the waves. The amplitude is somewhat increased and the slightly inductive load, with a power factor of 0.93, imposes a small lagging phase shift.

The waves are affected by some high-frequency harmonics that cause a ripple in the amplitudes. These are most easily seen in the distribution of no load operation as the waves are more or less symmetric around their peak and not influenced by loading. Seven deep dips in each amplitude are caused by the slots where the seven damper bars of the rotor are located. These slots cause a non-uniform permeability path for the flux emitting the poles which leads to decreased air-gap flux density. Other harmonics of lower frequency can be seen to impact the waves around their zero-crossing. These distortions of the sinusoidal waveform are caused by the natural harmonics at odd multiples of the fundamental frequency.

The selected time period from 0.08 - 0.12 seconds shown in the figure is representative for a full rotor rotation, as the symmetrical generator topology and steady-state operation cause periodic flux in the air-gap. Only the limited time period of the signal is included in the figure to enhance the resolution of the plot and emphasize the shape of the waves. The distribution for a full revolution, that is from 0 - 0.14 seconds, is included for SE in figure 5.40.

Figure 5.3 shows the FFT of the radial flux density in the air-gap from figure 5.2. The fundamental component caused by the seven rotor pole pairs corresponds to 50 Hz given by the synchronous electrical frequency. It dominates the spectrum with a ten times higher amplitude than the component at 150 Hz when the logarithmic values are converted to Tesla. Natural harmonics occur at its odd multiples, and the slight difference between no load and full load operation is visible here as well. The largest difference between the harmonics in no load and full load operation is seen at 250 Hz, where the logarithmic amplitude deviation corresponds to 18 mT.

Some inter-harmonics occur with magnitudes below -80 dB. -80 dB corresponds to 0.1 mT which means that these harmonics are relatively very small compared to the fundamental with an amplitude of 0.5 T. They are results of small distortions of the waveform in figure 5.2 such as some of the dips caused by the damper bars.

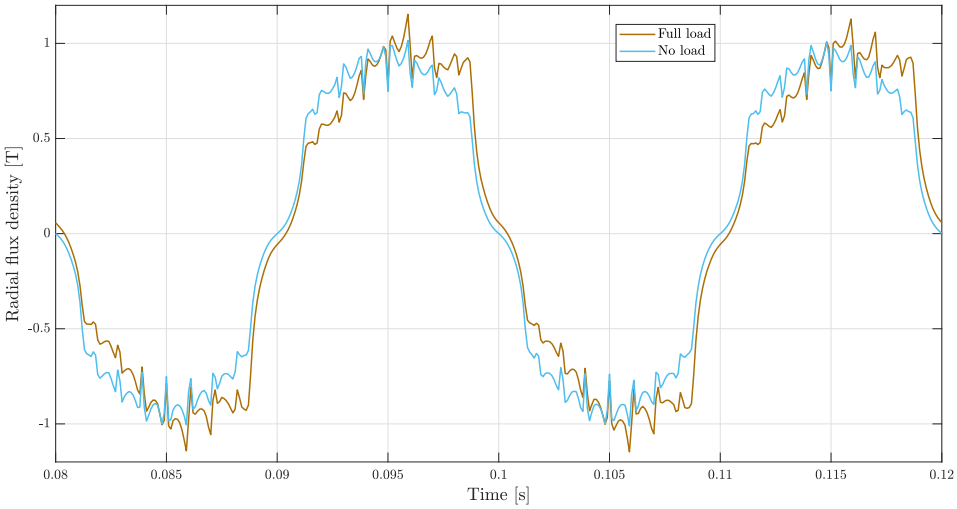

Figure 5.2: Time domain distribution of radial air-gap flux density during healthy operation.

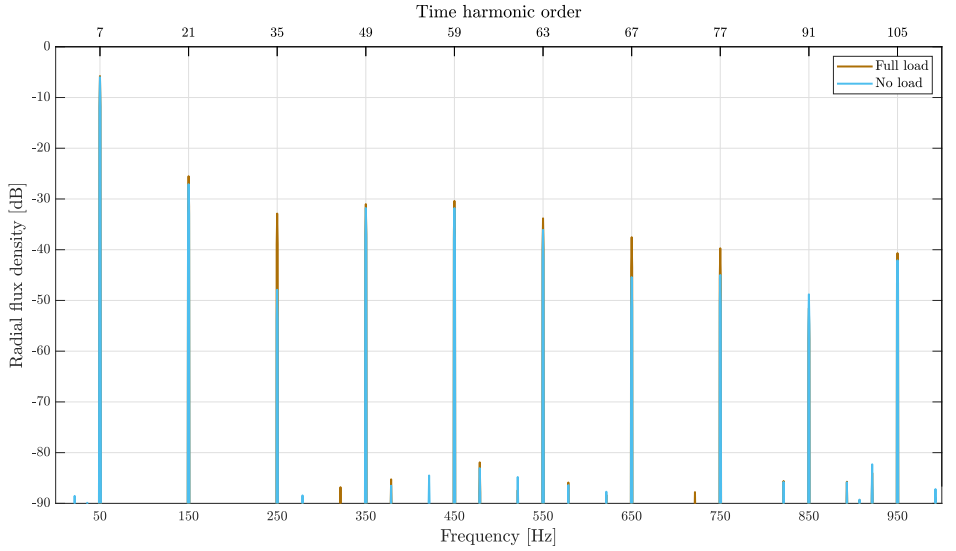

Figure 5.3: Frequency spectrum of the time distribution of the radial air-gap flux density during healthy operation.

The radial air-gap force density is depicted in figure 5.4 for the same time period as for the flux density. From Maxwell stress tensor in equation 2.3, squaring the flux density changes the negative flux density amplitudes to positive force density amplitudes at the corresponding time instants. The squaring also makes the impact of the damper bars even more notable in these waves. However, sinusoidal behavior is still recognizable and the difference between no load and full load operation is also increased compared to the distribution of the flux density. The lowest value of the wave is at -32 $\mathrm{N/m^2}$ which is too small to notice in the figure. This could indicate that the tangential flux density component, which imposes a negative term in the Maxwell stress tensor, is insignificant. However, as the waveform of the radial and tangential flux components is different, this conclusion can not be drawn based on this figure. To determine the influence of the tangential component, a more detailed study is presented at the end of this subsection.

In the frequency spectrum presented in figure 5.5, the 14th harmonic is the main component. It corresponds to 100 Hz and twice the frequency of the fundamental flux harmonic. This coherence is directly deduced from Maxwell stress tensor as the squaring the flux density causes the force density to peak when the flux is both at its positive and negative maximum. Natural harmonics are present at every multiple of 100 Hz, caused by the interaction between natural flux density harmonics, and the increased difference between no load and full load operation is visible in the frequency domain as well as in the time domain. Some minor inter-harmonics and subharmonics appear with amplitudes below 100 $\mathrm{N/m^2}$ and 30 $\mathrm{N/m^2}$, respectively. This is 0.1% and 0.04% of the main component, respectively, and likely inconsiderable for the vibration of the generator.

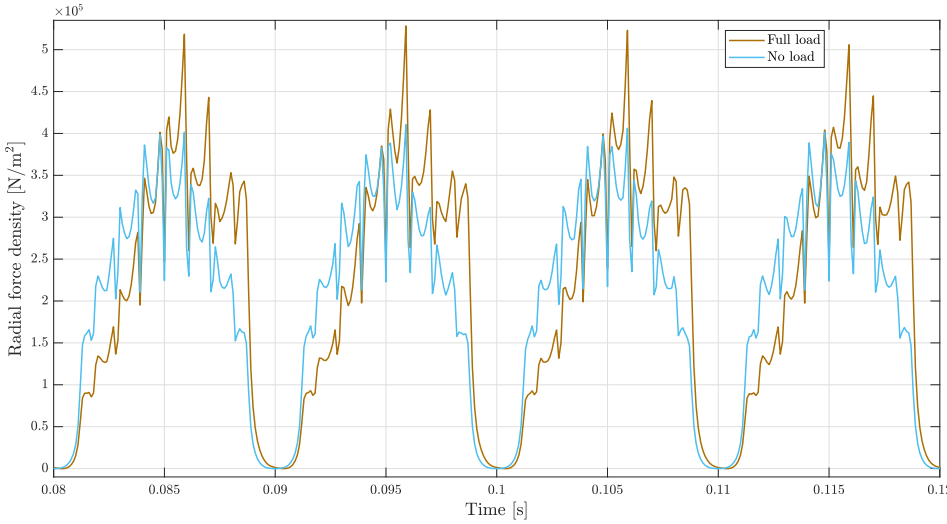

Figure 5.4: Time domain distribution of radial air-gap force density during healthy operation.

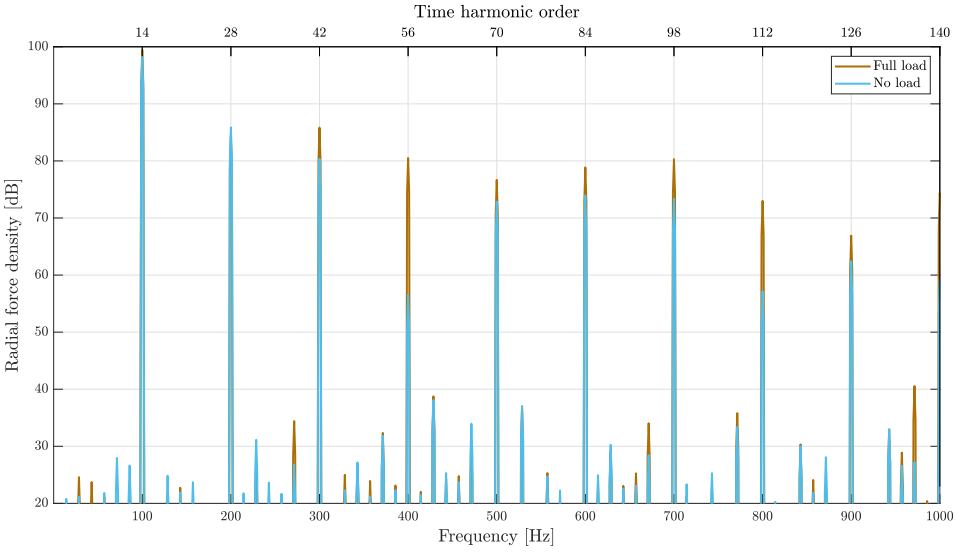

Figure 5.5: Frequency spectrum of the time distribution of the radial air-gap force density during healthy operation.

A simplification made during the formulation of the analytical model in section 2.2.6 was to only include the radial flux density and neglect the tangential component. Figure 5.6 compares the radial component, b_r, and tangential component, b_t, of the flux density during healthy, no load operation. Their waveforms are naturally different and the tangential component is considerably lower in magnitude. At the time instances when the smallest difference between b_r and b_t occurs, b_t has a amplitude of less than 10% of b_r.

This is also illustrated in the FFT of the two components shown in figure 5.7. The amplitude of b_t at 50 Hz and 150 Hz is 2.2% and 3.6% as large as b_r, respectively. The differences decreases as the frequency increases, and b_t reaches 46% of b_r at 750 and 94% at 950 Hz.

According to equation 2.3, the radial force density, f_r, consists of two components: one caused by the radial flux density, f_{rr}, and one caused by the tangential flux density, f_{rt}. Hence, 2.3 can be written in the following way

$$f_r = \frac{1}{2\mu_0}(b_r^2 - b_t^2) = \frac{b_r^2}{2\mu_0} - \frac{b_t^2}{2\mu_0} = f_{rr} - f_{rt}. \tag{5.2}$$

Figure 5.8 shows the relationship between these three components during healthy, no load operation. The contribution from the tangential flux density to the radial force density is relatively very small, which is due to its waveform and low magnitude. In fact, it can hardly be seen any difference between f_r and f_{rr} caused by $-f_{rt}$. At most, f_{rt} reaches less than 3% the amplitude of f_{rr}.

This is also illustrated in figure 5.9, where the frequency content of f_{rr} and f_{rt} is plotted with logarithmic scale. The 100 Hz component of f_{rt} is only 0.3% of the 100 Hz component of f_{rr} when their amplitudes are converted to Tesla. The differences between the higher-order natural harmonics are somewhat smaller, although still significant when the logarithmic conversion is taken into account. Finally, it can be seen that f_{rt} does not contain any harmonics that are not present in f_{rr}.

The same analyses with similar observations were made for healthy full load operation and for all fault scenarios in both no load and full load operation. In the following sections, only the radial component of the flux density will be presented since the influence of the tangential component is minor. However, it is emphasized here that b_t was indeed included in all FE simulations for accurate calculation of the radial force density.

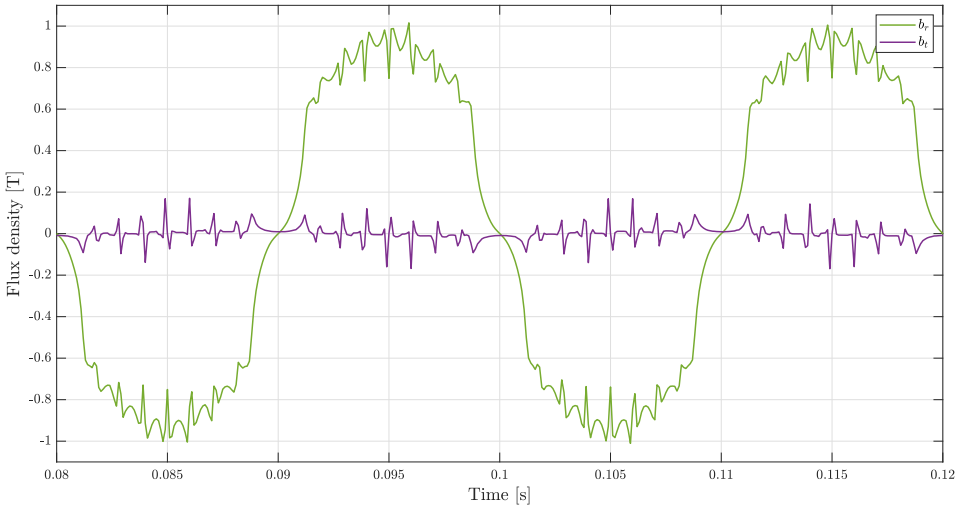

Figure 5.6: The time distribution of the radial component and the tangential component of the air-gap flux density during healthy, no load operation.

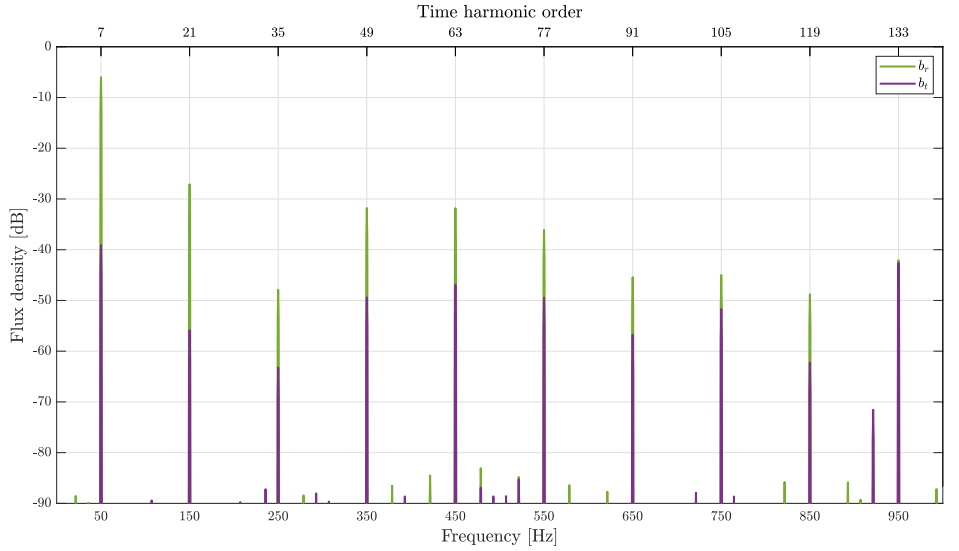

Figure 5.7: Frequency spectrum of the time distribution of b_r and b_t during healthy, no load operation.

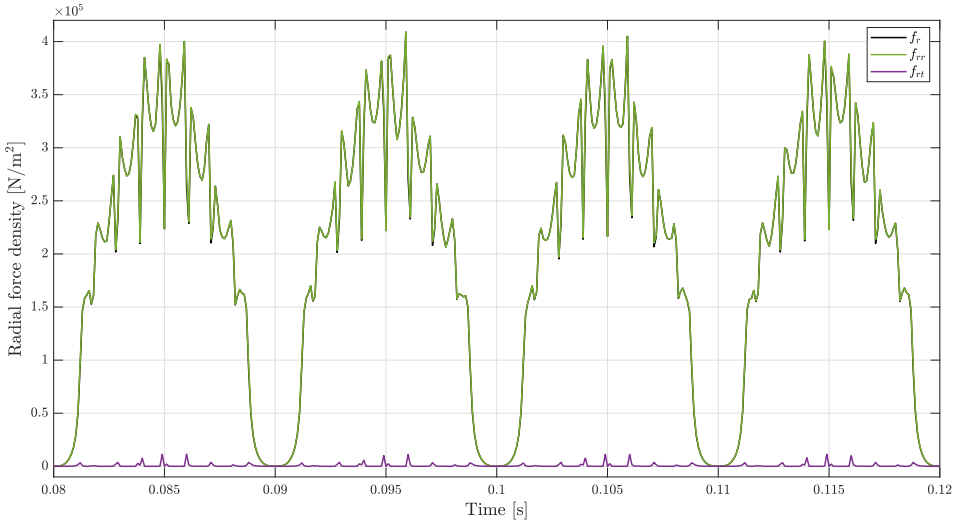

Figure 5.8: The time distribution radial force density caused by the radial flux density, f_{rr}, and by the tangential flux density, f_{rt}, together with the total radial flux density, f_r, in the air-gap during healthy, no load operation.

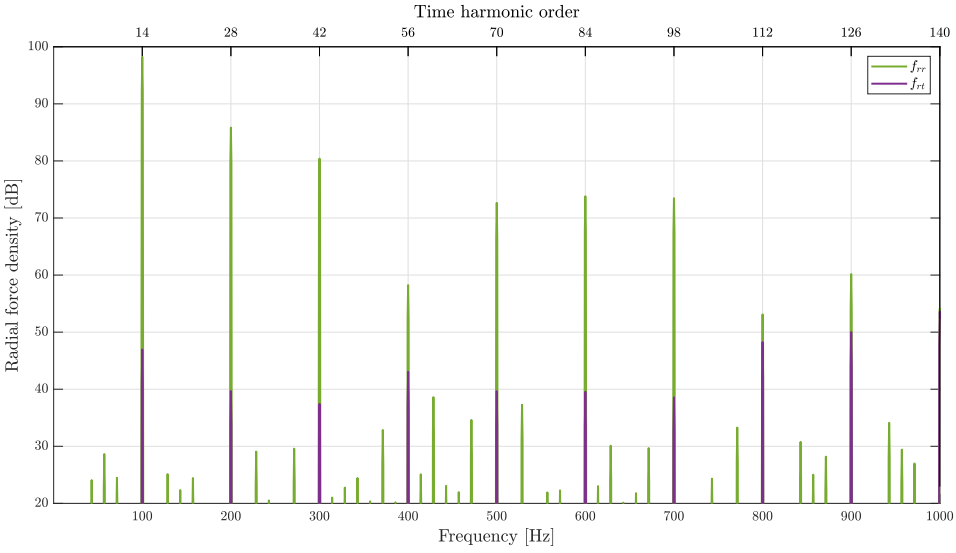

Figure 5.9: Frequency spectrum of f_{rr} and f_{rt} in the time domain during healthy, no load operation.

5.2.1.2 Spatial domain distributions with FFTs

Figure 5.10 shows the spatial distribution of the radial air-gap flux density in healthy condition under no load and full load operation. The distribution was acquired at a single time instant when the rotor was at position $\omega_r t = 0°$ with respect to the x-axis in the generator model in figure 4.5. This means that zero mechanical degrees on the x-axis of the spatial distribution corresponds to the positive x-axis in the generator model. The mechanical degrees on the x-axis in the figure increase according to the counter-clockwise rotation of the rotor, such that 90 degrees corresponds to the top rotor pole.

The sinusoidal behavior earlier seen in the time domain is also evident in figure 5.10. The seven positive and seven negative peaks are caused by the seven pole pairs and the rotor geometry produces a waveform that is not far from sinusoidal. However, the dips in the amplitudes are more significant than in the time domain and are now caused by the stator slots. The phase shift of the full load distribution is visible as amplified flux density at the left side of each peak. This is naturally the opposite side compared to the time domain distribution as the field strength is strongest at the lagging side of each pole.

Figure 5.11 presents the FFT of the spatial flux density distribution. As expected, the fundamental component is number seven, equal to the number of pole pairs, and natural harmonics appear at its odd multiple. Each natural harmonic has a small side-band component, which is the term for a component with an order that differs from a natural's order by one or two. In figure 5.11, the side-bands have orders that differ by two, which leads to the expectation of a second-order harmonic to appear in the force density spectrum due to the interaction between the side-bands and the natural components. Furthermore, two distinct harmonics are present with order 107 and 121. These are the slot harmonics determined by $m_{slots,flux} = Q_s \pm p = 114 \pm 7$. The difference between no load and full load operation is visible as various increments in the odd multiple natural harmonics with number 35 being most affected. The highest order slot harmonic and some of the side-band components are also increased in loaded operation.

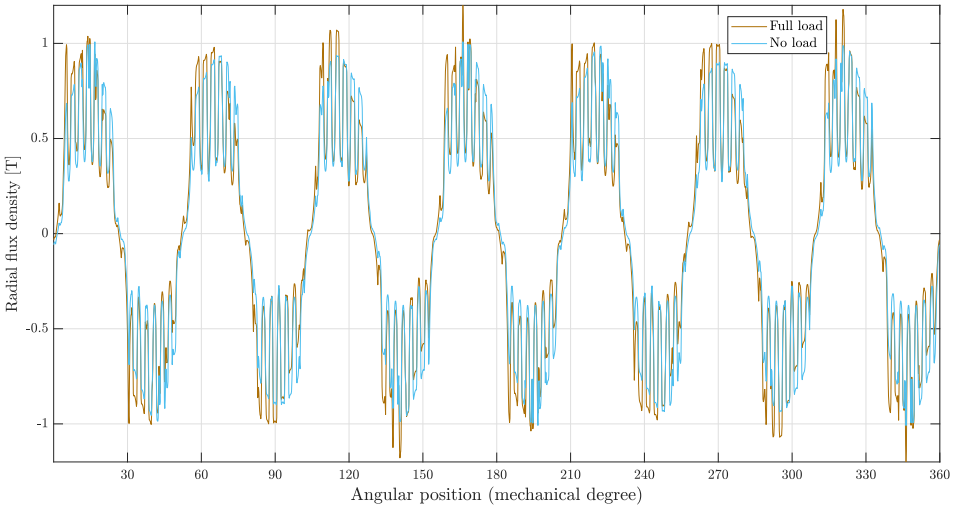

Figure 5.10: Spatial distribution of radial flux density in healthy condition during no load and full load operation.

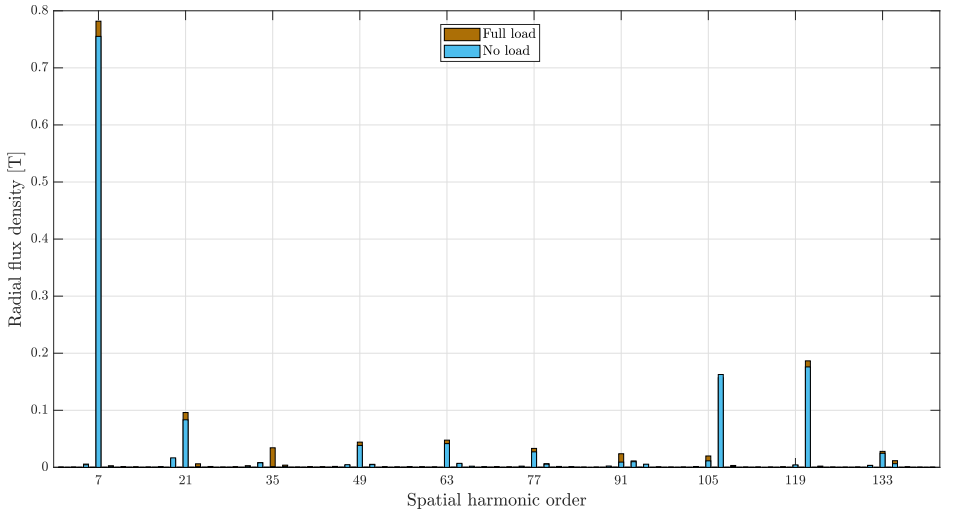

Figure 5.11: Frequency spectrum of the spatial distribution of radial flux density in healthy condition during no load and full load operation.

Figure 5.12 depicts the spatial distribution, obtained a single time instant with rotor position $\omega_r t = 0°$, of the radial force density in no load and full load healthy operation. The air-gap consists of fourteen positive force peaks caused by the seven positive and seven negative flux density peaks. The dips in the amplitudes caused by the slots are significant and almost as deep as the height of the waves.

The lowest spatial order can be recognized in the figure by the variable height of the peaks around the air-gap. In the no load distribution, a fictitious sinusoidal wave with two positive and two negative peaks is formed from variations of the maximum value of the fourteen waves. This is also visible in the full load distribution, as the wave pattern between 0 and 180 degrees is repeated from 180 to 360 degrees. These patterns imply that the lowest spatial harmonic order in the distributions is two.

This is confirmed in the FFT shown in figure 5.13. The second-order spatial harmonic was expected as the lowest order since the GCD between the number of poles and the number of slots in the laboratory generator equals two. The figure shows that its amplitude is larger in full load operation which is due to some of the amplified flux density harmonics with orders that differ by two. In specific, the amplitude of the second-order harmonic is about doubled during loading which means that the armature reaction may have a notable impact on the vibration level of the generator during healthy operation. In general, almost all harmonics are increased to some degree when the generator is loaded.

The largest slot harmonic is in the same size range as the main component. The large slot harmonics are results of factors such as the fact that the slots are open and the relatively large depth of the stator slots compared to the air-gap length. However, their high spatial orders make them insignificant for deformation and they will not impact the vibration level of the generator. Their orders are determined based on interaction between the fundamental and the slot harmonics in the spatial flux density distribution, in specific $m_{slot,force} = m_{slot,flux} \pm p = 107 \pm 7$ and 121 ± 7 which gives $m_{slot,force} = 100, 114$ and 128.

The radial force density provides detailed information about the air-gap. However, it is the total radial force that acts on the teeth and cause vibration. According to equation 2.5, the radial force density has been integrated over the tooth line and multiplied with the stator stack length. This is presented in figure 5.14 for healthy condition during no load operation where each dot on the graph represents a tooth. The distribution is obtained at the mentioned time instant and dominated by the peaks from the fourteen poles with a maximum value around 850 N, and the second-order spatial harmonic is clear from the symmetry around tooth number 58.

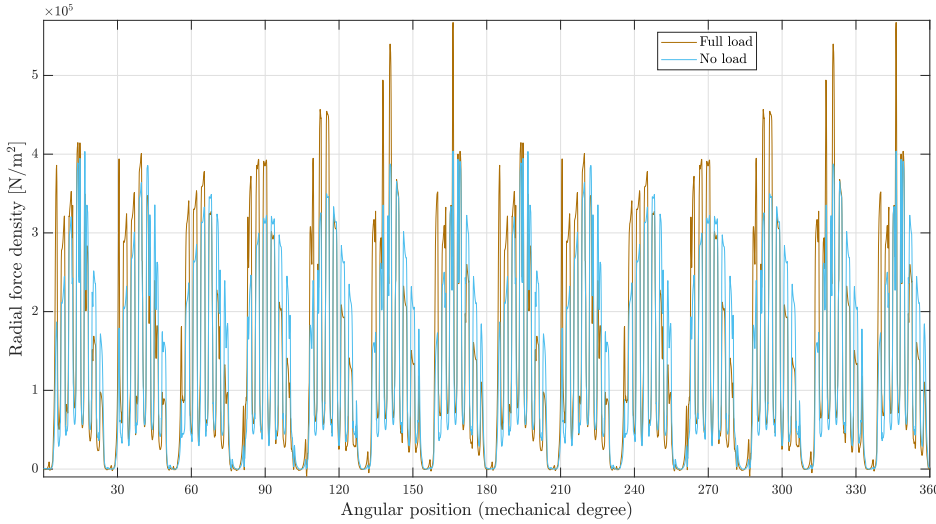

Figure 5.12: Spatial distribution of radial force density in healthy condition during no load and full load operation.

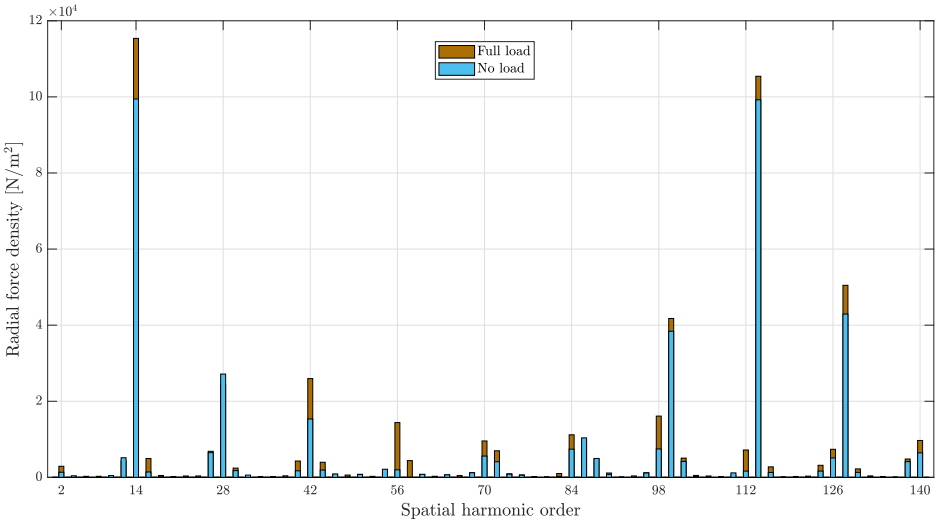

Figure 5.13: Frequency spectrum of the spatial distribution of radial force density in healthy condition during no load and full load operation.

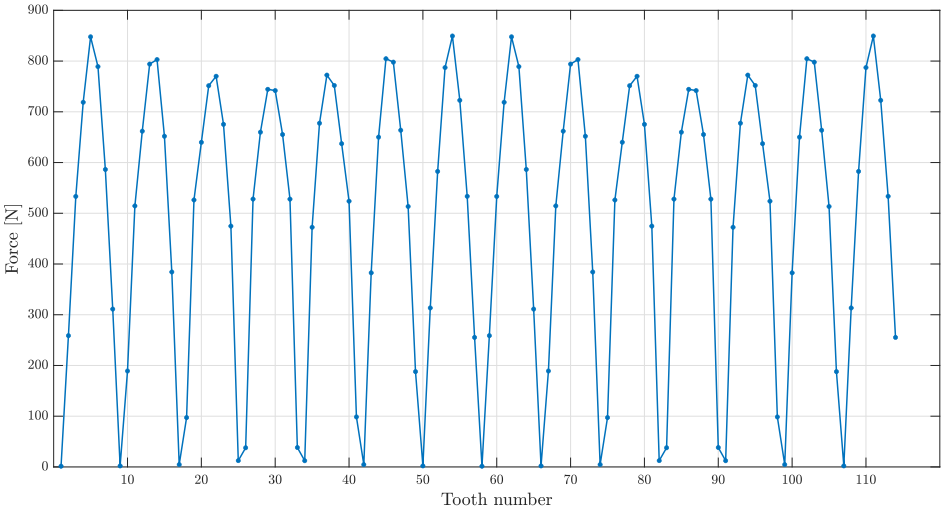

Figure 5.14: Total force acting on each tooth in healthy condition during no load operation.

As for the time domain distributions, the influence of b_t has been analyzed in the spatial domain. Figure 5.15 contains the spatial distribution of the radial flux density, b_r, and the tangential flux density, b_t, during healthy, no load operation. b_t is considerable in amplitude compared to b_r and reaches almost 30% of b_r at most. However, its waveform has an important difference in which it is dominated by a higher frequency component than the fundamental. This is also evident in the corresponding FFT presented in figure 5.16. The two figures show that the waves of b_t have only a small seventh order oscillation and the dominating variations are caused by the stator slots. In fact, the seventh order harmonic of b_t has an amplitude that is only 3.6% of b_r while the slot harmonics of b_t reach 40% of b_r.

The radial force density caused by the radial flux, f_{rr}, and by the tangential flux, f_{rt}, is depicted in figure 5.17 together with the total radial force density, $f_r = f_{rr} - f_{rt}$. The FFT of f_{rr} and f_{rt} is presented in figure 5.18. As seen, the impact of f_{rt} is very small despite its considerable slot harmonics, which is due to the small seventh order flux harmonic. Since the air-gap forces are produced by interactions between the flux density harmonics, the 14th order harmonic of f_{rt}, which is produced by the double product of the seventh order flux harmonic $b_{t,7th} \cdot b_{t,7th}$, is relatively small with an amplitude of 1% of f_{rr}. The same applies to the three slot harmonics of the force density, which are all caused by interactions between the slot harmonics and the seventh harmonic of the flux distribution. The largest harmonic of f_{rt} was found to be number 228, which is outside the limits of the figure, mainly caused by the two tangential slot harmonics $b_{t,107} \cdot b_{t,121}$. Its amplitude was 9% of the corresponding harmonic of f_{rr}. It can also be seen that f_{rt} does not contain any harmonics that are not present in f_{rr}.

Conclusively, the tangential component of the flux density has only a minor influence on the radial air-gap forces also in the spatial domain. The same analyses with similar observations as presented above were found for full load operation and all fault scenarios. Due to the very small impact of b_t, only the radial component of the flux density distribution will be included in the spatial analyses in the following sections, although it has indeed been included in the FE simulations.

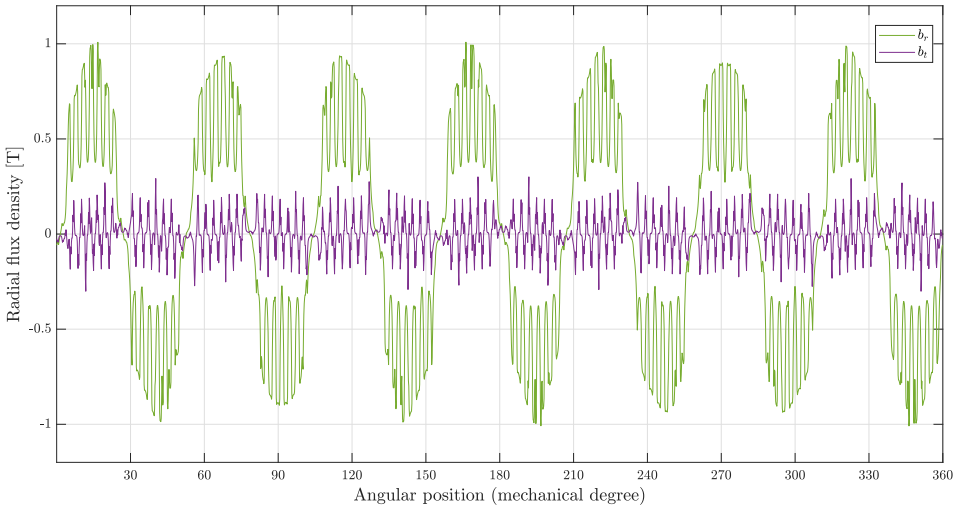

Figure 5.15: The spatial distribution of the radial component and the tangential component of the air-gap flux density during healthy, no load operation.

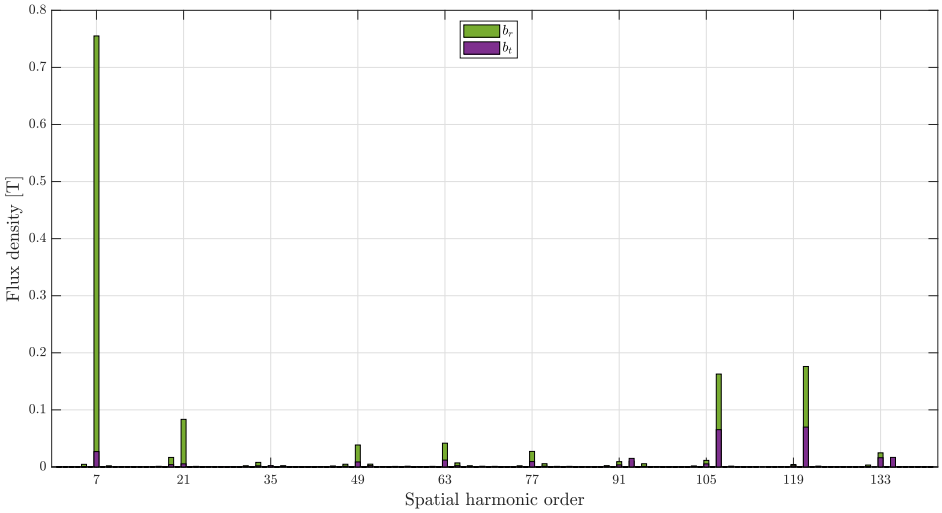

Figure 5.16: Frequency spectrum of the spatial distribution of b_r and b_t during healthy, no load operation.

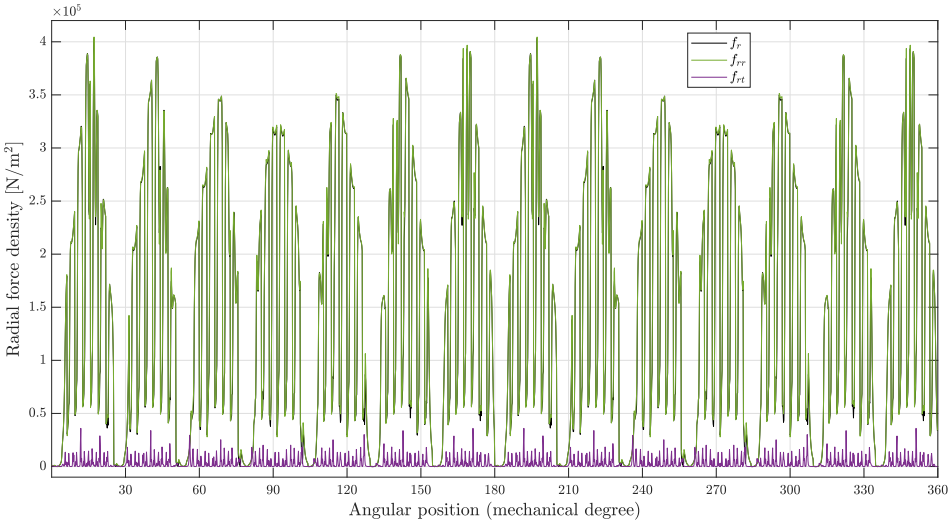

Figure 5.17: The spatial distribution of the radial force density caused by the radial flux density, f_{rr}, and by the tangential flux density, f_{rt}, together with the total radial flux density, f_r, in the air-gap during healthy, no load operation.

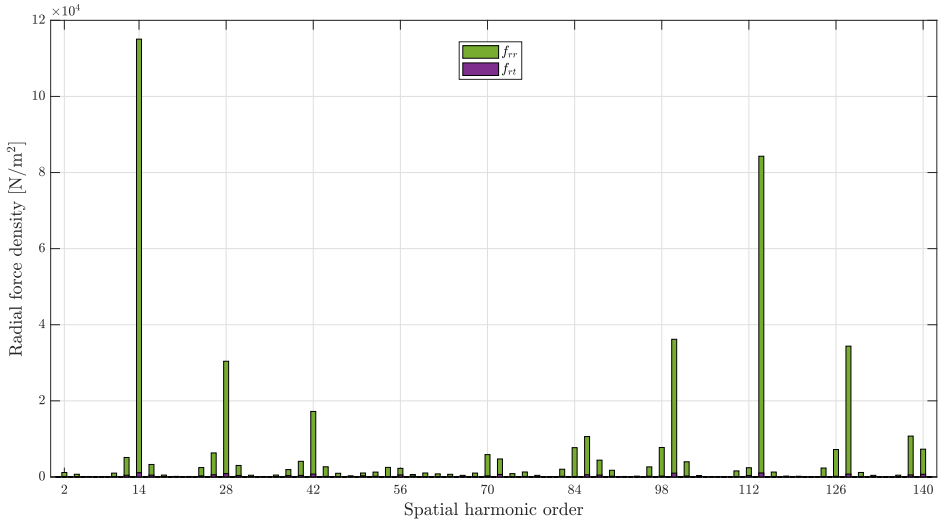

Figure 5.18: Frequency spectrum of f_{rr} and f_{rt} in the spatial domain during healthy, no load operation.

Due to its low order, the second spatial harmonic is expected to be of high importance for the vibration behavior of the generator. As seen, its amplitude is about doubled during full load operation and it may be of interest to investigate how it is produced. In general, it is excited by flux density harmonics with orders that differ by two. However, an interaction between two flux density harmonics may contribute positively or negatively to the excitement of the second-order force density harmonic dependent on their sign, which is determined by their direction of rotation in the air-gap. As mentioned before, the sign of the harmonics has not been included in the figures presented so far to ensure practical presentations and because they have not been important for the analyses.

The frequency spectrum of the spatial flux density in figure 5.11 shows that there are a few components with orders that differ by two and sufficient amplitude to excite the second-order force density harmonic to a noteworthy degree. It was found that the amplitudes of the components outside the limit of the figure, that is harmonic orders above 140, were too low to be considered. Consequently, it is possible to express the contribution to the second-order force density spatial harmonic according to equation 5.3. Based on the comparison between the radial flux density and the tangential flux density presented above, only the radial flux density is considered in this analysis.

$$f_{rr,2nd} = \frac{1}{2\mu_o} \sum_{i,j} b_{r,ith} \cdot b_{r,jth}, \tag{5.3}$$

$$i, j \in \{5, 7, 19, 21, 23, 33, 35, 37, 91, 93, 105, 107, 109, 119, 121, 123, 133, 135\},$$
$$j = i + 2$$

Figure 5.19 shows the selected harmonics with their signs included. The signs of the harmonics are variable and two adjacent harmonics with opposite signs will contribute negatively to the production of the second-order force density harmonic. This is illustrated in figure 5.20, where the result of the interactions between the selected flux harmonics is presented. The fundamental flux component with side-band and the lowest-order slot harmonic with side-band are the main reasons for the excitement of $f_{rr,2nd}$. These are also the main reason for the difference between $f_{rr,2nd}$ in no load and full load operation. There are some negative contributors, among them the other slot harmonic with its left side-band. The selected flux density harmonics produce in total $3.0\mathrm{kN/m^2}$ and $1.6\mathrm{kN/m^2}$ of $f_{rr,2nd}$ in total during full load and no load condition, respectively.

Figure 5.13 is the FFT of the radial force density distribution in figure 5.12 which is calculated by using both the radial and the tangential flux density component, that is $f_r = f_{rr} - f_{rt}$. In this figure, $f_{r,2nd}$ equals $2.9\mathrm{kN/m^2}$ and $1.5\mathrm{kN/m^2}$ during full load and no load operation, respectively. This means that all harmonics of the radial flux density with order that differ by two that is not included in equation 5.3, which was found to have a small influence, and all harmonics of the tangential flux density with orders that differ by two account for the $0.1\mathrm{kN/m^2}$ deviation between the second spatial harmonic from figure 5.13 and 5.20. This confirms the low influence of the tangential flux density in the laboratory generator and its invisible contribution to $f_{r,2nd}$ in figure 5.18.

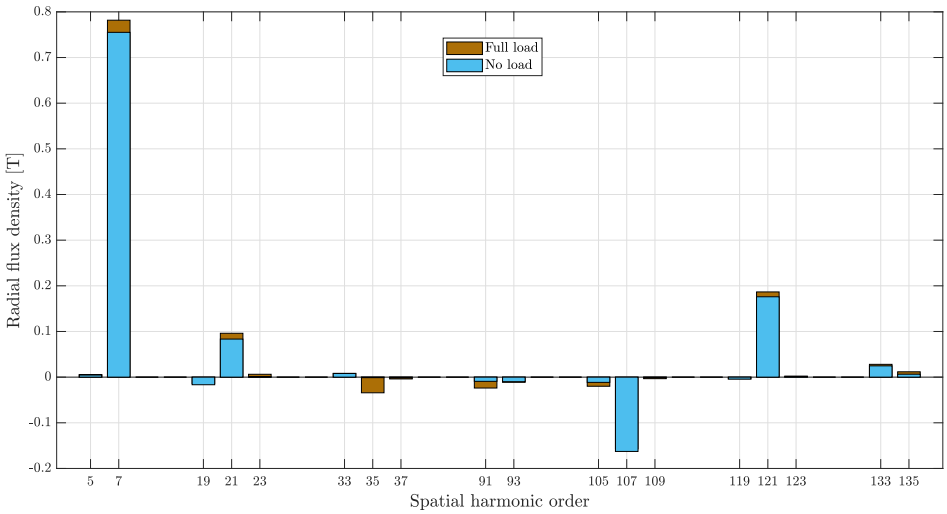

Figure 5.19: The most significant radial flux density components to produce the radial force density harmonic of second order during healthy operation.

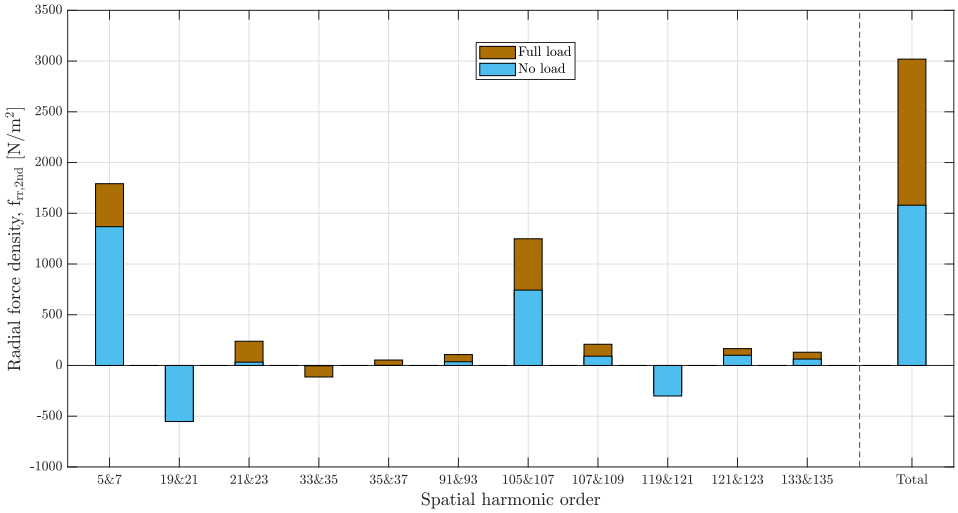

Figure 5.20: Contributions to the second-order radial force density harmonic from interactions between the most significant radial flux density harmonics during healthy operation.

5.2.2 Mechanical analysis

Figure 5.21 shows the simulated deformation of the stator yoke during healthy condition in no load and full load operation with a frequency spacing of 7.14 Hz between each circle on the graphs. The two plots contain the same data and the top one presents the actual deformation values in millimeters while the bottom plot is scaled logarithmically with the same conversion as used for flux density and force density from equation 5.1.

As expected, vibration at 100 Hz is dominating the spectrum caused by the main frequency component of the air-gap forces. Furthermore, vibration at 200 Hz and 300 Hz is also elevated due to the natural multiples of the 100 Hz force. The y-axis of the top plot is labeled with millimeters and the deformation at 100 Hz is in terms of tens of nanometres, which is not much. However, the laboratory generator, with a rating of 100 kVA, is small compared to a real hydropower generator and the magnitude of vibration may be higher for larger generators. Nevertheless, the numerical values in themselves are not much of interest in a fault detection point of view since they may vary from generator to generator. It is the relationship between the amplitude of the frequency components in the various operating conditions that are interesting as they can reveal patterns for fault detection.

The frequency content of both the time distribution and the spatial distribution of the radial force density must be considered when the difference between vibration at no load

and full load operation is studied. The time domain FFT of the radial force density in figure 5.5 shows that the main component during full load operation is slightly increased from no load operation, specifically by approximately 10%, which contributes somewhat to the augmented vibration at 100 Hz. However, the 200 Hz force density components are equally large and spatial harmonics must be taken into account to explain the increased vibration at 200 Hz. The FFT of the spatial force density in figure 5.13 shows that the lowest harmonic order, which is the second, is doubled in loaded condition. This means that the deformation will be larger at those vibration frequencies that are dominated by the second mode.

Figure 5.22 shows how the stator is deformed at six different frequencies during healthy operation. All shapes were found to be equal for both no load and full load operation and the severity of geometry deflection is increased in the figures in order to emphasize the deformed shape of the stators. The figure shows that deformation at 100 Hz is dominated by the second mode as the stator has two clear attraction points at the top center and bottom center. The shape is not completely circularly smooth but has 14 minor indents due to the 14th spatial harmonic. This means that the air-gap consists of several 100 Hz force density waves with different spatial harmonic orders. Although not as significant as at 100 Hz, the second mode is also the most prominent at 200 Hz. Thus, the amplified 200 Hz deformation during full load operation is caused by the increased second-order spatial harmonic. The same applies for the 100 Hz vibration, in combination with the slightly increased 100 Hz force density amplitude. On the other hand, the second vibration mode is absent at 300 Hz and the twisted stator teeth may indicate that modes with more complex deformation profile is involved. Hence, the small increase in 300 Hz vibration can be explained by the time domain force density harmonic at 300 Hz which is about doubled in loaded operation. It can be concluded from this that the second deformation mode is the most momentous in healthy operation and amplified vibration during full load operation is caused by the increased amplitude of the force wave with a spatial harmonic order of two and a frequency of 100 Hz.

The three top geometries in figure 5.22 illustrates how the stator is deformed at one, two, and three times the rotor frequency. Vibration at these frequencies is insignificant according to figure 5.21, but a modal inspection is necessary to clarify the reason for the small increase in low-frequency vibration during full load operation. As seen, deformation at 14.3 Hz and 21.4 Hz is clearly caused by the second mode. Deformation at 7.14 Hz is also somewhat influenced by the second mode as the stator has a slight oval shape. This means that the deformation at these frequencies is increased by the amplified second-order spatial harmonic during loaded operation. However, the increase is only minor due to the magnitude of the low-order harmonics in the frequency spectrum of the time domain force density in figure 5.5. That is, the forces at these frequencies have very low amplitude and, consequently, the augmented vibration is limited.

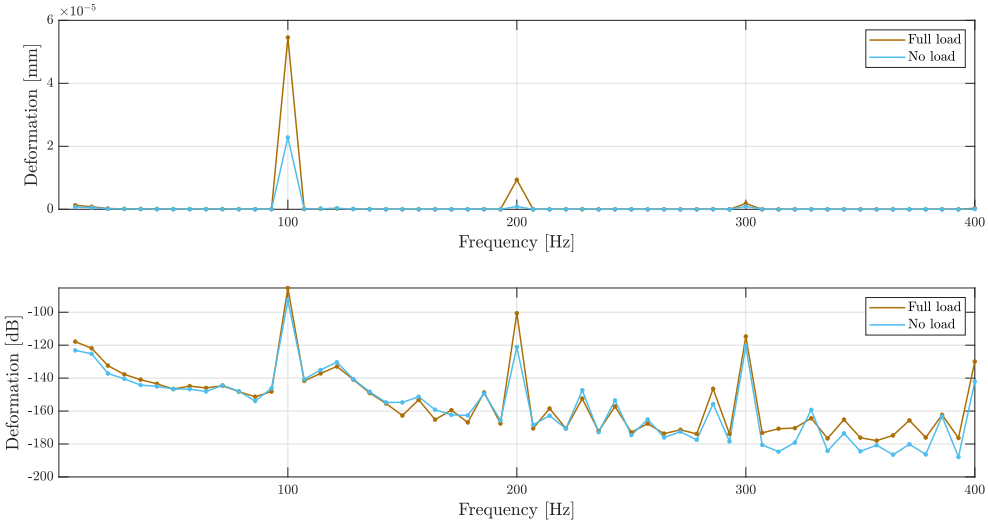

Figure 5.21: Frequency spectrum of stator yoke deformation during no load and full load operation in healthy condition. Top: actual values, bottom: logarithmic values.

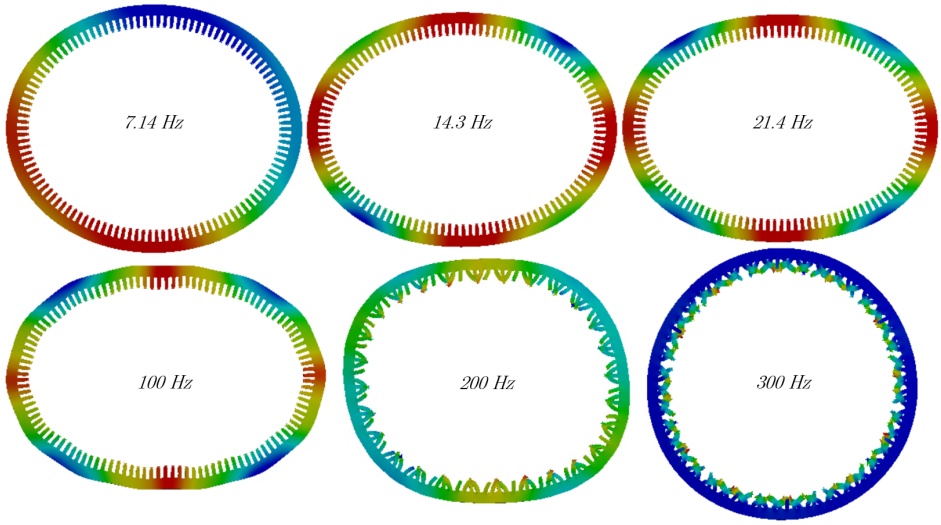

Figure 5.22: Deformation profiles of the stator at various frequencies during healthy operation.

As mentioned in section 4.3.2.2, a few additional simulations were performed with increased frequency resolution close to the natural frequencies obtained from the modal analysis to detect possible resonance effects. However, since the absence of the support bars would likely change the natural frequencies of the stator and cause these results to be unrepresentative for the real laboratory generator, they are given a separate figure and not included in the presentation of the main simulations above. This is also the case for simulation of the faults in the forthcoming sections.

Figure 5.23 shows the simulated vibration spectrum with two clear spikes at 118.3 Hz and 327.7 Hz. These frequencies correspond to the natural frequencies of the second and third vibration mode, respectively. The deformation during no load and full load operation is almost equally affected, with the no load condition being slightly more elevated, despite the higher vibration level during full load operation.

The deformation at the two natural frequencies of the stator is increased with a factor of approximately 100 compared to healthy operation. However, they do not exceed the 100 Hz vibration level, which indicates that the resonance effects are limited. This means that forces with a spatial harmonic order of two and three and a frequency close to 118.3 Hz and 327.7 Hz, respectively, are not excited to a sufficient degree. Conclusively, if the laboratory generator were to be operated without any supporting structure, it would not experience dangerous resonance between 7.14 Hz and 400 Hz during healthy operation.

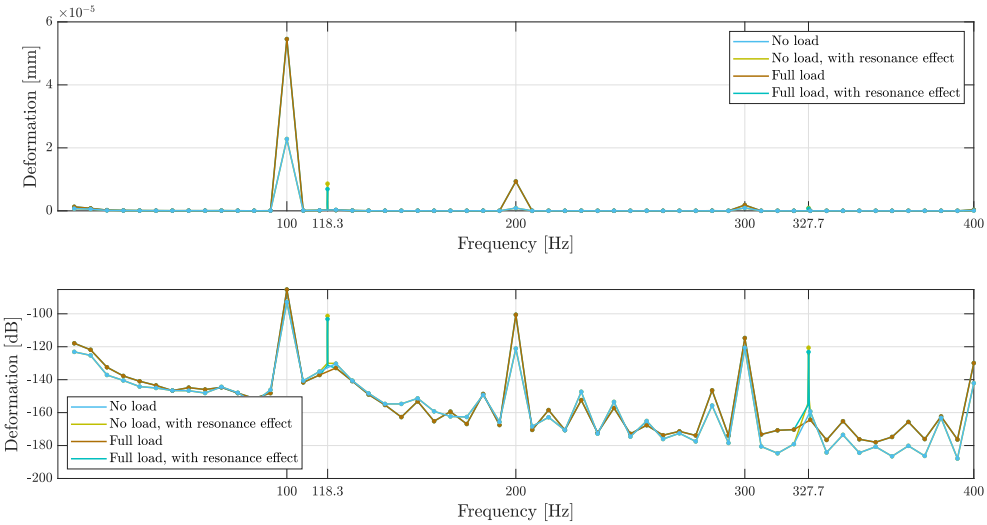

Figure 5.23: Frequency spectrum of stator yoke deformation during no load and full load operation in healthy condition with specific calculations around natural frequencies. Top: actual values, bottom: logarithmic values.

5.3 Inter-turn short circuit in the field winding

5.3.1 Magnetic analysis

5.3.1.1 Time domain distributions with FFTs

Figure 5.24 compares the time domain radial air-gap flux density produced by four poles during healthy and faulty operation. The simulated fault degree varies from 2.86% to 28.6%. The top rotor pole in the generator model, which has shorted turns in the field winding, passes the air-gap point from 0.10 to 0.11 seconds. As the figure shows, the pole with a faulty coil has negative polarity and the produced magnetic field weakens as the fault degree increases. This is a result of the reduced ampere-turns in the winding. Moreover, the decreased number of field lines emitting the faulty pole returns in the two adjacent poles, causing somewhat lower flux density in these poles as well. Although hardly seen in the figure due to only small changes, this process strengthens the magnetic field produced by the two next adjacent poles, represented by the graph in the lower-left corner of the figure, in order to compensate for the reduced field produced by the faulty coil. This pattern of reduced and increased flux in adjacent poles repeats itself throughout the whole rotor. Consequently, as clearly seen in the figure, the short circuit fault distorts the symmetry and periodicity of the flux density distribution in the air-gap which will impact its frequency content.

Figure 5.25 show the frequency spectrum of radial air-gap flux density in healthy operation and for the various degrees of ITSC. The influence of the fault on the natural components in the figure are covered by the lines from healthy operation since this scenario is plotted after the fault scenarios in MATLAB. However, the largest change in these harmonics is a reduction of 3.7 mT and they can therefore in practice be considered unaffected by the fault.

As the figure shows, the ITSCs have a substantial impact on interharmonics. The distorted periodicity of the time distribution causes induced side-band components at each natural component in the figure. The side-bands of the fundamental and all subharmonics are the most affected and amplified already after one shorted turn. Their magnitudes may indicate that their influence on the generator is not critical during low fault severities, while as the fault degree raises, they become significant compared to healthy operation. The lowest difference between the harmonic orders is one and interactions between them will excite the first-order force density harmonic, which again can be critical for the vibration of the generator.

The results from simulation of full load operation do not provide much new information. Consequently, and to limit the length of this chapter, they are included in appendix E.1. They are, naturally, a combination of the phase-shifted flux density distribution shown for healthy full load operation in figure 5.2 and the weakened field caused by the fault illustrated in figure 5.24. The subharmonics in the frequency domain are about equally large as in no load condition with only a marginally higher amplitude while a few higher-order frequency components are somewhat more amplified due to the loading.

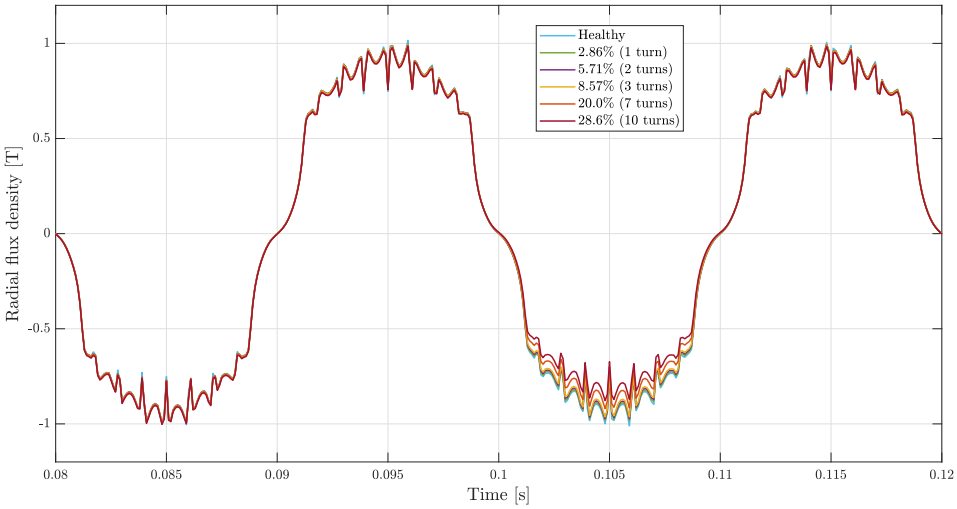

Figure 5.24: Time domain distribution of radial air-gap flux density during no load operation and inter-turn short circuit in the field winding.

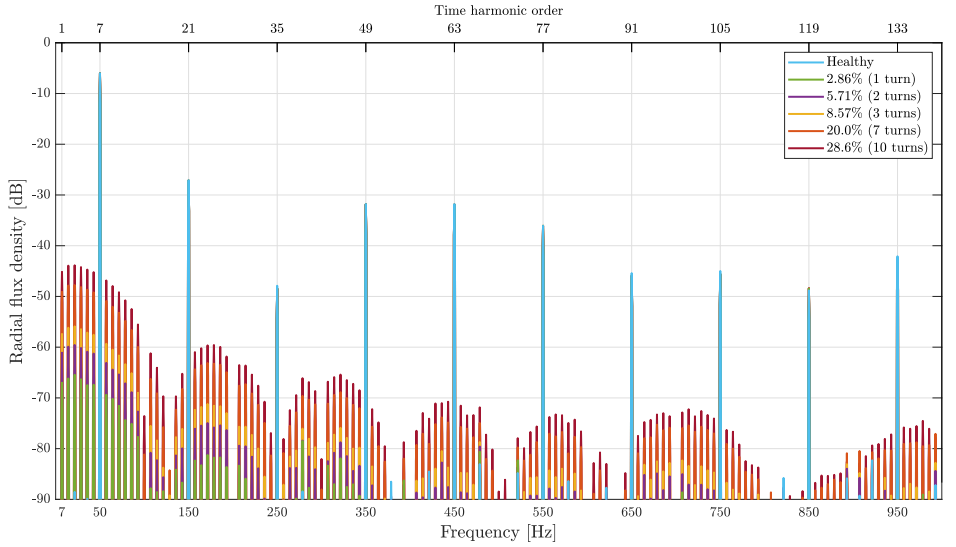

Figure 5.25: Frequency spectrum of radial air-gap flux density during no load operation and inter-turn short circuit in the field winding.

The time domain distribution of the radial force density during no load operation is shown in figure 5.26. The force produced by the pole with ITSC is reduced as a symptom of the weakened flux field and, since the relative reduction of the force is greater than for the flux due to the squaring of the magnetic field, the impact on the three other force waves is more visible than for the flux density. The force wave with reduced amplitude rotates in the air-gap and imposes a dynamic UMP which is significant as the fault degree raises. The distorted periodicity of the force distribution can be illustrated further in the frequency domain.

As shown in figure 5.27, unnatural harmonics in the radial force density is highly affected by the ITSC fault. While the main component of order 14 is caused by the fundamental flux harmonic, the low-order force density subharmonics are results of the interaction between adjacent flux density harmonics. The rich harmonic content of the radial flux density produces elevated harmonics across the entire force density frequency spectrum. With ten shorted turns, the first spatial harmonic reaches 71.7 dB, which corresponds to 3.8 $\mathrm{kN/m^2}$. This is 4.7% of the main component and in the same order of magnitude as the high-order natural harmonics. The resulting vibration can cause severe damage to the machine if the relatively high amplitudes of the low-order harmonics are combined with low-order spatial harmonics.

The subharmonics of the flux density spectrum were more or less equally large in no load and full load operation, and the same can be concluded for the radial force density. All the unnatural that are excited during no load operation are also present in the spectrum for full load operation, with slightly higher amplitude at some frequencies. Simulation results from full load condition with ITSC in the rotor are included in appendix E.1.

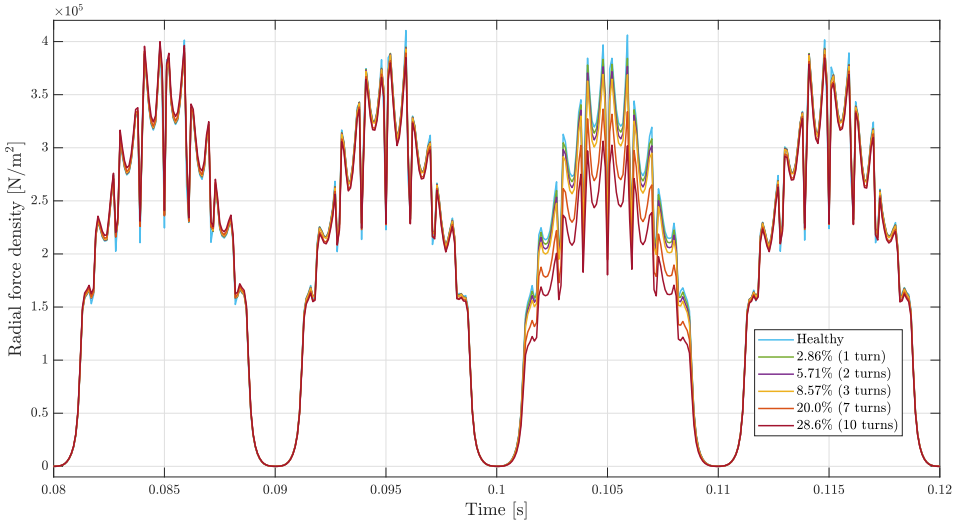

Figure 5.26: Radial air-gap force density during no load operation and inter-turn short circuit in the field winding.

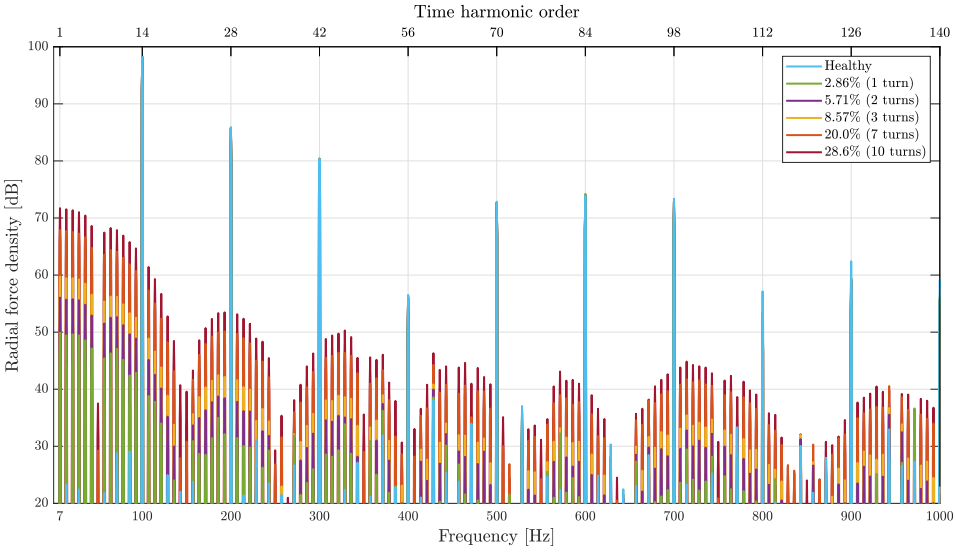

Figure 5.27: Frequency spectrum of radial air-gap force density during no load operation and inter-turn short circuit in the field winding.

5.3.1.2 Spatial domain distributions with FFTs

A comparison of the spatial distribution of the radial flux density during healthy and faulty no load operation is presented in figure 5.28. The top pole in the generator model, which is located 90 degrees from the x-axis of the model, has ITSC in the field winding and the produced flux is clearly affected by the reduced ampere-turns. The repetitive flux pattern around the air-gap is distorted and low-order spatial harmonics are excited in figure 5.29 as a symptom. Their orders differ by one and interaction between them will produce low-order spatial force harmonics. The main component reaches 0.76 T outside the limit of the figure and all of the natural harmonics are marginally decreased and practically unaffected by the fault. The results from simulation of full load operation are included in appendix E.1, where the excited harmonics are the same as in no load operation with a slight increment at some orders. The same accounts for the radial force density.

Figure 5.30 shows how the spatial distribution of the radial force density is affected by the fault. The force produced by the faulty pole is reduced with 23% when ten turns are shorted and the pattern created by the variations of the wave amplitudes is no longer a clear sinusoidal with two peaks. The symmetry around 180 degrees is lost and the air-gap has only one unique force density distribution which implies that the lowest spatial order is one. The same can be seen in figure 5.32 that depicts the total force acting on each tooth.

The FFT presented in figure 5.31 shows that low-order spatial harmonics are present as a result of interactions between the flux density harmonics. As expected, the lowest order is one and subharmonics of higher orders are also excited by flux density harmonics with orders that differ by two, three, four and up to 13.

The high number of excited subharmonics in the time domain and in the spatial domain makes it likely that the low-order spatial harmonics and the excited time domain subharmonics with relatively high amplitude can belong to the same force wave and impose large deformation to the stator. If this is the case, the dominant vibration of the laboratory generator will be changed from 100 Hz towards rotor frequency with a dramatically higher magnitude compared to healthy condition.

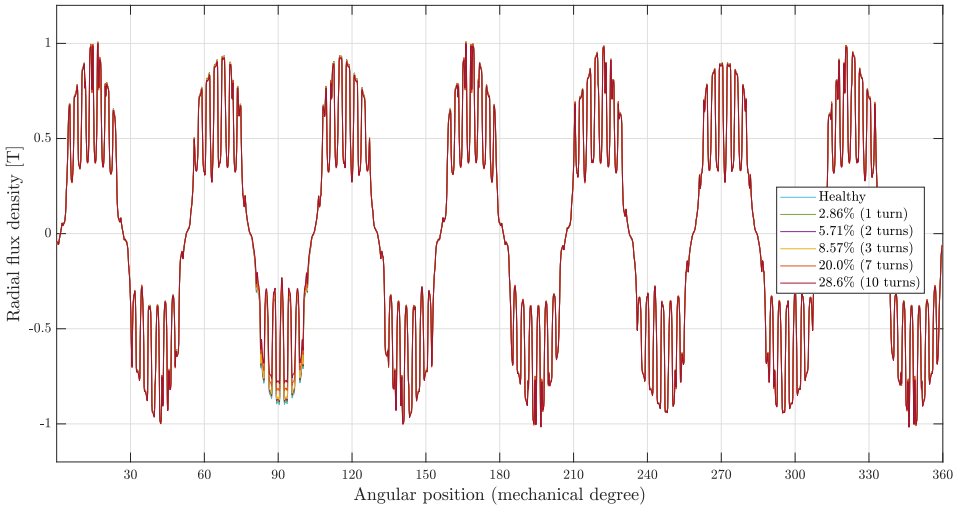

Figure 5.28: Spatial distribution of radial air-gap flux density during no load operation and inter-turn short circuit in the field winding.

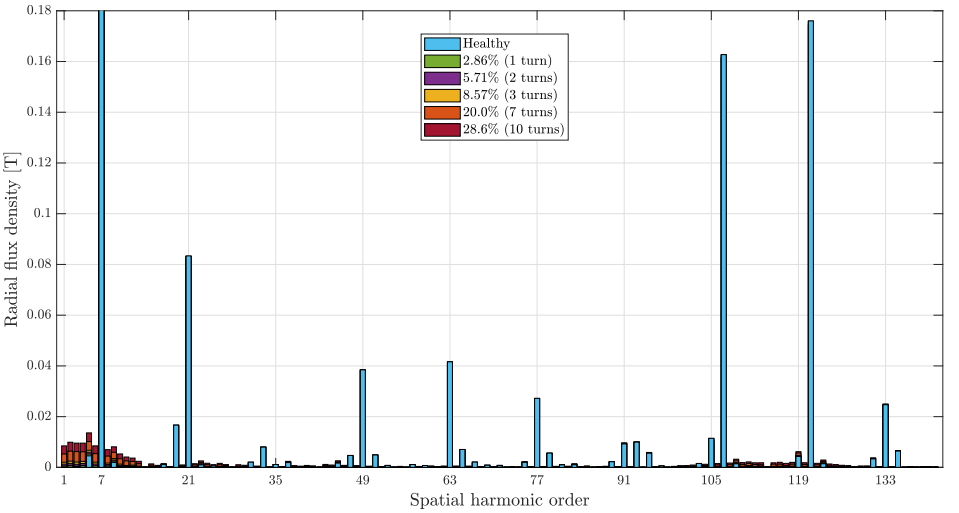

Figure 5.29: Frequency spectrum of the spatial distribution of radial air-gap flux density during no load operation and inter-turn short circuit in the field winding.

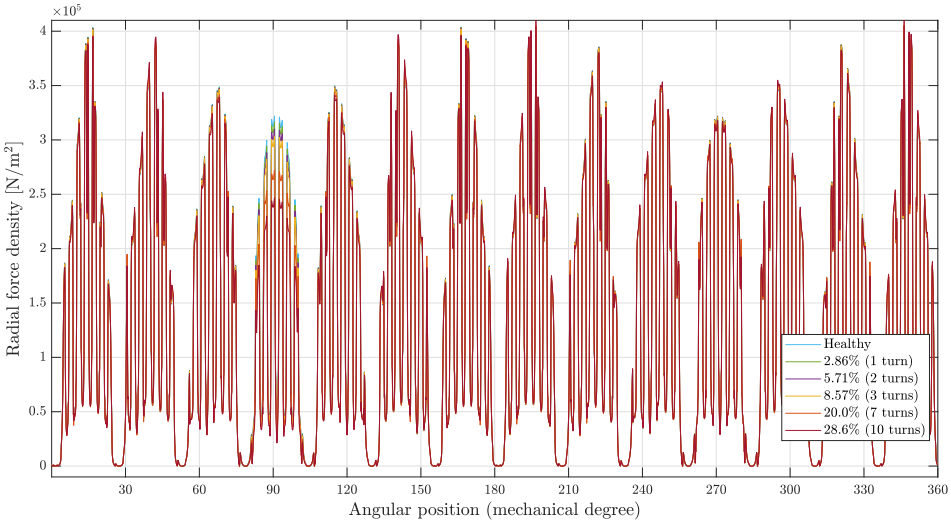

Figure 5.30: Spatial distribution of radial air-gap force density during no load operation and inter-turn short circuit in the field winding.

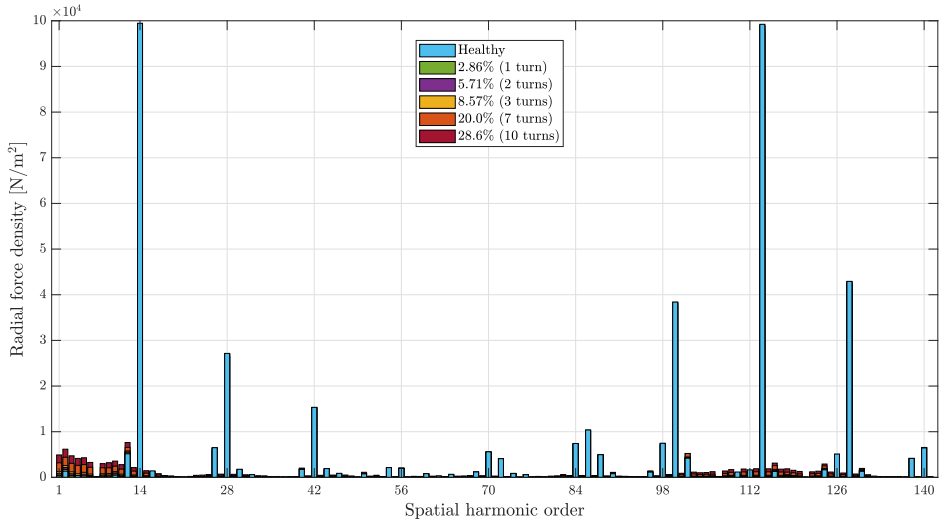

Figure 5.31: Frequency spectrum of the spatial distribution of radial air-gap force density from simulations during no load operation and inter-turn short circuit in the field winding.

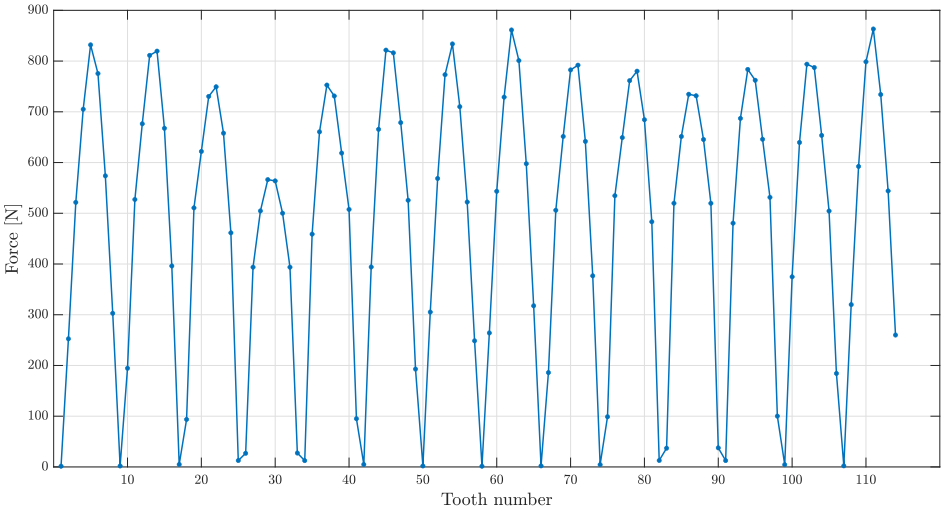

Figure 5.32: The total force acting on each tooth during no load operation and inter-turn short circuit in the field winding.

The modified frequency spectra of the radial flux density and the resulting low-order force density harmonics during ITSC fault are expected to increase the vibration level of the generator and shift the dominant vibration to the first mode. Among all the excited sub-harmonics, the first-order is of particular interest and it is interesting to investigate its origin in detail. The orders of the flux density harmonics that interact and produce the first-order force density harmonic differ by one, which means that there are quite many components that contribute when the harmonic content of figure 5.29 is examined. However, interaction between two flux harmonics causes their amplitudes to be multiplied, and when the amplitudes of the harmonics in figure 5.29 are considered, it is clear that only a few components have a notable impact. These are the fundamental with its two side-bands and the slot harmonics with their side-bands. Harmonics of orders higher than the 140 included in the figure were found to have a relatively very small influence. Thus, the main production of the first-order force density harmonic can be written as follows

$$f_{rr,1st} = \frac{1}{2\mu_0}(b_{r,6th} \cdot b_{r,7th} + b_{r,7th} \cdot b_{r,8th} + b_{r,106th} \cdot b_{r,107th} + b_{r,107th} \cdot b_{r,108th} + b_{r,120th} \cdot b_{r,121st} + b_{r,121st} \cdot b_{r,122nd}). \quad (5.4)$$

Apart from the amplitude of the listed b_r components, their sign is decisive for the resulting $f_{rr,1st}$. It was found from a similar analysis of the tangential flux density presented in subsection 5.2.1.2 that the tangential component of the spatial flux density distribution during faulty operation was very small compared to the radial component and is left out of

this analysis.

Figure 5.33 shows the radial flux density harmonics from equation 5.4 with their signs included. Component number seven has amplitude of 0.76 T for all five fault scenarios and only the green bars are visible for component number 107 and 121 since this is the last plotted scenario in MATLAB and due to their marginal decrease when the fault severity raises.

All side-bands have the opposite sign of their adjacent natural component which will cause a negative amplitude when they are multiplied together. This is illustrated in figure 5.34 where the contribution from the interactions between the chosen radial flux density harmonics is presented. They are all negative and produce 5.0 $\mathrm{kN/m^2}$ of the first-order radial force density harmonic in total, which is just above the amplitude of the first-order component in figure 5.31 of 4.9 $\mathrm{kN/m^2}$. This indicates that these six interactions, heavily dominated by the two related to the fundamental flux component, are the main contributors to the expected change in vibration of the generator during ITSC in the field winding. This also means that the negative 0.1 $\mathrm{kN/m^2}$ of $f_{rr,1st}$ is produced by the remaining radial flux density harmonics and the tangential field. As mentioned, the former was found to have insignificant influence due to their amplitude, such that the tangential flux density harmonics accounts for around 0.1 $\mathrm{kN/m^2}$. This is 2% of 4.9 $\mathrm{kN/m^2}$ and further illustrates the small impact of the tangential flux density in the laboratory generator.

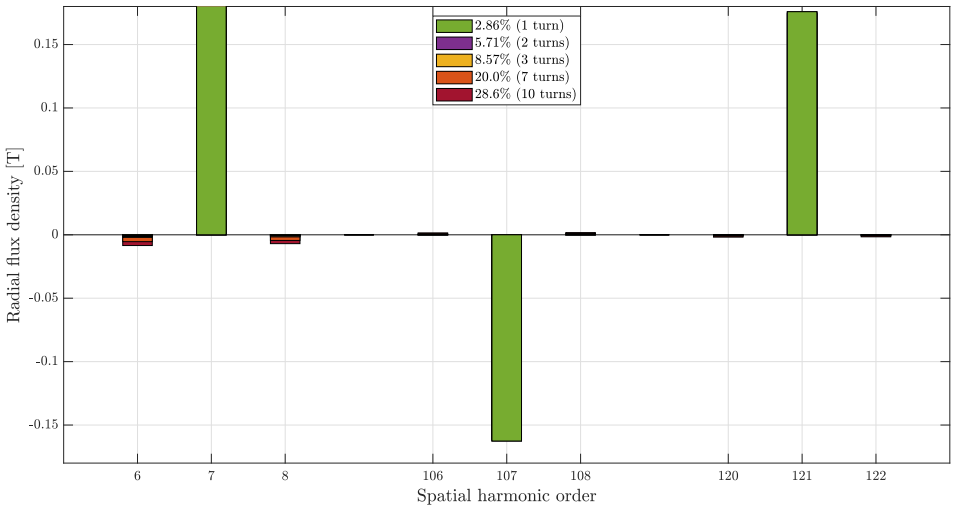

Figure 5.33: The most significant radial flux density components to produce the radial force density harmonic of first order during no load operation and inter-turn short circuit in the rotor winding.

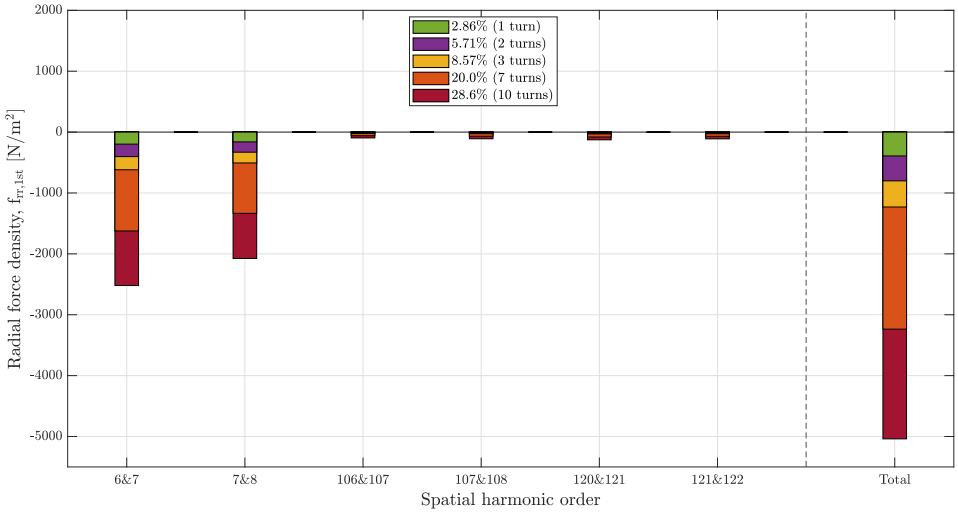

Figure 5.34: Contributions to the first-order radial force density harmonic from interactions between the most significant radial flux density harmonics during no load operation and inter-turn short circuit in the rotor winding.

5.3.2 Mechanical analysis

Figure 5.35 compares the simulated deformation during no load healthy operation to no load faulty operation. The figure shows a dramatic augmentation of vibration at 7.14 Hz during fault. Already after one shorted turn is the rotor frequency vibration increased approximately 6500 times from healthy condition and the most severe fault degree produces around 80000 times higher vibration than a healthy generator at this frequency. The deformation is heavily elevated also at 14.3 Hz, 21.4 Hz, and 35.7 Hz, and in general increased at every subharmonic frequency expect for 50 Hz. Vibration at 100 Hz is also affected by the fault.

The frequency spectrum of the time domain force density in figure 5.27 contains substantially increased subharmonics which are important contributors to the amplified low-frequency vibration. In addition, the same harmonic orders are excited in the spatial frequency domain in figure 5.31 which has a great impact on the deformation caused by the force waves they belong to.

Figure 5.36 illustrates how the stator is deformed at six different frequencies with increased deformation severity. It shows how the time harmonic number, k, and the spatial harmonic number, m, follow each other at low frequencies. That is, the stators at the four lowest frequencies, which correspond to $k = 1, 2, 3,$ and 4, are solely deformed by the first, second,

third, and fourth mode, respectively. Hence, the 7.14 Hz force density waves in the air-gap have $m = 1$ which explains why deformation at 7.14 Hz is most severe even though the amplitudes of the excited forces are more or less the same.

71.4 Hz was found to be the highest frequency where $m = k$ had a visible impact on the deformation, and it can be seen that the stator shape at this frequency is also influenced by the second mode. The deformed stator at 100 Hz is more or less identical with 14.3 Hz with two clear attraction points and the 14 minor indents from healthy operation are ineffectual due to the amplified second-order harmonic. This shows that the second mode, which is the lowest naturally occurring spatial harmonic order in the laboratory generator, is still the dominating vibration mode at the main force frequency of 100 Hz during fault, despite the excited first-order harmonic.

The deformation between 100 Hz and 200 Hz is in general not much affected by the fault, despite that they were found to be mostly deformed by two attraction points. This means that the amplitude of the second spatial harmonic is mainly dedicated to force waves with frequency of 14.3 Hz and 100 Hz. The low change in vibration between 100 Hz and 200 Hz means that the air-gap forces with these frequencies have a low impact on the vibration of the generator. This is despite the presence of the interharmonics shown in figure 5.27, which indicates that the low-order spatial harmonics in general have minor influence at these frequencies and that the amplitudes of the forces are too low to produce significant deformation. The vibration level above 300 Hz is somewhat higher during fault. The deformation shape of the stator at most of these frequencies was found to have three attraction points, such that the amplified deformation is a result of the increased third-order spatial harmonic. Vibration close to the third natural frequency of the stator at 327.7 Hz is especially elevated.

The same observations as presented above can be found in the simulation results of full load operation. The general trend in the magnetic analyses, in both the time domain and the spatial domain, was that the same harmonics are exited in no load and full load operation and that their amplitudes are somewhat increased under load. The vibration spectrum from full load condition is included in appendix E.1 and shows the same characteristics as figure 5.35. The 7.14 Hz vibration is increased by 5% from no load condition due to the small increase in the forces. The shapes of deformation illustrated in figure 5.22 was found to apply for both no load and full load operation.

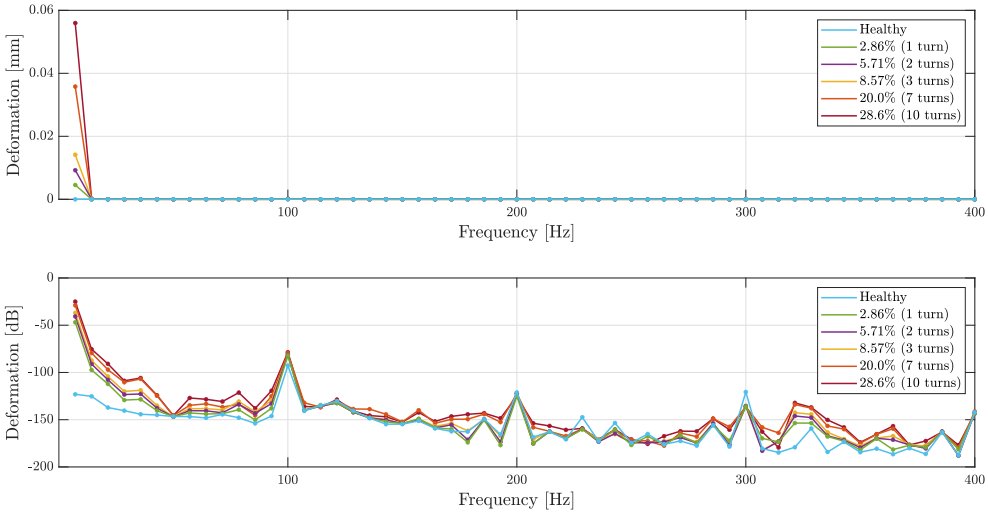

Figure 5.35: Frequency spectrum of stator yoke deformation during no load operation and inter-turn short circuit in the rotor winding. Top: actual values, bottom: logarithmic values.

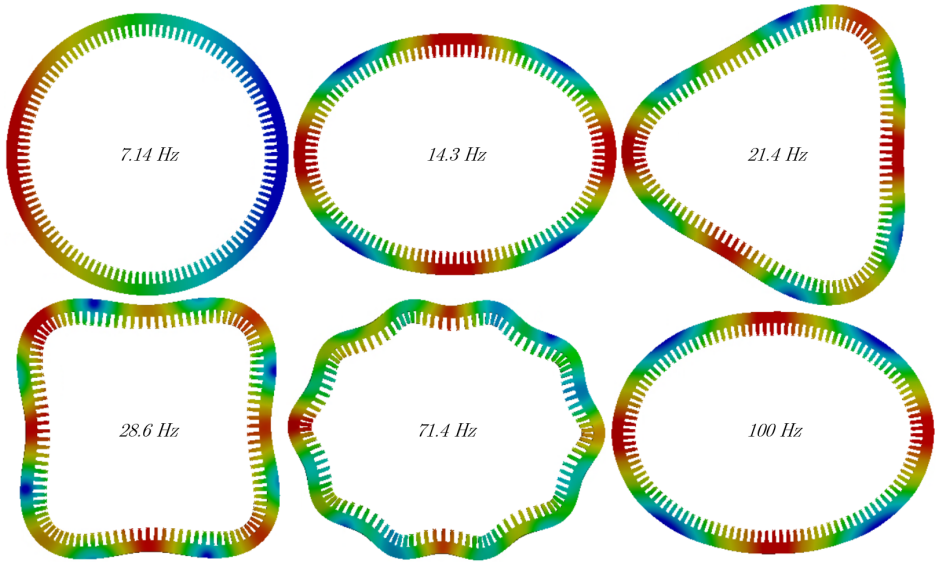

Figure 5.36: Deformation profiles of the stator at various frequencies during operation with inter-turn short circuit in the rotor winding.

Figure 5.37 shows the simulated deformation during no load operation with ten shorted rotor turns, with and without enhanced calculation resolution around the natural frequencies. A few interesting observations can be found in this figure. First, the light red line, which represents the simulations with increased frequency resolution, in not visible at 7.14 Hz because it is covered by the dark red line. In other words, the vibration at this frequency is unaffected by resonance effects, which means that the highly excited force at 7.14 Hz and mode number one is sufficiently separated from the first natural frequency at 0.21 Hz.

Moreover, the spike at 118.3 Hz is about equally high as for healthy operation, despite that the frequency spectrum of the time domain forces in figure 5.27 contains excited harmonics at both 114.3 Hz and 121.4 Hz. It was found that the deformed shape of the stator at 114.3 Hz, and to some degree at 121.4 Hz, was dominated by the second mode with two attraction points. The small increase in vibration at 118.3 Hz thus indicates that only a few hertz separation between an excited force and a natural frequency is sufficient to avoid dramatic resonance.

It could be argued that the increase in vibration at 118.3 Hz is similar to the one in healthy condition due to the small impact the forces have on vibration above 100 Hz, as commented related to figure 5.35. However, deformation at 327.7 Hz during ITSC fault is increased 40 times from healthy operation, which further indicates that the frequency of the excited force has to be very close to the natural frequency to cause resonance. That is, the time harmonic at 328.6 Hz, which is excited during fault, is less than one hertz away from the natural frequency. This may cause the vibration at this frequency to be considerably more amplified than during healthy condition, which is in contrast to the excited force at 121.4 Hz, which is approximately three hertz separated from the natural frequency.

Another factor that may play a role in the production of deformation at the natural frequencies is the excited spatial harmonics during ITSC fault. For instance, the excited third-order spatial harmonic may be the reason for the spike at 327.7 Hz. This is discussed in section 6.3.1.

Despite the observations presented above, the resonance effect during fault do not exceed the vibration at 100 Hz and is far from the vibration level at 7.14 Hz. Thus, the generator would not suffer from dramatic resonance effects between 7.14 Hz and 400 Hz if it were to be operated without support and with ITSC in the rotor winding.

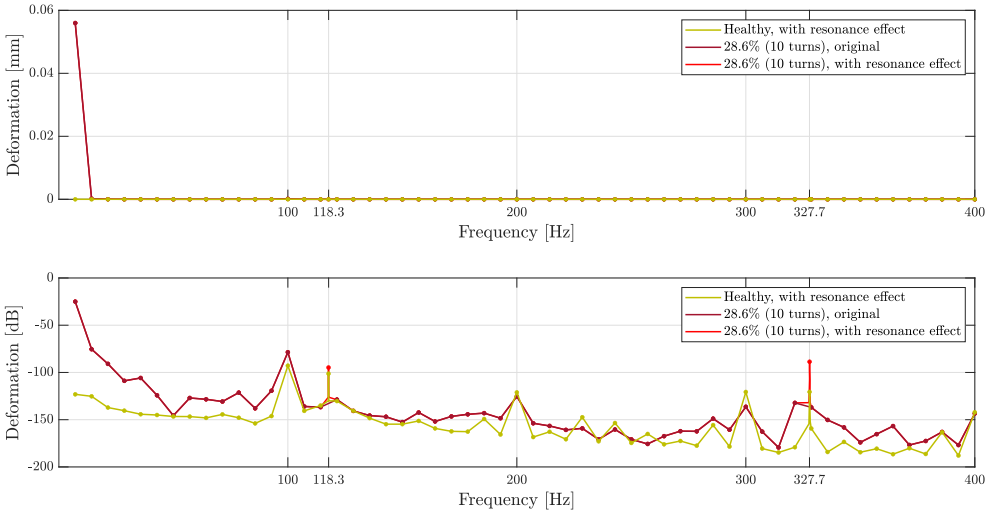

Figure 5.37: Frequency spectrum of stator yoke deformation during no load operation and 28.6% inter-turn short circuit in the rotor winding with specific calculations around natural frequencies. Top: actual values, bottom: logarithmic values.

5.4 Static eccentricity

5.4.1 Magnetic analysis

5.4.1.1 Time domain distributions with FFTs

Figure 5.38 presents the radial flux density distribution calculated at the two air-gap geometry point during 0.04 seconds of no load operation and 30% SE. The opposite sign of the waves is caused by the alternating polarity of the rotor poles. Static eccentricity was applied to the generator model by moving the rotor along the positive x-axis. Consequently, as the blue graph in the figure shows, the distance from the rotor to the right point used for time domain distribution analyses during healthy and short circuit conditions is reduced and the calculated flux density at this point is naturally increased. Harmonics that are normally not visible in the frequency spectrum of healthy operation can therefore appear simply due to the strengthened field and not as a consequence of the asymmetrical air-gap imposed by the fault. Thus, a second air-gap point was created at the exact opposite side of the generator such that the flux density was calculated at the location with maximum air-gap length and minimum field strength as well. At 30% eccentricity, the difference between the radial flux density at the two points is 17%.

The different field strength at the two points is visible in the frequency spectrum as well, presented in figure 5.39. Some of the side-band components are only visible in the figure for the right point. This indicates that the amplitude of these harmonics at the left point is lower than the defined figure limit. To ensure that only the harmonics that are not present in healthy operation are included in the figure, the following analyses will treat the radial flux density calculated at the left point. This is the controversial option and most convenient to investigate the effects of the fault in a condition monitoring and fault detection point of view.

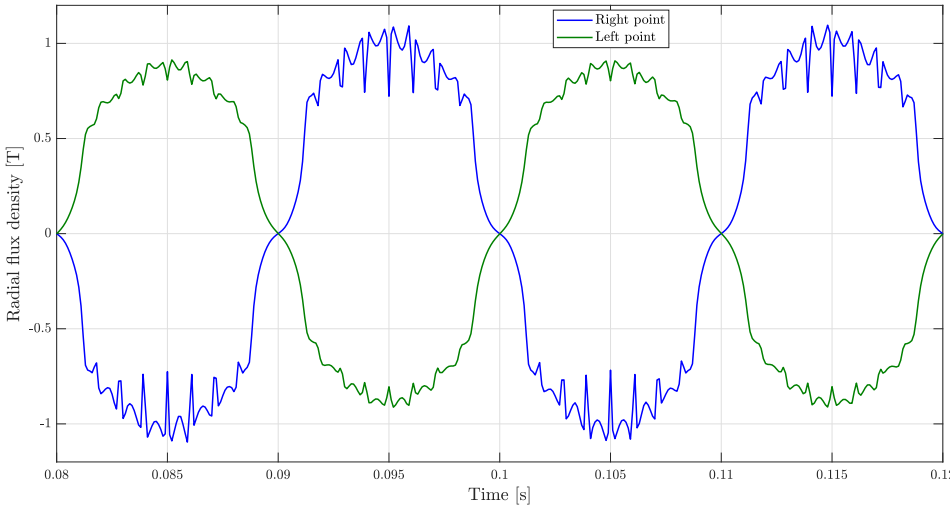

Figure 5.38: Time distribution of the radial flux density calculated at the right and the left air-gap point during no load operation and 30% static eccentricity.

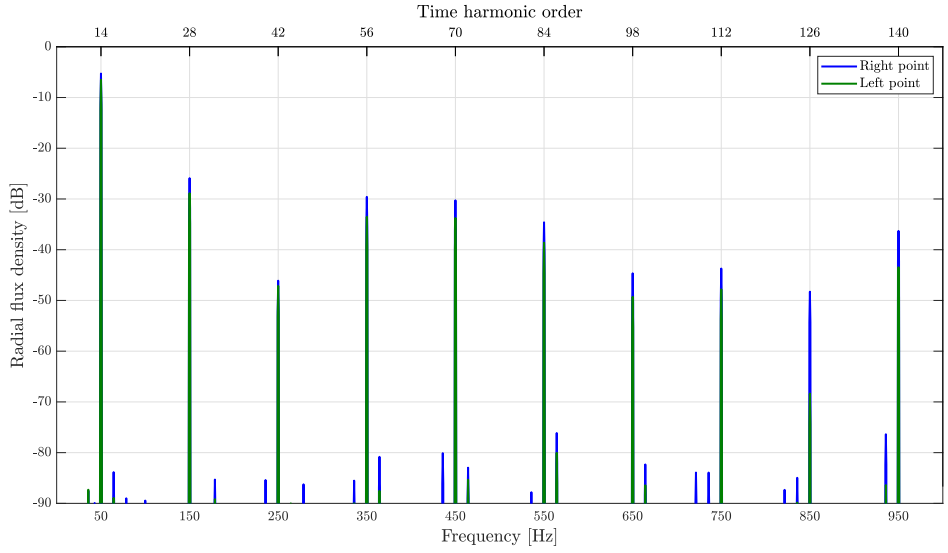

Figure 5.39: Frequency spectrum of the time distribution of the radial flux density calculated at the right and the left air-gap point during no load operation and 30% static eccentricity.

Figure 5.40 compares the radial air-gap flux density in healthy condition with increasing severity of SE. Since the left air-gap point is evaluated during SE, the field strength weakens when the fault degree increases as a symptom of the enlarged air-gap length. One full revolution is included in the figure to illustrate that the periodicity and symmetry of the waves are maintained during SE. The shape of the waves during SE is also practically equal to the ones from healthy operation, other than the reduced magnitudes. It should be mentioned that due to the different locations of the two points, they do not calculate the flux from the same pole at the same time. However, since the field produced by the rotor winding is unaffected during SE, figure 5.40 is still a good comparison of the air-gap field in faulty and healthy condition. It can also be mentioned that the figures containing FFTs during SE are unaffected by the different locations of the two points. Results from simulations of full load operation are included in appendix E.2.

Figure 5.41 presents the frequency spectrum of the time distribution shown in figure 5.40. The natural harmonics are slightly decreased during SE compared to healthy condition and a few new side-band components appear. This indicates that there are some differences between the distributions from healthy and faulty operation, however, they are small considering the amplitude of the harmonics. The largest of these side-bands appear at 564 Hz with amplitude around -80 dB, which corresponds to 0.1 mT and can be regarded as insignificant for the performance of the generator and practically invisible in figure 5.40. The interharmonics that are present in healthy condition between 350 Hz and 650 Hz do not appear in the spectrum during SE. This is caused by the fault and not just the reduced field strength at the left air-gap point as they are not present in figure 5.38 for the right point either. It can be concluded from figure 5.40 and 5.41 that SE has minor influence of the time domain radial flux density when the magnitude of the deviations is considered.

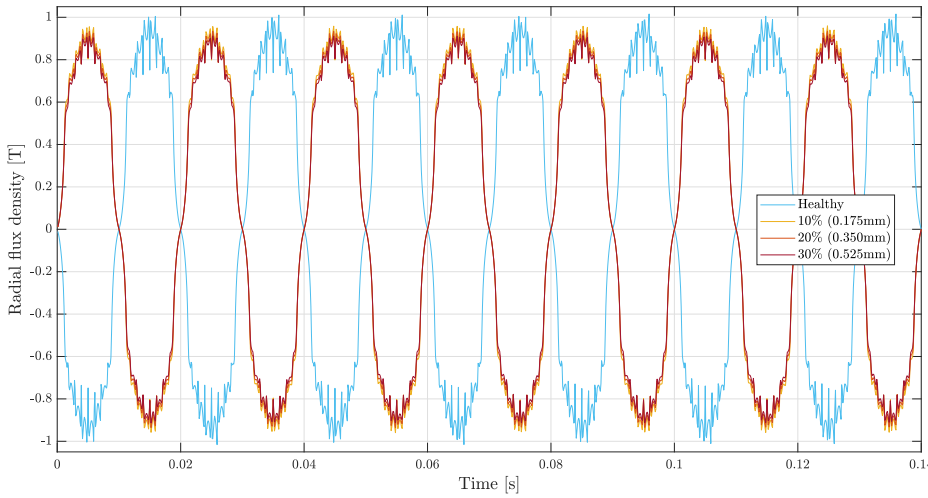

Figure 5.40: Time distribution of the radial air-gap flux density during no load operation and static eccentricity.

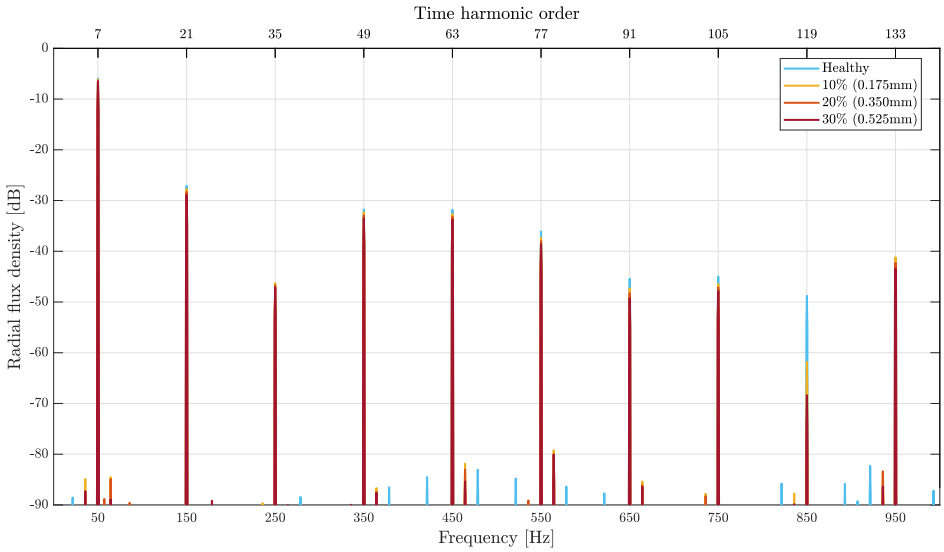

Figure 5.41: Frequency spectrum of the time distribution of the radial air-gap flux density during no load operation and static eccentricity.

Figure 5.42 shows the time domain distribution of the radial force density in the air-gap in healthy and faulty no load condition. The increased air-gap length at the left point reduces the amplitude of the calculated force density and characteristics in the waves such as the dips caused by the damper bars are less significant. Expect from this, the shape of the waves is mostly unchanged and the periodicity as the rotor revolves a whole rotation is maintained due to the marginally affected flux distribution. Thus, no UMP can be identified in the figure.

The same can be concluded from the FFT presented in figure 5.43. The natural harmonics are somewhat reduced and a couple of side-bands with amplitude between 30 dB and 40 dB are excited around 500 Hz and 600 Hz. The results from simulations of full load condition are included in appendix E.2 where no new noteworthy observations were found.

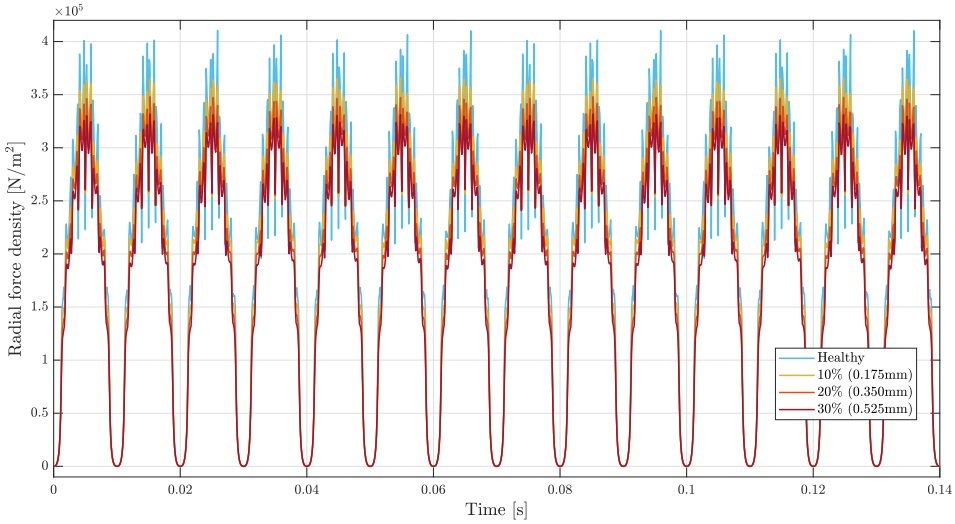

Figure 5.42: Time distribution of the radial air-gap force density during no load operation and static eccentricity.

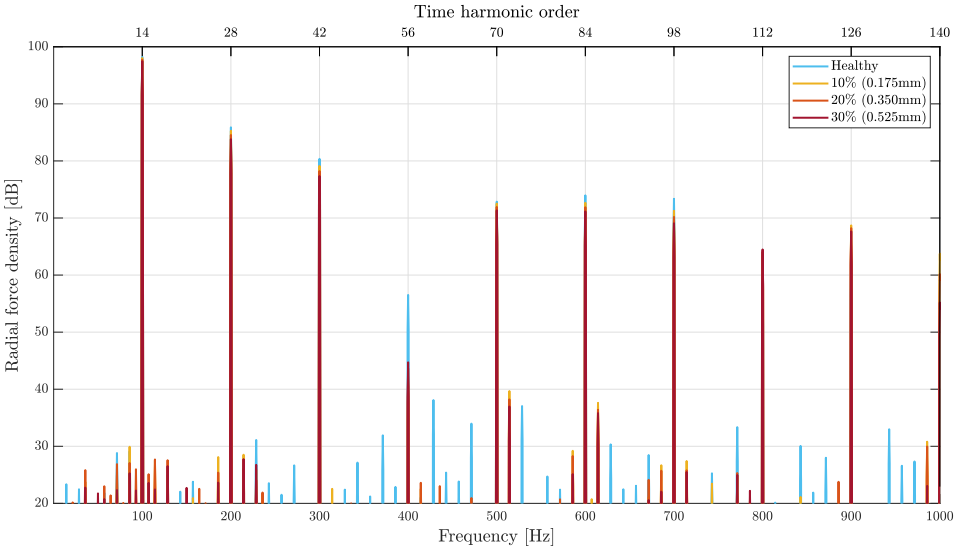

Figure 5.43: Frequency spectrum of the time distribution of the radial air-gap force density during no load operation and static eccentricity.

5.4.1.2 Spatial domain distributions with FFTs

The spatial distribution of the radial flux density during healthy and faulty no load operation is shown in figure 5.44. In contrast to the distribution in time domain, the spatial distribution is highly affected by SE. The flux density from zero to 90 degrees and from 270 to 360 degrees is increased as a result of the displacement of the rotor along the positive x-axis is the generator model, which corresponds to zero degrees. Naturally, the flux density in the mid-section of the figure is reduced due to the increased air-gap length. The periodic behavior is different compared to healthy operation and the frequency spectrum will consequently be changed.

As shown in figure 5.45, an FFT of the spatial distribution during SE results in additional harmonics compared to healthy condition. All of the natural components have noteworthy side-bands with orders that differ by one and the components adjacent to the fundamental and the two slot harmonics are the most affected by the fault. All of the harmonics that are excited due to SE have the potential to amplify a first-order force density harmonic when they interact with the natural components. The seventh-order harmonic reaches 0.76 T for all three fault scenarios and, in contrast to ITSC fault, its natural odd multiples have minor elevations and not reductions. The simulation results from full load operation are included in appendix E.2 where the amplitudes of the excited side-bands are more or less unchanged from no load operation.

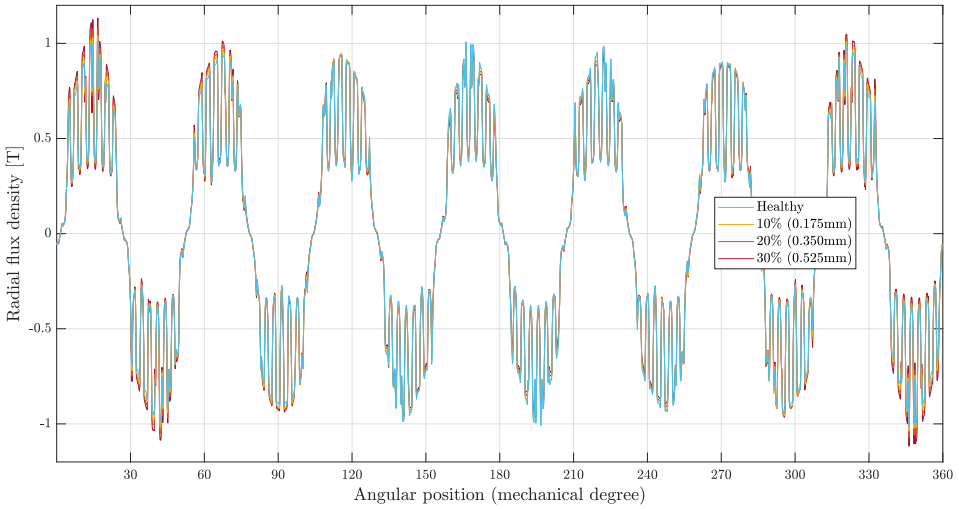

Figure 5.44: Spatial distribution of the radial air-gap flux density during no load operation and static eccentricity.

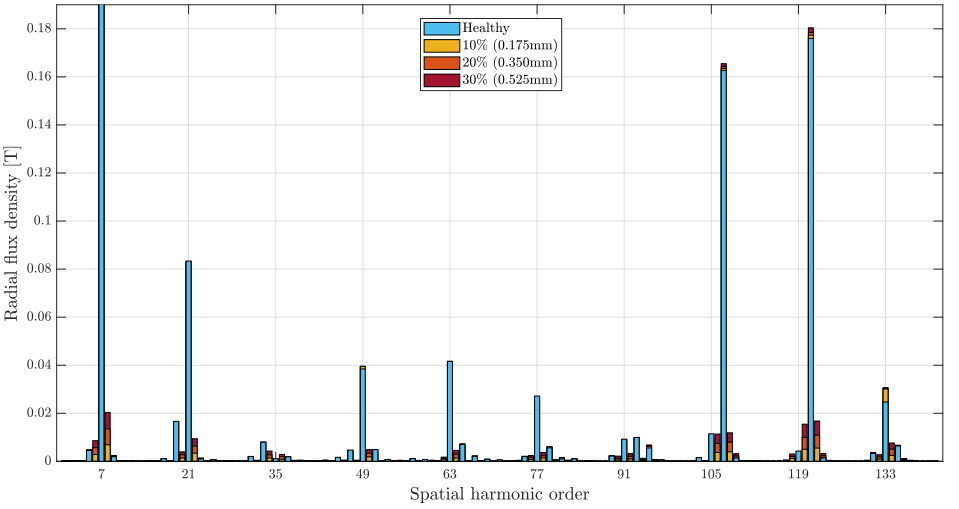

Figure 5.45: Frequency spectrum of the spatial distribution of the radial air-gap flux density during no load operation and static eccentricity.

The spatial radial force density is presented in figure 5.46 for healthy and faulty no load operation. The force waves during SE are clearly different from healthy condition due to the modified magnetic field and the lowest spatial order is changed. The second-order harmonic that is visible in the amplitude variations of the blue waves is not recognized in faulty condition. Instead, a single sinusoidal wave pattern is formed by the red, orange, and yellow waves which indicates that the lowest spatial order is one. The second-order spatial harmonic is still present due to the generator topology but it has not the lowest order anymore, and the lowest peak during fault occurs at 270 degrees due to the small increase around 180 degrees caused by the second-order harmonic. This is more apparent in the spatial distribution of the total forces in figure 5.48.

The mentioned observations are confirmed by the FFT presented in figure 5.47. The important difference between the frequency spectra from healthy and faulty condition is the first-order harmonic. It is significantly excited and reaches up to 14% of the amplitude of the fundamental during 30% SE. It can cause severe deformations in the stator if it belongs to one or more force waves with adequate amplitude. However, the frequency spectra from the time domain in figure 5.43 show that the low-order time harmonics have small amplitudes which will affect the magnitude of the resulting low mode vibration during SE. The FFT from full load operation, which is included in appendix E.2, does not provide any new observations and the amplitude of the first-order spatial harmonic is changed by less than two percent.

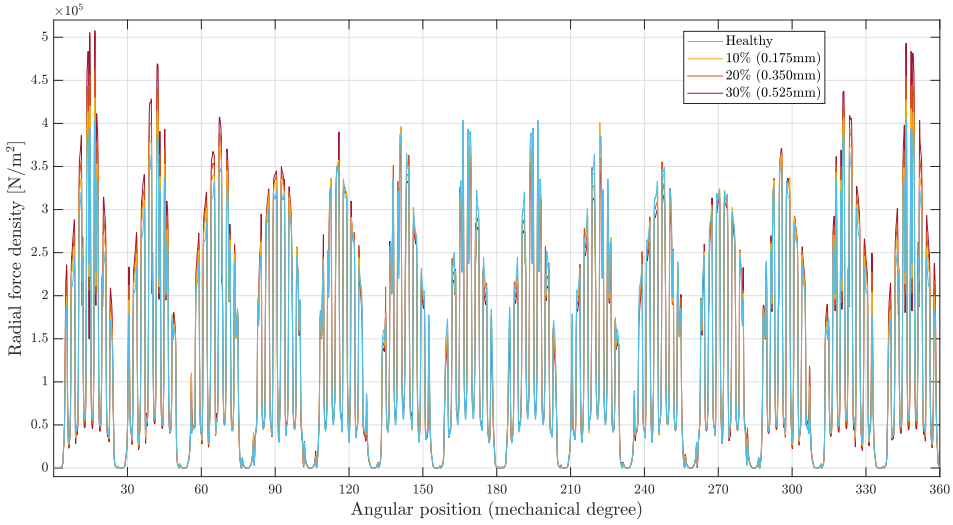

Figure 5.46: Spatial distribution of the radial air-gap force density during no load operation and static eccentricity.

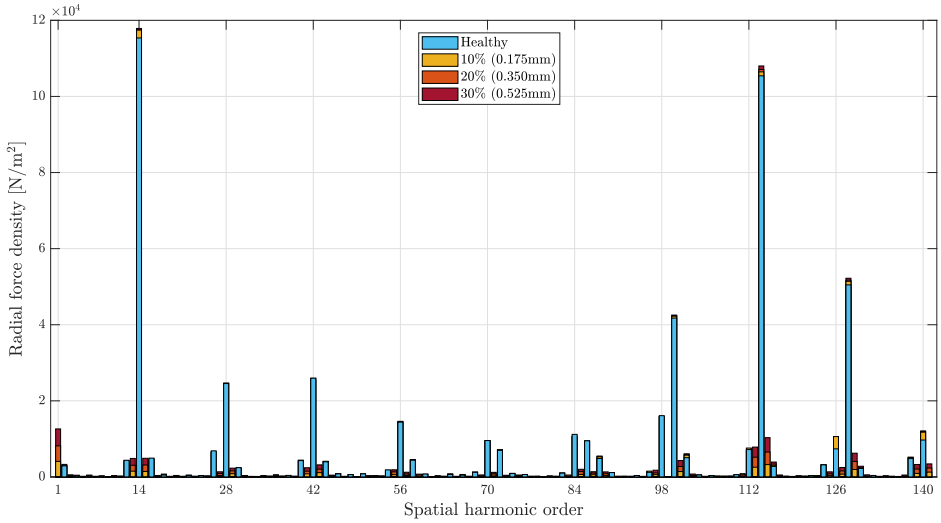

Figure 5.47: Frequency spectrum of the spatial distribution of the radial air-gap force density during no load operation and static eccentricity.

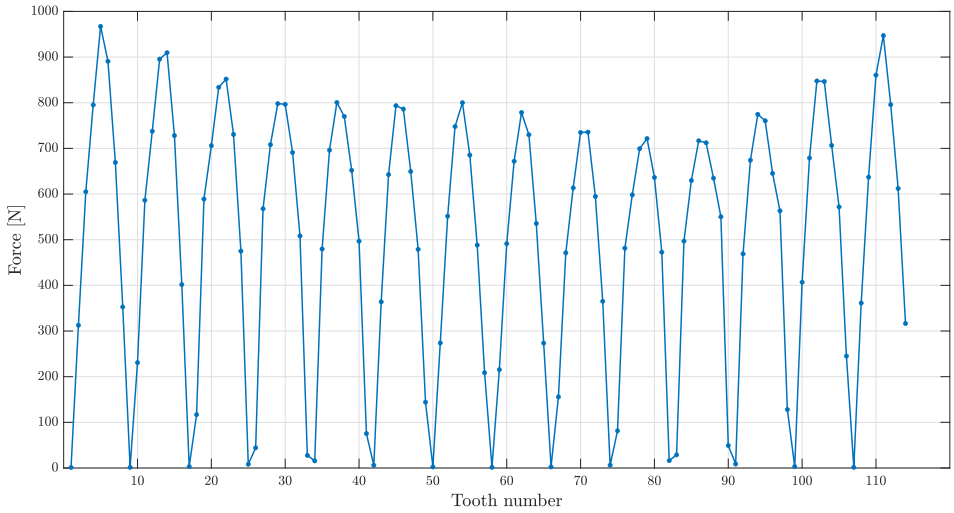

Figure 5.48: The total force acting on each tooth during no load operation and 30% static eccentricity.

The production of the first-order force density harmonic under SE condition can be examined in the same way as for operation with ITSC fault. The frequency spectrum of the radial flux density distribution in figure 5.45 shows that all of the natural components have one or two side-bands with orders that differ by one and the most relevant ones determined by their amplitudes are included in equation 5.5. These are also illustrated in figure 5.49 with their signs included. The seventh-order components have amplitudes of 0.76 T.

$$f_{rr,1st} = \frac{1}{2\mu_o} \sum_{i,j} b_{r,ith} \cdot b_{r,jth}, \tag{5.5}$$
$$i, j \in \{6, 7, 8, 20, 21, 22, 49, 50, 62, 63, 64,$$
$$76, 77, 78, 106, 107, 108, 120, 121, 122, 133, 134\},$$
$$j = i + 1$$

Figure 5.49 shows that all side-bands expect from number 64 and 78 have the same sign as the adjacent natural component and will contribute positively to the production of $f_{rr,1st}$. This is illustrated in figure 5.50. The fundamental with side-bands and the slot harmonics with side-bands are the main contributors due to their amplitudes and the negative components produced by flux harmonic number 63 and 64 and by flux harmonics number 77 and 78 are inconsiderable. Summation of the chosen interactions adds up to $f_{rr,1st} = 13.2\mathrm{kN/m^2}$, which is close to the lowest spatial harmonic $f_{r,1st} = 14.0\mathrm{kN/m^2}$ in figure 5.47. The remaining $0.8\ \mathrm{kN/m^2}$ is produced by all remaining radial flux density components with orders that differ by one and by all tangential flux density harmonics with orders that differ by one, which indicates the small influence of the tangential field. Conclusively, the fundamental with side-bands and the slots harmonics with side-bands of the radial flux density distribution during SE are the main reason for the excitation of the first-order radial force and the resulting vibration it may cause, similar as for ITSC in the field winding.

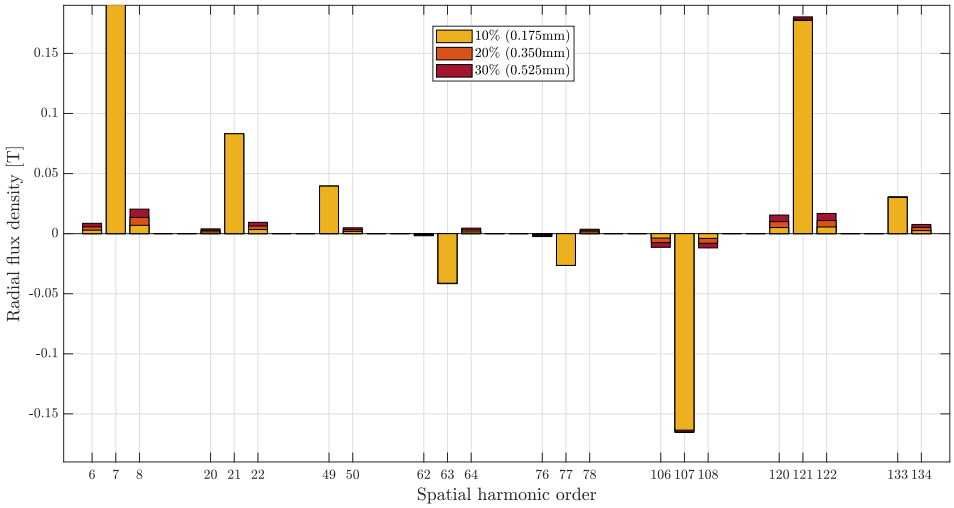

Figure 5.49: The most significant radial flux density components to produce the radial force density harmonic of first order during no load operation and static eccentricity.

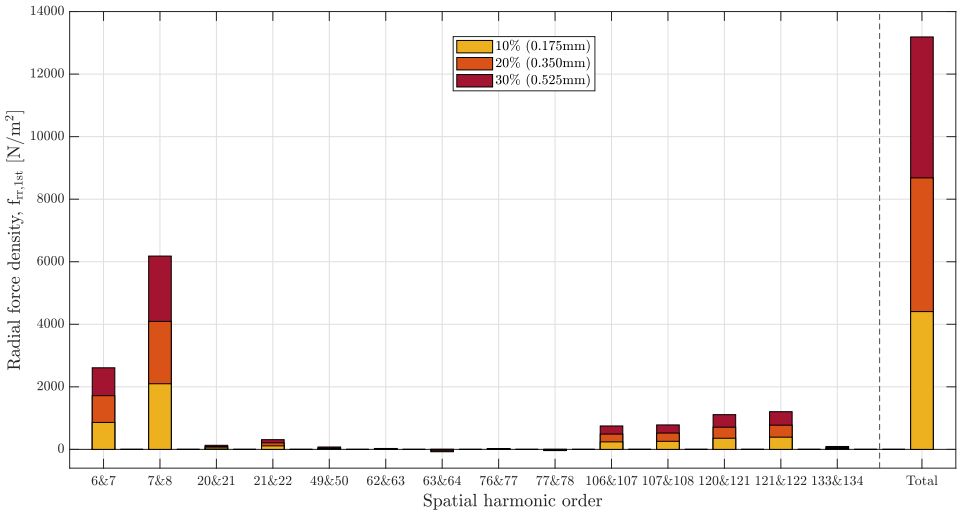

Figure 5.50: Contributions to the first-order radial force density harmonic from interactions between the most significant radial flux density harmonics during no load operation and static eccentricity.

5.4.2 Mechanical analysis

Figure 5.51 compares the simulated deformation from healthy no load condition to no load operation with static eccentricity. The figure shows a clear rise from 100 Hz towards 7.14 Hz. At 30% SE, rotor frequency vibration has increased by 131 times from healthy operation and is four times as large as vibration at 100 Hz. The 100 Hz component is nearly identical during faulty and healthy operation, while every frequency below 100 Hz is affected.

The change of vibration can be traced back to the earlier presented frequency spectra of the radial force density. The time domain FFT in figure 5.43 contains no noteworthy harmonics below 100 Hz and the origin of increased low-frequency vibration can not be found from this. On the other hand, the spatial domain FFT in figure 5.47 has a highly excited first-order harmonic. Moreover, figure 5.52 shows that this spatial harmonic order dominates the deformation at five of the frequencies below 100 Hz. The shapes of these stators are almost completely circular with no signs of higher-order deformation modes with more than one attraction point. The same tendency was found in all of the 13 sub-harmonic frequencies and the figure contains a representative selection. This means that the excited first-order spatial harmonic is distributed among force density waves at several frequencies and the reason for amplified vibration below 100 Hz. The vibration at 7.14 Hz has the highest elevation according to the vibration frequency spectrum, which indicates that the force density waves with $k = m = 1$ is affected the most.

As mentioned, rotor frequency vibration is amplified during SE, but it is not nearly as high as during ITSC fault. This is due to the low amplitude of the first time harmonic during SE. In fact, this component is not even present inside the limits of the y-axis in figure 5.43 and the deformation at this frequency is consequently not as high as during ITSC when the first-order time harmonic is excited. Despite the low time harmonics, vibration at 7.14 Hz is still induced due to the high impact of the excited first-order spatial harmonic.

Figure 5.52 also illustrates how the stator is deformed at 100 Hz during SE. The shape is almost identical to the one from healthy operation in figure 5.22 and dominated by the second mode with a minor influence of the 14th mode. The colors on the left side of the stator in figure 5.52 is somewhat more red than the right side, which indicates that it is also slightly impacted by the first mode. However, the vibration spectrum at this frequency shows only a marginal elevation during fault and it can be considered as unaffected by the excited first-order harmonic. This also means that the small increase in the second-order harmonic does not affect the 100 Hz to a noteworthy degree, but is more likely to be the cause of the small elevation at 200 Hz, as this frequency was also found to be dominated by the second mode as shown in the analysis of healthy operation.

Vibration between 100 Hz and 300 Hz is more or less unaffected by the fault and there is a general increase in the graphs between 300 Hz and 400 Hz. The vibration level in this range is around 2000 to 3000 times smaller than at 100 Hz, thus relatively very small. It was found that the deformed shape at the frequencies from 307.14 Hz to 371.4 Hz was heavily dominated by the third mode. In figure 5.47, the third spatial harmonic is increased

from 0 $\mathrm{N/m^2}$ during healthy condition to 550 $\mathrm{N/m^2}$ at 30% SE. This explains the amplification of deformation at these frequencies.

There are hardly any changes in vibration below 100 Hz from no load to full load operation during SE. This can be explained by the marginal differences between the subharmonic forces in the two operating conditions, both in time domain and the spatial domain. The vibration frequency spectrum during full load operation is included in appendix E.2 and contains the same characteristics as figure 5.51. The deformation profiles in figure 5.52 were found in the simulation results of both no load and full load condition.

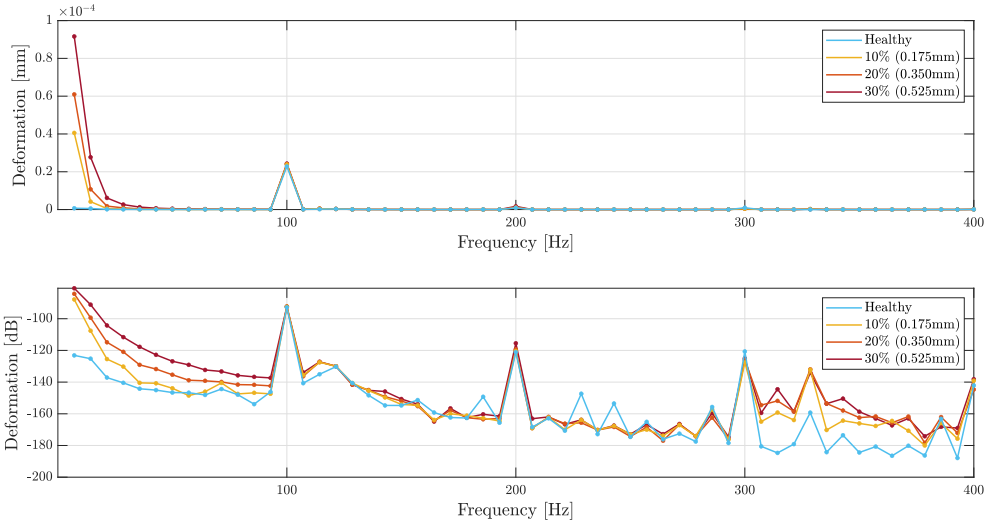

Figure 5.51: Frequency spectrum of stator yoke deformation during no load operation and static eccentricity. Top: actual values, bottom: logarithmic values.

Figure 5.53 shows the deformation spectrum during 30% SE with and without increased calculation frequency resolution. The rotor frequency vibration is unaffected by the first natural frequency at 0.21 Hz due to sufficient frequency spacing. The vibration at the second natural frequency is affected somewhat less than in healthy condition, while the spike at 327.7 is 31 times higher during SE and exceeds the 100 Hz peak. There are no excited time harmonics around this frequency and the reason for the large increase may appear somewhat unclear. However, the dominance of the third vibration mode at the frequencies between 307.14 Hz to 371.4 Hz and the slight increase in the third spatial harmonic is likely a reason. Nonetheless, the resonance effects do not cause vibration beyond the one at rotor frequency, and the laboratory generator would not experience dramatic resonance between 7.14 Hz and 400 Hz if it were to be operated with SE and no supporting structure.

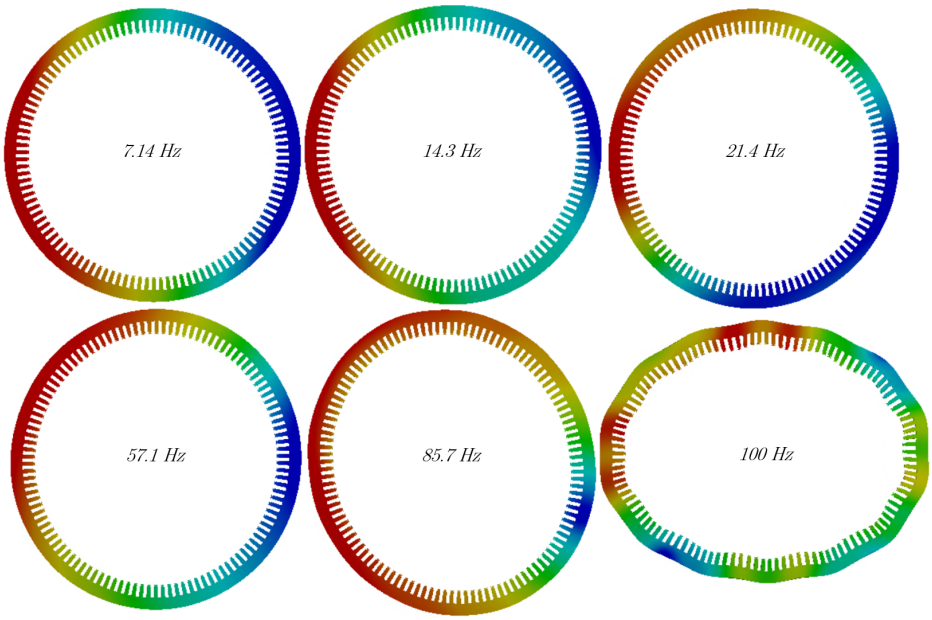

Figure 5.52: Deformation profiles of the stator at various frequencies during operation with static eccentricity.

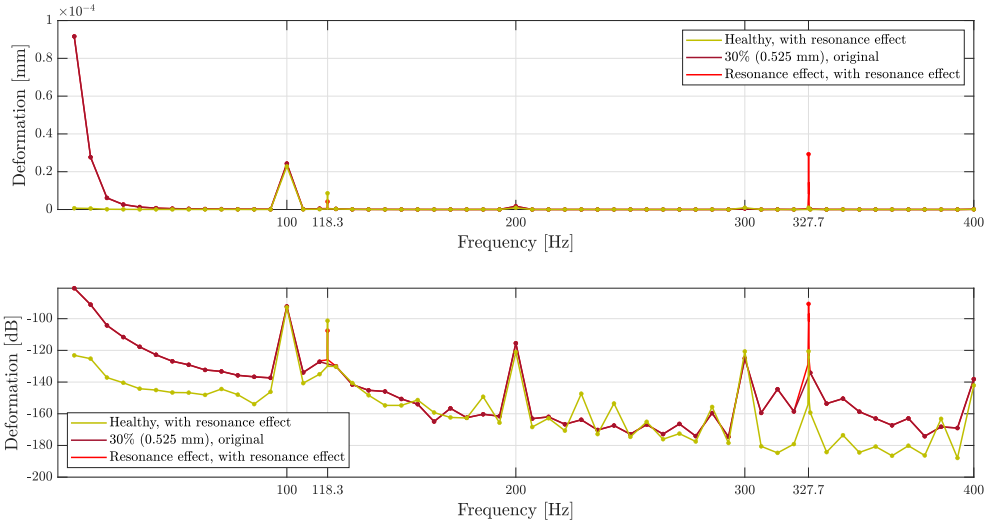

Figure 5.53: Frequency spectrum of stator yoke deformation during no load operation and 30% static eccentricity with specific calculations around natural frequencies. Top: actual values, bottom: logarithmic values.

Chapter 6

Discussion

This chapter is dedicated to discussion of the material presented so far. It is divided into sections that treat the main activities and findings of the thesis. First is the procedure of modeling and simulation from chapter 4 commented, before the analytical model formulated in section 2.2.6 is evaluated from a conditioning monitoring point of view. Next are the simulation results from the various operating conditions compared to each other with the figures and comments presented in chapter 5 used as a starting point. This section is further divided into subsections in order to separate the various simulation results from each other. However, there are indeed coherences among them and some overlap between the subsections is unavoidable. Thereafter, the results are further discussed and assessed based on the objective of the thesis and, finally, a suggestion of further work based on the discussions is presented. References to literature will be included to relate the presented material to existing research of the field.

6.1 Modeling and simulation

The model used for simulations in this thesis has been a salient-pole synchronous generator with, other than the size, a design typically found in hydropower stations. Separate models with various degrees of ITSC in the rotor winding or SE caused by rotor displacement have been used for fault simulations. Apart from these faults, the models are accurately created based on technical drawings and, thus, represent an ideal machine without any defects. However, an ideal machine is not always realistic. As introduced in section 1.1, a drawback of the high efficiency accomplished through a hundred and thirty years of design perfection is that real hydropower generators today are large and heavy constructions with tiny margins and no room for inaccuracy in manufacturing and assembling to achieve a flawless machine. The high precision required makes a small degree of imperfections such as eccentricity, rotor unbalance, or asymmetry in the field winding and damper winding in reality difficult to avoid [15]. These may induce additional harmonics in the air-gap magnetic field, force, and the stator vibration, and are not included in the simulations models of this thesis.

Detailed inspection of the real laboratory generator could have been performed in order to create the model as realistic as possible with potential deviations from the technical drawings included. However, such inherent imperfections are likely to vary from generator to generator and including these in the simulations could have caused excitement of harmonics that belong to the laboratory generator only and would not be applicable for salient-pole synchronous generators in general. Thus, it has purposely not been in the scope of this thesis to replica the real laboratory generator to its very detail, but to investigate the effects of faults on the vibration behavior of a generator with typical hydropower topology. By making the model ideal, the discussions and conclusions can be generalized to a broad range of salient-pole synchronous generators.

The generator in The National Smart Grid Laboratory at NTNU was chosen to be the objective for modeling and simulation as it offers the possibility for verification of the simulation results through vibration measurements with the investigated faults applied during operation. Unfortunately, the outbreak of the coronavirus resulted in shut down of the laboratory which disabled this possibility. Nevertheless, the modeling and simulation procedures have been thoroughly executed and the results provide detailed information about the air-gap flux, force, and the resulting stator vibration. As will be discussed later in this chapter, the work of this thesis can be validated by existing research and it is believed that the findings are applicable to real hydropower generators, despite the absence of laboratory measurements.

Time-stepping FEM has been used for all simulations through two software provided by the company ANSYS which is, according to its website, the global leading company of engineering simulation [79]. Other numerical problem-solving techniques are for instance the Finite Difference Method, the Boundary Element Method and the Montecarlo Method, however, advantages like non-linear problem solving without restricting the geometry and easy refinement of the element mesh at critical areas make the 2D FEM the clearly most utilized technique for analysis of rotating electrical machines in the literature reviewed

during this project.

The time step used for the simulations in Maxwell has been 0.1 ms, corresponding to a sampling frequency of 10 kHz. This resulted in a high-resolution representation of the air-gap flux and force with a sufficient amount of sampled data to produce accurate FFTs. A master's thesis project conducted at the Department of Electric Power Engineering at NTNU in 2019 investigated fault detection in hydropower generators through magnetic flux monitoring [80]. The very same laboratory generator was examined through similar FE simulations and compared to laboratory flux measurements. However, the simulations were performed with a 0.25 ms time step which was, according to the author, too large and caused inconsistencies in the simulated air-gap flux density. On the other side, the time step of 0.1 ms chosen for the simulations in this thesis was based on a sensitivity analysis that showed no significant differences in the simulated magnetic field for simulations with time step ranging from 0.12 ms to 0.02 ms, thus providing high accuracy and high-quality acquirement of flux and forces.

The simulations in Mechanical were based on the most commonly utilized method for vibration analysis in rotating electrical machines. Tooth arcs consisting of a high number of separate points resulted in precise calculation of the total force acting on each tooth in Maxwell. These were obtained with a high frequency resolution and the vibration was calculated for each multiple of the rotor frequency, which was chosen based on the smallest frequency interval between the produced deformation.

To summarize, thorough modeling, phenomenal simulation software, deliberated definitions of solution setups, and utilization of reliable methods in both Maxwell and Mechanical make the results presented in this thesis trustworthy and expected to be a valid representation of a hydropower generator.

It should be mentioned that a possible source of error in the simulated vibration compared to reality is the exclusion of structural support. The correct definition of the support bars was not possible to determine without inspection of the laboratory generator and, due to the laboratory shut down, the bars were excluded from the model. Possible effects of not including supporting structure on the vibration simulations are discussed in section 6.3.1. The support bars can be seen present in the Maxwell model in figure 4.5, however, they were located outside the zero flux boundary and did not influence the simulations. They were included in the model for the sole purpose of being a part of the 3D geometry required in Mechanical but were discarded in this 3D model due to the mentioned lack of knowledge about realistic definition of the support.

6.2 Analytical model

The analytical model was formulated based on the wave-permeance method by finding the air-gap radial flux density through multiplication of the permeance and MMF. Thereafter, Maxwell stress tensor was applied to obtained the radial force density and the total forces were found by integration. The reason for creating the model was to fulfill the need of accurate descriptions of the air-gap force density and total force in faulty salient-pole synchronous generators with important aspects like rotor geometry, stator slots, and saturation effects taken into account. To the present knowledge, this has not been done before.

The model neglects the tangential component of the air-gap flux density which is a common approach in analytical models describing rotating electrical machines due to its small impact on the radial force density compare to the radial flux component [49, 50]. Based on the simulation results presented in section 5.2.1, this simplification can be justified by the analyses of the tangential field which did not excite any force density harmonics, in time or the spatial domain, that were not present due to the radial flux. Consequently, excluding the tangential flux density component in the analytical model did not impose errors in the predicted frequencies or spatial harmonic orders. It was also found that the amplitude of the radial force density produced by the tangential flux was relatively very small, which further illustrates the small impact of the tangential field.

Despite a few simplifications, such as neglecting the tangential flux and assuming pure sinusoidal behavior of the rotor and stator current density, the predicted time and spatial harmonic orders are in good agreement with the FFT figures from the FEA during ITSC fault. The model formulates time harmonics to appear every 7.14 Hz which is confirmed by the simulated frequency spectra. The same observation can be found for the spatial domain. Despite that component number seven and the interharmonics above order 14 are excited with small amplitudes hardly seen in the figures, all the predicted harmonic orders are present in the spectrum. In fact, as mentioned in section 2.2.6.2, it was expected that the amplitude of the harmonics decreased as their frequency and order increased. In other words, the analytical predictions for operation with ITSC in the rotor winding are validated by the numerical simulations and can be considered reliable from a theoretical point of view. Furthermore, the agreements emphasize the strength of an analytical model, namely that it formulates the same harmonics to be affected by the fault without the computational time and resources required during FE simulations.

For operation with SE, the time domain forces are in general not much affected by the fault which is according to expectations from the analytical model. The frequency spectra contain a few new harmonics that are not predicted by the analytical expression, however, their small amplitudes suggest them to be inconsiderable. On the other hand, the correspondence between the analytical and numerical results is not as evident for the spatial domain. The model predicts harmonics to appear at each order while the simulated spectra contain clear excitation of only the first component and the side-bands of the naturals. However, there are minor elevations of the other unnatural harmonics as well, which is hardly seen in the spectra. Thus, the analytical expression for spatial harmonics correctly formulates the orders that appear during SE but most of the excited harmonics can be con-

sidered insignificant due to their low amplitude. In total, the analytical model provides only fairly good results during SE due to the somewhat unconvincing agreement at several spatial harmonic orders.

As known from the theory presented in chapter 2, and as shown in the presented simulation results in chapter 5, production of deformation in a generator can have a complicated origin due to the relationship between the time harmonic order, k, and the spatial harmonic order, m, and the fact that they influence the vibration in different ways. For instance, the k of a force density wave corresponds to the frequency of vibration produced by that wave, while the m has an impact on the amplitude of the static deformation that is proportional to $1/m^4$. This means that the k- and m-predicting expressions from the analytical model must be interpreted differently for vibration than for forces.

The results from vibration simulation of all three conditions, that is healthy operation, ITSC in the rotor winding, and SE, show that the deformation of the highest amplitude is the one caused by the lowest harmonic order present in the spatial force density distribution. For both fault types, this is the first mode. This means that in a condition monitoring point of view, determination of the lowest spatial harmonic is mostly of interest, which is correctly predicted by the analytical model during both faults.

The simulation results from ITSC fault show that if subharmonics of the same order are excited in both the time domain and the spatial domain, the resulting vibration will be caused by force density waves with $k = m$ such that the first mode causes deformation at rotor frequency, the second mode at two times rotor frequency, the third mode at three times rotor frequency and so forth. Moreover, since vibration at a certain frequency depends on the amplitude of the time domain harmonic at that frequency, the low-frequency vibration during ITSC fault is significantly higher than during SE. In other words, the correctly predicted presence of time harmonics during ITSC fault contributes to increased low-frequency vibration, while the correctly predicted absence of time harmonics during SE limits the low-frequency vibration. These observations and the agreement with the analytical model shows the value of its formulated time domain harmonics for vibration monitoring.

It was suggested in section 3.2 that the expected highest vibration during SE would be at 100 Hz due to the absence of forces with a frequency below this. This is not the case in the simulated vibration spectra due to the high impact of the first-order spatial harmonic. The fact that vibration at 7.14 Hz is excited during SE despite the absence of the time harmonic with $k = 1$ illustrates the great importance of the spatial harmonic order. Vibration at 7.14 Hz is significantly higher than at other subharmonic frequencies which means that the first spatial harmonic mainly acts at 7.14 Hz corresponding to the first time harmonic, despite that the deformation pattern at higher subharmonic frequencies was also dominated by the first mode. From these observations, prediction of vibration based on time and spatial harmonics should emphasize the lowest spatial order and it can be expected that it produces dominating vibration with frequency at the corresponding time harmonic order, that is at $k = m$, despite non-existence of time harmonics at this order. The analytical model pre-

dicts the lowest-order spatial harmonic correctly during both faults, which illustrates the usefullness of the model's spatial domain formulation for vibration monitoring.

It can be summarized from the above discussions that the formulated analytical model can serve as a good tool for prediction of vibration during ITSC in the rotor winding or SE. The model is a novel contribution to the field of research and can be regarded as valuable in force and vibration analysis of salient-pole synchronous generators. This is despite the somewhat lacking consistency between the analytical predictions and the FE simulation results for some of the spatial subharmonics during SE, due to the dominating impact of the correctly predicted first-order harmonic. In short, predictions from both domains must be considered and the lowest predicted m should be in focus since it will be the dominating vibration mode. It can be expected that it causes the worst deformation at $k = m = 1$, that is at rotor frequency, and that the vibration will be severely further amplified if the time harmonic of $k = 1$ is excited. This will be the case during ITSC in the rotor winding but not the case during SE.

The simulation results indicate that the amplitude of the force density distribution in both the time domain and the spatial domain influence the resulting vibration, which is supported by the presented theory. However, detailed calculation of amplitudes was excluded from the analytical model since they do not influence the harmonic orders of the force. In light of the simulation results, it would indeed be interesting to analyze the agreement between analytically computed force amplitudes and simulations, and to investigate their impact on the resulting vibration in detail. However, this would increase the computational effort related to the formulation of the model and some of the parameters that determine the amplitudes require measurements and practical work on the generator in scope. Despite that the information provided by the model can be increased by including amplitude calculations, it fulfills its objective of formulating orders of time and spatial harmonics that can be used for analytical prediction of vibration related to fault detection.

6.3 Simulation results

6.3.1 Modal analysis and resonance

The modal analysis provided the first six natural frequencies of the stator which belonged to the first six vibration modes in chronological order and the stator shapes were deformed by a number of attraction points equal to the mode number. These results are consistent with the presented theory. The main objective of the modal analysis was to investigate how the natural frequencies affected the simulated vibration in relation to the analyzed forces. However, the exclusion of the support bars is likely to decrease the natural frequencies due to their stiffening effect on the stator such that the obtained frequencies can not be expected to apply to the real laboratory generator. In fact, it was found in [81] that a stator frame affects the resonance frequencies substantially and despite that the laboratory generator does not have a full frame directly in contact with the stator, the supporting bars may have the same effect. Moreover, a FE modal analysis of a stator with 120 slots performed in [57] found that the natural frequency of the second and fourth mode increased by a factor of five and four, respectively, when support was included compared to when the stator was unsupported. This indicates that a modal analysis with the support bars included would result in higher natural frequencies and decrease the risk of resonance, for instance by moving the second natural frequency at 118.3 Hz further away from the dominating second-mode vibration at 100 Hz. In conclusion, vibration analysis without any support is likely more exposed to resonance than when supporting structure is included, which means that the small influence of resonance effects found in this thesis may be even less significant in the laboratory generator in reality.

The support bars may also have a damping effect on the vibration of the generator. For instance, it was found in [82] that the amplitude of vibration in presence of a frame is smaller than without a frame, and the authors of [83] concluded that the stator frame causes slight damping of vibrations. Thus, the vibration level of the real laboratory generator may be smaller than presented in chapter 5. However, the authors of the mentioned research found uniform damping along the frequency spectrum, which means that the same vibration characteristics and observations as found in this thesis are expected to be present also when support is included, only with reduced amplitude. As mentioned earlier, the numerical value of the vibration amplitudes is not of relevance as they can vary from generator to generator dependent on size and topology, while how the vibration frequency spectrum changes in presence of a fault can be generalized to a typical hydropower generator and is of interest since it may reveal patterns suitable for fault detection. Conclusively, exclusion of the support bars does not invalidates the simulation results from a fault detection point of view, despite that it may cause numerical values that deviate from reality.

It can also be mentioned here that the frame of real hydropower generators is usually not connected to the stator in a completely tight manner in order to ensure some available space for the iron to expand due to temperature variations between stand-still and operation. This means that the vibrations, which is in terms of micrometers for the laboratory generator, might be free to move inside the available space and not be affected by the frame at all. However, this is not possible to determine without detailed practical examination of

how the frame is connected in a real hydropower generator and how much the iron naturally expands when the temperature rises.

Despite that the values of the resonance frequencies acquired from the modal analysis may not be applicable to the laboratory generator, a few interesting observations were found from the vibration simulations with increased calculation resolution around the natural frequencies. First, the higher increase in deformation at and close to 327.7 Hz compared to 118.3 Hz, that is respectively the third and second natural frequency, during 28.6% ITSC fault indicates that the frequency of an air-gap force has to be very close to the natural frequency in order to produce resonance. That is, the frequency spacing between the closest force harmonic and the value of the natural frequency is approximately one hertz for 327.7 Hz, while it is approximately three hertz for 118.3 Hz.

The simulation result form operation with 30% SE and increased calculation frequency suggests something else. During this fault, there are no excited forces close to the third natural frequency and the deformation at 327.7 Hz is still spiked. This indicates that it is the excitement of the spatial harmonic with order equal to the order of the natural frequency that is responsible for the presented resonance effect. This third harmonic is slightly amplified from healthy condition during 30% SE which causes a 31 times higher deformation at 327.7 Hz, while it is heavily amplified during 28.6% ITSC which causes 40 times higher deformation at 327.7 Hz. It should be emphasized here that it is indeed a fact that a force with a frequency equal to the natural frequency of the same mode will cause resonance, but the simulation results may imply that the spatial harmonics influence vibration at natural frequencies as well and that the time harmonics excited during ITSC have too low amplitude to cause noteworthy effects. For instance, the excited time harmonic at 328.6 Hz during 28.6% fault degree has an amplitude of 327 $\mathrm{N/m^2}$, which is only 0.4% of the main component. Unfortunately, seen from an analysis point of view, there are no excited forces in the generator with high amplitude close to, or exactly at, a natural frequency such that this can be further investigated.

To sum up, the excitement of unnatural spatial harmonics is likely to play a role in production of resonance. However, taken into account that the overall magnitude of the amplified deformation at the natural frequencies is relatively not dramatically high, even during 30% ITSC fault with a highly excited third-order spatial harmonic, their importance seems to be limited. Furthermore, it is not possible to determine their influence compared to forces with a frequency close to a natural frequency due to the lack of time harmonics with significant amplitude.

6.3.2 Flux and force

6.3.2.1 Evaluation of the results

The analyses of the tangential magnetic field in the time domain and the spatial domain revealed its relatively very small impact on the radial force compared to the radial magnetic field. This observation was further emphasized through analyses of the second-order spatial harmonic during healthy operation and the first-order spatial harmonic during both investigated faulty conditions. Thus, the presented figures of the radial flux density give a good representation of the total flux present in the air-gap. The findings indicate that the radial flux density is the main cause of the vibration in salient-pole synchronous generators and that neglecting the tangential flux density does not impose considerable errors, which supports the exclusion of the tangential flux density component commonly done in the literature.

The results from simulation of the radial flux density were according to expectations from the presented theory. For instance, the fundamental time-harmonic had frequency equal to the synchronous frequency at 50 Hz and the fundamental spatial harmonic had an order of seven equal to the generator's number of pole pairs. Natural harmonics appeared at their odd multiples in both domains. The same accounts for the radial force density, where there was a clear coherence between the interacting flux density harmonics and the resulting force density harmonics.

It was found that the time domain spectrum of the radial flux density during no load and full load operation with ITSC fault was highly enriched by additional harmonics, while the spectrum during SE was more or less unaffected. Similar simulations and time domain analyses were performed during a master's thesis project in 2019 and the results are in full agreement [80]. Moreover, the authors of [84] investigated the effects on the air-gap radial flux density and force density from ITSC in one of the salient poles of a synchronous generator through FE simulations. The examined generator had eight poles and 126 slots. The spatial harmonic spectrum of the radial flux density and force density show similar effects by the fault as the results presented in chapter 5. Radial forces were analyzed also in [53], where the spatial harmonics of three healthy salient-pole synchronous generators obtained from FEA are presented. The rotor of the investigated generators had 14, 14, and 70 poles while the stators had 114, 180, and 432 slots, respectively. That is, one equal and two different pole-slot-combinations as the laboratory generator. The appearance of the spatial harmonics orders based on the generator topologies are in agreement with the results presented in chapter 5.

Consistency with literature shows that the simulations executed in this thesis have produced reliable results and that they are applicable to salient-pole synchronous generators with different rotor and stator topology. Moreover, some of the above-mentioned work was verified by experimental measurements, which indicates that the magnetic analyses in this thesis are also valid in practical applications for real hydropower generators. No work that investigates fault detection with vibration simulations as in this thesis has been found in the literature. However, the reliable simulation results of the magnetic forces, which

has been used as input for the vibration simulations, and the fact that the utilized modeling and simulation methods are the most common approaches for examination of rotating electrical machines, make it likely that the vibration simulation results are valid as well. In addition, the lack of similar investigation in the literature as performed in this thesis illustrates the importance of the findings and that they contribute with novel and valuable knowledge about how fault detection in salient-pole synchronous generators through vibration analysis can be performed.

6.3.2.2 The time domain and the spatial domain

The air-gap flux density and radial force density has been analyzed in both the time domain and the spatial domain in this thesis. Healthy condition and the two faults have been treated equally, and the relationship between the two domains has been found variable depending on the generator condition. During healthy condition, the distributions and frequency spectra in the two domains have large similarities, which is not surprising as it is indeed the same flux and forces that are analyzed, only that the position is held constant for the time analysis and that the time is held constant for the spatial analysis. Moreover, the generator is of the synchronous kind which links the natural harmonics in the two domains to the same orders. However, a few differences appear due to the fact that the rotor and the stator have different geometries, such as the damper bar harmonics in the time domain and the slot harmonics in the spatial domain.

The same can be found for the analyses of operation with ITSC in the rotor winding. The flux and force in the air-gap are affected by a reduction of the MMF produced by the pole with faulty winding and the rotation of the rotor imposes dynamic UMP to the air-gap. This UMP depends on both time and position and, consequently, a high number of unnatural harmonics are excited in both domains. On the other hand, SE induces a static UMP with increased force density close to one side of the stator, which is time-independent. Thus, the time domain is more or less unaffected by SE while the spatial domain is enriched by additional harmonics.

The static UMP caused by SE and the different effects it has on the two domains has been found to make analysis more challenging. That is, since the harmonic content of both domains affects the resulting vibration, inconsistency between them underlines that the relationship between their harmonics can be advanced. This can be further emphasized by inspecting the presented deformed stator shapes at healthy and faulty conditions. First, in healthy operation and during SE, the 100 Hz vibration is affected by both the second mode and the 14th mode, which indicates that several force density waves with the same frequency can have a different spatial harmonic order. Second, during SE, the first mode dominates the deformation at all 13 subharmonic frequencies, which means that waves with different frequencies can have the same spatial order. Finally, during ITSC fault, the majority of the vibration frequencies below 100 Hz are dominated by their individual mode while, simultaneously, the second mode is the cause of vibration at both 14.3 Hz and 100 Hz. In short, the relationship between k and m varies from condition to condition based on the harmonic content of both the spatial distribution and the time distribution,

and simple rules or analytical expressions for this coherence is therefore not easy to obtain.

A successful method for determining the relationship between the harmonics in the two domains, that is which spatial harmonic order and time harmonic order that belong to the same force wave, during faulty operations has not been found in the literature. On the other hand, several authors, such as those of [58, 59, 62, 85–87], have done this for healthy machines based on a technique that performs the FFT twice on the same data, one for each domain. This method has also been utilized during the thesis. However, the magnetic asymmetry caused by the faults increases the required amount of data significantly from healthy condition. That is, the data, which is samplings of the force density, is collected in a square matrix, and not simply a one-dimensional array as required by a single domain analysis, which quickly increases to an unmanageable large size due to the high amount of required data. Consequently, results with adequate accuracy for useful analysis has not been achieved. However, the relationship between the harmonics in the two domains can reveal useful information about the produced vibration and this method, or other methods with the same objective, should be explored further if similar work is to be conducted in the future.

It should be mentioned here that despite the lack of an exact method for determining the relationship between the time and spatial harmonics, the procedure of combining the harmonic spectra in the two domains with the deformation profiles of the stators at specific frequencies and modes has provided adequate information to establish the cause of vibration and analyze the change of vibration behavior in detail. A method that provides the relationship between k and m would be beneficial for verification of this procedures and for lightening the workload of the conducted analyses.

6.3.2.3 Excitation of the lowest-order spatial harmonic

It is clear from the analyses presented in this thesis that the spatial harmonic of the lowest order present in the air-gap is essential for the vibration of the generator as it represents the dominating deformation mode. The lowest order during healthy condition was two and found to be the dominating mode of the highest vibration, which was at 100 Hz. Both the lowest spatial order and the frequency of the highest vibration is in agreement with the presented theory. During faulty operation, the lowest order was shifted to the first as a symptom of the UMP caused by the faults, which is also consistent with theory. Moreover, the amount of deformation was dependent on the amplitude of the spatial harmonic, which for instance can be seen in the results from healthy operation where the increased second-order harmonic during full load operation causes a higher 100 Hz vibration than during no load.

The production of the lowest-order spatial harmonic based on interactions between radial flux density harmonics has been investigated for healthy operation and all fault scenarios. For every condition, the fundamental flux harmonic is responsible for the highest contribution to the lowest-order force harmonic. In fact, the amplitude of the fundamental is decisive for the amount of flux in the air-gap and, consequently, the induced voltage in

the armature and the generated output power. Thus, reducing the fundamental flux component in order to decrease the lowest-order spatial harmonic will negatively impact the performance of the generator. However, during healthy condition, the flux density slot harmonics are large contributors to the second-order force density harmonic as well. This is also the case for the first-order harmonic during SE due to the excited side-band components, while the contributions from the slot harmonics are close to inconsiderable during ITSC in the rotor winding. Thus, a reduction of the slot harmonics can reduce the vibration level during healthy condition and during SE.

The authors of [54] investigated how the slot harmonics affected the flux, force, and vibration in healthy low-speed permanent-magnet machines with concentrated windings through FEA verified by experimental work. Four cases with different stator slot characteristics were examined: one with open slots, two with magnetic wedges of different relative permeability and one with semi-closed slots, hereafter denoted case 1 to 4, respectively. The authors emphasize that from a manufacturing point of view, open slots are preferred compared to semi-closed slots, and that a stator with open slots can easily be equipped with magnetic wedges even for large machines. In relation, the laboratory generator examined in this thesis has open slots.

The authors found that the flux density slot harmonic under investigation was highest with open slots, lowest with semi-closed slots, and its amplitude with magnetic wedges was in-between case 1 and 4. Consequently, the lowest-order spatial force density harmonic and the resulting vibration of the generator was reduced gradually from case 1 to 4. The eddy-current losses in the rotor were also analyzed and were discovered to follow the same trend as the vibration. However, the fundamental component of both the radial and the tangential flux density varied between the cases and, according to equation 2.2, impacted the tangential force and the resulting production of useful electromagnetic torque. It was found that the torque slightly increased from case 1 to case 2, while reduced to case 4 and was lowest during case 3. Thus, the authors concluded that there is possible to use magnetic wedges with an optimal relative permeability such that the torque is increased simultaneously as the slot harmonic and rotor losses are reduced, resulting in lower vibration level and higher output power.

It can be concluded from the findings in [54] combined with the results presented in chapter 5 that it can be possible to limit the production of the lowest-order spatial force density harmonic during healthy condition and with SE. This can be achieved by reducing the flux density slot harmonics by choosing a stator design with semi-closed slots or, in order to avoid torque reduction and for manufacturing advantages, equip the slots with magnetic wedges. Limitation of the lowest-order spatial force density harmonic will reduce the resulting vibration and restrain the consequences of a SE fault. This is favorable from a condition monitoring point of view, however, a decrease in the rotor-frequency vibration can impede detection of the fault. Hence, a convenient solution may be to insert magnetic wedges after the fault is detected to reduce its impact.

6.3.3 Vibration

6.3.3.1 Vibration mode and frequency

While the frequency of a force wave is decisive for the frequency of the produced vibration, its spatial harmonic order determines the vibration mode based on the number of circumferential attraction points between the force and the stator. The various modes and how they deform the stator have been illustrated in the modal analysis and in the mechanical analyses of healthy and faulty conditions. The results from healthy operation show how the second mode dominates the natural vibration at 100 Hz with slight influence from mode 14 such that the deformation is not completely oval. This is also the case during SE despite the excitation of a lower-order spatial harmonic. The first order harmonic is also excited during ITSC fault, while the 100 Hz vibration is still dominated by the second mode. This means that the force density wave with a spatial harmonic order of two and a frequency of 100 Hz is still present in the air-gap during fault. The conclusion is that the force waves which are naturally present during healthy condition are unaffected by the faults and that the change in vibration behavior is caused by interactions between newly excited flux density harmonics. This is supported by the marginal changes in the natural time and spatial harmonics from healthy to faulty condition.

The strongly elevated first-order spatial harmonic during SE may cause expectations of a higher vibration level than obtained during the simulations presented in section 5.4.2. Compared to ITSC fault, the first harmonic during SE is higher while the low-frequency vibration is lower. However, the time domain during ITSC shows that excited forces have low frequencies, thus causing low-frequency vibration, while the time domain during SE is more or less unaffected and does not provide information about at which frequency the first-order spatial harmonic acts. However, the illustrated deformed stator profiles during SE show that the first mode influence all frequencies below 100 Hz, which indicates that the first-order spatial harmonic is distributed among several force waves with different frequencies, thus causing a less prominent vibration at each of these frequencies. Compared to the deformed stators during ITSC fault, the excited spatial harmonics act mostly at a single frequency, resulting in more severe vibration.

As mentioned in theory section 2.2.5.2, it is commonly not useful to consider modes above eight due to their low impact on vibration. This is supported by the simulation results. First, the 14 indents of the 100 Hz deformation profile during healthy condition and during SE is relatively very small compared to the second mode attraction, despite that the 14th spatial harmonic is around 70 and 40 times higher than the second-order harmonic during no load and full load, respectively. This means that mode 14 is too high to be effective. Moreover, spatial harmonic 12 is elevated during healthy operation, and none of the deformed shapes were found to have 12 attraction points. Thus, this mode number is also too high to be effective. Finally, the vibration frequency spectrum during ITSC fault can be inspected as it was found that the order of the low vibration modes was the same as the time harmonic order of the frequency it vibrated. That is, the force waves with $m = k$ dominated the vibration at low frequencies. The spectrum shows that the vibration below 42.9 Hz, which is caused by the sixth mode, can be considered as noteworthy amplified

from healthy operation. Frequencies above this do not have dramatic elevation in deformation despite that the spatial harmonics are equally excited as for lower orders. It should be reminded here that the severity of deflection in the presented deformed stator profiles has been increased to emphasize the mode shapes, such that the illustrated deformation at 71.4 Hz by mode number ten, which was presented as the highest frequency with visible high-order vibration mode, must be interpreted in combination with the frequency spectrum. Conclusively, due to the inverse proportionality between the amplitude of static deformation and the mode number to the power of four, spatial harmonics with order higher than five do not affect the laboratory generator to a notable degree.

6.3.3.2 Effects of loading

The simulations in this thesis were performed with and without load connected to the generator terminals for all investigated operating conditions. The load consisted of 65 kVA with a power factor of 0.93 and was obtained by modeling an external circuit with resistive and inductive parameters calculated from the available setup in the laboratory. It has been referred to as "full load" since it is the maximum load that can be achieved in the laboratory, despite that it is lower than the generator's rated value of 100 kVA. Thus, related to fault detection applications, the results and conclusions labeled with "full load" should be considered as 65% loading in real hydropower generators. "Full load" will continue to be used as a term for the load scenario investigated in this thesis in order to keep consistency.

The most important difference between no load and full load operation was found in the spatial domain during healthy operation. The results show that the second-order harmonic is about twice as high with full load, mainly due to amplified fundamental and slot harmonics in the flux density distribution. The dominance of the second vibration mode at 100 Hz and 200 Hz consequently causes an increase in vibration at these frequencies, particularly with a factor of 2.4 and 10.6, respectively. Thus, full load operation increases the vibration level of the laboratory generator during healthy condition.

On the other hand, vibration during faulty operation is not considerably affected by the load. The excited harmonics in both domains are more or less equally large during full load as during no load which results in only minor differences in the vibration spectra. For instance, the rotor-frequency vibration during full load was less than 5% higher than during no load under the most severe scenario of both fault types. Conclusively, the loading specifications investigated in this thesis does not have a considerable impact on vibration during SE or ITSC in the rotor winding.

A few considerations should be discussed related to the observations found from the load simulations. First, only one loading case has been investigated due to the large amount of computational time and resources needed for the simulations in general. This means that the results may differ with a larger or small load, or if the power factor is more inductive, capacitive or purely resistive. It was found in [55] from FEA verified by experimental measurements how the vibration level of a healthy low-speed round-rotor permanent-magnet machine with concentrated windings changed when the load varied between highly induc-

tive, highly capacitive and purely resistive. The very same conclusions does not necessarily apply to hydropower generators due to the different designs, however, it is reasonable to expect from these findings that the vibration level of salient-pole synchronous generators can differ when the power factor is changed.

Second, the external load circuit used for simulations in this thesis was passive, which means that it did not contain any voltage sources, according to the available setup in the laboratory. Most hydropower generators are connected to the main grid where unnatural variations in the line voltages can occur. Such variations affect the armature currents with additional harmonics which again affect the stator MMF and induce additional time harmonics in the air-gap magnetic field. This can change the harmonic content of the radial force density and, finally, influence the vibration of the generator. In short, the absence of possible voltage variations from the main grid may cause the effects of loading found in this thesis to differ from real hydropower generators.

6.3.3.3 Other fault scenarios

The static and dynamic UMP caused by SE and ITSC fault, respectively, have different effects on the force density distributions and the excited harmonics in the two domains. During ITSC in the rotor winding, every subharmonic in both domains are affected which results in a tremendous increase in rotor-frequency vibration. On the contrary, SE mainly excites the first of the low order spatial harmonics and none of the subharmonics in the time domain. In return, the amplitude of the first-order spatial harmonic is over twice as large as during ITSC fault, and the resulting vibration is significant at rotor frequency.

The different consequences of static and dynamic UMP make it natural to consider combining them. The fact that some degree of static eccentricity is hard to avoid in a new hydropower generator due to the large dimensions and practical circumstances combined with the fact that ITSC is one of the most common faults in synchronous generators, enables the possibility for them to exist simultaneously. Thus, it would be interesting to investigate the consequences of the two faults together. A superposition between the two vibration spectra, which means that they are added together, would not be dramatically different from the one obtained during ITSC fault since its vibration level at rotor frequency is relatively much higher than during SE. However, the faults might have an intensifying effect on each other, such that the consequences are beyond a simple summation, which is possible considering the $1/m^4$ term. This has not been explored in this thesis but would be of interest if further work is to be conducted.

Since a generator with SE may develop DE as a symptom of the static UMP over time, it would also be of interest to explore the effects of ME, or simply DE, on vibration. Similar to ITSC in the rotor winding, DE induces dynamic UMP in the generator. However, DE has been found to impact the harmonic content of the radial flux density somewhat differently than ITSC on the rotor, which implies that the vibration behavior may also be different [80]. During ME, both the geometrical center and the rotational center of the rotor is displaced from the stator center, which could cause a similar effect as combining

SE with ITSC fault since static and dynamic UMP is merged. This is, however, uncertain and could be relevant to investigate if continuing work is to be performed. DE and ME have not been a part of this thesis since one of its objectives originally was to verify the simulations through experimental measurement, and DE is not possible to apply to the laboratory generator.

6.3.4 Fault detection

The numerous advantages of using vibration signals for fault detection are the reason for its prevalence in the field of condition monitoring. For instance, stator vibration is a symptom of most electrical and mechanical faults in the rotor and the stator due to their impact on the air-gap magnetic field, making it a broadly applicable fault detection method. Moreover, accelerometers can be placed easily accessible on non-invasive places on the generator and the measurements can be obtained online without the need for generator shut down or operation adjustments.

The vibration spectra presented in chapter 5 are the basis for the formulation of fault detection classifiers in this section. The spectra have been acquired from Mechanical with the results from Maxwell used as input. This means that simulations in Maxwell must have been performed in order to be able to examine vibration, while the analyses of flux density, force density, and total forces in themselves have in fact not been necessary to obtain the deformation results. However, it has been of great interest to explore how the vibration origin from the air-gap magnetic field and the analyses have indeed been indispensable in order to explain and discuss the vibration characteristics during the various operating conditions. They have also been essential in order to relate the vibration to theory and important for validation of the simulation results.

Displacement, referred to in this thesis as deformation, has been used for expressing vibration since it can be less complicated to describe theoretically than velocity or acceleration. It is also easily derived from the acceleration measured during condition monitoring through integration features commonly available in the accelerometers or their provided analysis software.

An important difference between real vibration measurements and simulations is the hardly avoidable measurement noise and other disturbances that cause deviations between theory and practice. High-quality, modern, shear-type piezoelectric accelerometers have a high signal-to-noise ratio, however, some deviation between the presented spectra and vibration signals obtained during condition monitoring should be expected. This means that the effects of faults might not be as distinctive in reality as in the FEA.

Table 6.1 summarizes how the vibration changes from healthy condition during the investigated fault scenarios at no load operation. The six lowest frequencies, generalized to multiples of the rotor frequency f_r, are included together with two of the frequencies where vibration naturally occurs, generalized to the synchronous frequency f_s. These eight frequencies are employed as they were evaluated to be the most relevant for fault

detection based on the vibration frequency spectra. The vibration during fault is expressed as multiples of the level during healthy condition. Figure 6.1 depicts the data in table 6.1 with logarithmically scaled y-axis for practical presentations. Vibration at healthy condition with relative value 1 equals zero decibels and values between 0 and 1 are converted to negative decibels.

Table 6.1: Vibration at certain frequencies caused by faults relative to healthy condition during no load operation. f_r denotes the rotor frequency and f_s the synchronous frequency.

	Healthy	ITSC in the rotor winding					SE		
Frequency		2.86%	5.71%	8.57%	20.0%	28.6%	10%	20%	30%
f_r (7.14 Hz)	1	6513.7	13255.0	20277.5	51307.3	80225.6	58.1	87.4	131.3
$2f_r$ (14.2 Hz)	1	24.7	51.0	78.8	194.5	311.2	7.6	19.6	50.6
$3f_r$ (21.4 Hz)	1	17.7	29.2	44.2	100.9	204.9	3.8	13.0	44.2
$4f_r$ (28.6 Hz)	1	3.6	7.1	10.5	32.0	53.9	3.2	9.5	27.7
$5f_r$ (35.7 Hz)	1	6.1	11.8	18.6	73.5	82.9	1.5	5.7	21.0
$6f_r$ (42.9 Hz)	1	1.7	2.3	3.1	10.4	11.1	1.6	4.6	12.9
$2f_s$ (100 Hz)	1	3.5	3.8	3.8	4.7	5.2	1.0	1.1	1.1
$4f_s$ (200 Hz)	1	0.6	0.6	0.9	0.9	0.9	1.1	1.2	1.9

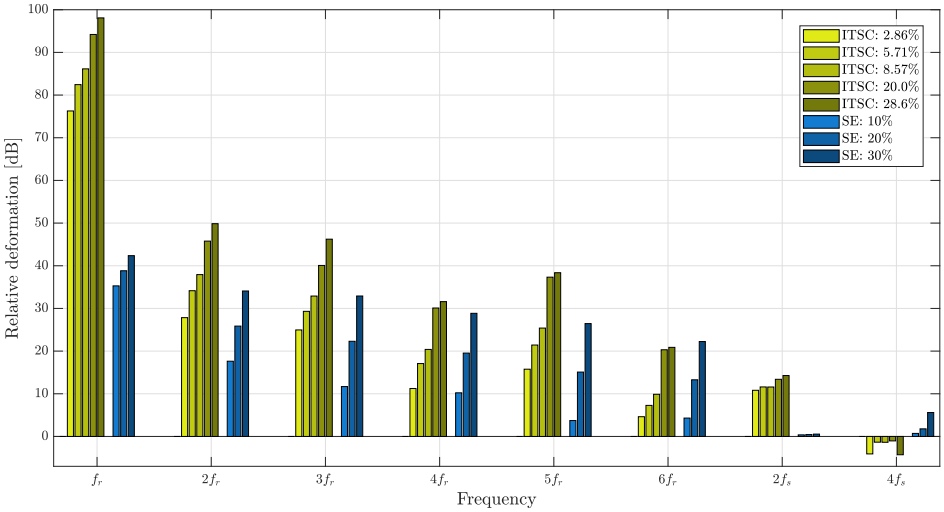

Figure 6.1: Logarithmic comparison of deformation at certain frequencies caused by faults during no load operation.

The table and the figure show how strongly vibration at f_r is affected by ITSC in the rotor winding during no load operation. Even 2.86% fault severity causes a dramatic relative increase in deformation. Conclusively, elevation of rotor-frequency vibration can be used to detect this fault without loading. Increased vibration at frequencies up to six times f_r, as well as three to five times higher vibration at $2f_s$, can be used as an additional index to diagnose the generator as faulty.

The table and the figure also show how SE increases vibration at f_r during no load operation. 10% fault severity causes almost 60 times higher vibration which can be considered sufficiently distinctive and easily distinguishable from a healthy vibration level during condition monitoring. In conclusion, amplified rotor-frequency vibration can be used for detection of SE without loading. Elevated vibration at frequencies up to six times f_r can also be used to confirm the fault with high severities.

Similar formulations can be made for full load operation. However, as presented in from table 6.2 and figure 6.2, the vibration at $2f_s$ and $4f_s$ have some differences compared to no load condition. Especially the latter frequency, which is increased around ten times for both faults, must be treated differently if the generator is monitored in presence of a load. Loaded operation with ITSC fault causes in practice the same vibration at $2f_s$ as no load while SE produces two to three times higher vibration than in healthy state which may be too low to distinguish from healthy condition during real condition monitoring due to presence of measurement disturbances. It must be emphasized again that "full load" in this thesis corresponds to 65% of the rated value of the laboratory generator, such that the stated conclusions should only be applied to real hydropower generator loaded with 65% of rated value. 100% loading could result in a different vibration behavior, likely with the same trend as 65% but with increased differences compared to no load.

To sum up, the same vibration indicators as in no load operation at one to six times the rotor frequency can be used for detection of ITSC in the rotor winding and SE in salient-pole synchronous generators loaded with 65% of rated value. Moreover, amplified vibration at $2f_s$ and $4f_s$ characterizes the effects of ITSC fault while SE increases vibration at $4f_s$ in particular.

Table 6.2: Vibration at certain frequencies caused by faults relative to healthy condition during full load operation. f_r denotes the rotor frequency and f_s the synchronous frequency.

	Healthy	ITSC in the rotor winding					SE		
Frequency		2.86%	5.71%	8.57%	20.0%	28.6%	10%	20%	30%
f_r (7.14 Hz)	1	6373.8	13567.1	21242.2	55624.8	84157.6	61.1	91.8	136.1
$2f_r$ (14.2 Hz)	1	23.9	49.9	76.7	191.4	278.6	9.0	23.1	54.3
$3f_r$ (21.4 Hz)	1	14.7	31.1	57.3	151.7	204.6	3.1	10.4	33.1
$4f_r$ (28.6 Hz)	1	3.9	8.4	12.5	34.7	64.0	2.7	8.0	24.5
$5f_r$ (35.7 Hz)	1	1.7	5.7	7.7	16.8	17.0	1.5	4.2	12.1
$6f_r$ (42.9 Hz)	1	1.1	2.0	3.5	9.5	20.2	1.5	4.2	12.1
$2f_s$ (100 Hz)	1	3.9	4.0	4.2	4.3	4.8	2.4	2.5	2.5
$4f_s$ (200 Hz)	1	8.8	8.9	8.9	8.9	9.3	10.6	10.8	11.0

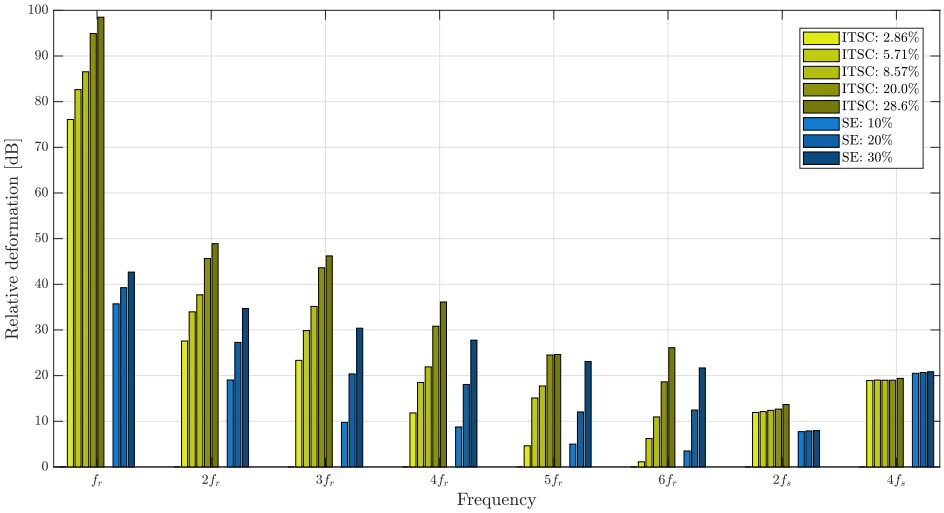

Figure 6.2: Logarithmic comparison of deformation at certain frequencies caused by faults during full load operation.

A fault-specific diagnose of a generator is beneficial for an operator as the actions required for clearance are likely to differ from fault type to fault type. However, the indicators for detection of ITSC in the rotor winding and SE formulated above have clear similarities. That is, they both heavily rely on amplified vibration at rotor frequency. On the other hand, there are some important differences that distinguish the two fault types from each other.

First, vibration at f_r is in a different league when the generator suffers from ITSC in the rotor compared to when SE is present. For instance, 2.86% and 28.6% shorted turns causes about 50 and 600 times higher vibration than 30% SE, respectively. This means that even ITSC fault with low severity is distinguishable from a high degree of SE through examination of the rotor-frequency vibration. Second, as easily seen in the figures above, SE excites vibration at the six lowest multiples of rotor frequency more evenly than ITSC. That is, the relative difference between vibration at f_r and $2f_r$ is much higher for ITSC than SE, and ITSC has some inconsistency in the reduction of vibration when the frequency increases compared to SE. These two features apply for both no load and loaded operation and can be applied for determination of the fault type. Moreover, if vibration measurements are performed during no load operation, elevated 100 Hz vibration can also be used to diagnose the generator as affected by ITSC in the rotor in contrast to SE.

In general, fault detection typically involves comparison between a certain signal from healthy state to the same type of signal acquired when the generator is suspected to be faulty. This procedure is also fundamental for the fault detecting methods presented in this section. However, a signal from healthy condition is not necessarily available. The robust construction and long lifetime cause many generators to be several decades old and

vibration measurements might not have been performed when generation was initiated for the first time. There can also be incidents where a completely new generator is suspected to be faulty due to manufacturing errors, installation troubles, or inaccurate assembling of generator parts.

The vibration spectrum during healthy operation shows that the vibration level at f_r and the other subharmonic frequencies are in the same range as the level of some of the frequencies between 107.14 Hz and 192.9 Hz. Moreover, in the spectra from the two faults presented in section 5.3.2 and 5.4.2, vibration between 107.14 Hz and 192.9 Hz is more or less unaffected by the faults. This means that if vibration measurements from healthy state are not available for comparison, the highest vibration between $2f_s$ and $4f_s$ during fault can be used as a reference value for the low-frequency vibration at healthy condition. This will be a rough estimation but can be sufficient for detection since the elevated vibrations caused by the faults are relatively very high.

6.3.4.1 Determination of fault severity

Knowledge about how seriously a generator is defected is important since it determines the urgency of reparation. An operator may be willing to continue generation with a machine that suffers from a low-severity fault if, for instance, the economical consequences of an overhaul exceed the benefit of clearing the fault. Moreover, if a fault of a high degree is detected, an instant production stoppage may be the only reasonable choice to avoid total generator failure.

Figure 6.3 illustrates the relationship between the fault severity and vibration level at rotor frequency from table 6.1. The top plot contains five data points from the simulated scenarios with ITSC fault and the bottom plot contains the three SE cases. The pink line in each plot represents the best fitted first-degree polynomial function which is expressed in the legend box with respect to both y and x. In other words, the y-equation in top of the box describes the deformation as a function of the fault severity, while the x-equation expresses the fault severity as a function of deformation. For instance, if a generator is diagnosed with SE and produces a vibration at rotor frequency which is 120 times higher than during healthy condition, the fault degree can be estimated as $x = 0.27 \cdot 120 - 5.68 = 27$ percent.

The best-fitted polynomial is based on regression and provides an approximation rather than an exactly correct answer. For instance, the expressions are unreliable for small fault severities as the lines do not go through the origins. However, establishment of the exact fault degree is rarely necessary as long as the expressions provide good indications. In fact, the relationship between the data points in each plot is not far from linear as the pink lines are close to every point. Conclusively, apart from for faults of small degree, equation 6.1 and 6.2 can be used as good estimators for fault severity during ITSC in the rotor and SE, respectively. S is the severity of fault while RD_{f_r} represents the deformation at rotor frequency relative to healthy condition. The same trends and relationships were found for the full load scenarios since loading has been found to affect the deformation at rotor frequency to a small degree.

$$S_{ITSC} = 0.00033 \cdot RD_{f_r} + 1.2 \tag{6.1}$$

$$S_{SE} = 0.27 \cdot RD_{f_r} - 5.68 \tag{6.2}$$

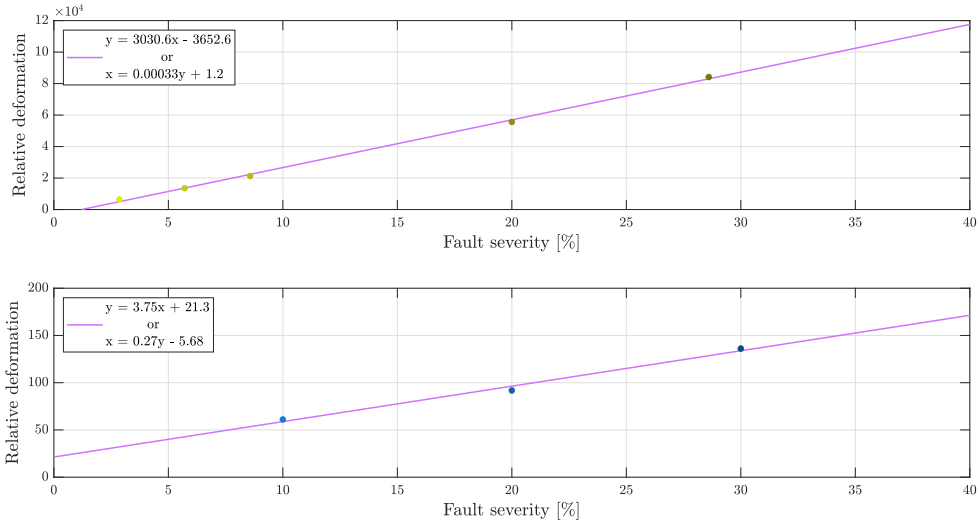

Figure 6.3: Relationship between fault severity and vibration at rotor frequency relative to healthy condition at no load operation. Top: Inter-turn short circuit in the rotor winding. Bottom: Static eccentricity.

6.4 Further work

This section presents a suggestion of work that has been found interesting during the master's thesis but for various reasons not been performed.

First and foremost, performing real vibration measurements on the laboratory generator has been inaccessible during this thesis and should be conducted for comparison to the simulation results. They should be executed for all the scenarios that have been investigated through FEA in this thesis, that is no load and loaded operation of healthy condition, with one, two, three, seven and ten ITSC in one of the rotor poles, and with 10%, 20% and 30% SE. The load specifications should be the maximum load that was available during this thesis, that is 65 kVA with a power factor of 0.93 achieved by connecting a 2.78 Ω resistance in parallel to an inductance of 8 mH.

The measurements should be executed in steady-state operation a while after generator startup, such that the temperature of the iron and copper is constant. This ensures consistency between the measurements since the temperature of these materials, which is expected to increase during some time after initiation, can affect the magnetic field in the air-gap and, thus, the vibration of the stator. Moreover, since the housing of the laboratory generator is open, accelerometers should be attached directly to the outside of the stator yoke. Multiple transducers, that is minimum two, should be symmetrically distributed around the circumference of the stator for adequate data collection and the piezoelectric shear-type accelerometer should be used for reliable results.

The laboratory generator is supported by rigid bars that may influence the vibration of the stator. These have not been a part of the model used for vibration simulations in this thesis but should be included to ensure as realistic results as possible. To do so, inspection of the generator is necessary such that the simulation model can be defined with the correct support assignment. Consequently, new vibration simulations must be performed.

To extend the work of this thesis, new fault scenarios can be investigated. For instance, it would be interesting to study the effects of ITSC in the rotor and SE being present simultaneously or the impact of ITSC fault in two rotor poles. Both these two scenarios can be applied to the laboratory generator and FEA should be conducted for comparison to vibration measurements. The analytical model should, after necessary modification, be evaluated for these scenarios as well. Moreover, damper winding faults are also possible to impose on the laboratory generator and can be a part of further work. However, this would require a different setup of simulations and laboratory measurements since the damper winding is expected to be inactive during steady-state condition. Furthermore, different fault types, such as DE, should be considered to be examined despite the lack of possibility for practical verification in the laboratory. Finally, regarding further work on the laboratory generator, new loading cases could be analyzed to see the effects of load variations and different power factors on the vibration.

In addition to experimental work in the NTNU laboratory, vibration measurements on real hydropower generators should be considered. Various loading cases should be studied

and extra focus can be dedicated to the effects of grid connection, which is not possible to study in the laboratory generator. For the topology of the generators, two options are possible: a GCD between the number of poles and slots equal to two or different from two. The former should be investigated to see the correspondence of the vibration behavior of real hydropower generators to the presented FEA and results from laboratory measurements, such that the findings can be evaluated based on their objective of being used in real applications. The latter option is also interesting as it will reveal the effect of the lowest spatial harmonic order. Two cases are also available regarding the health of the hydropower generators: known condition or unknown condition. If the health of the generators is known, vibration measurements will serve as comparisons to FEA and laboratory work. If the health condition is unknown, the fault detection methods presented in this thesis can be used to diagnose the machine. Ideally, the generator will be inspected afterwards such that its condition is revealed and the methods are verified or disproved. Both cases are of interest and should be considered for further work. For all examinations of real hydropower generators, FEA should be conducted to form a theoretical basis and the analytical model could be employed for predictions.

Analyses of how the harmonic content of the time domain and the spatial domain affect the vibration of a generator has been an important part of this thesis. However, a way to determine the exact relationship between the time harmonic order and the spatial harmonic order of a force has not been found. This could lead to easier analyses and reduce the work required to decide the cause of vibration at certain frequencies. Thus, designation of further work to find such a way is suggested.

Chapter 7

Conclusion

Through analytical modeling of air-gap forces and FE simulation, this master's thesis has investigated whether and how vibration signals can be used for fault detection in salient-pole synchronous generators with ITSC in the field winding or SE. It has been found that both faults can be detected by comparing the vibration at one to six times the rotor frequency and two to four times the synchronous frequency during faulty operation to the vibration at the same frequencies during healthy condition. A method to estimate the vibration level in healthy state from measurements on a faulty generator has been formulated from the minor effect the faults have on the vibration in-between two and four times the synchronous frequency. Moreover, despite that detection of both ITSC and SE relies on the same frequencies, the correct type of fault can be determined by a proposed method of evaluating the vibration severity compared to healthy condition. Furthermore, based on the nearly linear relationship between the rotor frequency vibration under several fault degrees, analytical equations for determination of the fault severity have been deduced for both ITSC in the rotor and SE.

FEA of the air-gap flux density and radial force density revealed that ITSC in the rotor winding excites unnatural harmonics in the time domain and the spatial domain which causes a dramatic elevation in low-frequency vibration compared to healthy condition, specifically by over 80000 times at rotor frequency during 28.6% fault degree. On the other hand, SE mostly affects the spatial domain only which leads to a less dramatic amplification in rotor frequency vibration, in specific by a factor of around 130 compared to healthy condition. Thus, ITSC fault is more dangerous for a generator than SE in terms of the vibration they cause.

The FEA also showed that the lowest-order spatial harmonic is the reason for the dominating vibration. During both faults, this is the first order while it is the second order in healthy condition. It was found that the lowest-order spatial harmonic is caused by the flux density slot harmonics at healthy operation and during SE such that the vibration level can be reduced by utilizing magnetic wedges or semi-closed slots.

It has been found that loading does not impact the dominating vibration of a generator with ITSC in the rotor or SE to a noteworthy degree, which means that fault detection through vibration monitoring can be achieved regardless of the load. However, the natural vibration level in healthy condition is about doubled when the load is increased from no load to 65% of rated value.

How the tangential component of the magnetic field influences the radial force density, and thereby the vibration of the generator, was investigated and found to be inconsiderable compared to the radial component. Moreover, a sensitivity analysis on where the total force which is used for FE vibration simulations should be obtained in the air-gap was conducted. It showed that calculations performed at the edge of the stator tooth cause relatively large errors and that the computation should be moved further into the air-gap for reliable acquirement of the total force.

The novel analytical model formulates unnatural time harmonics and spatial harmonics to appear at every order as a result of ITSC fault, which is consistent with the simulations. There is also good agreement between the time domain predictions and FEA for SE, however, the model produces some deviations in the spatial domain during this fault. Despite these, the model formulates the lowest-order spatial harmonic correctly and can, therefore, provide accurate expectations about the vibration behavior during the two faulty conditions when deformation theory is taken into account.

In conclusion, this thesis shows that vibration signals can, in theory, be used for detection and severity determination of ITSC in the rotor winding and SE in salient-pole synchronous generators. The results are applicable to hydropower generators and can be an important part of ensuring profitable and stable power production. The main recommendation for further work is to perform experimental vibration measurements on the laboratory generator, as well as on real hydropower generators, in order to study the validity of the findings in practice.

Bibliography

[1] Statistics Norway (2019). *Elektrisitet*. Accessed 06.04.20 at https://www.ssb.no/energi-og-industri/statistikker/elektrisitet/aar.

[2] International Hydropower Association (2019). *Fast facts about hydropower*. Accessed 06.04.20 at https://www.hydropower.org/facts.

[3] G. Neidhofer. The evolution of the synchronous machine. *Engineering Science and Education Journal*, 1(5):239–248, 1992.

[4] Nagrath I.J. Kothari, D.P. *Electric Machines*. McGraw Hill, 2010.

[5] T. Wildi. *Electric Machines, Drives and Power Systems*. 6th edition. Ohio: Pearson Education, 2006.

[6] P.J. Tavner *et al. Condition monitoring of rotating electrical machines*. United Kingdom: The Institution of Engineering and Technology, 2008.

[7] G.L. Rødal. *Online Condition Monitoring of synchronous generators using vibration signals*. 2019, NTNU, unpublished: Trondheim.

[8] Department of Information Security and Communication Technology (02.12.2020). Reusing text from the project in your master thesis. Accessed 04.26.20 at https://innsida.ntnu.no/wiki/-/wiki/English/Reuse+of+text.

[9] M. F. b. Abdullah, Z. Baharudin, and N. H. b. Hamid. The third harmonic model for salient pole synchronous generator under balanced load. *IEEE Transactions on Energy Conversion*, 29(2):519–526, June 2014.

[10] G. Angst and J. L. Oldenkamp. Third-harmonic voltage generation in salient-pole synchronous machines [includes discussion]. *Transactions of the American Institute of Electrical Engineers. Part III: Power Apparatus and Systems*, 75(3):434–441, Jan 1956.

[11] S. Nandi and H. A. Toliyat. Condition monitoring and fault diagnosis of electrical machines - a review. In *Conference Record of the 1999 IEEE Industry Applications Conference. Thirty-Forth IAS Annual Meeting (Cat. No.99CH36370)*, volume 1, pages 197–204 vol.1, Oct 1999.

[12] I. Sadeghi, H. Ehya, J. Faiz, and H. Ostovar. Online fault diagnosis of large electrical machines using vibration signal - a review. In *2017 International Conference on Optimization of Electrical and Electronic Equipment (OPTIM) 2017 Intl Aegean Conference on Electrical Machines and Power Electronics (ACEMP)*, pages 470–475, May 2017.

[13] I. Sadeghi, H. Ehya, J. Faiz, and A. A. S. Akmal. Online condition monitoring of large synchronous generator under short circuit fault — a review. In *2018 IEEE International Conference on Industrial Technology (ICIT)*, pages 1843–1848, Feb 2018.

[14] IEEE. Guide for online monitoring of large synchronous generators (10 mva and above). *IEEE Std 1129-2014*, pages 1–62, April 2014.

[15] H.A. Toliyat *et al.* *Electric Machines: Modeling Condition monitoring and fault diagnosis*. CRC Press, 2013.

[16] J. R. Cameron, W. T. Thomson, and A. B. Dow. Vibration and current monitoring for detecting airgap eccentricity in large induction motors. *IEE Proceedings B - Electric Power Applications*, 133(3):155–163, May 1986.

[17] H. Ehya, I. Sadeghi, and J. Faiz. Online condition monitoring of large synchronous generator under eccentricity fault. In *2017 12th IEEE Conference on Industrial Electronics and Applications (ICIEA)*, pages 19–24, June 2017.

[18] B. M. Ebrahimi and J. Faiz. Magnetic field and vibration monitoring in permanent magnet synchronous motors under eccentricity fault. *IET Electric Power Applications*, 6(1):35–45, January 2012.

[19] VibroSystM (2006). *Mechanical Tolerance Guidelines for Hydroelectric Generators*. Accessed 06.04.20 at https://library.vibrosystm.com/en/Application_Notes/AN001-a.pdf.

[20] R.K Aggarwal. *Power System Protection, Vol. 1: Principles and Components*. London, United Kingdom: The Institution of Electrical Engineers, 1996.

[21] M. Walker. *The Diagnosing of Troubles in Electrical Machines*. Harlow, United Kingdom: Longmans Green and Co, 1921.

[22] D. G. Dorrell, W. T. Thomson, and S. Roach. Analysis of airgap flux, current, and vibration signals as a function of the combination of static and dynamic airgap eccentricity in 3-phase induction motors. *IEEE Transactions on Industry Applications*, 33(1):24–34, Jan 1997.

[23] D. de Canha, W. A. Cronje, A. S. Meyer, and S. J. Hoffe. Methods for diagnosing static eccentricity in a synchronous 2 pole generator. In *2007 IEEE Lausanne Power Tech*, pages 2162–2167, July 2007.

[24] B. M. Ebrahimi and J. Faiz. Magnetic field and vibration monitoring in permanent magnet synchronous motors under eccentricity fault. *IET Electric Power Applications*, 6(1):35–45, January 2012.

[25] I. Sadeghi, H. Ehya, and J. Faiz. Eccentricity fault indices in large induction motors an overview. In *2017 8th Power Electronics, Drive Systems Technologies Conference (PEDSTC)*, pages 329–334, Feb 2017.

[26] B. M. Ebrahimi, J. Faiz, and M. J. Roshtkhari. Static-, dynamic-, and mixed-eccentricity fault diagnoses in permanent-magnet synchronous motors. *IEEE Transactions on Industrial Electronics*, 56(11):4727–4739, Nov 2009.

[27] M. Cuevas, R. Romary, J. Lecointe, and T. Jacq. Non-invasive detection of rotor short-circuit fault in synchronous machines by analysis of stray magnetic field and frame vibrations. *IEEE Transactions on Magnetics*, 52(7):1–4, July 2016.

[28] S. Nadarajan, R. Wang, A. Kumar Gupta, and S. Kumar Panda. Vibration signature analysis of stator winding fault diagnosis in brushless synchronous generators. In *2015 IEEE International Transportation Electrification Conference (ITEC)*, pages 1–6, Aug 2015.

[29] S. Djurović, D. S. Vilchis-Rodriguez, and A. C. Smith. Investigation of wound rotor induction machine vibration signal under stator electrical fault conditions. *The Journal of Engineering*, 2014(5):248–258, 2014.

[30] M. Cuevas, R. Romary, J. Lecointe, F. Morganti, and T. Jacq. Noninvasive detection of winding short-circuit faults in salient pole synchronous machine with squirrel-cage damper. *IEEE Transactions on Industry Applications*, 54(6):5988–5997, Nov 2018.

[31] I. Sadeghi, H. Ehya, J. Faiz, and A. A. S. Akmal. Online condition monitoring of large synchronous generator under short circuit fault — a review. In *2018 IEEE International Conference on Industrial Technology (ICIT)*, pages 1843–1848, Feb 2018.

[32] H.Z. MA. Fault diagnosis based on ann for turn-to-turn short circuit of synchronous generator rotor windings. *Journal of Electromagnetic Analysis and Applications*, 1(3):187–191, Jan 209.

[33] Y. Gritli, A. O. Di Tommaso, R. Miceli, F. Filippetti, and C. Rossi. Vibration signature analysis for rotor broken bar diagnosis in double cage induction motor drives. In *4th International Conference on Power Engineering, Energy and Electrical Drives*, pages 1814–1820, May 2013.

[34] Y. Gritli, A. O. Di Tommaso, R. Miceli, C. Rossi, and F. Filippetti. Quantitative rotor broken bar evaluation in double squirrel cage induction machines under dynamic operating conditions. In *2013 Eighth International Conference and Exhibition on Ecological Vehicles and Renewable Energies (EVER)*, pages 1–6, March 2013.

[35] A. O. Di Tommaso, R. Miceli, and G. R. Galluzzo. Monitoring and diagnosis of failures in squirrel-cage induction motors due to cracked or broken bars. In *8th IEEE Symposium on Diagnostics for Electrical Machines, Power Electronics Drives*, pages 39–44, Sep. 2011.

[36] C. Concari, G. Franceschini, and C. Tassoni. Differential diagnosis based on multivariable monitoring to assess induction machine rotor conditions. *IEEE Transactions on Industrial Electronics*, 55(12):4156–4166, Dec 2008.

[37] J. d. J. Rangel-Magdaleno, R. d. J. Romero-Troncoso, R. A. Osornio-Rios, E. Cabal-Yepez, and L. M. Contreras-Medina. Novel methodology for online half-broken-bar detection on induction motors. *IEEE Transactions on Instrumentation and Measurement*, 58(5):1690–1698, May 2009.

[38] K. Agoston. Fault detection of the electrical motors based on vibration analysis. In *8th International Conference Interdisciplinary in Engineering*, pages 547–553, Dec. 2015.

[39] J. Martinez, A. Belahcen, and A. Muetze. Analysis of the vibration magnitude of an induction motor with different numbers of broken bars. *IEEE Transactions on Industry Applications*, 53(3):2711–2720, May 2017.

[40] S. S. Patil and J. A. Gaikwad. Vibration analysis of electrical rotating machines using fft: A method of predictive maintenance. In *2013 Fourth International Conference on Computing, Communications and Networking Technologies (ICCCNT)*, pages 1–6, July 2013.

[41] T. Plante, A. Nejadpak, and C. Xia Yang. Faults detection and failures prediction using vibration analysis. In *2015 IEEE AUTOTESTCON*, pages 227–231, Nov 2015.

[42] B. Marcin. Vibration diagnostic method of permanent magnets generators - detecting of vibrations caused by unbalance. In *2014 Ninth International Conference on Ecological Vehicles and Renewable Energies (EVER)*, pages 1–6, March 2014.

[43] W. Zhou, T. G. Habetler, and R. G. Harley. Bearing condition monitoring methods for electric machines: A general review. In *2007 IEEE International Symposium on Diagnostics for Electric Machines, Power Electronics and Drives*, pages 3–6, Sep. 2007.

[44] A. Shrivastava and S. Wadhwani. An approach for fault detection and diagnosis of rotating electrical machine using vibration signal analysis. In *International Conference on Recent Advances and Innovations in Engineering (ICRAIE-2014)*, pages 1–6, May 2014.

[45] T. C. A. Kumar, G. Singh, and V. N. A. Naikan. Effectiveness of vibration and current monitoring in detecting broken rotor bar and bearing faults in an induction motor. In *2016 IEEE 6th International Conference on Power Systems (ICPS)*, pages 1–5, March 2016.

[46] W. Zhou, T. G. Habetler, and R. G. Harley. Bearing condition monitoring methods for electric machines: A general review. In *2007 IEEE International Symposium on Diagnostics for Electric Machines, Power Electronics and Drives*, pages 3–6, Sep. 2007.

[47] P. J. Tavner. Review of condition monitoring of rotating electrical machines. *IET Electric Power Applications*, 2(4):215–247, July 2008.

[48] I. Sadeghi, H. Ehya, R. N. Zarandi, J. Faiz, and A. A. S. Akmal. Condition monitoring of large electrical machine under partial discharge fault - a review. In *2018 International Symposium on Power Electronics, Electrical Drives, Automation and Motion (SPEEDAM)*, pages 216–223, June 2018.

[49] J.F. Gieras, C. Wang, and J.C.Lai. *Noise of polyphase electric motors*. CRC Press, 2006.

[50] B. Cassoret, J.P. Lecointe, and J.F. Brudny. *Chapter 9 of Power electronics and motor drives, 2nd edition*. CRC Press, 2011.

[51] G. Traxler-Samek, T. Lugand, and M. Uemori. Vibrational forces in salient pole synchronous machines considering tooth ripple effects. *IEEE Transactions on Industrial Electronics*, 59(5):2258–2266, May 2012.

[52] Z. Q. Zhu, Z. P. Xia, L. J. Wu, and G. W. Jewell. Analytical modelling and finite element computation of radial vibration force in fractional-slot permanent magnet brushless machines. In *2009 IEEE International Electric Machines and Drives Conference*, pages 144–151, May 2009.

[53] E. L. Engevik, M. Valavi, and A. Nysveen. Influence of winding layout and airgap length on radial forces in large synchronous hydrogenerators. In *2017 20th International Conference on Electrical Machines and Systems (ICEMS)*, pages 1–6, 2017.

[54] M. Valavi, A. Nysveen, R. Nilssen, and T. Rølvåg. Slot harmonic effect on magnetic forces and vibration in low-speed permanent-magnet machine with concentrated windings. *IEEE Transactions on Industry Applications*, 50(5):3304–3313, Sep. 2014.

[55] M. Valavi, A. Nysveen, and R. Nilssen. Effects of loading and slot harmonic on radial magnetic forces in low-speed permanent magnet machine with concentrated windings. *IEEE Transactions on Magnetics*, 51(6):1–10, June 2015.

[56] E. Devillers, M. Hecquet, X. Cimetiere, J. Lecointe, J. L. Besnerais, and T. Lubin. Experimental benchmark for magnetic noise and vibrations analysis in electrical machines. In *2018 XIII International Conference on Electrical Machines (ICEM)*, pages 745–751, 2018.

[57] M. Valavi, A. Nysveen, R. Nilssen, R. D. Lorenz, and T. Rølvåg. Influence of pole and slot combinations on magnetic forces and vibration in low-speed pm wind generators. *IEEE Transactions on Magnetics*, 50(5):1–11, 2014.

[58] I. Jang and W. Kim. Study on electromagnetic vibration analysis process for pm motors. *IEEE Transactions on Applied Superconductivity*, 30(4):1–6, 2020.

[59] I. Jang, S. Ham, W. Kim, C. Jin, S. Cho, K. Lee, J. Lee, D. Kang, and J. Lee. Method for analyzing vibrations due to electromagnetic force in electric motors. *IEEE Transactions on Magnetics*, 50(2):297–300, 2014.

[60] S. P. Verma and A. Balan. Determination of radial-forces in relation to noise and vibration problems of squirrel-cage induction motors. *IEEE Transactions on Energy Conversion*, 9(2):404–412, 1994.

[61] D. Guo, F. Chu, and D. Chen. The unbalanced magnetic pull and its effects on vibration in a three-phase generator with eccentric rotor. In *Journal of Sound and Vibration 254(2)*, pages 297–312, 2002.

[62] Y. Lu, J. Li, R. Qu, D. Ye, H. Lu, J. Sun, M. Ge, and H. Xu. Electromagnetic force and vibration analysis of permanent-magnet-assisted synchronous reluctance machines. *IEEE Transactions on Industry Applications*, 54(5):4246–4256, 2018.

[63] Maple®. Release 2019, Waterloo Maple Inc.

[64] X. Tu, L. Dessaint, M. El Kahel, and A. O. Barry. A new model of synchronous machine internal faults based on winding distribution. *IEEE Transactions on Industrial Electronics*, 53(6):1818–1828, Dec 2006.

[65] I. Sadeghi, H. Ehya, and J. Faiz. Analytic method for eccentricity fault diagnosis in salient-pole synchronous generators. In *2017 International Conference on Optimization of Electrical and Electronic Equipment (OPTIM) 2017 Intl Aegean Conference on Electrical Machines and Power Electronics (ACEMP)*, pages 261–267, May 2017.

[66] C. Bruzzese and G. Joksimovic. Harmonic signatures of static eccentricities in the stator voltages and in the rotor current of no-load salient-pole synchronous generators. *IEEE Transactions on Industrial Electronics*, 58(5):1606–1624, May 2011.

[67] A. Tessarolo and M. Olivo. A new method for the analytical determination of the complex relative permeance function in linear electric machines with slotted air gap. In *2016 International Symposium on Power Electronics, Electrical Drives, Automation and Motion (SPEEDAM)*, pages 1330–1335, June 2016.

[68] M. Babaei, J. Faiz, B. M. Ebrahimi, S. Amini, and J. Nazarzadeh. A detailed analytical model of a salient-pole synchronous generator under dynamic eccentricity fault. *IEEE Transactions on Magnetics*, 47(4):764–771, April 2011.

[69] J. C. Moreira and T. A. Lipo. Modeling of saturated ac machines including air gap flux harmonic components. *IEEE Transactions on Industry Applications*, 28(2):343–349, March 1992.

[70] S. Nandi. A detailed model of induction machines with saturation extendable for fault analysis. *IEEE Transactions on Industry Applications*, 40(5):1302–1309, Sep. 2004.

[71] A. Ghoggal, S. E. Zouzou, M. Sahraoui, H. Derghal, and A. Hadri-Hamida. A winding function-based model of air-gap eccentricity in saturated induction motors. In *2012 XXth International Conference on Electrical Machines*, pages 2739–2745, Sep. 2012.

[72] ANSYS® Maxwell®. Release 2019 R3.7, ANSYS, Inc.

[73] ANSYS® Mechanical®. Release 2019 R3.7, ANSYS, Inc.

[74] M. Valavi (ANSYS® Support). Personal communication, 02.19.2020.

[75] Z. Q. Zhu, Z. P. Xia, L. J. Wu, and G. W. Jewell. Analytical modeling and finite-element computation of radial vibration force in fractional-slot permanent-magnet brushless machines. *IEEE Transactions on Industry Applications*, 46(5):1908–1918, Sep. 2010.

[76] MATLAB®. Release R2019b, The MathWorks, Inc.

[77] ANSYS®. NVH Good Practices, 2019. *Relationship between Maxwell solving time, number of repeated sample windows and mechanical frequency range*.

[78] ANSYS® Workbench ®. Release 2019 R3, ANSYS, Inc.

[79] ANSYS® (2020). *About ANSYS*. Accessed 06.04.20 at https://www.ansys.com/about-ansys.

[80] I. L Groth. On-line magnetic flux monitoring and incipient fault detection in hydropower generators. *Master's thesis*, Dept. of Electric Power Engineering, NTNU, Trondheim, 2019.

[81] S. P. Verma and R. S. Girgis. Considerations in the choice of main dimensions of stators of electrical machines in relation to their vibration characteristics. *IEEE Transactions on Power Apparatus and Systems*, 94(6):2151–2159, 1975.

[82] R. K. Singal, K. Williams, and S.P.Verma. The effect of windings, frame and impregnation upon the resonant frequencies and vibrational behavior of an electrical machine stator. *Experimental Mechanics*, 30:270–280, 1990.

[83] R. S. Girgis and S. P. Verma. Resonant frequencies and vibration behaviour of stators of electrical machines as affected by teeth, windings, frame and laminations. *IEEE Transactions on Power Apparatus and Systems*, PAS-98(4):1446–1455, 1979.

[84] M. Valavi, K. G. Jørstad, and A. Nysveen. Electromagnetic analysis and electrical signature-based detection of rotor inter-turn faults in salient-pole synchronous machine. *IEEE Transactions on Magnetics*, 54(9):1–9, Sep. 2018.

[85] B. Hannon, P. Sergeant, and L. Dupré. Time- and spatial-harmonic content in synchronous electrical machines. *IEEE Transactions on Magnetics*, 53(3):1–11, 2017.

[86] B. Hannon, P. Sergeant, and L. Dupré. Time- and spatial-harmonic content in electrical machines and its application in fourier-based models. In *2016 XXII International Conference on Electrical Machines (ICEM)*, pages 592–598, 2016.

[87] L.D. Patricio, M. Hecquet, F. Gillon, and J. LeBesnerais. Analysis of radial force harmonics in pmsm responsible for electromagnetic noise. In *2015 Tenth International Conference on Ecological Vehicles and Renewable Energies (EVER)*, 2015.

[88] J. Faiz, I. Ardekani, and E. Sharifi. A precise electromagnetic modeling and performance analysis of a three-phase squirrel-cage induction motor under mixed eccentricity condition. In *Electromagnetics, vol.25, numb. 6*, pages 471–489, 2012.

[89] Li Yonggang, Li Heming, Zhao Hua, and Wan Shuting. Fault identification method of rotor inter turn short-circuit using stator winding detection. In *Sixth International Conference on Electrical Machines and Systems, 2003. ICEMS 2003.*, volume 2, pages 856–860 vol.2, Nov 2003.

[90] J. Pyrönen, T. Jokinen, and V. Hrabavcová. *Design of Rotating Electrical Machines*. John Wiley & Sons, Ltd, 2008.

Appendix

A Analytical modeling of eccentricity

This section contains the deduction of how DE and SE is included in equation 2.2.6.1 in the analytical model with the accompanying degree of eccentricity, δ_{ec} in equation 2.19, and eccentricity angle, ϕ in equation 2.20. The given formulations are based on reference [88] and exemplified with a round rotor generator for simplicity. The deduction is still valid for salient-pole generators as it is independent on rotor geometry and the rotor saliency is included separately in the analytical model in equation 2.11.

Figure 7.1 illustrates the position and rotation pattern of the rotor during healthy operation (a), SE (b) and DE (c). g_0 denotes the air-gap length during healthy operation, which in this illustration is constant around the air-gap while variable in a rotor with salient poles. The various points C represents the center point of the stator, rotor, and rotor rotation denoted with subscripts s, r and ω, respectively. The subscripts are combined when multiple points coincide. From this figure, the degree of eccentricity during SE, δ_{se}, is defined as the distance between the stator center and the rotor center as follows

$$\delta_{se} = \frac{||\overrightarrow{C_s C_{r,\omega}}||}{g_0}. \tag{7.1}$$

For the DE condition shown in figure 7.1 (c), the eccentricity degree is defined as the distance between the center of rotation and the geometrical center of the rotor as follows

$$\delta_{de} = \frac{||\overrightarrow{C_{s,\omega} C_r}||}{g_0}. \tag{7.2}$$

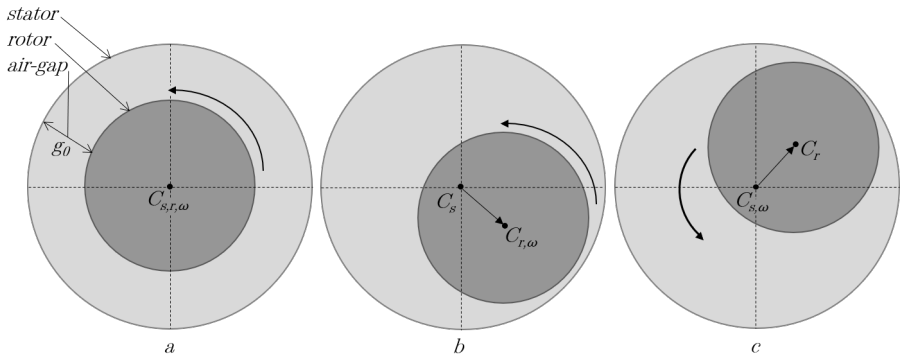

Figure 7.1: Rotor conditions during healthy operation (a), static eccentricity (b) and dynamic eccentricity (c).

Static eccentricity

An arbitrary point, P, is defined on the rotor circumference as shown in figure 7.2. The distance C_sC_r is substituted according to equation 7.1 and ϕ represents an arbitrary angle around the stator frame, here chosen to start from the horizontal axis for convenient illustration. R_r is the rotor radius and the eccentricity angle ψ is defined as $\angle C_rC_sP$.

The distance C_sP can be expressed as

$$||\overrightarrow{C_sP}||= g_0\delta_{se}cos(\psi) + \sqrt{R_r^2 - g_0^2\delta_{se}^2 sin^2(\psi)}. \tag{7.3}$$

In hydropower generators, the air-gap length g_0 is much smaller than the rotor radius R_r such that equation 7.3 can be simplified to

$$\begin{aligned}\sqrt{R_r^2 - g_0^2\delta_{se}^2 sin^2(\psi)} \approx \sqrt{R_r^2} = R_r,\\ ||\overrightarrow{C_sP}||\approx g_0\delta_{se}cos(\psi) + R_r.\end{aligned} \tag{7.4}$$

If the inner radius of the stator is R_s, the radial air-gap length at point P can be written as

$$\begin{aligned}g_{ec}(\psi) = R_s - ||\overrightarrow{C_sP}||= R_s - g_0\delta_{se}cos(\psi) - R_r =\\ g_0 - g_0\delta_{se}cos(\psi) = g_0(1 - \delta_{se}cos(\psi)).\end{aligned} \tag{7.5}$$

During SE, it can be seen from the figure that $\psi = \phi$, such that the air-gap length of a static eccentric generator is

$$g_{ec}(\phi) = g_0(1 - \delta_{se}cos(\phi)). \tag{7.6}$$

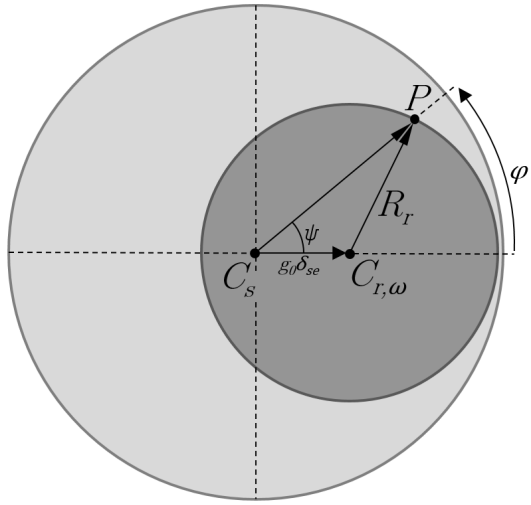

Figure 7.2: Generator with static eccentricity.

Dynamic eccentricity

The same procedure can be performed for a generator with DE. An arbitrary point, P, is defined at the rotor circumference and the distance from C_s to C_ω is substituted according to equation 7.2. The same reasoning as for SE leads to the expression for air-gap length during DE to be

$$g_{ec}(\psi) = g_0(1 - \delta_{de}cos(\psi)). \tag{7.7}$$

However, since the rotor position changes when the rotor spins during DE, ψ is a function of both position and time and can be expressed as

$$\psi = \psi(\phi, t) = \phi - \omega_r t, \tag{7.8}$$

where ω_r is the rotor speed. Thus, equation 7.7 becomes

$$\begin{aligned} g_{ec}(\phi, t) = g_0(1 - \delta_{de}cos(\phi - \omega_r t) = g_0(1 - \delta_{de}cos(\phi - \frac{\omega_s t}{p}) \\ = g_0(1 - \delta_{de}cos(\frac{\omega_s t}{p} - \phi). \end{aligned} \tag{7.9}$$

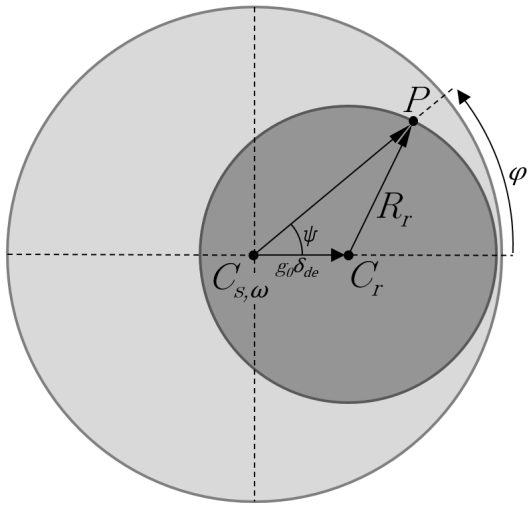

Figure 7.3: Generator with dynamic eccentricity

The analytical modeling of eccentricity is summarized as follows

$$g_{ec} = g_0(1 - \delta_{ec}cos(\psi)),$$

$$\delta_{ec} = \begin{cases} \delta_{se}, & \text{if SE} \\ \delta_{de}, & \text{if DE} \end{cases} \qquad \psi = \begin{cases} \phi, & \text{if SE} \\ \frac{\omega_s t}{p}, & \text{if DE} \end{cases}$$

B Analytical modeling of short circuit in rotor winding

When wires in the winding of a rotor pole are internally short circuited, the number of ampere-turns and the resulting MMF produced by this pole is reduced. Thus, while the MMF produced by a healthy rotor can be approximately expressed as a sinusoidal function, an ITSC distorts the periodicity and can be modeled as a superposition between the MMF in healthy operation and a fictitious demagnetizing component [89].

Figure 7.4 (a) illustrates a simplified representation of the MMF produced by a healthy six-pole salient rotor. The MMF distribution in the figure is spatial with respect to the rotor, denoted by ϕ_r, and can be approximately expressed as a sinusoidal function. The one rectangle below the x-axis in figure 7.4 (b) illustrates the fictitious demagnetizing component caused by the short circuit. Its amplitude, F_N depends on the number of shorted turns. To satisfy flux containment between the poles, demagnetizing of the faulty pole affects the other poles and the combined area of the rectangles above the x-axis equals the area of the demagnetizing component. Figure 7.4 (c) depicts the resultant rotor MMF when (a) and (b) are added. Red, broken lines represent reduction of the MMF while green, broken lines represent increased MMF. Mathematically, the distribution of the MMF in (c), $\mathcal{F}^r_{sc}$, can be written in terms of the healthy MMF distribution in (a), $\mathcal{F}_h$, and the MMF distribution during fault in (b), $\mathcal{F}_f$, according to equation 7.10. Seen from the stator reference angle ϕ, $\mathcal{F}_h$ can be expressed as equation 7.11 according to Ampère's law when sinusoidal MMF is assumed, where j^r is the current density of the field winding with amplitude J^r.

$$\mathcal{F}^r_{sc}(\phi, t) = \mathcal{F}_h(\phi, t) + \mathcal{F}_f(\phi_r) \tag{7.10}$$

$$\mathcal{F}_h(\phi, t) = \oint j^r(\phi, t)d\phi = \oint J^r sin(\omega_s t - p\phi)d\phi = \frac{J^r}{p} cos(\omega_s t - p\phi) \tag{7.11}$$

$\mathcal{F}_f$ can be expressed in term of Fourier series in the following way

$$\mathcal{F}_f(\phi_r) = a_0 + \sum_{n=1}^{\infty} a_n cos(n\phi_r) + b_n sin(n\phi_r), \tag{7.12}$$

where the Fourier coefficient is calculated in equation 7.13 to 7.15.

$$a_0 = \frac{1}{2\pi}\int_0^{2\pi} \mathcal{F}_f(\phi_r)d\phi_r = \frac{1}{2\pi}\left[\int_0^{\phi_1} \mathcal{F}_f d\phi_r + \int_{\phi_1}^{2\pi} \mathcal{F}_f d\phi_r\right] = 0 \tag{7.13}$$

$$\begin{gathered}
a_n = \frac{1}{\pi}\int_{-\pi}^{\pi} \mathcal{F}_f cos(n\phi_r)d\phi_r = \\
\frac{1}{\pi}\left[\int_{-\pi}^{-\phi'} \mathcal{F}_f cos(n\phi_r)d\phi_r + \int_{-\phi'}^{\phi'} \mathcal{F}_f cos(n\phi_r)d\phi_r + \int_{\phi'}^{\pi} \mathcal{F}_f cos(n\phi_r)d\phi_r\right] \approx \\
\frac{1}{\pi}\left[\int_{-\pi}^{-\phi'} F_P cos(n\phi_r)d\phi_r + \int_{-\phi'}^{\phi'} F_N cos(n\phi_r)d\phi_r + \int_{\phi'}^{\pi} F_P cos(n\phi_r)d\phi_r\right] = \\
\frac{1}{\pi}\left[\frac{F_P}{n}(sin(-n\phi') - sin(-n\pi) + sin(n\pi) - sin(n\phi')) + \frac{F_N}{n}(sin(n\phi') - sin(n\phi'))\right] \\
\frac{1}{\pi}\left[\frac{F_P}{n}(-sin(n\phi') - sin(n\phi')) + \frac{F_N}{n}(sin(n\phi') + sin(n\phi'))\right] = \\
\frac{1}{\pi}\left[\frac{-2F_P}{n}sin(n\phi') + \frac{2F_N}{n}sin(n\phi')\right] = \frac{2(F_N - F_P)}{n\pi}sin(n\phi')
\end{gathered} \tag{7.14}$$

$$\begin{gathered}
b_n = \frac{1}{\pi}\int_{-\pi}^{\pi} \mathcal{F}_f sin(n\phi_r)d\phi_r = \\
\frac{1}{\pi}\left[\int_{-\pi}^{-\phi'} \mathcal{F}_f sin(n\phi_r)d\phi_r + \int_{-\phi'}^{\phi'} \mathcal{F}_f sin(n\phi_r)d\phi_r + \int_{\phi'}^{\pi} \mathcal{F}_f sin(n\phi_r)d\phi_r\right] \approx \\
\frac{1}{\pi}\left[\int_{-\pi}^{-\phi'} F_P sin(n\phi_r)d\phi_r + \int_{-\phi'}^{\phi'} F_N sin(n\phi_r)d\phi_r + \int_{\phi'}^{\pi} F_P sin(n\phi_r)d\phi_r\right] = \\
\frac{1}{\pi}\left[\frac{F_P}{n}(-cos(-n\phi') + cos(-n\pi) - cos(n\pi) + cos(n\phi') + \frac{F_N}{n}(-cos(n\phi') + cos(-n\phi'))\right] \\
\frac{1}{\pi}\left[\frac{F_P}{n}(-cos(n\phi') + cos(n\pi) - cos(n\pi) + cos(n\phi') + \frac{F_N}{n}(-cos(n\phi') + cos(n\phi'))\right] \\
= 0
\end{gathered} \tag{7.15}$$

The MMF distribution of the demagnetizing component can noe be written as

$$\mathcal{F}_f(\phi_r) = \sum_{n=1}^{\infty} \frac{2(F_N - F_P)}{n\pi}sin(n\phi')cos(n\phi_r). \tag{7.16}$$

From a moving rotor point of view, the location of this component is determined by the reference angle, ϕ_r. However, seen from the stator, $\mathcal{F}_f$ rotates in the air-gap with velocity $\omega_r = \frac{\omega_s}{p}$ and, thus, its location depends on both the stator reference angle, ϕ, and the time,

t. Consequently, with 7.16 referred to the stator reference and with simplified notation for the amplitude of each term of the Fourier series, the total MMF of a rotor with an ITSC can be expressed as

$$\mathcal{F}^r_{sc}(\phi,t) = \mathcal{F}_h(\phi,t) + \mathcal{F}_f(\phi,t) = \frac{J^r}{p} cos(\omega_s t - p\phi) + \sum_{n=1}^{\infty} F_{f,n} cos\left(\frac{n}{p}\omega_s t - n\phi\right) \tag{7.17}$$

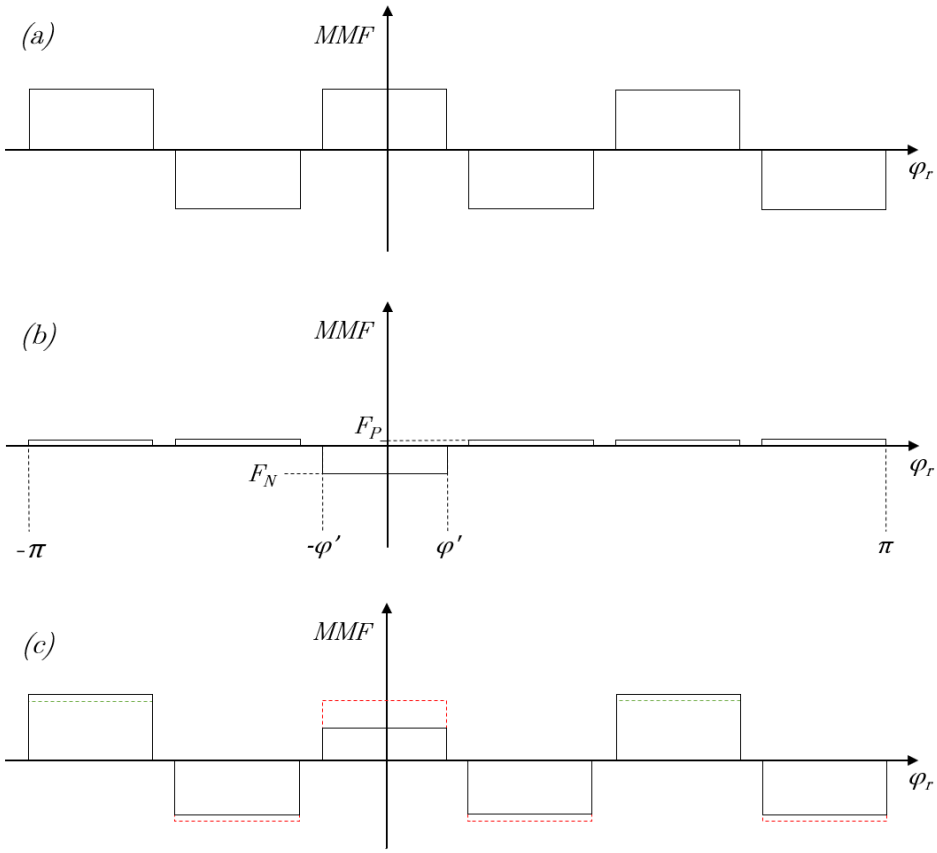

Figure 7.4: Approximate distribution of rotor MMF during healthy operation (a) and with an ISTC (c) influenced by a demagnetizing component (b).

C Winding layout of the laboratory generator

Slot	Top	Bottom
1	A	A
2	A	A
3	A	-B
4	-B	-B
5	-B	-B
6	-B	C
7	C	C
8	C	-A
9	C	-A
10	-A	-A
11	-A	B
12	B	B
13	B	B
14	B	-C
15	-C	-C
16	-C	-C
17	-C	A
18	A	A
19	A	-B
20	-B	-B
21	-B	-B
22	-B	C
23	C	C
24	C	C
25	C	-A
26	-A	-A
27	-A	B
28	-A	B
29	B	B
30	B	-C
31	-C	-C
32	-C	-C
33	-C	A
34	A	A
35	A	A
36	A	-B
37	-B	-B
38	-B	C

Slot	Top	Bottom
39	C	C
40	C	C
41	C	-A
42	-A	-A
43	-A	-A
44	-A	B
45	B	B
46	B	-C
47	B	-C
48	-C	-C
49	-C	A
50	A	A
51	A	A
52	A	-B
53	-B	-B
54	-B	-B
55	-B	C
56	C	C
57	C	-A
58	-A	-A
59	-A	-A
60	-A	B
61	B	B
62	B	B
63	B	-C
64	-C	-C
65	-C	A
66	-C	A
67	A	A
68	A	-B
69	-B	-B
70	-B	-B
71	-B	C
72	C	C
73	C	C
74	C	-A
75	-A	-A
76	-A	B

Slot	Top	Bottom
77	B	B
78	B	B
79	B	-C
80	-C	-C
81	-C	-C
82	-C	A
83	A	A
84	A	-B
85	A	-B
86	-B	-B
87	-B	C
88	C	C
89	C	C
90	C	-A
91	-A	-A
92	-A	-A
93	-A	B
94	B	B
95	B	-C
96	-C	-C
97	-C	-C
98	-C	A
99	A	A
100	A	A
101	A	-B
102	-B	-B
103	-B	C
104	-B	C
105	C	C
106	C	-A
107	-A	-A
108	-A	-A
109	-A	B
110	B	B
111	B	B
112	B	-C
113	-C	-C
114	-C	A

D Modeling specifications

D.1 Input parameters for the rotor UDP

Name	Value	Unit	Evaluated Value	Description
Command	CreateUserDefinedPart			
Coordinate System	Global			
Name	RMxprt/SalientPoleCore			
Location	syslib			
Version	17.0			
DiaGap	646.5	mm	646.5mm	Core diameter on gap side, DiaGap<DiaYoke for outer cores
DiaYoke	0	mm	0mm	Core diameter on yoke side, DiaYoke<DiaGap for inner cores
Length	0	mm	0mm	Core length
Skew	0	deg	0deg	Skew angle in core length range
Slots	7		7	Number of damper slots per pole
SlotType	1		1	Slot type: 1 to 4
Hs0	2	mm	2mm	Slot opening height
Hs01	0	mm	0mm	Slot closed bridge height
Hs1	0	mm	0mm	Slot wedge height
Hs2	0	mm	0mm	Slot body height
Bs0	2.5	mm	2.5mm	Slot opening width
Bs1	7.3	mm	7.3mm	Slot wedge maximum width
Bs2	7.3	mm	7.3mm	Slot body bottom width, 0 for parallel teeth
Rs	0	mm	0mm	Slot body bottom fillet
FilletType	1		1	0: a quarter circle; 1: tangent connection; 2&3: arc bottom.
SlotPitch	3.3	deg	3.3deg	Slot pitch in mechanical degrees, refer to offset point
CenterPitch	3.3	deg	3.3deg	Center slot pitch in mechanical degrees, refer to offset point
Poles	14		14	Number of poles
PoleType	1		1	Pole type: 1 or 2 (not valid for inner cores)
WidthShoe	108	mm	108mm	Pole shoe width
HeightShoe	22	mm	22mm	Pole shoe height at pole center
WidthBody	50	mm	50mm	Pole body width
HeightBody	70	mm	70mm	Pole body Height
AirGap2	0	mm	0mm	Second air gap length
Offset	53.25	mm	53.25mm	Pole arc offset
Off2_x	0	mm	0mm	The second pole arc offset perpendicular to the pole-center line
Off2_y	0	mm	0mm	The second pole arc offset parallel with the pole-center line
Bp1/Rp1	0	mm	0mm	Bp1: for pole type 1; or Rp1: shoe fillet radius for pole type 2, or for inner cores
Bp2/Rp2	0	mm	0mm	Bp2: for pole type 1; or Rp2: pole fillet radius for pole type 2 (not valid for inner cores)
CoilEndExt	2	mm	2mm	One-side coil end extended Length
EndRingType	2		2	0: whole press board; 1: pole press board; 2: pole ring; 3: whole ring
BarEndExt	2	mm	2mm	One-side damper bar end extended Length, for types 2 & 3 only
RingLength	5	mm	5mm	One-side axial ring length, or conductor press board thickness
RingHeight	6	mm	6mm	Radial ring height, for types 2 & 3 only
SegAngle	0	deg	0deg	Deviation angle for slot arches (10~30, <10 for true surface).
LenRegion	260	mm	260mm	Region length
InfoCore	0		0	0: core; 1: core & coils; 2: coil; 3: damper; 4: terminal1; 5: terminal2; 6: poles; 7: yoke

D.2 Calculation of leakage inductance

Leakage inductance can be estimated by equation B.1

$$L_l = \frac{4m_p}{Q_s} N^2 \mu_0 l_w \lambda_w q, \tag{B.1}$$

where m_p is the number of phases, Q_s is the number of slots, q is the number of slots per pole and phase and μ_0 is the permeability of vacuum [90]. For the laboratory generator, $m_p = 3$, $Q_s = 114$ and $q = 2 + \frac{5}{7}$. N is the number of series-connected turns in a phase winding given by

$$N = \frac{Q_s z_Q}{2am_p}, \tag{B.2}$$

where z_Q is the number of conductors per slot and a is the number of parallel current paths, respectively equal to 2 and 1 in the laboratory generator. The product $l_w \lambda_w$ can be calculated as

$$l_w \lambda_w = 2l_{ew} \lambda_{lew} + W_{ew} \lambda_W, \tag{B.3}$$

where l_{ew} is the axial length of the end winding measured from the end of the stack, W_{ew} is the coil span and λ_{lew} and λ_W are permeance factors. The two latter parameters are difficult to calculate due to end winding geometry [90]. However, since the end windings are relatively far from the iron parts, the end winding inductances are not very high, and empirically determination of λ_{lew} and λ_W is sufficient. For the topology of the laboratory generator, these were found to be 0.518 and 0.138, respectively. With $l_{ew} = 0.09$m and $W_{ew} = 0.150$m, the product $l_w \lambda_w = 0.114$m.

This leads to the calculation of end winding inductance to be

$$L_l = \frac{4 \cdot 3}{114} \cdot \left(\frac{114 \cdot 2}{2 \cdot 1 \cdot 3} \right)^2 \cdot 4\pi \cdot 10^{-7} \cdot 0.114 \cdot \left(2 + \frac{5}{7} \right) H = 0.236mH. \tag{B.4}$$

E Additional simulation results: full load operation

E.1 Inter-turn short circuit in the field winding

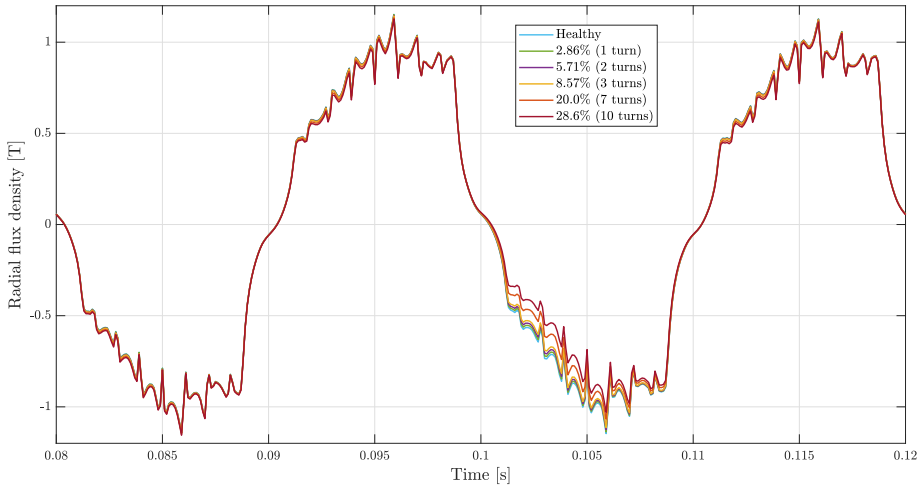

Figure 7.5: Time domain distribution of radial air-gap flux density during full load operation and inter-turn short circuit in the field winding.

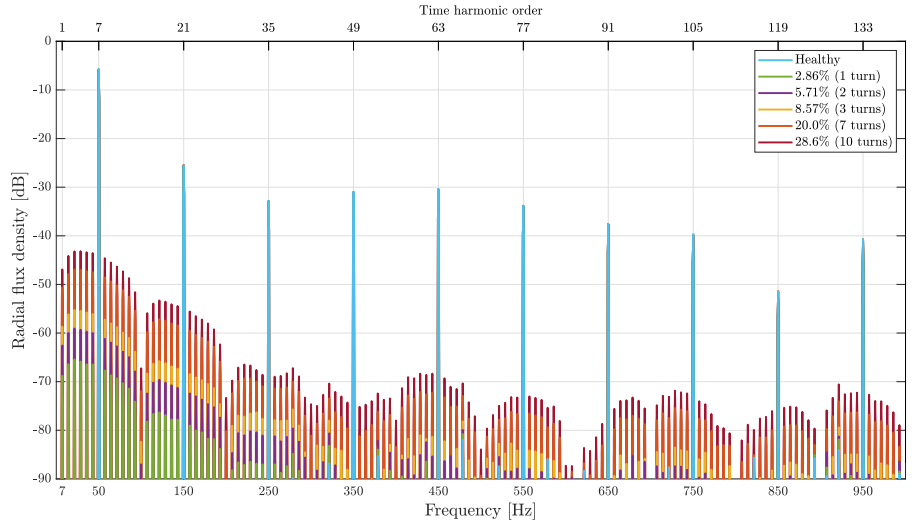

Figure 7.6: Frequency spectrum of the time domain distribution of radial air-gap flux density during full load operation and inter-turn short circuit in the field winding.

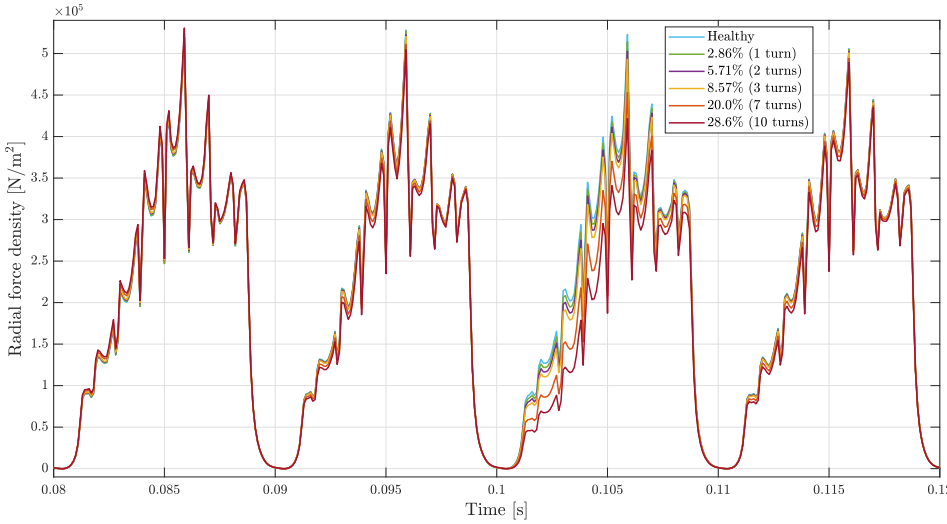

Figure 7.7: Time domain distribution of radial air-gap flux density during full load operation and inter-turn short circuit in the field winding.

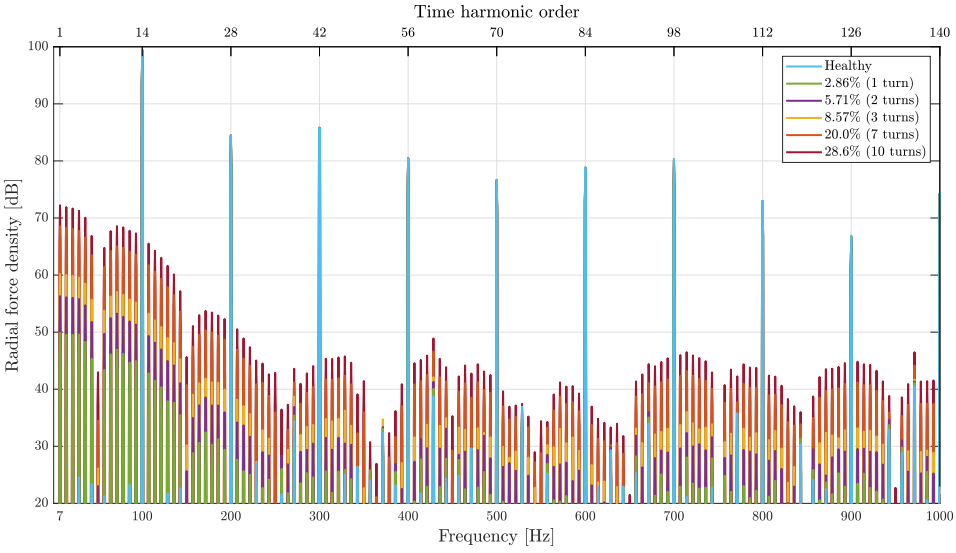

Figure 7.8: Frequency spectrum of the time domain distribution of radial air-gap force density during full load operation and inter-turn short circuit in the field winding.

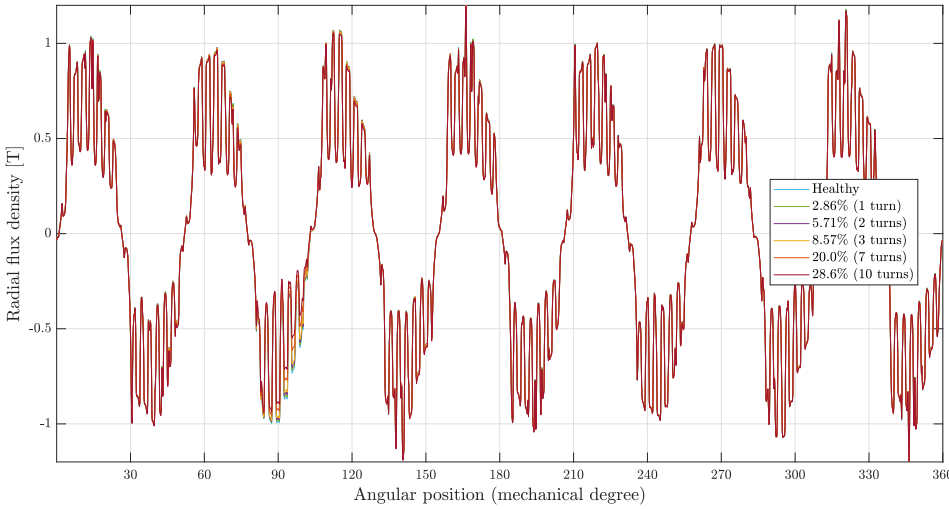

Figure 7.9: Spatial distribution of radial air-gap flux density during full load operation and inter-turn short circuit in the field winding.

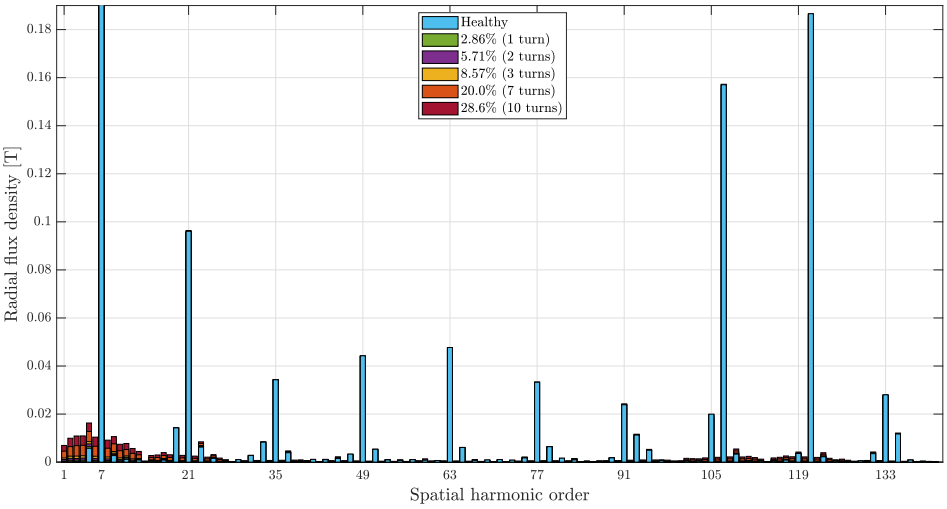

Figure 7.10: Frequency spectrum of the spatial distribution of radial air-gap flux density during full load operation and inter-turn short circuit in the field winding. The amplitude of the seventh-order harmonic is 0.78 T for all scenarios.

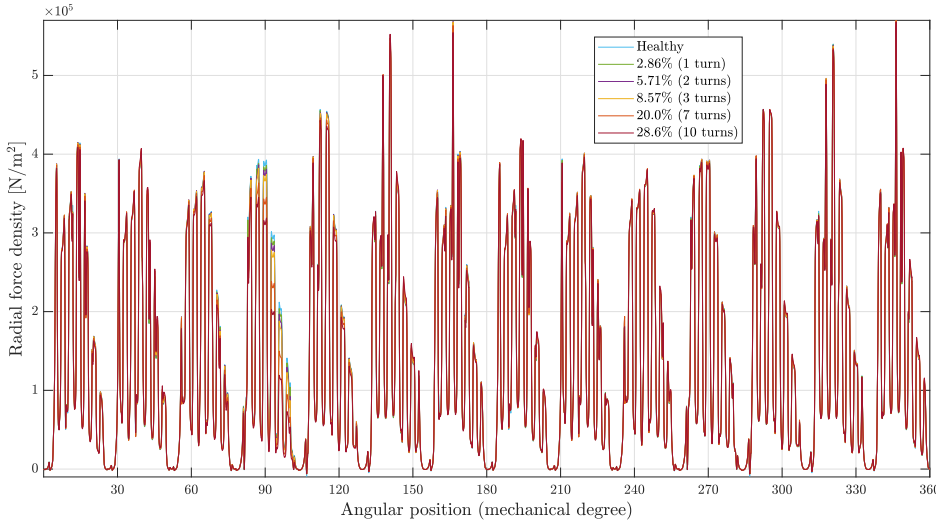

Figure 7.11: Spatial distribution of radial air-gap force density during full load operation and inter-turn short circuit in the field winding.

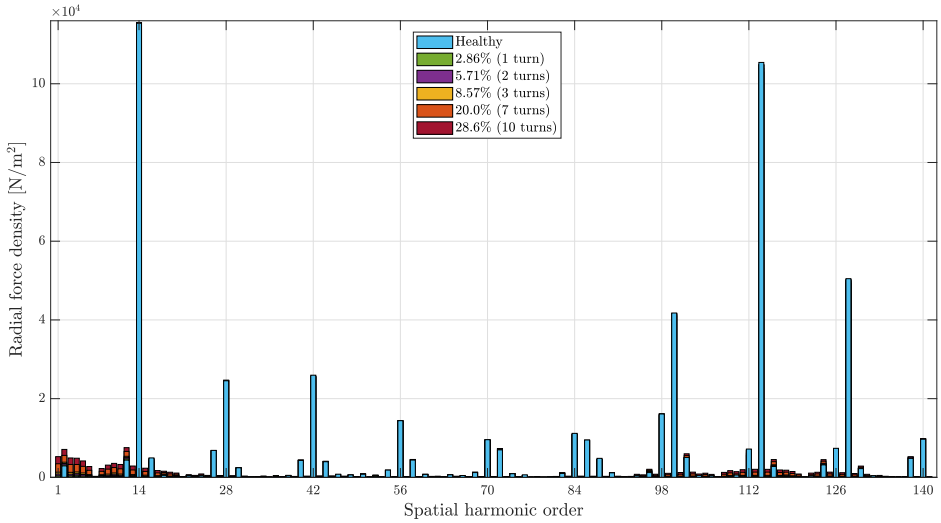

Figure 7.12: Frequency spectrum of the spatial distribution of radial air-gap force density during full load operation and inter-turn short circuit in the field winding.

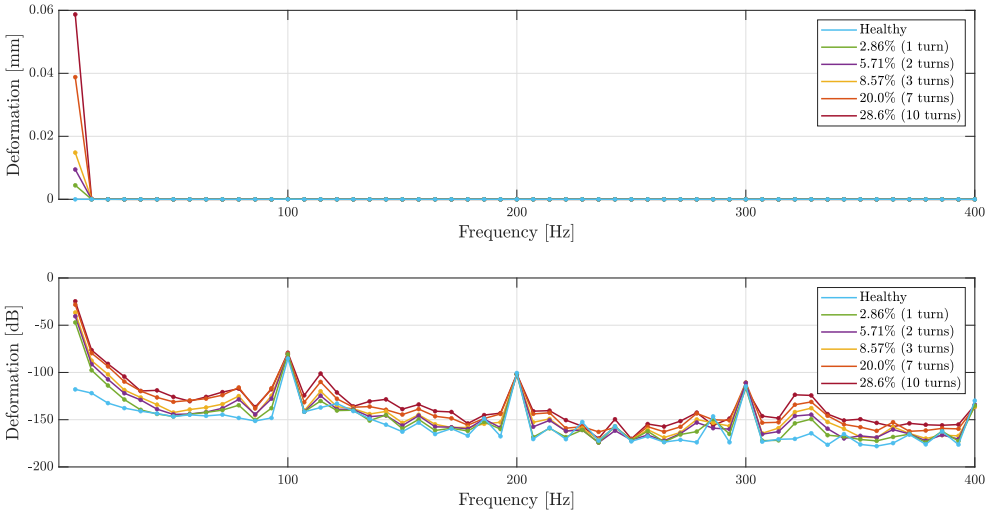

Figure 7.13: Frequency spectrum of stator yoke deformation during full load operation and inter-turn short circuit in the rotor winding. Top: actual values, bottom: logarithmic values.

E.2 Static eccentricity

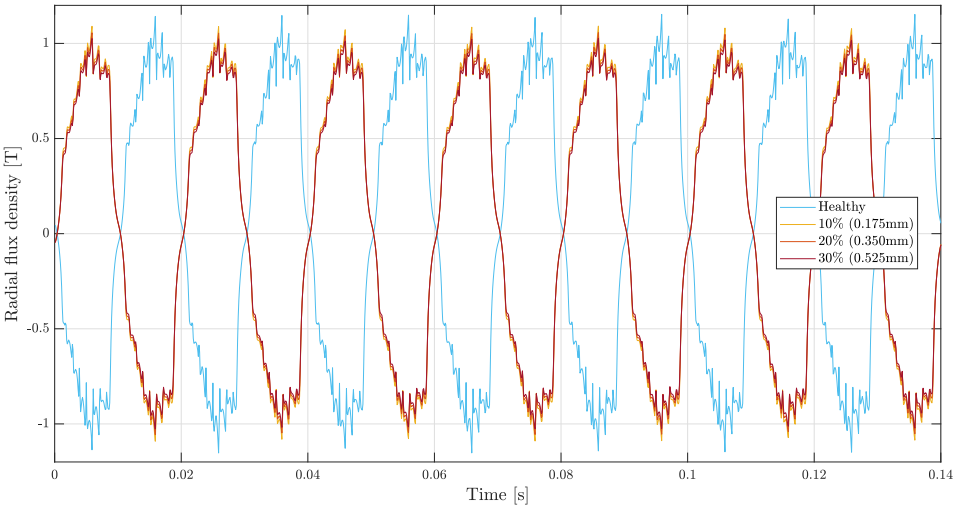

Figure 7.14: Time domain distribution of radial air-gap flux density during full load operation and static eccentricity.

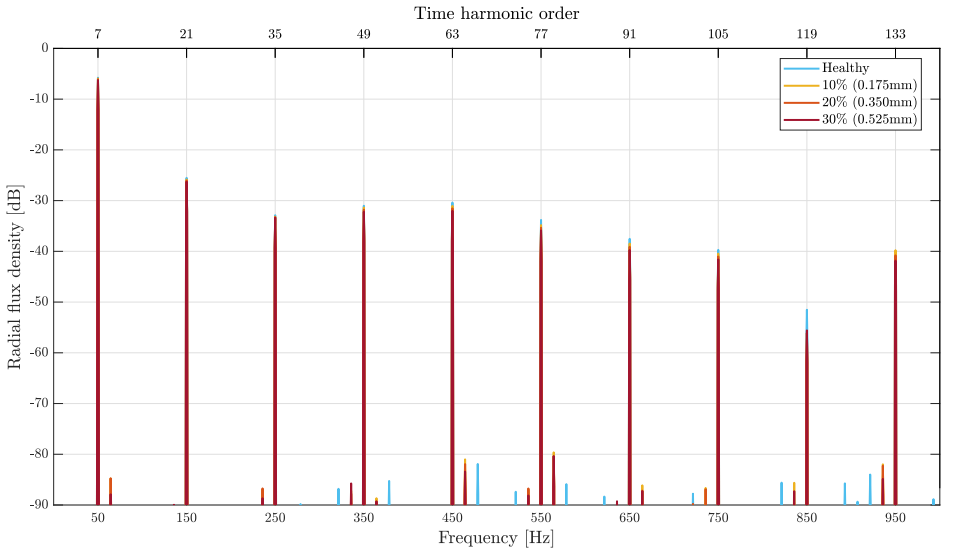

Figure 7.15: Frequency spectrum of the time domain distribution of radial air-gap flux density during full load operation and static eccentricity.

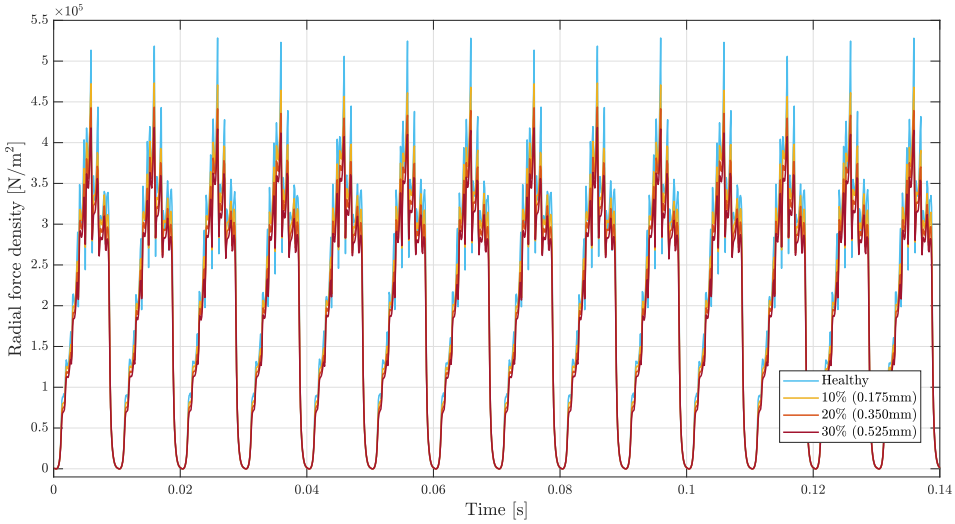

Figure 7.16: Time domain distribution of radial air-gap force density during full load operation and static eccentricity.

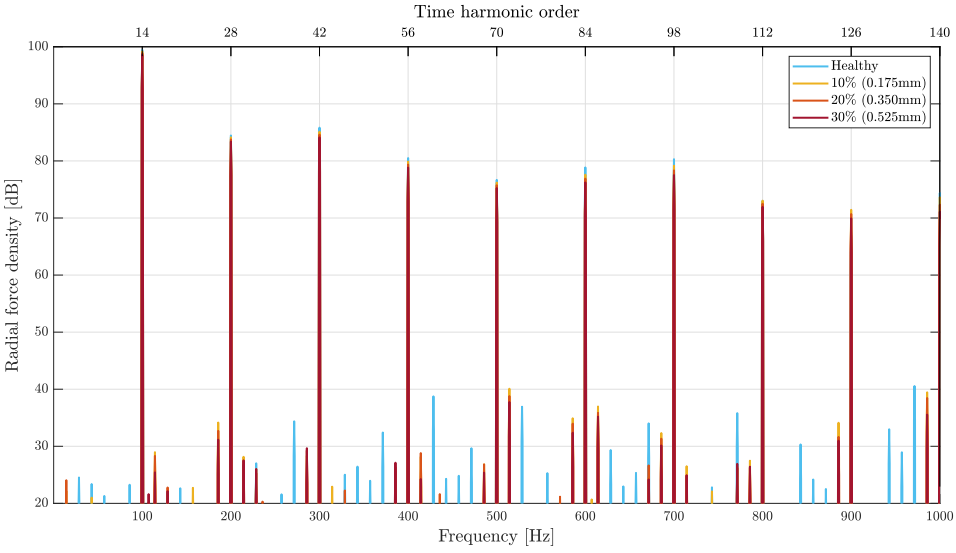

Figure 7.17: Frequency spectrum of the time domain distribution of radial air-gap force density during full load operation and static eccentricity.

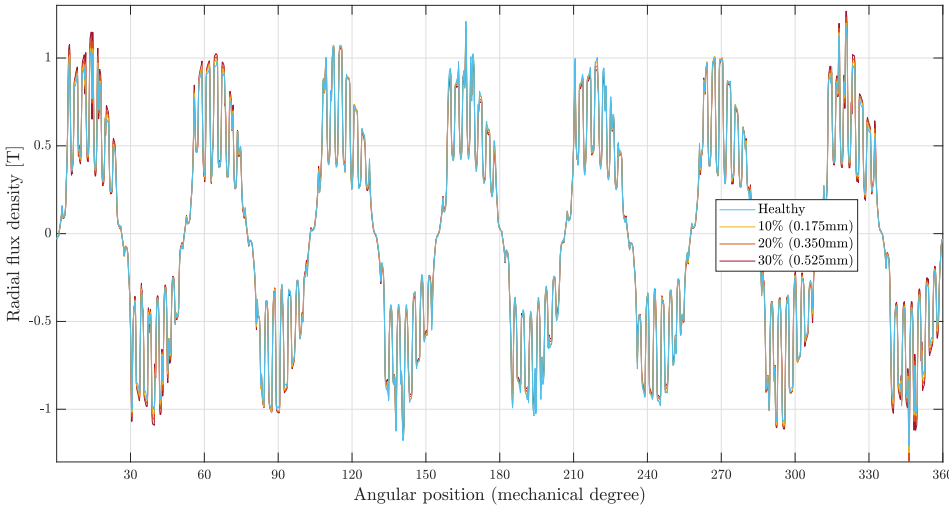

Figure 7.18: Spatial distribution of radial air-gap flux density during full load operation and static eccentricity.

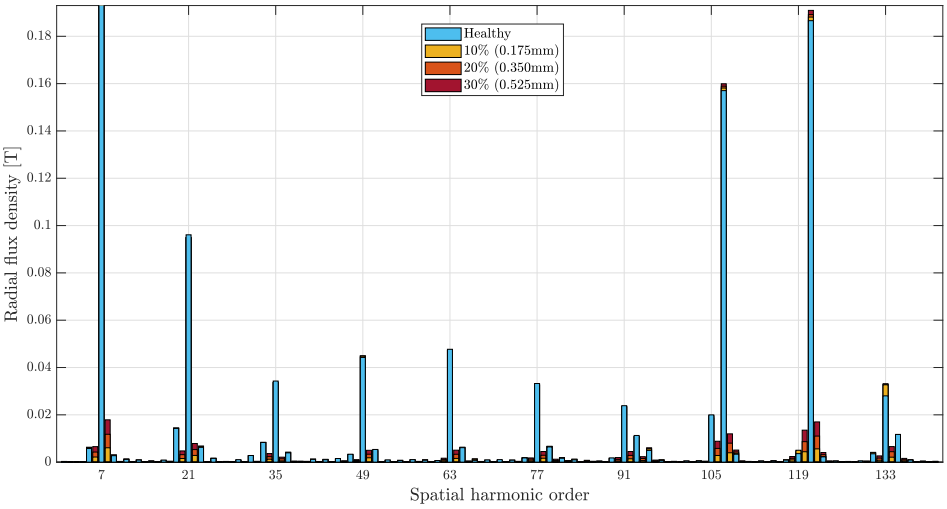

Figure 7.19: Frequency spectrum of the spatial distribution of radial air-gap flux density during full load operation and static eccentricity. The amplitude of the seventh-order harmonic is 0.78 T for all scenarios.

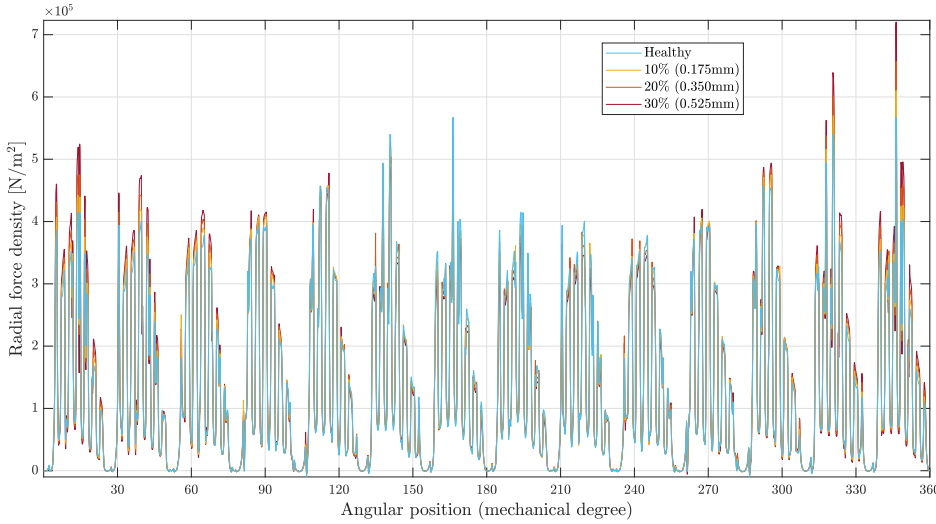

Figure 7.20: Spatial distribution of the radial air-gap force density during full load operation and static eccentricity.

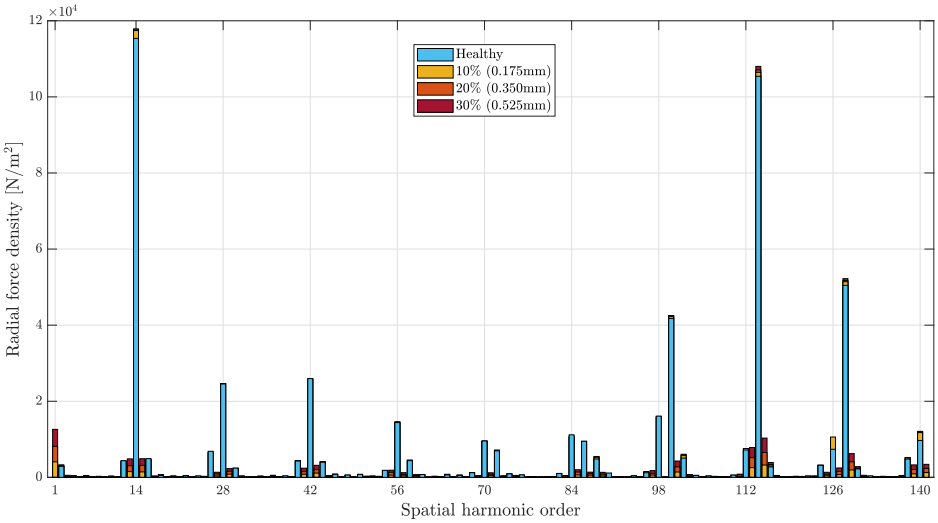

Figure 7.21: Frequency spectrum of the spatial distribution of the radial air-gap force density during full load operation and static eccentricity.

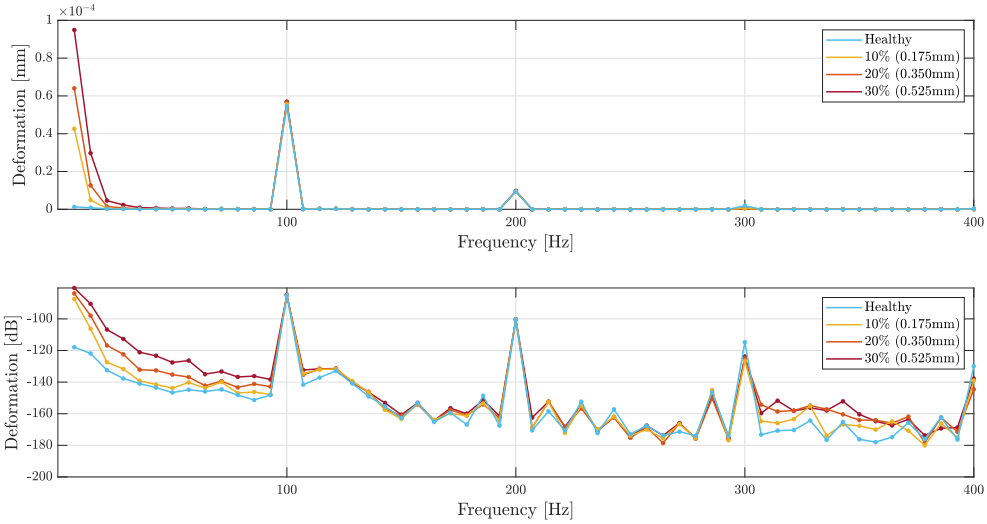

Figure 7.22: Frequency spectrum of stator yoke deformation during full load operation and static eccentricity. Top: actual values, bottom: logarithmic values.

Gaute Lyng Rødal

Online Condition Monitoring of Synchronous Generators using Vibration Signal

NTNU
Kunnskap for en bedre verden